Study of the Charmless b-hadron decay using the LHCb spectrometer

Hossein Afsharnia

UNIVERSITÉ CLERMONT AUVERGNE
ÉCOLE DOCTORALE DES SCIENCES FONDAMENTALES

THÈSE

présentée pour obtenir le grade de

Docteur d'Université

Spécialité : CONSTITUANTS ÉLÉMENTAIRES

par

Hossein AFSHARNIA

Study of the Charmless b-hadron decay using the LHCb spectrometer

Thèse soutenue publiquement le 12 décembre 2022 devant la commission déxamen :

Examinateurs :	Mme.	Sophie TRINCAZ-DUVOID	Rapporteure
	M.	Matthew CHARLES	Rapporteur
	Mme	Frédérique BADAUD-GRADY	
	M.	Philippe CROCHET	
Directeurs de thèse :	M.	Stephane MONTEIL	Directeur de thèse
	M.	Eric COGNERAS	Co-Directeur de thèse

Remerciements

C'est avant tout à Stéphane MONTEIL, mon directeur de thèse, que je voudrais témoigner ma profonde gratitude pour le rôle de coordinateur et de conseil qu'il a joué tout au long de ces quatre années. Il s'est montré d'une aide précieuse pour me guider et atténuer les périodes de tension au cours de la réalisation de cette thèse de doctorat et a été un conseiller clé pour la conduire vers ce qu'elle est devenue aujourd'hui.

J'adresse également mes sincères remerciements à Eric COGNERAS, mon co-directeur de thèse, que je respecte pour son engagement scientifique et dont j'ai beaucoup apprécié le soutien.

Je remercie tous les membres du jury, Sophie TRINCAZ-DUVOID, Matthew CHARLES, Frédérique BADAUD-GRADY et Philippe CROCHET pour l'intérêt qu'ils ont porté à mon travail, et le temps qu'ils m'ont accordé.

En outre, j'aimerais exprimer toute ma gratitude à l'Université Clermont Auvergne et au Laboratoire de physique de Clermont pour avoir initié et financé mes travaux de recherche durant les trois premières années de mon doctorat.

Je voudrais adresser des remerciements tout particuliers à Golriz, ma femme, qui m'a aidé et soutenu avec patience pendant toutes ces années et pour l'amour qu'elle m'a donné. De surcroît, j'ai grandement apprécié le soutien que mes parents et mon frère, bien qu'éloignés géographiquement, m'ont apporté renforçant ainsi au quotidien la motivation dont j'ai eu besoin pour traverser avec succès toutes ces années. De plus, je ne peux pas oublier l'amour et le soutien de Françoise qui m'aide comme une maman le fait vis-à-vis de ses enfants.

J'aimerais dédier une mention spéciale aux membres du LPC Régis, Vincent, Hervé, et aux anciens et actuels doctorants : Arthur, Mike, Halime, Sofia, Boris et Florian.

Je tiens aussi à souligner toutes les discussions que nous avons eues et le temps que nous avons passé avec Marie-Noëlle, Serge, Catherine, Jean-Louis, Hoda, Alireza, Aurélie et Georges-Henry.

Et je ne saurais oublier de mentionner Hannah et Parto dont la présence m'a donné de l'énergie positive et un enthousiasme débordant.

C'est grâce à vous tous qui m'avaient entouré et accompagné, et ce sans exception, que j'ai finalement mené à bien ce travail et réalisé ce rêve.

Aux femmes et aux hommes iraniens,
qui luttent actuellement pour leurs droits.
Pour
Femmes, Vie, Liberté.

Abstract

This document presents the methods and strategies to develop the unique tool to perform the studies on the charmless three body decay of $B^0_{d,s}$. Through this study the data collected at LHCb experiment during the RunI (2011-2012) and RunII (2015-2018) of LHC which corresponds to the integrated luminosity $\sim 9\,\text{fb}^{-1}$ is used. In all the method implementations, the concern to minimally biasing the phase space of the decay is taken into account.

First, the discrepancies between the MC and data according to the PID variables are studied and corrected by using the new method of `PIDCorr`.

The advantage of using this method, with respect to the previous PID correction method, is to preserve the correlation between PID variables during the process of PID correction. Then using the corrected PID variables, a PID MVA tool is trained to distinguish between the signal and the cross-feed background which results from the mis-identification of the decay products at the time of the event reconstruction. In training of this MVA tool, XGBoost algorithm and Scikit-Learn package is used.

In addition, another MVA which is trained against combinatorial background is used next to PID MVAs and a two dimensional optimization is performed in order to maximize the significance of signal events.

Furthermore, the signal efficiency study is performed across the phase space of the decay. During this study, other sources of discrepancies between MC and data, namely tracking and L0 triggering, are corrected and the efficiency patterns is provided. Then, a systematic study is done in order to evaluate the existing biases according to the methods which are used in data preparation.

Finally, using the existing mas-fit result a consistency check is done between efficiencies and mass-fit result and it approves the reliability of the method which is used in this development and study.

Keywords:

LHCb experiment - Standard Model - Flavour Physics - Charmless b-hadron decay - $B^0_{d(s)} \to K^0_S h^\pm h'^\mp$ - XGBoost .

Résumé

Ce document présente les méthodes et les stratégies pour développer un outil commun pour effectuer les études sur les désintégrations à trois particules non charmées de $B^0_{d,s}$. A travers cette étude, les données collectées à l'expérience LHCb pendant les RunI (2011-2012) et RunII (2015-2018) du LHC qui correspondent à la luminosité intégrée $\sim 9\,\text{fb}^{-1}$ sont utilisées. Dans toutes les implémentations du procédé, le souci de polariser au minimum l'espace des phases de la désintégration est pris en compte.

Tout d'abord, les écarts entre le MC et les données selon les variables PID sont étudiés et corrigés en utilisant la nouvelle méthode de `PIDCorr`. L'avantage d'utiliser cette méthode, par rapport à la méthode de correction PID précédente, est de préserver la corrélation entre les variables PID pendant le processus de correction PID. Ensuite, en utilisant les variables PID corrigées, un outil PID MVA est formé pour faire la distinction entre le signal et le fond d'alimentation croisée qui résulte de la mal-identification des produits de désintégration au moment de la reconstruction de l'événement. Dans la formation de cet outil MVA, l'algorithme XGBoost et le package Scikit-Learn sont utilisés.

En sus, un autre MVA qui est formé sur fond combinatoire est utilisé à côté des MVA PID et une optimisation bidimensionnelle est effectuée afin de maximiser le significance des événements de signal.

De plus, l'étude de l'efficacité du signal est effectuée dans l'espace des phases de désintégration. Au cours de cette étude, d'autres sources d'écarts entre MC et les données, à savoir le tracking and L0 triggering, sont corrigées et les modèles d'efficacité sont fournis. Ensuite, une étude systématique est effectuée afin d'évaluer les biais existants selon les méthodes qui sont utilisées dans la préparation des données.

Enfin, en utilisant le résultat de mass-fit existant, une vérification de cohérence est effectuée entre les rendements et le résultat de mass-fit, et elle approuve la fiabilité de la méthode utilisée dans ce développement et cette étude.

Mots Clés:

Expérience LHCb - Modèle Standard - Physique des Saveurs - Désintégration des b-hadrons non charmées - $B^0_{d(s)} \to K^0_S h^\pm h'^\mp$ **- XGBoost**.

Contents

Introduction

One of the well-known open question in physics and cosmology is the observed matter-antimatter asymmetry in universe [1,2]. An excess of matter with respect to the produced antimatter leads to its survival through the process of matter-antimatter annihilation, and in turn it forms a matter-dominated universe. However, to have this difference in production mechanism, matter and antimatter must have a difference to which the production mechanism is sensitive. Up to now, the only non-trivial difference which is observed between matter and anti matter is $\mathcal{CP}$ asymmetry and the condition which is required to generate this asymmetry is called $\mathcal{CP}$-violation [3].

$\mathcal{CP}$-violation has been established in K- and B-meson systems [4–6] . More specifically, the B-meson decays to two light pseudoscalars have shown the asymmetries up to 10%. Although the Quantum Chromodynamics (QCD) approach predicts that the asymmetries in $\bar{B}^0 \to \pi^+ K^-$ and $B^- \to \pi^0 K^-$ to be the same [7], the measured values are different [8,9]. This difference is known as $K\pi$ puzzle [10–12]. Therefore, the flavor-specific study for decays such as $B^0_{d,s} \to K^0_S \pi^+ \pi^-$ using quasi-two-body methods can provide a good measure for $\mathcal{CP}$-violation. To be more specific, study of the final state comprised of a vector and a pseudoscalar might help in order to solve the $K\pi$ puzzle[†]

Within the Standard Model (SM) weak phase measurement, the measured value for $b \to q\bar{q}s$ and $b \to c\bar{c}s$ (where q is either one of the light quarks of up, down or strange, and c is the charm quark) decays are expected to be different; however, the determined $\mathcal{CP}$ asymmetry in specific contributions ($e.g. B^0 \to \phi K^0_S$ and $B^0 \to \rho^0 K^0_S$) is approximately equal or can be controlled using flavor symmetries [14–16]. The existence of physics beyond the SM can help in this respect. The addition of new weak phase which can contribute next to the existing SM mixing phase can result into much greater deviation for $b \to q\bar{q}s$ results compared to $b \to c\bar{c}s$ measurements [17–19]. As a result, precision measurements of these weak mixing phases is required. A flavour-tagged time-dependent analysis of the Dalitz plot can be used to measure the mixing-induced $\mathcal{CP}$-violating phase [20–24].

Another important measurements relevant to $B^0_{d,s} \to K^0_S h^\pm h'^\mp$ study are the branching fractions. Several scenarios($e.g.$ PQCD and QCD factorisation) are implemented in order to model the hadronization process and each can result into its corresponding branching fraction results (see the refs. [25–31]). Using experimental data, the theoretical models can be improved and the improved models enable us to enhance the predictions of branching

[†]The details of the first $\mathcal{CP}$ asymmetry observation in $\bar{B}^0 \to K^*(892)^- \pi^+$ as an example of such decay is given in Ref. [13]

fractions and CP asymmetries for other charmless decay modes. Furthermore, this results can be utilized to implement flavour symmetry breaking tests (*e.g.* isospin, U-spin and $SU(3)$) [32]

According to the the interconnection between $\mathcal{CP}$ measurement and determination of branching fraction, a common tool is developed to perform optimal selections for the future $B^0_{d,s} \to K^0_S h^\pm h'^\mp$ studies and present the possible correction and systematic which are subject to each analysis in a common way.

Through this study in the first chapter, the theoretical framework $B^0_{d,s} \to K^0_S h^\pm h'^\mp$ is developed. Then in Chapter two, LHCb spectrometer and its sub-systems are described briefly to highlight the performances of the experimental apparatus which is used for detection, measurement and data taking.

In chapter three the development of a novel algorithm for Particle Identification PID is described. The novel method of `PIDcorr` to provide a correction for the PID variables of the Monte Carlo (MC) samples is discussed and implementation of XGBoost algorithm to develop a new tools to discriminate between signal and cross-feed background, is explained.

In chapter four, by introducing another XGBoost algorithm, developed by LPNHE `Kshh` group, a 2 dimensional optimization is developed to provide an optimal point to maximize the significance of signal events.

In chapter five using the optimized cuts in chapter 4, the efficiency patterns according to online and offline selection is studied. Also other than PID two other discrepancies between the MC and data according to tracking and triggering system is discussed. The final part of this chapter is dedicated the result of the studies on the possible sources of systematics according to the utilized methods in this analysis.

In chapter six, using the above described and devised methods, a corrected efficiency pattern is determined across the phase space of the analysis. Then using this pattern an averaged efficiency of each sample is determined and by utilizing the mass-fit results which are developed by LPNHE `Kshh` group, a comparison between efficiencies and mass-fit results are presented and a preliminary estimation for determination of ration branching fraction is performed.

Chapter 1

Theoretical framework

1.1 The Standard Model

Since the 5th century BC the idea that all things can be composed of innumerable combinations of hard, small, indivisible particles, called atoms, enter in to the philosophical mindset of the human [33, 34]. However, it takes 23 centuries till this philosophy formed into a scientific theory of matter. This new theory introduced by John Dalton, and he stated that these small indivisible constituent of the matter cannot be changed by chemical reactions and their combination define the chemical properties of the matter [35]. This idea holds for about a century till J.J Thomson and his discovery of the electron as the first elementary particle [36].

Thereafter, subsequent studies on internal structure of the atoms revealed the nature of different phenomena, such as radioactivity and lead in to new theory of quantum mechanics. Meanwhile, studies on the cosmic rays and discovery of pions and muons has caused physicist to categorize the particles. This was the time that "baryons", "mesons" and "leptons" were introduced in the particle physics terminology.

Little by little and due to the vast improvement in accelerator sciences and engineering, numerous amount of particles were discovered. These discoveries indicated that there must be a more profound structure of the matter, which lead into quark model and theory of strong interactions. In parallel, study of β-decay formed the theory of weak interactions and then through unification with electromagnetism, the electroweak theory is formulated. Finally, the introduction of Higgs mechanism along with combination of strong, weak and electromagnetic interactions formed the most accurate theory of the physics, called Standard Model(SM) which describes how fermions (quarks and leptons) are interacting and make up all known matter.

Within SM, in order to describe the matter content of the universe fermions are defined as the constituent of matter, while the bosons are the mediators of the forces and interactions between them. It was through this theory that we could predict the existence of $W^{\pm}$ and Z^0 bosons as well as top quark fermion and determine some of their expected properties before their discovery. Finally, in 2012 the discovery of the Higgs boson revealed the last piece of SM. In order to challenge SM and its predictions, many

precision measurements have performed on it which confirmed its accuracy.

In QFT, the particles are nothing but excitation of quantized fields. Each of these fields can carry out an individual spin, which is known as an intrinsic form of the angular momentum. Depending on the value of this spin, we can categorize these fields as fermionic or bosonic fields whose quanta obey the Fermi-Dirac statistics or Bose-Einstein, respectively. The fermionic fields whose excited states are called fermions have a half-integer spin while bosonic fields, and consequently bosons as their excited states, have an integer spin.

Within the SM formalism, the matter is comprised of fermions. They are distributed between leptons (which do not sense the strong force) and quarks (which are sensitive to all interactions). The quark category itself comprises six various flavor named as up, down, charm, strange, top and bottom (beauty) whose symbols are u, d, c, s, t and b respectively. Furthermore, they can be divided into three generations, which is shown in the following $SU(2)_L$ doublets:

$$\begin{pmatrix} u \\ d \end{pmatrix}, \begin{pmatrix} c \\ s \end{pmatrix} and \begin{pmatrix} t \\ b \end{pmatrix},$$

where the first one is the lightest and the last one is the heaviest generation. The heavier generations are decaying by means of weak interaction into lighter generations. (u, c, t) is the group of quarks with electric charge of $+\frac{2}{3}e$ of the elementary electric charge e and (d, s, b) are forming a group with electric charge of $-\frac{1}{3}e$. The quark masses covering the range of few MeV/c^2 for u and d up to 173 GeV/c^2 for t quark. Quark masses are free parameters in the SM. Their definition is not unique, their mass depend on the energy scale.

The quarks cannot be observed in an isolated stated. This behavior is described through the phenomenon called color confinement [37]. All quarks but the top are forming a bound state called hadron by means of strong interaction (*i.e.* hadronization) with a timescale of $10^{-23}s$. However, top quark is an exception, because its mass is large enough for it to decay faster than the timescale of hadronization. The combination of quarks into hadrons results in states that must be colorless. Therefore, the possible combinations are $q\bar{q}'$ and qqq which are known as Mesons and Barons, respectively. Also, some other exotic combination such as $qq\bar{q}q$ (*i.e.* tetraquarks) and $qqqq\bar{q}$(*i.e.* pentaquarks) are possible, which are subject to many studies in recent years.

Similar to quarks in SM, there are six types of leptons which can be categorized in three generations of $\begin{pmatrix} e^- \\ \nu_e \end{pmatrix}$, $\begin{pmatrix} \mu^- \\ \nu_\mu \end{pmatrix}$ and $\begin{pmatrix} \tau^- \\ \nu_\tau \end{pmatrix}$. Each generation consists of a charged lepton (the second element of the weak isospin doublet) and its neutral counterpart, which cannot sense the electromagnetic force. The Fig.1.1 represents the particle content of the SM and their properties as table.

1.2 Symmetries in SM

Along with the continuous time-space transformations (translations and rotations) that are yielding the conservation of energy, momentum and angular momentum, one can find

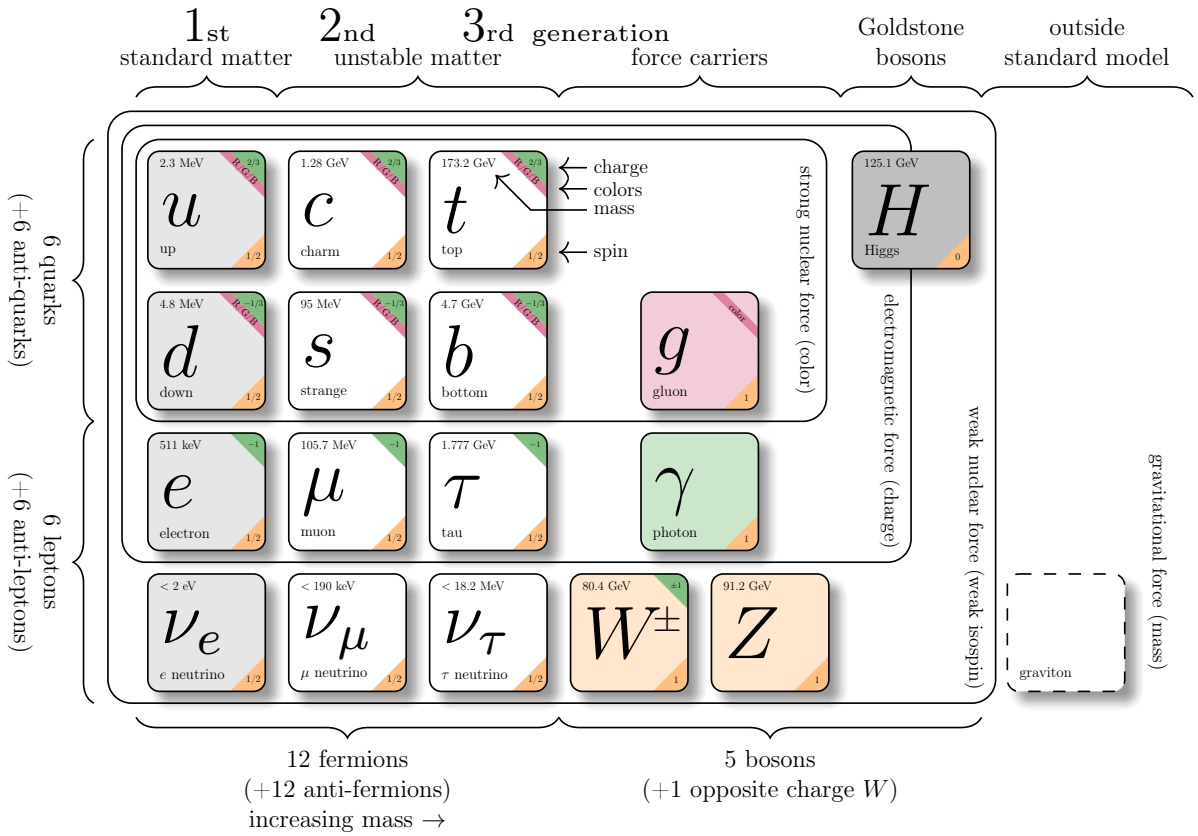

Figure 1.1: Table of particles and their properties in the Standard Model of particle physics. Taken from ref. [38].

discrete space-time transformations that have a specific status in the building of the SM: parity, charge conjugation and time reversal symmetries. The former two are maximally broken in the SM and are used to define the symmetry groups of the SM gauge theory.

1.2.1 Parity

Parity is the spatial inversion, embodied the Poincaré symmetry group. When applying the Parity operator, we would have $\vec{x} \to -\vec{x}$ and $t \to t$; thus, this operator preserves the angular momentum of the system. Therefore, it is possible to specify another observable for the particle under consideration by combining momentum $\vec{P}$ and angular momentum $\vec{L}$. This new quantity is called Helicity, i.e. $H = \frac{\vec{L}.\vec{P}}{|\vec{P}|}$, which is simply the projection of angular momentum in the direction of linear momentum. According to the definition of helicity, the particles are divided into two categories of left-handed ($H = -1$) and right-handed ($H = +1$) particles. Consequently, it is possible to observe that the parity operator can change a right-handed particle to a left-handed particle and vice-versa.

Parity was first applied to the electromagnetic and strong interactions, and in fact it

was verified to be conserved in these interactions. By contrast, the observation of θ^+ and τ^{+*} decays to opposite parity eigenstates 2π and 3π at the same time, while showing the same lifetime and masses, cannot be justified. Yang and Lee in 1956 [39] have indeed posited that parity can be violated by weak interaction. The famous ^{60}Co experiment by Prof. Wu [40], and also pion beta decay [41, 42] experiment, have firmly established this violation. The Goldhaber experiment furthermore showed that only left-handed chiral particles and right-handed chiral antiparticles are involved in the charged weak interactions of the Standard Model.

1.2.2 Charge conjugation

Charge conjugation intrinsically transforms a particle into its corresponding antiparticle without changing momentum and spin. Thus, by definition, this operator negates all internal quantum numbers of the field which are electric charge, baryon number, lepton number and flavor of it. The charge conjugation, analogous to the parity, is invariant in electromagnetic and strong interactions while it is maximally violated in charged weak interactions [43].

1.2.3 Time reversal

A Poincaré time reversal operator changes the time component of the spacetime four-vector as $(t, \vec{x}) \rightarrow (-t, \vec{x})$. This property of time reversal is due to the antilinearity and antiunitarity features of this operator that exchanges the initial and final states. The fact that the time-reversal symmetry is not invariant was initially inferred from CP violation constraints [44] while the first definitive observation of this non-invariance has been recently made in the B^0 system [45].

1.2.4 $\mathcal{CP}$ and CPT combinations

Although the aforementioned symmetries of charge conjugation and parity ($\mathcal{C}$, $\mathcal{P}$) are broken individually the invariance of the combined symmetry, i.e. $\mathcal{CP}$, had been suggested [46]. The first desirable characteristics of the combined inversion operator is the restoration of the left-right symmetry. The second appealing point is the absence of conflicts with the understanding of the other forces. And yet, experimental confirmation for $\mathcal{CP}$ violation was later reported in the neutral kaon [6] and B meson [4] systems.

In this framework, one of the most fundamental principles to describe nature is the CPT theorem, which formally expresses the invariance of the Hamiltonian density under the combined operators' product. Since the CPT theorem relates the Lorentz invariance and causality, it is considered of great significance within the community. It is interesting to notice that, in the event of time-reversal violation, $\mathcal{CP}$ violation is in fact implied in order to preserve the CPT symmetry. To this date, there is no experimental evidence for the violation of CPT symmetry.

*Later, θ^+ and τ^+ have been associated to the same particle, now known as the K^+ meson

1.2.5 Violation of $\mathcal{CP}$ in SM

The electroweak Standard Model is a theory that formalizes the fundamental interactions of elementary particles as a local gauge theory, which is itself expressed as the product of symmetry groups [47]

$$SU(3)_C \times [SU(2)_L \times U(1)_Y] \ , \tag{1.1}$$

The unification of quantum electrodynamics (QED) and weak interactions is realised by requiring the local gauge invariance of kinetic fermion lagrangian density under the transformation of the symmetry group $SU(2)_L \times U(1)_Y$ [48–50]. The lagrangian mass terms of fermions and gauge bosons are however breaking the local gauge invariance. It is overcome by the introduction of a $SU(2)_L$ doublet of complex scalar fields, that is spontaneously breaking the symmetry when the field acquires a non-zero vacuum expectation value. This is referred to as Brout-Englert-Higgs mechanism [51, 52]. The gauge fields are acquiring a mass by absorbing three out of the four degrees of freedom of the complex scalar field doublet. The remaining degree of freedom is the so-called Higgs boson. A narrow boson so far consistent with the SM Higgs boson, has been discovered at the LHC [52, 53]. Fermions can interact in turn with the scalar field, exhibiting Yukawa couplings proportional to their mass. Their value however cannot be predicted by the model.

The underlying Lagrangian of this model has several main contributions: gauge-boson kinematics and self-interaction terms; fermion fields kinematics and interactions; a potential, ruled by the scalar field and its self-couplings; and Yukawa couplings. All the quantities are formulated as $\mathcal{CP}$ invariant terms but the Yukawa couplings, that we detail below:

Fermions of the standard model, i.e. quarks and leptons, are grouped into either right-handed singlets or left-handed doublets. The Yukawa Lagrangian is formulated as:

$$\mathcal{L}_{Yukawa} = -Y^d_{ij}\overline{Q^i_L}\phi d j_R - Y^u_{ij}\overline{Q^i_L}\tilde{\phi} u j_R - Y^l_{ij}\overline{L^i_L}\phi l^j_R + h.c. \ , \tag{1.2}$$

in which the labels i and j represent flavour generations, the subscripts of L and R indicate the handedness of the fermion, Y_{ij} are complex coupling matrices, $Q(L)$ and $u/d(l)$ are respectively the doublets and singlets for quarks (leptons) and $\phi(\tilde{\phi})$ is the field (charge conjugate field) of the Higgs doublet. Only quarks are considered in the following. When the symmetry is spontaneously broken, the Higgs couplings obtain their vacuum expectation value, which in the unitary gauge choice is

$$\begin{aligned}\mathcal{L}_{Yukawa} &= -Y^d_{ij}\overline{d^i_L}\frac{v+h(x)}{\sqrt{2}}d^i_R - Y^u_{ij}\overline{u^i_L}\frac{v+h(x)}{\sqrt{2}}u^j_R \\ &= \sum_{f,i,j}\overline{f^i_L}M^{ij}_f f^j_R(1+\frac{h(x)}{v})\end{aligned} \tag{1.3}$$

where M^{ij}_f matrices represent all information related to the Yukawa couplings, $h(x)$ is the real scalar Higgs particle and v is the vacuum expectation value. Within this

representation, the Lagrangian provides a mass term for the considered fermion as a consequence of interaction between the Higgs field and a pair of fermion-antifermion.

Although the matrices M_f^{ij} are generally complex-valued, which naturally leads to the complex phase needed for the $\mathcal{CP}$ violation, this term is non-physical. However, it should be noted that the flavor eigenstates related to this coupling matrix are not identical to the mass eigenstates. In fact, it is necessary to diagonalise this matrix, using a unitary transformation, in order to extract the fermion masses:

$$M_f^{\text{diag}} = (U_L^f)^\dagger M_f U_R^f \tag{1.4}$$

In this basis, known as the mass basis, the diagonal elements are real and positive. Therefore, the fermion mass-eigenstates, and the corresponding eigenvalues of the fermion masses, are derived by applying the transformation:

$$f'^i_{L,R} = (U^f_{L,R})_{ij} f^j_{L,R}.$$

Eventually, by inserting Eq. 1.4 into Eq. 1.3, the invariant Lagrangian is derived in the new basis. The handedness property of the unitary transformation matrix introduces a key feature in the model. Only charged current interactions, mediated by $W^\pm$ bosons, can result in changes in quark flavor. In contrast, it should be noted that here we only consider the tree-based diagrams while we can take into account, by means of loop processes, the flavor changing process for neutral current interactions. The corresponding Lagrangian prior to the rotation, and afterward, is provided in the quark scenario as

$$\mathcal{L}_{W^\pm} = -\frac{g}{\sqrt{2}} \overline{u}_L \gamma^\mu d_L W^+_\mu + h.c. \tag{1.5}$$

$$= -\frac{g}{\sqrt{2}} \overline{u}_{Li} \gamma^\mu \left(U_L^u U_L^{d\dagger} \right)_{ij} d_{Lj} W^+_\mu + h.c. \ , \tag{1.6}$$

where the u_L and d_L quark families are coupled through the expression $\left(U_L^u U_L^{d\dagger} \right)$, known as the Cabibbo-Kobayashi-Maskawa (CKM) matrix. The CKM matrix now absorbs the complex phases of the Yukawa couplings which are responsible for all $\mathcal{CP}$ violation effects in the SM as mentioned above.

1.3 CKM Matrix

From an historical point of view, the first approach to explain mixing between quark families was suggested to allow the universality of weak interactions [54]. It was noticed that the evidence of $\mathcal{CP}$ violation in the neutral kaon sector suggests the presence of a complex phase factors in the mixing matrix, which is not possible in a 2×2 matrix featuring only two generations of quarks. Indeed, once the quark field phases are redefined, this matrix can be described with a unique real parameter. Therefore, Kobayashi and Maskawa generalized the Cabibbo matrix to three generations of quarks. In this case a

single complex phase exists [55]. This quark-mixing matrix is schematically depicted as,

$$V_{\rm CKM} = \begin{pmatrix} V_{ud} & V_{us} & V_{ub} \\ V_{cd} & V_{cs} & V_{cb} \\ V_{td} & V_{ts} & V_{tb} \end{pmatrix}, \tag{1.7}$$

where the magnitude squared of each element provides the transition probability between quarks with corresponding indices.

As a unitary 3x3 complex matrix, the CKM matrix can be described with four independent parameters, three being real and one being a phase responsible for the violation of $\mathcal{CP}$ symmetry

The flavor mixing matrix could be parameterized in different ways; however, one of the most standard forms of this matrix could be obtained by the product of three complex rotation matrices as follows [56],

$$V_{CKM} = \begin{pmatrix} c_{12}c_{13} & s_{12}c_{13} & s_{13}e^{-i\delta} \\ -s_{12}c_{23} - c_{12}s_{23}s_{13}e^{i\delta} & c_{12}c_{23} - s_{12}s_{23}s_{13}e^{i\delta} & s_{23}c_{13} \\ s_{12}s_{23} - c_{12}c_{23}s_{13}e^{i\delta} & -c_{12}s_{23} - s_{12}c_{23}s_{13}e^{i\delta} & c_{23}c_{13} \end{pmatrix} \tag{1.8}$$

in which $s_{ij} = \sin\theta_{ij}$, $c_{ij} = \cos\theta_{ij}$ for $i, j = 1, 2, 3$ while, the phase δ describes $\mathcal{CP}$ violation. In addition to this representation, there is another method for representing the flavor mixing matrix (first introduced by Wolfenstein [57]) which arranges the elements of the matrix in order of their magnitudes as follows,

$$\lambda = s_{12},\ A = \frac{s_{23}}{s_{12}^2},\ \rho = \frac{s_{13}}{s_{12}s_{23}}\cos\delta \text{ and } \eta = \frac{s_{13}}{s_{12}s_{23}}\sin\delta, \tag{1.9}$$

in which $\lambda \approx 0.22$ is $\sin\theta_c$ where θ_c is Cabbibo angle while η, ρ and A are real parameters of the order of unity.Writing the CKM-matrix elements in orders of λ, one could find the next simplified expansion as:

$$V_{CKM} = \begin{pmatrix} 1 - \frac{1}{2}\lambda^2 & \lambda & A\lambda^3(\rho - i\eta) \\ -\lambda & 1 - \frac{1}{2}\lambda^2 & A\lambda^2 \\ A\lambda^3(1 - \rho - i\eta) & -A\lambda^2 & 1 \end{pmatrix} + \mathcal{O}(\lambda^4),$$

in which it is convenient to define

$$\bar{\rho} = \rho(1 - \frac{\lambda^2}{2})\ ,\ \bar{\eta} = \eta(1 - -\frac{\lambda^2}{2})$$

to find an even more simplified representation.

The fact that the CKM matrix is unitary results in a number of important relations between its elements. As an instance, we have

$$\sum_{i=1}^{3} V_{ji}V_{ki}^* = \sum_{j=1}^{3} V_{ij}V_{ik}^* = 0\,,$$
$$\sum_{i=1}^{3} |V_{ij}|^2 = \sum_{j=1}^{3} |V_{ij}|^2 = 1\,, \tag{1.10}$$

in which $i = d, s, b$ and $j, k = u, c, t$ and $(j \neq k)$ on the top left and reversed in the top right in the first equation, whereas in the second equation we have $i = u, c, t$ and $j = d, s, b$. In the complex plane, the first system of conditions can be interpreted geometrically. Rewriting these conditions explicitly, we have,

$$\underbrace{V_{ud}V_{us}^*}_{\mathcal{O}(\lambda)} + \underbrace{V_{cd}V_{cs}^*}_{\mathcal{O}(\lambda)} + \underbrace{V_{td}V_{ts}^*}_{\mathcal{O}(\lambda^5)} = 0, \tag{1.11}$$

$$\underbrace{V_{us}V_{ub}^*}_{\mathcal{O}(\lambda^4)} + \underbrace{V_{cs}V_{cb}^*}_{\mathcal{O}(\lambda^2)} + \underbrace{V_{ts}V_{tb}^*}_{\mathcal{O}(\lambda^2)} = 0, \tag{1.12}$$

$$\underbrace{V_{ud}V_{ub}^*}_{\mathcal{O}(\lambda^3)} + \underbrace{V_{cd}V_{cb}^*}_{\mathcal{O}(\lambda^3)} + \underbrace{V_{td}V_{tb}^*}_{\mathcal{O}(\lambda^3)} = 0, \tag{1.13}$$

$$\underbrace{V_{ud}^*V_{cd}}_{\mathcal{O}(\lambda)} + \underbrace{V_{us}^*V_{cs}}_{\mathcal{O}(\lambda)} + \underbrace{V_{ub}^*V_{cb}}_{\mathcal{O}(\lambda^5)} = 0, \tag{1.14}$$

$$\underbrace{V_{cd}^*V_{td}}_{\mathcal{O}(\lambda^4)} + \underbrace{V_{cs}^*V_{ts}}_{\mathcal{O}(\lambda^2)} + \underbrace{V_{cb}^*V_{tb}}_{\mathcal{O}(\lambda^2)} = 0, \tag{1.15}$$

$$\underbrace{V_{ud}^*V_{td}}_{\mathcal{O}(\lambda^3)} + \underbrace{V_{us}^*V_{ts}}_{\mathcal{O}(\lambda^3)} + \underbrace{V_{ub}^*V_{tb}}_{\mathcal{O}(\lambda^3)} = 0, \tag{1.16}$$

in which the order of magnitude of each term is given as a function of λ^n. Here, one emphasizes that only the terms in Eqs. 1.13 and 1.16 have the same order of magnitude of λ which eventuates in triangles with comparable internal angles in the complex plane while others possess flat representations.

The triangle derived from Eq.1.13 is called the unitarity triangle where the sides of the triangle are normalized by $V_{cd}V_{cb}^*$ and the internal angles are defined, as

$$\alpha = \arg\left(-\frac{V_{td}V_{tb}^*}{V_{ud}V_{ub}^*}\right) = \arg\left(-\frac{1-\rho-i\eta}{\rho+i\eta}\right), \tag{1.17}$$

$$\beta = \arg\left(-\frac{V_{cd}V_{cb}^*}{V_{td}V_{tb}^*}\right) = \arg\left(\frac{1}{1-\rho-1\eta}\right), \tag{1.18}$$

$$\gamma = \arg\left(-\frac{V_{ud}V_{ub}^*}{V_{cd}V_{cb}^*}\right) = \arg\left(\rho+i\eta\right), \tag{1.19}$$

These angles can be measured separately in different particle decays and mixing phenomena and such measurements can provide a direct probe (through a consistency check) of the mechanism of $\mathcal{CP}$ violation in the Standard Model. Measurements for which their SM predictions do not suffer fro large theoretical errors are retained. Fig. 1.2 shows a graph of the unitarity triangle, while Fig. 1.3 represents the status of the global fit of the SM parameters.

The angle β is of particular interest for the decay modes studied in this work.

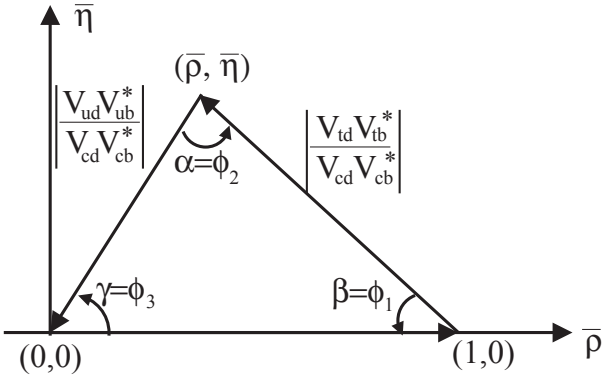

Figure 1.2: *Graphical representation in the complex plane* $(\overline{\rho},\overline{\eta})$ *of the unitarty triangle of Eq. 1.13 as normalized to* $V_{cd}V_{cb}^*$ *:* $1 + V_{ud}V_{ub}^*/V_{cd}V_{cb}^* + V_{td}V_{tb}^*/V_{cd}V_{cb}^* = 0$.

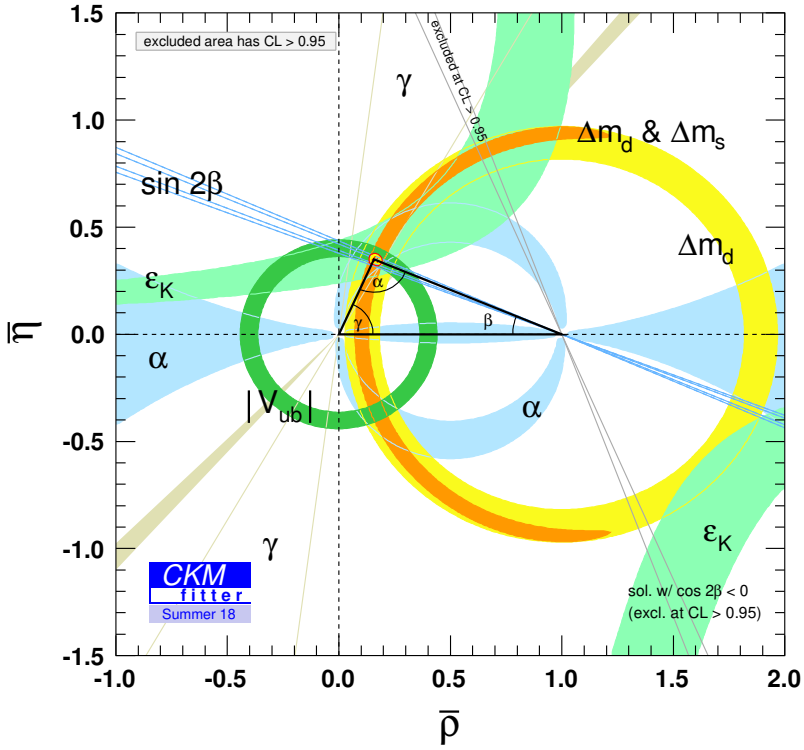

Figure 1.3: *Constraints on the unitarity triangle at a 95% confidence level [58].*

1.4 $\mathcal{CP}$ Violation

Considering the assumption of symmetric matter-antimatter state in an initial state of the universe evolution or a condition where the inflation washed out the evidence of existed asymmetry, the SM cannot provide an explanation for the existing baryonic asymmetry through its sources of $\mathcal{CP}$ violation [59, 60]. Therefore, additional sources of $\mathcal{CP}$ violation are required in New Physics (NP) models. The $\mathcal{CP}$ violation is based on differences between decays and their corresponding $\mathcal{CP}$-conjugates. The observation of $\mathcal{CP}$ violation is associated with the interference between at least two amplitudes of the contributing decays. A difference between a particle and antiparticle amplitude under $\mathcal{CP}$ transformation lies in the CKM phase (receiving an opposite sign for antiparticles in the complex conjugation).

Before introducing different types of $\mathcal{CP}$ violation it is good to briefly describe the quantum mechanics of neutral meson mixing.

The spontaneous oscillations are properties of neutral mesons such as B^0, K^0 and D^0 that, with the evolution of time, can transit between particles and antiparticles. This mixing phenomenon in meson system, which is particular to weak interaction, has been reported in the K/B neutral meson systems [61] and recently the first evidence of mixing has been observed in D mesons system [62, 63].

Let us suppose a generic neutral meson P^0, with an antiparticle $\bar{P}^0 \neq P^0$. The evolution of this particle (and its antiparticle) would in general results in a time-dependent quantum superposition of states. Particularly, an initial arbitrary state which is a linear combination of $|P^0\rangle$ and $|\bar{P}^0\rangle$ eigenstates at $t = 0$, evolves in a way that at any time t it can be seen with a very good approximation as a superposition of the functions described by the following wave function,

$$|P^0(t)\rangle = \psi_1(t)|P^0\rangle + \psi_2(t)|\bar{P}^0\rangle, \tag{1.20}$$

where $\sum_{i=1,2} |\psi_i(t)|^2 = 1$. This wave function satisfies the the Schrödinger equation $i\hbar\partial_t|P^0(t)\rangle = \mathcal{H}_{eff}|P^0(t)\rangle$ whose Hamiltonian given by

$$\mathcal{H}_{eff} = \mathbf{M} - \frac{i}{2}\mathbf{\Gamma} = \begin{pmatrix} M_{11} & M_{12} \\ M_{21} & M_{22} \end{pmatrix} - \frac{i}{2}\begin{pmatrix} \Gamma_{11} & \Gamma_{12} \\ \Gamma_{21} & \Gamma_{22} \end{pmatrix} \tag{1.21}$$

in which $\mathbf{\Gamma}$ and $\mathbf{M}$ are respectively the decay width and the mass matrices which are Hermitian (Therefore, $\Gamma_{12}^* = \Gamma_{21}$ and $M_{12}^* = M_{21}$). The former term is usually referred to as the absorptive term, while the latter is often known as the dispersive term. Although $\mathbf{\Gamma}$ and $\mathbf{M}$ are hermitian, the existence of complex term, i.e $i\mathbf{\Gamma}/2$, makes $\mathcal{H}_{eff}$ to be non-hermitian. The $\mathcal{H}_{eff}$ enables us however to mathematically describe the oscillation and decay of the mesons.

Because of CPT invariance, it is necessary for the diagonal elements of $\mathcal{H}$ to satisfy $M_{11} = M_{22}$ and $\Gamma_{11} = \Gamma_{22}$ conditions. By diagonalising the Hamiltonian, the $\mathcal{CP}$ eigenstates could be described in terms of linear combinations of flavor eigenstates,

$$|P_L\rangle = p|P^0\rangle + q|\bar{P}^0\rangle \ , \ |P_H\rangle = p|P^0\rangle - q|\bar{P}^0\rangle \,, \tag{1.22}$$

whose eigenvalues are,

$$\lambda_H = M_{11} - \frac{i}{2}\Gamma_{11} + \frac{q}{p}(M_{12} - \frac{i}{2}\Gamma_{12}) = M_H - \frac{i}{2}\Gamma_H, \tag{1.23}$$

$$\lambda_L = M_{11} - \frac{i}{2}\Gamma_{11} - \frac{q}{p}(M_{12} - \frac{i}{2}\Gamma_{12}) = M_L - \frac{i}{2}\Gamma_L, \tag{1.24}$$

where p and q are complex parameters modelling possible $\mathcal{CP}$ violation in the mixing (which must satisfy $|p|^2 + |q|^2 = 1$) while the subscripts H and L refer to the heavier and lighter eigenstates. The p and q parameters are related to the off-diagonal elements of $\mathcal{H}_{eff}$ in the following form,

$$(\frac{q}{p})^2 = \frac{M_{12}^* - \frac{i}{2}\Gamma_{12}^*}{M_{12} - \frac{i}{2}\Gamma_{12}}. \tag{1.25}$$

The 2-particle system $\{B^0, \bar{B}^0\}$ is characterized by 5 physical observables (also known as mixing observables): the mass and decay rate averages, the differences in mass and decay rate, and its "composition fraction" $|q/p|$. The mass and decay rate averages are given by,

$$m = \frac{M_H + M_L}{2} \ , \ \Gamma = \frac{\Gamma_H + \Gamma_L}{2}. \tag{1.26}$$

Δm and $\Delta\Gamma$ are differences between mass and width of the two $\mathcal{CP}$ eigenstates and define as,

$$\Delta m = M_H - M_L \ , \ \Delta\Gamma = \Gamma_L - \Gamma_H \, . \tag{1.27}$$

Δm is positive by definition and since we are dealing with B^0 and $\bar{B}^0$, $\Delta\Gamma$ can be neglected. The $\mathcal{CP}$ symmetry means that $|q/p|$ =1.

The time evolution of B^0 meson systems are providing us with four different time dependent decay rates for the initial state of B^0 and at $t = 0$ to the final f or $\bar{f}$ at a given time t. Two of these decay rates are given as follows,

$$\frac{d\Gamma_{B^0\to f}(t)}{dt} = \frac{e^{-\Gamma t}}{2}|A_f|^2(1 + |\lambda_f|^2)[1 + C_f\cos(\Delta m t) - S_f\sin(\Delta m t)] \, , \tag{1.28}$$

$$\frac{d\Gamma_{\bar{B}^0\to f}(t)}{dt} = \frac{e^{-\Gamma t}}{2}|\frac{q}{p}|^2|\bar{\mathcal{A}}_f|^2(1 + |\bar{\lambda}_f|^2)[1 - C_f\cos(\Delta m t) + S_f\sin(\Delta m t)] \, . \tag{1.29}$$

where $A_f = \langle f|\mathcal{H}_{eff}|B^0\rangle$ and $\bar{A}_f = \langle f|\mathcal{H}_{eff}|\bar{B}^0\rangle$ and λ_f and $\bar{\lambda}_f$ are defined as follows,

$$\lambda_f = \frac{1}{\bar{\lambda}_f} = \frac{q\bar{\mathcal{A}}_f}{p\mathcal{A}_f}, \tag{1.30}$$

and C_f and S_f can be defined in the following forms,

$$S_f = \frac{2\Im(\lambda_f)}{1 + |\lambda_f|^2} \tag{1.31}$$

$$C_f = \frac{1 - |\lambda_f|^2}{1 + |\lambda_f|^2}. \tag{1.32}$$

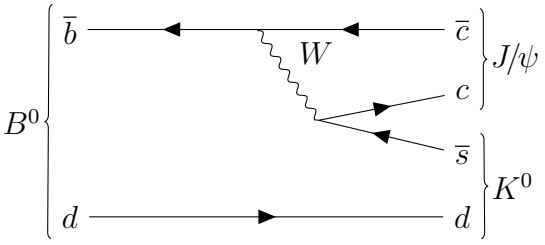

Figure 1.4: Feynman diagram of the decay $B^0 \to J/\psi\, K^0_{\rm S}$, golden mode for β angle determination.

The C_f factor is a measure of the $\mathcal{CP}$ violation in the decay. The S_f factor is the measure of the mixing-induced $\mathcal{CP}$ violation. They can be measured by studying the time-dependent $\mathcal{CP}$ asymmetry observable:

$$A_{\mathcal{CP}}(t) = \frac{\Gamma_{\bar{B}^0 \to f}(t) - \Gamma_{B^0 \to f}(t)}{\Gamma_{\bar{B}^0 \to f}(t) + \Gamma_{B^0 \to f}(t)}. \tag{1.33}$$

1.5 New physics related to β angle

The charmed decay governing the $b \to sc\bar{c}$ transitions into $\mathcal{CP}$ eigenstantes can be named as a clean theoretical way for β-angle determination. Since this transition is dominated by tree-level diagrams, it is expected to capture the weak mixing phase through the observable $\sin 2\beta$. We'll discuss as an example the canonical decay mode $B^0 \to J/\psi\, K^0_{\rm S}$. The $B^0 \to J/\psi\, K^0_{\rm S}$ decay whose Feynman diagram is presented in Fig.1.4. The decay is governed by a $\bar{b} \to (c\bar{c})s$ quark transition; its amplitude is proportional to $V^*_{cb}V_{cs}$. The measurement of $\sin(2\beta)$ arises from the interference between the mixing and the decay amplitudes. The mixing amplitude features box diagrams (involving dominantly virtual Wtb currents in the SM and is proportional to the product of CKM matrix elements $\frac{V^*_{td}V_{tb}}{V_{td}V^*_{tb}}$. The final bit of contribution to the amplitudes of interest comes from the mixing of the $K^0 - \bar{K}^0$, proceeding through box diagrams as $B^0 - \bar{B}^0$ oscillation, introducing a factor $\frac{V^*_{cd}V_{cs}}{V_{cd}V^*_{cs}}$. As a result, the λ_f parameter is determined by,

$$\begin{aligned}\lambda_f &= \eta_f(\frac{V_{td}V^*_{tb}}{V^*_{td}V_{tb}}) \times (\frac{V_{cb}V^*_{cs}}{V^*_{cb}V_{cs}}) \times (\frac{V_{cd}V^*_{cs}}{V^*_{cd}V_{cs}}) \\ &= \eta_f(\frac{V_{td}V^*_{tb}}{V^*_{cb}V_{cd}})(\frac{V_{tb}V^*_{td}}{V^*_{cd}V_{cb}})^{-1}.\end{aligned} \tag{1.34}$$

Considering $\arg(\frac{V_{td}V^*_{tb}}{V^*_{cb}V_{cd}}) = \pi - \beta$ and $|\frac{V_{td}V^*_{tb}}{V^*_{cb}V_{cd}} = 1|$ we have,

$$\lambda_f = \eta_f \exp(-2i\beta). \tag{1.35}$$

For this specific mode by taking into account the Eq. 1.31 we have:

$$S_f = \sin(2\beta). \tag{1.36}$$

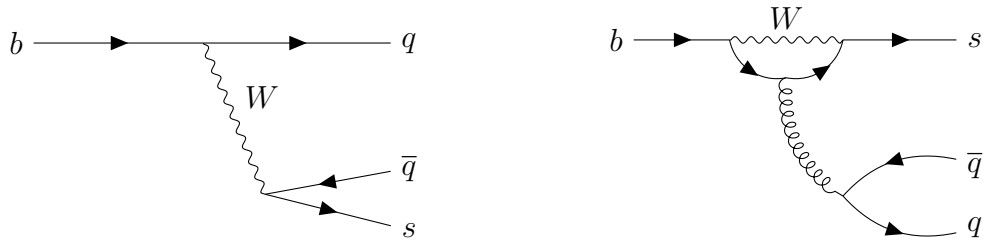

Figure 1.5: The $b \to sq\bar{q}$ transition Left: at tree level Right: at first loop order also known as Penguin diagram.

The average of $\sin 2\beta$ for all the charmonia modes, according to [64] is given by $\sin 2\beta = 0.70 \pm 0.02$.

The decays $B^0 \to K^0_S\pi^+\pi^-$ and $B^0 \to K^0_S K^+K^-$ are governed by quark transitions $b \to sq\bar{q}$, where q can be either of u, d or s quarks. The possible Feynman diagram to describe these decays are shown in Fig.1.5. The tree-level diagram is expected to not add any $\mathcal{CP}$ violating phase while,in presence of new physics, the loop diagram can see heavier particles circulating in the loop that might come with an additional $\mathcal{CP}$ phase, modifying in turn the determined value of $\sin(2\beta)$ in charmonia modes.

This search is the physics motivation, in the long term, to study the decays $B^0 \to K^0_S\pi^+\pi^-$ and $B^0 \to K^0_S K^+K^-$ decays, and more generally the decays $B^0_{d,s} \to K^0_S h^\pm h'^\mp$.

1.6 Branching fraction measurement of $B^0_{d,s} \to K^0_S h^\pm h'^\mp$ decay

The theoretical description of hadronic decays is an extremely difficult task, since it involves non-perturbative QCD amplitudes. Approximations are employed (such as QCD factorisation or pQCD) to model the hadronic processes and yields predictions of decay rates (e.g refs. [25–31]). The comparison of these various theoretical predictions with the measurements of the branching fractions is therefore useful to select the most accurate avenues. This can in turn improve the future predictions of $\mathcal{CP}$ asymmetries. Moreover, the charmless branching fraction measurement results (and in particular the decay modes under scrutiny in this work) can also be implemented in other studies to test the level of breaking flavor symmetries, namely isospin, U-spin, and $SU(3)$ (see ref. [32]).

Among the $B^0_{d,s} \to K^0_S h^\pm h'^\mp$ decays where h can be either π or K, only $B_s \to K^0_S K^+K^-$ decay mode is not observed yet [65–70]. First, using the 1 fb^{-1} data sample collected at LHCb in 2011 a search is performed for the B_s decays, where first observations were made for the $B_s \to K^0_S\pi^+\pi^-$ and $B_s \to K^0_S K^\pm\pi^\mp$ modes [70]. However, no evidence for the decay $B_s \to K^0_S K^+K^-$ was found. Second, the full RunI data sample, which corresponds to the integrated luminosity of 1.0 fb^{-1} at a center-of-mass energy of 7 TeV in 2011 and 2.0 fb^{-1} at a center-of-mass energy of 8 TeV in 2012, was considered and the branching fractions

measured with a better accuracy [20]. Ratios of branching fractions of $B_s \to K^0_S \pi^+\pi^-$, $B^0 \to K^0_S K^\pm \pi^\mp$ and $B_s \to K^0_S K^\pm \pi^\mp$ were actually determined with respect to the known $B^0 \to K^0_S \pi^+\pi^-$ branching fraction measured accurately at B-factories (citation):

$$\frac{\mathcal{B}(B^0 \to K^0_S K^\pm \pi^\mp)}{\mathcal{B}(B^0 \to K^0_S \pi^+\pi^-)} = 0.123 \pm 0.009\,(\text{stat.}) \pm 0.015\,(\text{syst.})\,, \tag{1.37}$$

$$\frac{\mathcal{B}(B^0 \to K^0_S K^+ K^-)}{\mathcal{B}(B^0 \to K^0_S \pi^+\pi^-)} = 0.549 \pm 0.018\,(\text{stat.}) \pm 0.033\,(\text{syst.})\,, \tag{1.38}$$

$$\frac{\mathcal{B}(B_s \to K^0_S \pi^+\pi^-)}{\mathcal{B}(B^0 \to K^0_S \pi^+\pi^-)} = 0.191 \pm 0.27\,(\text{stat.}) \pm 0.031\,(\text{syst.}) \pm 0.011\,(f_s/f_d) \tag{1.39}$$

$$\frac{\mathcal{B}(B_s \to K^0_S K^\pm \pi^\mp)}{\mathcal{B}(B^0 \to K^0_S \pi^+\pi^-)} = 1.70 \pm 0.07\,(\text{stat.}) \pm 0.11\,(\text{syst.}) \pm 0.10(f_s/f_d)\,, \tag{1.40}$$

where f_s/f_d represents the ratio of hadronisation fraction of the b quark in B^0_s over that of b in B^0. The $B_s \to K^0_S K^+ K^-$ decay is left unobserved as the significance of this signal was found to be at a level of 2.5 σ and the measurement was compatible with 0,

$$\frac{\mathcal{B}(B_s \to K^0_S K^+ K^-)}{\mathcal{B}(B^0 \to K^0_S \pi^+\pi^-)} \in [0.008 - 0.051]\text{at}\,90\%\,\text{confidencelevel.} \tag{1.41}$$

The chapters 3, 4 and 5 will describe novel tools and methodologies towards an updated analysis to perform more accurately the branching fraction ratios of the modes of interest with a higher statistics and continue the search for the yet unobserved $B_s \to K^0_S K^+ K^-$ decay mode. To do so multivariate tools are developed to distinguish between the signal and backgrounds and are described in chapters 3 and 4. An optimization method is described in section 5. Using the optimal selection cuts, the selection efficiency is studied in the phase space of the decay. The description of the phase space of a three-body decay is referred to as the Dalitz Plot Dalitz plane formalism that I will introduce in the next section. Finally, the Chapter 6 will gather the preliminary determination of the selection efficiency averaged in the phase space of the decay and the preliminary measurement of the decay yields from a fit to the invariant-mass distribution of the candidates to provide a determination of the ratio of branching fractions.

1.7 Kinematics of three-body-decay and Helicity angle

As stated in the previous section, the knowledge of the kinematics of the decay is required to determine the total selection efficiency of the decays of interest in view of measuring the branching fractions. The set of descriptive variables necessary for that purpose are built considering a set of 4-vector energy-momenta related to the mother and daughters (final state particles) of the decay. Here for $B^0 \to K^0_S \pi^+\pi^-$, the final state consists of three daughters of π^+,π^- and K^0_S. Hence, one can define the set of four-vectors:

$$p_{B^0} = (m_{B^0}, \vec{0})\,,\ p_{K^0_S} \equiv p_0 = (E_0, \vec{p}_0)\,, \tag{1.42}$$
$$p_{\pi^+} \equiv p_+ = (E_+, \vec{p}_+)\,,\ p_{\pi^-} \equiv p_- = (E_-, \vec{p}_-),$$

The partial decay rate follows:

$$d\Gamma = \frac{(2\pi)^4}{2m_{B^0}}|\mathcal{A}|^2 d\Phi_3(p_{B^0}, p_0, p_+, p_-), \tag{1.43}$$

in which $\mathcal{A}$ is the aforementioned decay amplitude and $d\Phi_3$ as the phase space of the decay. It can be written as:

$$d\Phi_3(p_{B^0}, p_0, p_+, p_-) = \delta(m_{B^0} - \sum_{\alpha=0,+,-} E_\alpha) \prod_{\alpha=0,+,-} \frac{dp_\alpha}{E_\alpha}. \tag{1.44}$$

The primary number of free parameters in this decay is twelve. It can however be decreased to 2 independent free parameters thanks to the 10 following physical constraints:

3 degrees of freedom are fixed from the on-shell daughters known masses.

4 degrees of freedom are fixed based on the conservation of energy-momentum.

3 degrees of freedom are fixed by the knowledge of the Euler angles of the spinless particle that decays.

The remaining two independent free parameters can be implemented by redefining the Eq.1.43 in terms of two two-body invariant masses. Further details, related to deduction of these variables, named as Dalitz plot variables, can be found in Appendix A of Ref [71]. In the context of $B^0 \to K^0_S\pi^+\pi^-$ decay, the DP variables are,

$$m^2_{K^0_S\pi^+} \equiv s_+ = (p_+ + p_0)^2, \tag{1.45}$$

$$m^2_{K^0_S\pi^-} \equiv s_- = (p_- + p_0)^2, \tag{1.46}$$

$$m^2_{\pi^+\pi^-} \equiv s_0 = (p_+ + p_-)^2. \tag{1.47}$$

The boundary equation:

$$\sum_{\alpha=0,+,-} s_\alpha = (\sum_{\alpha=0,+,-} p_\alpha)^2 + \sum_{\alpha=0,+,-} p^2_\alpha = (m^2_{B^0}) + m^2_{K^0_S} + m_{\pi^+} + m_{\pi^-} \tag{1.48}$$

allows to pick the two DP variables which are used in redefinition of $B^0 \to K^0_S\pi^+\pi^-$ decay rate as,

$$d\Gamma = \left(\frac{1}{8\pi^3}\right) \frac{|\mathcal{A}|^2}{32m^2_{B^0}} ds_+ ds_-, \tag{1.49}$$

An alternative description with s_0, the invariant-mass square of the two pions, could equivalently been used. Fig.1.6 shows the schematic view of the decay phase space after 1.45 and 1.46 redefinitions. This will also help to represent the orientation of the final states in a better way, where the edges are demonstrating an extreme case of parallel or antiparallel situation for these decay products.

Another aspect of this representation of the decay is that it helps us to determine the spin content of the resonances. This can be done by defining a new variable in the rest

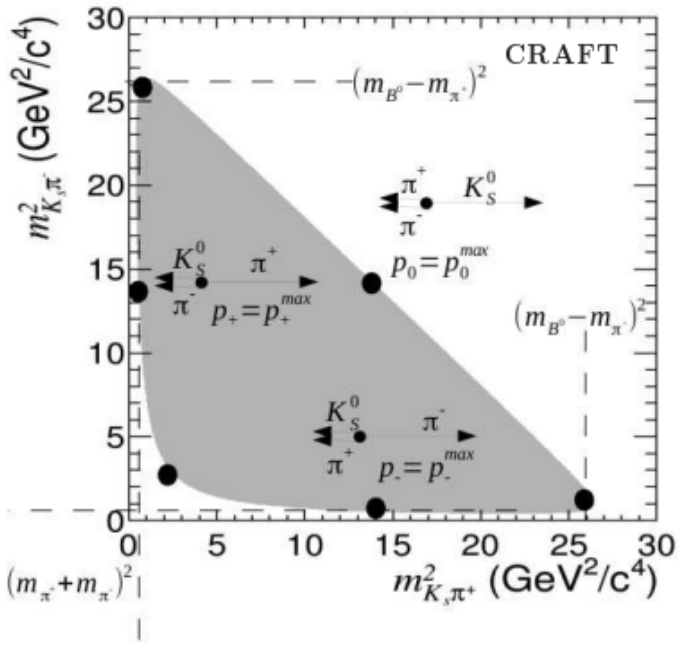

Figure 1.6: Graphical representation for the kinematics of the $B^0 \to K^0_S\pi^+\pi^-$ decay final states. The limits are shown by dashed line representation.

frame of resonances: the helicity angle. To define this variable, the daughter of the decay can be labeled as i, j and k. In this ij rest frame, the angle between the k daughter and the j final state is defined as the ij-helicity angle and denoted by $(\theta_H)_{ij}$. The cos of this angle can be determined with respect to the Dalitz plot variable as follows:

$$\cos(\theta_H)_{ij} = \frac{(m^2_{jk})_{\max} + (m^2_{jk})_{\min} - 2(m^2_{jk})}{(m^2_{jk})_{\max} - (m^2_{jk})_{\min}}. \tag{1.50}$$

This variable and its distribution across the DP is indicative of the spin of the resonance. For instance, a spin 0 particle is represented by a uniform distribution. If the distribution of $\cos(\theta_H)_{ij}$ consists of n peak, the spin of the associated resonance would be $n-1$. The Fig.1.7 shows an example of such distribution in Dalitz plane.

1.8 The Square Dalitz Plane

The decay process of $B^0 \to K^0_S\pi^+\pi^-$ proceeds with amplitudes that are dominantly located in the boundaries of the Dalitz plane. It is therefore relevant to find an alternative description of the Dalitz plane that would magnify these regions of interest. This is the purpose of the Square Dalitz Plane (sqDP) [72]. This map is defined by:

$$dm^2_{ij}dm^2_{jk} \to |det\mathcal{J}|dm'd\theta' \tag{1.51}$$

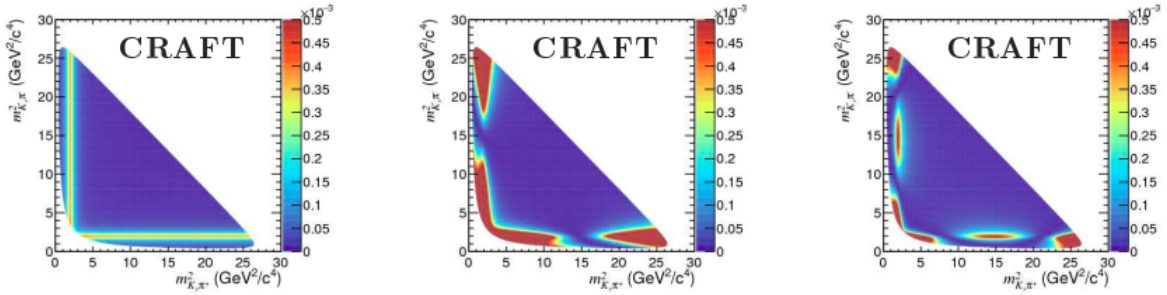

Figure 1.7: Distribution of resonances across the Dalitz plane for the K^* (1430) for phase space of $B^0 \to K^0_S \pi^+ \pi^-$. The left, middle and right pictures are showing the different expected distributions according to the spin of the resonance which is 0, 1 and 2 respectively (plot made with simulated pseudoexperiments.

in which $\mathcal{J}$ is the Jacobian matrix of the transformation. The sqDP variables are hence defined as a function of the standard Dalitz plane variables:

$$m' = \frac{1}{\pi} \arccos\left(2\,\frac{m_{ij} - m_{ij}^{\min}}{m_{ij}^{\max} - m_{ij}^{\min}} - 1\right), \tag{1.52}$$

$$\theta' = \frac{1}{\pi}\theta_{ij}, \tag{1.53}$$

where m_{ij} is the invariant mass of the i and j particle whose minimum and maximum value are denoted by $m_{ij}^{\min} = m_i + m_j$ and $m_{ij}^{\max} = M - m_k$, respectively. Applying it to the decay $B^0 \to K^0_S \pi^+ \pi^-$:

$$ds_+ ds_- \equiv dm^2_{K^0_S\pi+} dm^2_{K^0_S\pi^-} \to |det\mathcal{J}| dm' d\theta' \,, \tag{1.54}$$

$$m' = \frac{1}{\pi} \arccos\left(2\,\frac{m_{\pi^+\pi-} - m_{\pi^+\pi-}^{\min}}{m_{\pi^+\pi-}^{\max} - m_{\pi^+\pi-}^{\min}} - 1\right), \tag{1.55}$$

$$\theta' = \frac{1}{\pi}\theta_{\pi^+\pi-}, \tag{1.56}$$

The Fig.1.8 shows the distribution of a flat distribution in the Dalitz plane and its version mapped into the sqDP.

The use of the sqDP is relevant for the amplitude analysis of this decay. It is as well instrumental for the selection efficiency determination, since one can focus for instance the production of simulated events into the Dalitz plane regions where the actual physics occurs.

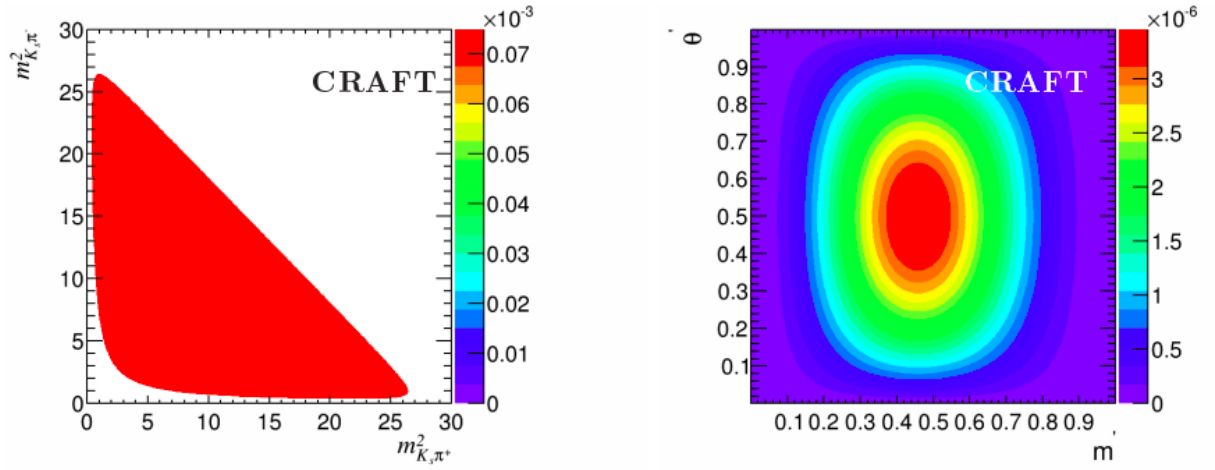

Figure 1.8: Left: Flat Distribution over the nominal DP for$B^0 \to K^0_S\pi^+\pi^-$ decays Right: Displays the transformation of the left plot to sqDP coordinates. Here according to flatness of the primary plot, the distribution is nothing but the determinant of the Jacobian matrix of the transformation, provided by Eq.1.54.

Chapter 2

The LHC and the LHCb experiment

The knowledge about instrumentation in each experiment and the algorithms which retrieve information from their measurements are inevitable part of each (experimental)physics analysis. This information help the physicist (analysts) to determine the existing limitation and biases which are subject to the analysis.

Through the following chapter, the details of the LHC and LHCb subsystems are shortly discussed. The physics behind the measurements in each subsystem is slightly explained. Then the implementation of algorithms in order to use these measurements are briefly reviewed. It is by mean of these algorithms that the measurements are transformed in to more informative variables.

2.1 The Large Hadron Collider

The Large Hadron Collider (LHC [73]), the most powerful accelerator in the world in terms of centre-of-mass energy, is located at the Laboratoire Européen de Physique des Particules (CERN), and is built under the French-Swiss border close to Geneva. It is the last point in a series of accelerators at CERN, as depicted in Fig. 2.1. These series of accelerators accelerate protons in clusters up to 13 TeV. Protons are first accelerated by passing through the LINAC2, from which they emerge with a 50 MeV energy. After that, they pass via the PSB (Proton Synchrotron Booster) and the PS (Proton Synchrotron), attaining energies of 1.4 GeV and 26 GeV, respectively. Finally, the SPS (Super Proton Synchrotron) boosts protons' energies to 450 GeV before they are injected into the LHC. At the collider, the protons are held in their orbits by superconducting magnets that generate an 8.34 T magnetic field and more than a thousand superconducting Nb-Ti dipole magnets are responsible for this magnetic field generation. The two proton beams going in opposite directions must be subjected to opposing magnetic fields. Quadrupole magnets situated along the ring focus the beams. Protons are clustered into bunches, with a spacing of 50 ns in Run-I(2010-2012) and 25 ns in most of the Run-II(2015-2018). The LHC rings contain 2808 proton bunches per ring in the nominal operation regime, each of which comprises 1.1×10^{11} protons colliding at a frequency of 40 MHz. Therefore, For proton-proton collisions, this combination reaches an instantaneous luminosity of

10^{34} cm^{-2}s^{-1}.

As it is shown in Fig. 2.2 and through yellow dots in Fig. 2.1, particle detectors are positioned at four places along the 27 km ring. The two proton beams collide in these locations. Two general-purpose detectors, ATLAS and CMS, are among the four largest experiments at the LHC, and they almost hermetically surround their interaction locations. They have a broad physics program oriented towards high-transverse-momentum physics, Standard Model precision tests, top-quark physics and study of the Higgs boson properties which was discovered in 2012 [53] as well as studies for the physics phenomena beyond the SM. Although, they can provide flavor physics study and specially perform the hadron spectroscopy. The lack of a charged hadron identification, tight trigger thresholds, and a harsh environment with a high track multiplicity and number of interactions per collision (pileup) are their key drawbacks in this direction. These features are optimized in a separate experiment called LHCb, a detector dedicated to heavy flavor physics studies with charm and beauty hadrons and to $\mathcal{CP}$ violation, which is discussed in the sections below. At LHC, heavy ions (Pb) can be accelerated up to 2.8 TeV per nucleus. ALICE, as the fourth main experiment at CERN is mainly studying the quark-gluon plasma and makes use of Pb-Pb and Pb-p collisions.

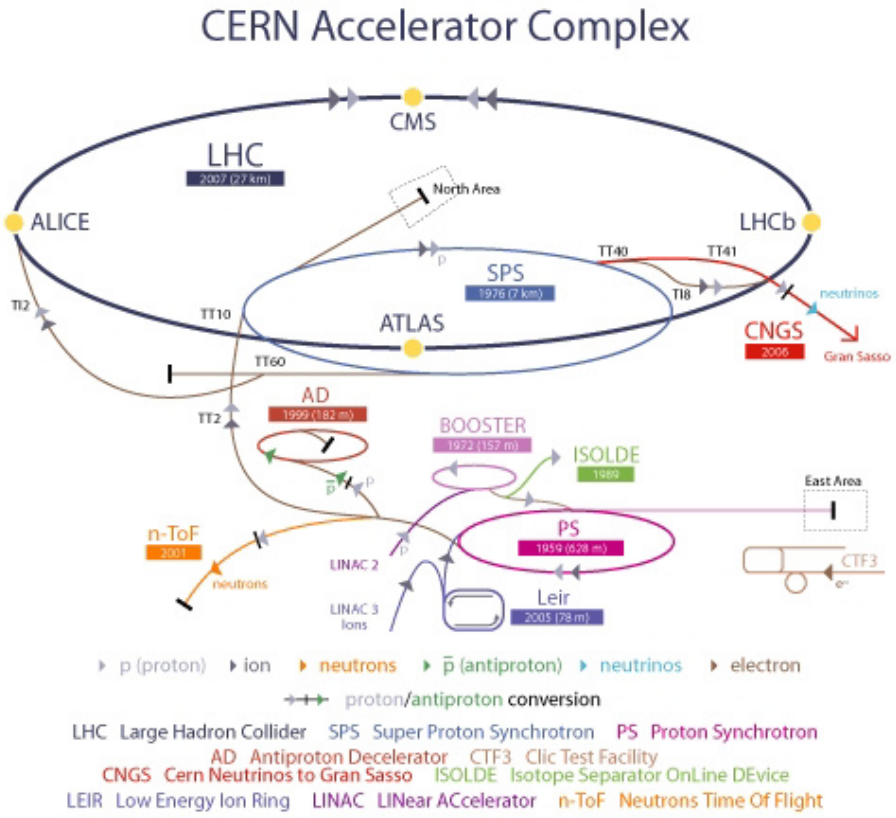

Figure 2.1: *Sketch representing the various pre-accelerating machines and four main detectors (yellow points) as of 2018 [74]*

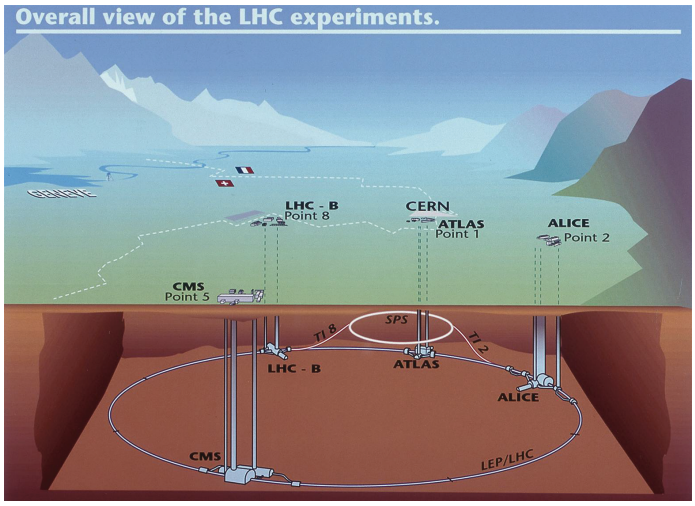

Figure 2.2: *Schematic view of the LHC collider. The figure also shows the four main experiments (ALICE, ATLAS, CMS and LHCb).*

2.2 The LHC and its LHCb(eauty) detector

2.2.1 b hadron production at LHC

A proton as a non-fundamental particle, comprised of three valence quarks (uud), sea quarks, and gluons which mediated strong interactions and keep it bounded This structure, inside the proton, causes the proton-proton collisions to become an extremely complex process compared to the e^+e^- collisions. The collision, up to the first order, is mediated by a strong flavor-conserving interaction. This suggests that the processes of b quark creation in the first order are pair creations and resulting into $b\bar{b}$ pairs. The contribution in this process come from annihilation of quark-antiquark $q\bar{q} \to b\bar{b}$ along with gluon-gluon fusion, $gg \to b\bar{b}$ which is dominant at the energy scales of the LHC. The resulting $b\bar{b}$ pair is frequently boosted in the forward or backward direction along the beam axis due to huge momentum asymmetries between the partons (gluons or quarks) involved in the collision and the fact that the LHC energy is substantially larger than the mass of the b quark. Therefore, in order to determine the closeness of a particle to the beam axis, the *pseudorapidity* parameter η has been defined as

$$\eta = -\ln\left[\tan\left(\frac{\theta}{2}\right)\right] \tag{2.1}$$

where θ is the polar angle between the beam and the particle direction. Since pseudorapidity is symmetric with respect to the beam axis, it becomes an applicable variable for the detectors which are symmetric around the beam line.

Moreover, the difference between the pseudorapidity of two tracks is invariant under the boost along the beam axis, therefore it becomes one of the important variable in

high energy physics. The large boosts result in a more displaced b-hadrons decay vertices. This makes the pseudorapidity of boosted b-quark production to be a very handy feature, because it allows b hadrons to be identified in the busy environment of the hadronic collision.

As a b quark is generated, it can combine with one or two lighter (anti)quarks to create a meson or baryon. This process is called hadronization. The associated probabilities for a quark to be paired with any of the u, d, s and c quarks and hadronize into a meson is usually given by f_u, f_d, f_s and, f_c parameters, respectively. Although, the hadronization into a baryon are less studied, it is known and accepted that the most possible scenario for such b hadronization is by means of the production of Λ_b^0 and its associated probability is denoted by $f_{\Lambda_b^0}$ [75, 76]

As it can be seen in [75] The B^0 meson production at LHC is twice the Λ_b^0 production and this ratio is increased with the transverse momentum p_T. As an instance, the measure value at LHCb in the Run-II and 13 TeV, is [76]:

$$\frac{f_{\Lambda_b^0}}{f_u + f_d} = 0.259 \pm 0.018 \tag{2.2}$$

where it was averaged over kinematics. This inverse correlation between the Λ_b^0 production and p_T can be explained through the following parameterization:

$$\frac{f_{\Lambda_b^0}}{f_u + f_d} = A\left[p_1 + exp(p_2) + p_3 \times p_T\right], \tag{2.3}$$

where $A = 1 \pm 0.061$, $p_1 = (7.93 \pm 1.41) \times 10^{-2}$, $p_2 = -1.022 \pm 0.047$ and $p_3 = -0.107 \pm 0.002\,\mathrm{GeV}^{-1}$.

The advantage of LHC over the e^-e^+ machines (e.g. B-factories) is that its environment gives a greater boost and a higher $b\bar{b}$ production cross-section [77]. This cross-section at the LHC energies has been measured to be around 280 µb and 560 µb at center of mass energy of $\sqrt{s} = 7\,\mathrm{TeV}$ and $\sqrt{s} = 13\,\mathrm{TeV}$ respectively [78, 79].

2.2.2 The LHCb detector

As it is aforementioned, LHCb is an experiment dedicated to heavy flavor physics studies [80–82].. During the Run-I and Run-II periods of data taking at LHC, the large beauty and charm production cross-sections enabled LHCb to gather significant amount of heavy flavor samples. Especially, the main goal of this detector is the measurement of $\mathcal{CP}$ violation and indirect search for new physics effects in the rare decays of b and c hadrons. It is located in point-8 of the LHC ring(Fig. 2.2).

The LHCb detector is designed as a single-arm forward spectrometer covering the region of $\eta \in (2, 5)$. This range of η corresponds to the region of angular acceptance between 10 mrad and 300 mrad in the horizontal plane (xz) and between 10 mrad and 250 mrad in the vertical plane (yz). Due to the fact that the 4 Tm LHCb dipole magnet bends charged particles in the horizontal plane, the horizontal coverage is designed to be bigger

than the vertical coverage [83]. Although this coverage only accounts for roughly 4% of the solid angle, the $b\bar{b}$ pairs' largely forward production, as mentioned in the preceding section, allows for roughly 25% of them to be accepted by the LHCb. Therefore, the cross-section for production of $b\bar{b}$ which is measured by the LHCb are $72.0 \pm 0.3 \pm 0.6.8\,\mu b$ and $144 \pm 1 \pm 21\,\mu b$ at 7 TeV and 13 TeV center-of-mass energy, respectively. Although in ATLAS and CMS the coverage of pseudorapidity in range of $(-2.4, 2.4)$ allows them to access over 90% of the solid angle and get $\sim 45\%$ of the produced b-pairs, because of being less boosted in small pseudorapidity their decay vertices are less displaced, and they suffer from more combinatorics. Although we have mentioned the advantages of LHC environment over the B-factories, it consists of disadvantages too. Comparing the cross-section $b\bar{b}$ production which is measured by LHCb for inelastic pp collisions($pp \to b\bar{b}X$) and the total inelastic cross-section has shown that the $b\bar{b}$ cross-section is 2-3 order of magnitude smaller in the same acceptance [78, 79]. This means that the in comparison with B-factories the LHC environment is more overwhelmed by the background.

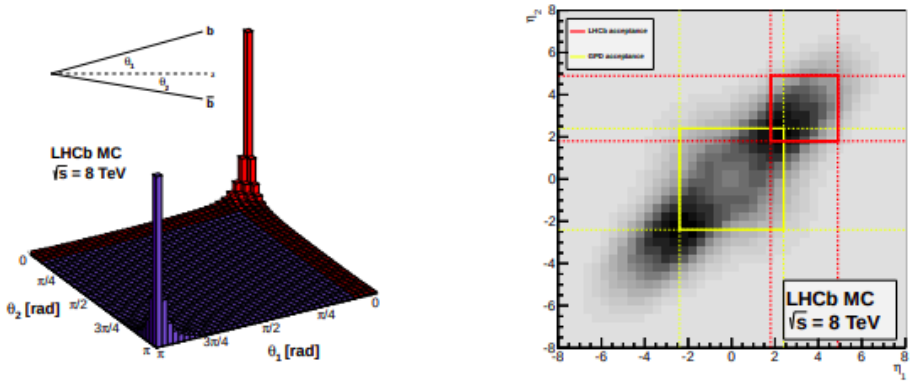

Figure 2.3: *left: $b\bar{b}$ production in terms of polar angles, θ_s right: $b\bar{b}$ production in terms of pseudorapidities. The regions fully covered by the LHCb, are presented in red [84].*

At LHCb the z-axis is defined along the beam axis and pointing from interaction point toward a part of a detector which is called muon chamber. The y-axis is perpendicular to the LHC tunnel and pointing toward the surface, and the x-axis is oriented in a way that they form a right-handed Cartesian coordinate system (Fig. 2.5). The idea behind choosing small solid angle for detection at LHCb is beyond just being a cost-efficient instrument. This condition allows us to record the decay vertices with larger displacement and on top of that it enabled us to straightforwardly elaborate an important particle identification sub-detectors such as ring-imaging cherenkov system. The other advantage of this system is that it allows to use the electronics for readout systems outside this solid angle to reduce the material inside detector acceptance.

Through the following chapter, we will discuss the LHCb apparatus as during the RunI(*i.e.* 2011, 2012 pre-June and 2012 post-June) and RunII(*i.e.* 2016, 2017 and 2018) periods of data taking. Due to the fact that the LHCb cannot perform optimally in the high-multiplicity hadronic environment, the provided collisions for LHCb (by LHC)

is at the rate which is significantly lower than other experiments, namely ATLAS and CMS. To do so, LHC beams are defocused prior to collisions at Intersection Point 8 in order to lower the collision rate. This collision rate at LHC is often described in terms of instantaneous luminosity $\mathcal{L}(t)$. As it was expressed in [85] the provided instantaneous luminosity for LHCb is almost constant through the whole LHC fill. This enables to reduce the systematic uncertainty by maximizing the collected integrated luminosity during the LHC fill, while maintaining the trigger configuration of LHCb. The integrated luminosity corresponding to the various years of data taking are shown in Fig. 2.4. A full data set of about 3 fb^{-1} was collected during the RunI and during the RunII phase, an additional 6 fb^{-1} of data was collected by LHCb.

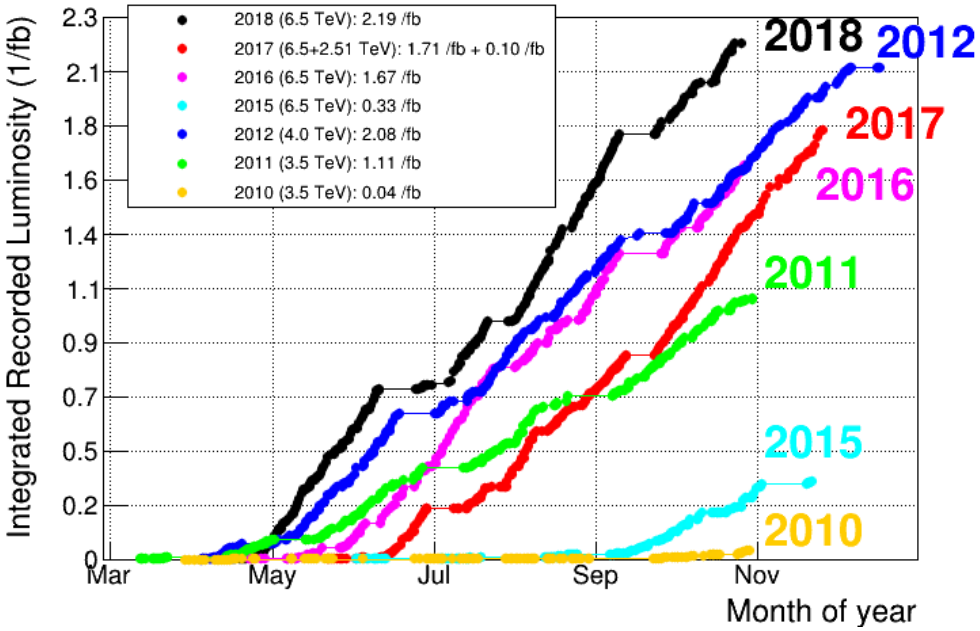

Figure 2.4: *Integrated luminosities recorded by the LHCb experiment during Run 1 (2010-2012) and Run 2 (2015-2018) data taking periods, for p-p collisions. Corresponding beam energies are also displayed.*

The design of the LHCb was done in order to reconstruct exclusive decays of beauty and charm hadrons in a variety of final states involving charged leptons, charged and neutral hadrons, and photons. These particles or final states can be divided in two main following categories :

- The so-called stable particles which can live sufficiently enough to traverse the detector and this allows them to be detected directly .These particles are: charged pions ($\pi^{\pm}$), charged kaons ($K^{\pm}$), protons (p and $\bar{p}$), electrons and positrons($e^{\pm}$), muons ($\mu^{\pm}$), photons(γ) and deuterons(d).

- Unstable particles whose lifetime is much shorter than the first category. These final states are reconstructed by using the information of the stable products.

One should take into account that there is also one specific long-lived subset of particles which decays through the weak interaction, and this will allow them to cross several stations of the detector before they decay. (e.g K_S^0, Λ and Ξ^-). In order to identify these particles, we need to measure their properties and reconstruct them. These reconstructions are done based on the information which is recorded by several specialized sub-detector. These sub detectors are:

- the VErtex LOcator (**VELO**) is placed around the interaction region and allows the reconstruction of primary and secondary vertices;

- the first Ring Imaging CHerenkov (**RICH1**) detector is placed just after the VELO and is dedicated to the identification of charged particles;

- the Tracker Turicensis (**TT**) is placed after the first RICH and is part of the tracking system;

- the dipole magnet of LHCb provides the magnetic field used to bend particles tracks in order to evaluate their charge and momentum;

- the three tracking stations (**T1,T2,T3**) are placed behind the magnet and are also dedicated to track reconstruction;

- the second Ring Imaging CHerenkov detector (**RICH2**) is designed to provide efficient particle identification in a different momentum range with respect to RICH1;

- the Electromagnetic CALorimeter (**ECAL**) system is placed just after the RICH2 and is necessary for an efficient trigger and for the identification of electrons and photons. It is preceded by two auxiliary sub-detectors : the Scintillating Pad Detector (**SPD**) and the PreShower (**PS**);

- the Hadronic CALorimeter (**HCAL**) is placed behind the ECAL and is exploited by the hadronic trigger;

- the Muon Stations are placed just before the SPD/PS (**M1**) and at the end of the detector (**M2** to **M5**), where only muons can arrive without being stopped by the calorimeter system. They are used both for an efficient trigger on decays with muons in the final state and for muon identification.

which is shown in Fig. 2.5

Finally, one should take into account that all these individual sections which were mentioned above can be categorized in to two main systems of LHCb: Tracking and particle identification. The electromagnetic and hadronic calorimeters next to the muon stations form the LHCb particle identification system while, VELO, the TT and the three tracking stations together with the magnetic dipole form the LHCb tracking system.

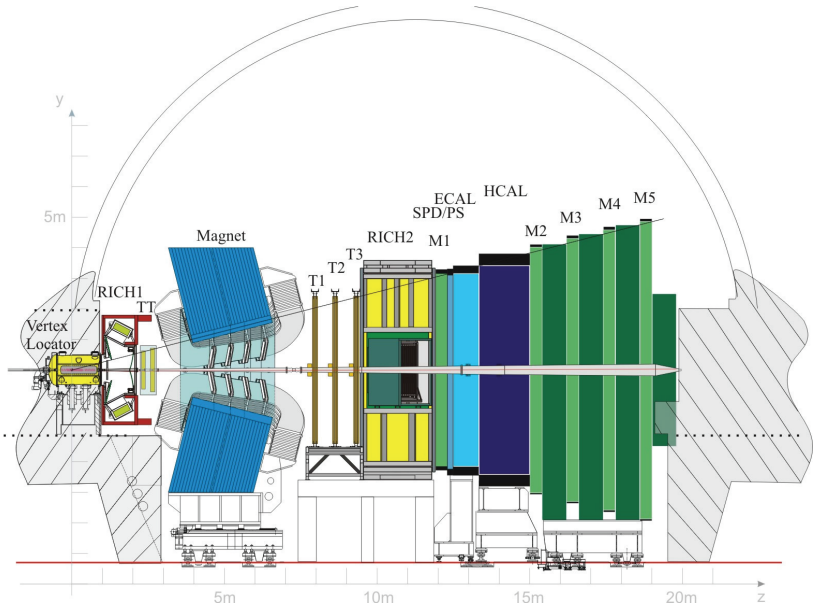

Figure 2.5: *Overview of the entire LHCb detector [86].*

2.3 LHCb vertexing and tracking systems

Due to the fact that the detector's performance depends on precise vertex reconstruction and high momentum resolution, identifying the particle trajectories, measuring their momenta and reconstruction of interactions and decay vertices are the goals which are set for the entire tracking system. As it was mentioned before, the VELO was built to accomplish the latter goal, which is also enabled us to reconstruct the tracks together with the Tracker Turicensis and the three tracking stations placed after the magnet.

2.3.1 The Vertex Locator

The LHCb detector's vertex locator (VELO) [87] is one of a kind at the LHC since it can be moved between 35 mm and 7 mm from the LHC beam. This movement is required to protect the VELO during proton injection, while the beam is unstable and may deviate from its normal direction.

In order to provide this, the VELO is devided into two halves and each of them installed on top of a movable device. This device can move the two halves (horizontally) away from the beam pipe and situated inside a vessel to maintain the vacuum. Prior to the beginning of the normal data taking and after each fill of the LHC the VELO aperture is at the open position. Then the position of the beam is measured and the VELO is steered into place (called closed position) and provides precise measurements of the track coordinates close to the interaction point. These coordinates are utilized to locate any displaced secondary vertex, which is a distinctive feature of B hadron decays. Since the typical lifetime of the

B hadrons is of the order of 1.5×10^{-12} s they cover, at LHC energies, a mean distance of about 1 cm inside the detector and gives rise to secondary vertices distant from the primary pp interaction vertex. For this reason, in order to select signals and reject most of the combinatorial background, it is necessary for the vertex detector to have a micrometric precision. Furthermore, this precise measurement of the B-meson allows us to perform the precision lifetime measurements and study the process such as $B^0_{(s)}$ mixing [88].

Each of the aforementioned two halves of the VELO consists of a series of 21 circular silicon modules arranged perpendicularly along the beam line direction as shown in Fig. 2.6. When ionizing particles are passing through the active material of the VELO they generate hits in each module. Each of these modules consist of two planes of 300 μm thick silicon microstrip sensors and by capturing the signal from radial and polar sensors, the module can provide a measurement of the $R = \sqrt{x^2 + y^2}$ and ϕ coordinates of each individual hit. At the same time, the position of the module which was precisely measured can provide the z coordinate of the hit, knowing which modules provided a signal for a given particle hit. The R sensors of each half comprised of four parts of about 45° each. The microstrips are modeled in a semi-circular shape and their width varies from 38 μm (close to the beam) to 102 μm (far from the beam): the smaller width close to the interaction region is because higher number of particles are expected in that zone.

The ϕ sensors are split into inner and outer regions. For the inner regions, As the radius increased from 38 μm to 78 μm, the pitch size grows linearly and for the outer region, that starts at a radius of 17.25 mm, the pitch size ranging from 39 μm to 97 μm. Furthermore, in order to improve the pattern recognition, different tilts with respect to the radial direction were decided for the Inner and outer regions. These tilts are 20° for the inner regions and 10° for the outer regions. In addition, the opposite skew was considered for the longitudinally adjacent ϕ sensors to have a better track reconstruction.

Using 2011 collected data [90], the VELO detector's performance has been thoroughly investigated and as a result the proximity of VELO to the LHC beam enabled us to achieve the primary vertex resolution of 13 μm in the transverse plane (x, y) and 71 μm along the beam axis for vertices with 25 tracks or more while achieving an impact parameter resolution of less than 35 μm for particles with transverse momentum of greater than 1 GeV/c.

2.3.2 The Tracker Turicensis

One of two silicon tracker sub-detectors at LHCb is the TT, which stands for'Tracker Turicensis' (TT, [91]). The importance of the TT is because of its role in improvement of momentum resolution and trajectory of reconstructed tracks. To reach to this goal, TT provides references which are used in order to combine the tracks reconstructed in VELO and those which are reconstructed in after-magnet tracking stations. In the Run-II tracking algorithm, the TT information* is used to expedite the tracking process by allowing the algorithm to narrow down the possible window for track searching in tracking stations [92].

*it provides the first hit after the VELO

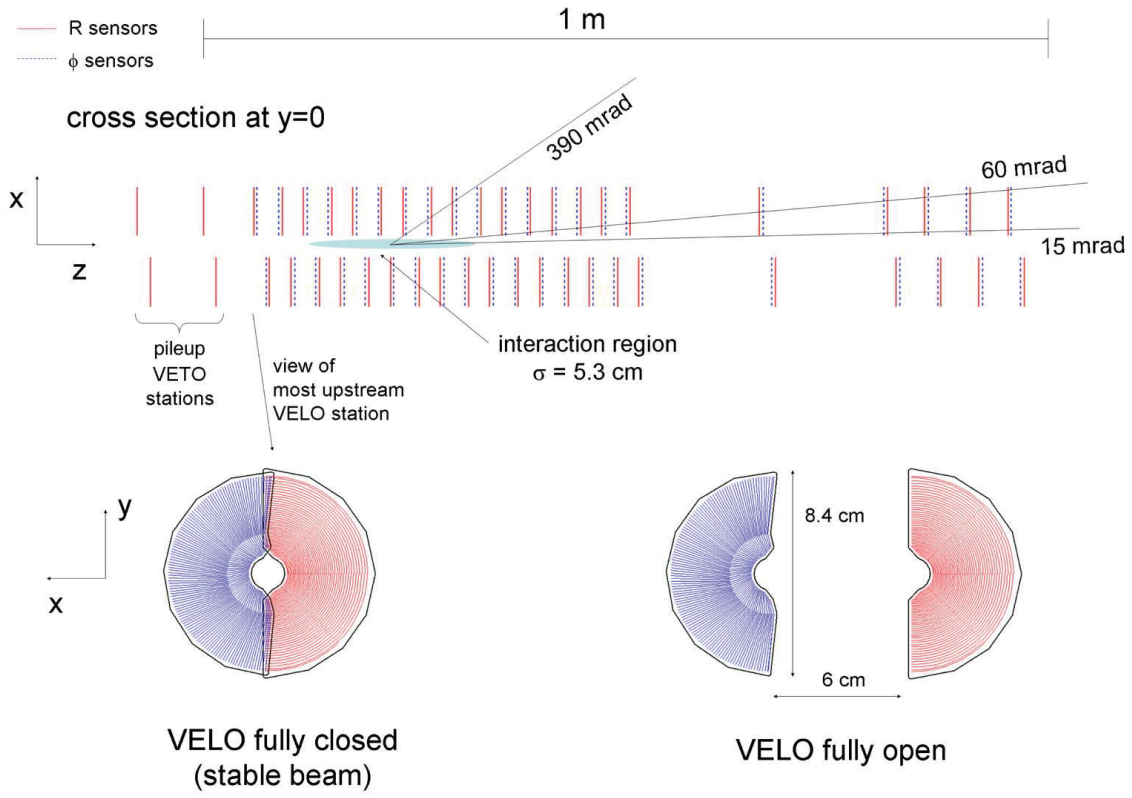

Figure 2.6: *Top view of the VELO silicon modules, with the detector in the fully closed position (top). Front view of the modules in both the closed (bottom left) and open positions (bottom right) [89].*

This setup consists of two station, which are called TTa and TTb, and each of these stations composed of two layers. The setup is installed in between the RICH1 sub-detector and dipole magnet[†] whereas each station in it were separated by 30 cm from the adjacent ones the whole setup distance from the interaction region is about 2.4 m. The area of their coverage is rectangular, with the height of 130 cm and the width of 150 cm. This sub-detector and its components are shown in Fig. 2.7. Moreover, each of the four TT stations is made up of silicon microstrip sensors with a 200 μm pitch that are organized into 38 cm long readout strips. In order to have the possibility of three-dimensional track reconstruction, two of these four layers, namely second and third ones, are tilted with respect to the vertical axes and the rest are parallel with respect to that axis. The amount of tilt for second and third layers are $+5^\circ$ (u-layer) and -5° (v-layer), respectively. Also, it should be noted that the single-hit resolution for TT sector is about 50 μm [92].

[†]At this region the residual magnetic field 0.15Tm exists

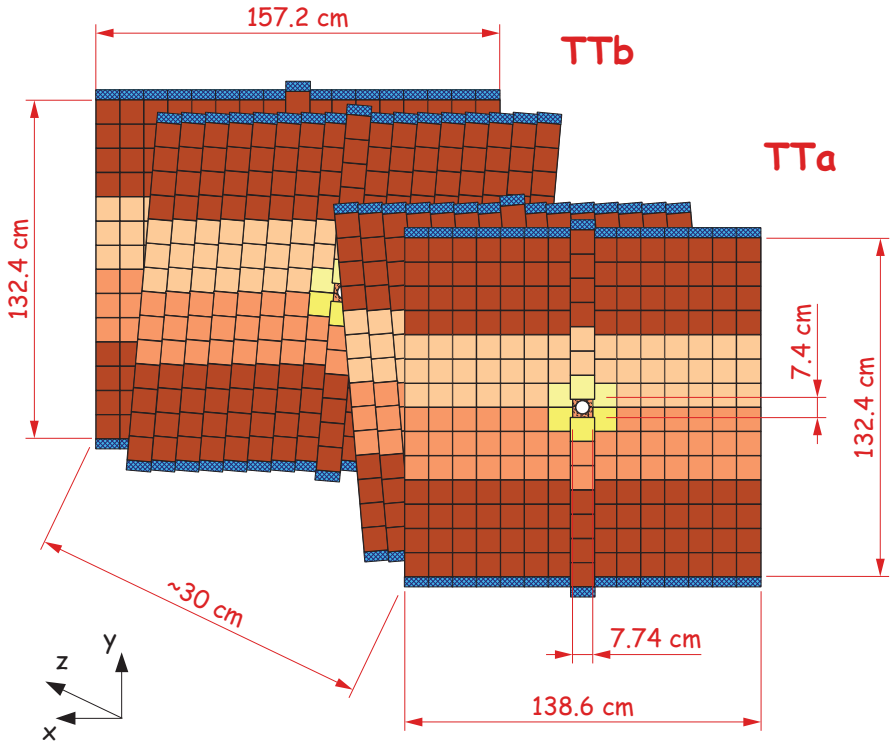

Figure 2.7: *Scheme of the two TT stations and its four layers [81].*

2.3.3 Downstream tracking stations

As you can see in the Fig.2.5 after the dipole magnet there are three tracking stations, namely T1, T2 and T3. These tracking stations are divided into two main parts: inner and outer part. The inner part of the tracking stations, the Inner Tracker (IT), same as another silicon tracker TT, uses four vertical silicon microstrip detectors with a strip pitch of around 200 μm. Also, this part has the same tilting in its 4 layer as we described for TT sector. Although, TT and IT has similar structure, they have difference with respect to covering of detector acceptance. While TT covers the full acceptance region, IT is situated in the down stream of the magnet and innermost acceptance region, which are close to the beam pipe. The Fig. 2.8 and 2.9 have shown the IT [93]. Meanwhile, the outer part is composed of 55000 hollow tubes whose diameters are 4.9 mm. This set up for a drift-time detector, which is called Outer Tracker (OT). This sector same as the other sector has 4 plates which are placed in the same way as we explained for TT and IT sector. In order to have the optimal sensitivity, each of the tubes we filled with a mixture of Ar, CO_2 and O_2 with the proportion of 70, 28.5 and 1.5 % respectively. The mechanism of this detector is based on the phenomenon which is known as Townsend discharge [94]. Each time a charged particle enters a tube, it ionizes the containing gas inside it. Then, electrons are attracted toward the charged wire at the center of the tube. As these electron drifts, due to the Townsend discharge, the number of electron can be increased to a level which can

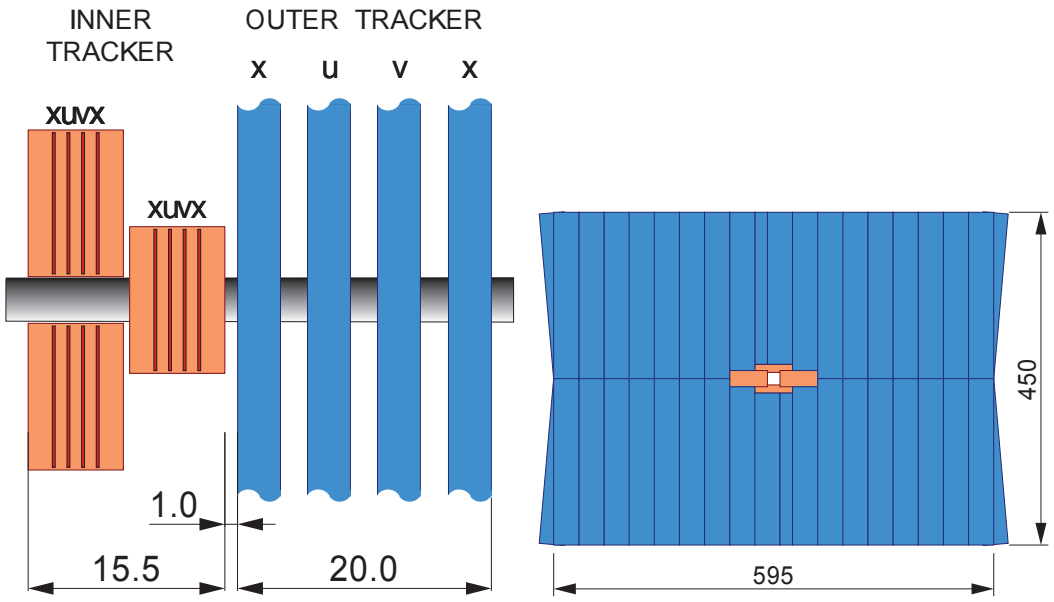

Figure 2.8: *Layout of a T station from a side view (left) and from a front view (right). The dimensions are in centimeters. In the left part it can be seen that the IT sub-detector is placed in front of the OT sub-detector and the x- u- v-planes mentioned in the text are shown. In the right scheme, it can be seen that the IT sub-detector (in orange) is placed around the beam pipe, while the OT sub-detector covers the outer region of the station.*

be detected by the electronics which are installed at the end of these wires. In order to optimize the performance of OT instead of concerning the spacing of the tubes, the ratio of the drift time to the interaction time can be considered and determine the distance from the wires. Also, inside the tubes in order to achieve the drift time of 50 ns for electrons, the aforementioned gas proportion was deduced [95].

2.3.4 The LHCb magnet

Since we cannot measure the momentum of a charged particle directly, the best way to determine its corresponding momentum is to use the Lorentz force law and by measuring the curvature of its trajectory, caused by a magnetic field. For this same propose, the magnet sector of LHCb detector was installed between first tracking T1 and TT sectors. This magnet is non super-conducting type which is known as warm dipole magnet. It provides the maximum intensity of 1 T whereas its integrated magnetic files amounted

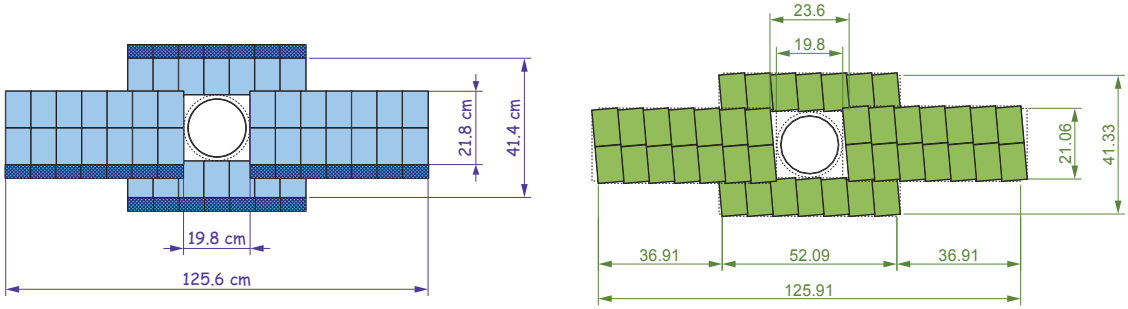

Figure 2.9: *Frontal view of the x-plane (left) and u-plane (right) of the IT sub-detector [80].*

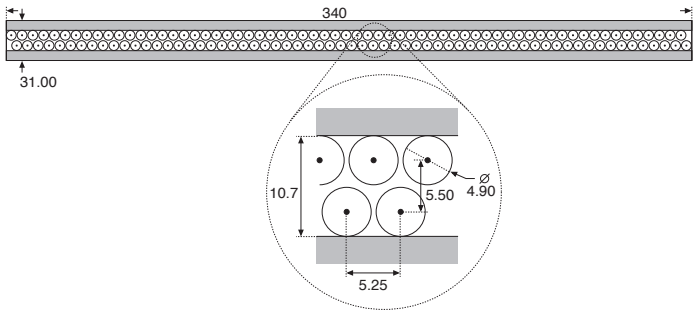

Figure 2.10: *Cross-section of a straw tube plane in the OT. The zoomed part shows the honeycomb structure of the two rows of tubes [80].*

to $\int Bdl = 4\text{T.m}$ [83]. Its yoke has a total weight of 1500 tons and total weight of the two coils is 54 tons. To bend the trajectory of charged tracks in the horizontal plane (x-z plane) the magnet was installed in a way to generate a magnetic field with vertical orientation (along y-axis). Due to the design of the magnet and the bending power of it, the measured moment of each charged particle(charged track) can be determined with the resolution of 0.4 % and 0.6 % at 2 GeV and 100 GeV, respectively. Like any other detector, LHCb has its own defects and these defects might mimic asymmetric behavior same as $\mathcal{CP}$-violating ones. In order to avoid such bias, a periodicity, was considered for the polarity of magnetic field (typical amount of this period is two weeks) during the data tacking moment in order to collect the same amount of data for each category. Depending

on polarity direction, the data are name as `MagUp` and `MagDown`.

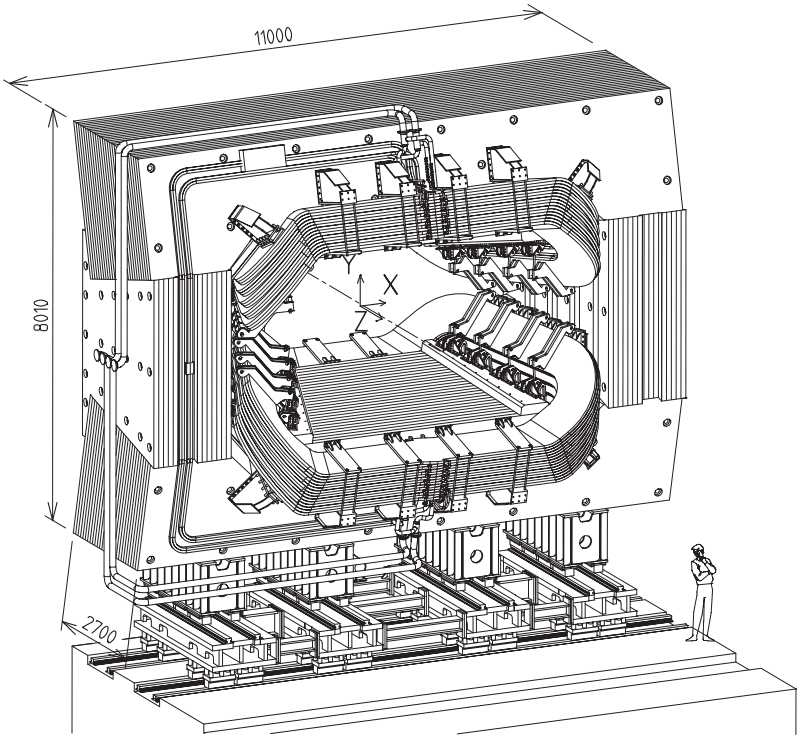

Figure 2.11: *Sketch of the dipole magnet of LHCb [80].*

2.3.5 (Reconstructed) Track Categories

So far different sectors of tracking system at LHCb detector was described. These sectors and their corresponding captured information about each hit, combined in order to reconstruct the trajectory (so-called track) of a given particle. Depending on the information that are accessible from VELO, TT, IT and OT stations at the time of reconstruction, these tracks are categorized into five different groups (classes) of tracks:

- **Long tracks**: The relevant hits of this type of tracks shows that the corresponding particle was passing through the full tracking system(*i.e.*from the VELO to the T stations). Since the momentum determination of this type of tracks are the most precise ones, they are considered as the most important class of track for reconstruction of b-hadrons.

- **Upstream tracks**: The hits related to these trajectories are only captured in VELO and TT sectors. Normally these tracks are corresponding to low momentum particles, whose curvature in the magnetic fields are high enough to get out of the acceptance area of the T stations.

- **Downstream tracks**: The hits of these type of tracks are obtained by TT and T stations. Most of the relevant events to this type of track are the daughters of K_S^0 and Λ^0 decays which are occurred outside the VELO detector.

- **VELO tracks**: The hits of such tracks are only captured in VELO sector, and they are normally corresponds to either backward track or large angle ones. The information of these hits are important in order to reconstruct the primary vertex properly.

- **T tracks**: The recorded hits of these type of tracks are only captured in T stations. They are mainly associated tracks to the products of secondary interactions and providing useful information for the global pattern recognition in RICH2.

  Fig. 2.12 has shown a schematic view of each type of these tracks. In case of having multiple track reconstruction for a particle, with different track type, the only track that is most suited for analysis purposes is maintained. In this respect, long tracks are the most preferred track type, upstreams are preferred over VELO types, and downstream tracks are preferred over T tracks [96]

2.4 LHCb particle identification systems

The details of tracking system and reconstructed track by LHCb was described previously. In this section, another LHCb setup will be described whose duty is identifying the nature of particles(tracks). The identifying procedure of each track at LHCb is based on either information that comes from one of the sub detectors or by defining a global likelihood

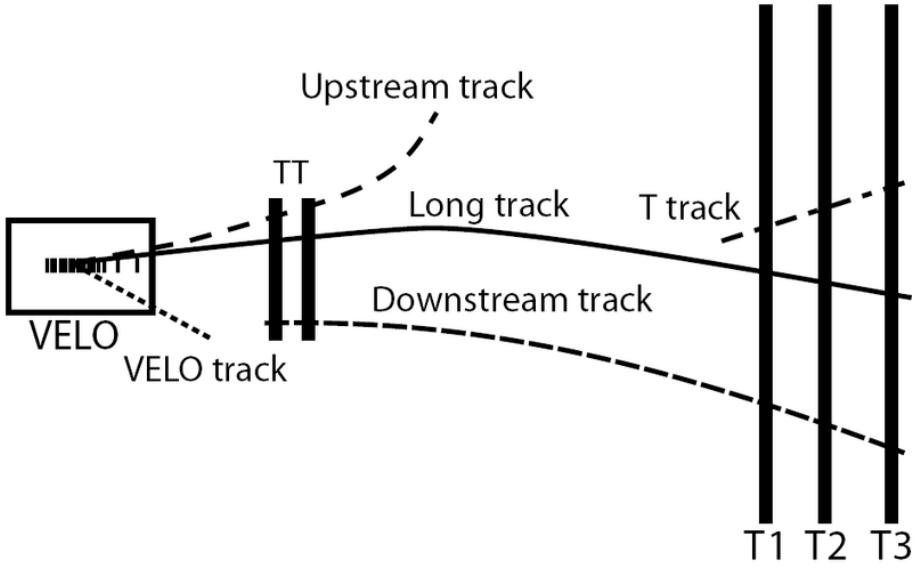

Figure 2.12: Illustration of the different track types: long, upstream, downstream,VELO and T tracks [86].

or neural network output for a collection of sub sector responses. As a result, we could distinguish between the charged leptons and hadrons while providing the same information for neutral particles such as photons and π^0s. To fulfill this requirement, this set up comprised of:

- two Ring Imaging Cherenkov detectors, namely RICH1 and RICH2, the former one installed in front of the magnet and used for identification of lower-momentum particles and the latter one which is place after tracking stations and dedicated to particle identification of the high-momentum tracks.
- Calorimeter sector which is devoted to energy measurement of each track and to meet this requirement it should absorb its energy.
- The muon sub-detector, whose name also indicates that it is built to detect the muons. All the muon detectors but one are installed after the calorimeter. These muon sectors are separated by an iron shield from the calorimeter. This is due to the fact that almost all the tracks except muons could be captured by this amount of material, and only muons with energies above few GeV can traverse and reach to the M-stations.

2.4.1 RICH detectors

In order to provide a powerful tool to distinguish between protons, Kaons and pions LHCb is using two RICH detectors. These detectors provide an identification for the ranges of energies between few GeV to 100 GeV. Moreover, the information of these two

sub-detectors play a crucial role in determining the nature of muon and electron tracks. As their names indicate, they are built based on the Cherenkov effect. This effect described how a charged particle emitting electromagnetic radiation in case of passing through a dielectric medium with a velocity bigger than the speed of light in that medium, c/n where n indicates the refraction index of that medium. As a result, the particle emits photons in the direction defined by a cone around its direction of flight. The opening angle of this cone is defined by $\theta = \arccos(\frac{1}{\beta n})$ where $\beta = v_{\text{particle}}/c$. Fig. 2.13 shows a schematic view of Cherenkov effect and θ_C.

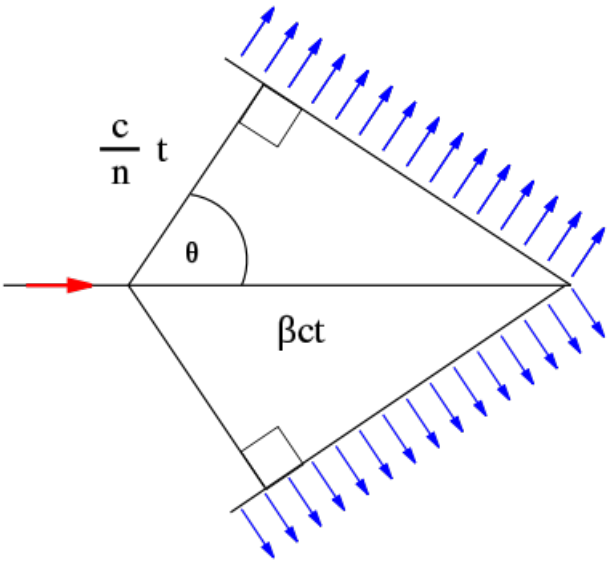

Figure 2.13: *Geometric representation of the Cherenkov emission.*

Since θ_C in this formula depends on the velocity instead of the momentum and momentum is the measured quantity at LHCb (using tracking system) this relation can be redefined by using 4-momentum relation of $p^\mu p_\mu = m^2c^2 = \frac{E^2}{c^2} - p^2$ as follows:

$$\beta = \frac{cp}{E} = \frac{cp}{\sqrt{p^2c^2 + m2c^4}} = \frac{1}{\sqrt{1 + (\frac{mc}{p})^2}} \tag{2.4}$$

$$\cos\theta_C = \frac{1}{\beta n} = \frac{1}{n}\sqrt{1 + (\frac{mc}{p})^2} \tag{2.5}$$

Thus, using this formula, by measuring θ_C together with the momentum, the mass of particle related to this track can be determined. When particles' velocity approach the speed of light we have,

$$\lim_{v_{\text{particle}} \to c} \theta_C = \arccos(1/n)$$

which is called the saturation value of Cherenkov angle. In order to avoid that saturate conditions, RICH detector utilize different medium with various refraction indices, named radiators. For instance, RICH1 [91], which is installed adjacent to the VELO with a

geometrical acceptance from 25 mrad to 330 mrad, is optimized for low momentum tracks identification whose momentum are between 1 GeV/c and 60 GeV/c. Thus, its design composed of two sub layers as follows:

- The first media which is 5 cm thick and comprised of Aerogel layers with refractive index of 1.03. This layer was designed optimally for low momentum tracks with $p \leq 10\,\mathrm{GeV}/c$
- The second layer which contains the C_4F_{10} gas with $n = 1.0015$ and its design was devoted to particles with higher momentum but less than 60 GeV/c.

The Second RICH detector, as the complementary to the RICH1, is designed optimally for the identification of the tracks whose momentum are within the range of 15 GeV/c up to 100 GeV/c. Its installation place is after T3 station, and it covers the acceptance range of 100 mrad in the vertical plane and 120 mrad in the horizontal plane. Same as the second layer of RICH1 the radiator of RICH2 is gaseous which contains CF_4 that has a refraction index of 1.00046.

The schematic view of two RICH detectors is shown in Fig. 2.14. Also, it is shown that each of RICH1 and RICH2 includes an optical system. Each of these separate optical systems is composed of spherical and plane mirrors which are designed to reflect and focus the emitted Cherenkov light toward the photodetectors, which are installed out of the detector acceptance and are carefully shielded from the residual magnetic field. These photodetectors which are Hybrid PhotoDetectors (HPD) can detect the photons with the wavelength range of the 200 nm to 600 nm. Single photons are assigned to rings using devoted algorithms that calculate the Cherenkov angle. These reconstructed Cherenkov angles θ_C as a function of momentum, for the tracks passing through the C_4F_{10} medium is shown in Fig. 2.15. These tracks are the isolated ones, among the data tracks, which means that their Cherenkov rings do not overlap with other reconstructed rings for the same medium [97]. The distribution in this figure has shown distinct patterns, each of which related to a track with specific mass. Although the main propose of designing RICH is to distinguished hadron tracks from each other, the fourth distinct pattern in Fig. 2.15 has shown its benefits in order to identify muons as well. The LHCb RICH detectors have excellent particle identification performances and provide a very clear discrimination of charged pions, kaons and protons. Fig. 2.15 shows the Cherenkov angle as a function of particle momentum using information from the C_4F_{10} radiator for isolated tracks selected in data (a track is here defined as isolated when its Cherenkov ring does not overlap with any other ring from the same radiator) [97].

2.4.2 Calorimeters

Up to now, the LHCb's system design related to charged hadrons' identification was described. Another sector at LHCb which is devoted to the identification of electrons, photons and neutral pions is called calorimeter [98]. This sector was designed to absorb the energies of the particles and measure their energies through this absorption mechanism.

Figure 2.14: *Schematic view of the RICH1 (left) and RICH2 (right) detectors. The different radiators and the optical systems are also shown [80].*

Since the response of this subdetector is sufficiently fast, its provided information about the transverse energy E_T of the hadrons, electrons and protons, can be used by L0 trigger and plays an important role in L0 triggering process. The calorimeter sector comprises four main parts :

- Scintillator Pad Detector (SPD);
- PreShower (PS);
- Electromagnetic CALorimeter (ECAL);
- Hadronic CALorimeter (HCAL).

These parts (medium) are illustrated in Fig. 2.16. Also, it provides a schematic overview on how electrons, hadrons and photons are interacting with each of these medium. Moreover, in each of the four medium, the cell size are varied across their covering range. The rationale behind this design is that as we get closer to the pipeline, the hit density will increase and as a result we require to increase the granularity of the detector in these regions. In order to fulfill this requirement, while having an optimal choice between occupancy and a reasonable number of read-out channels the following design was devised for the aforementioned medium:

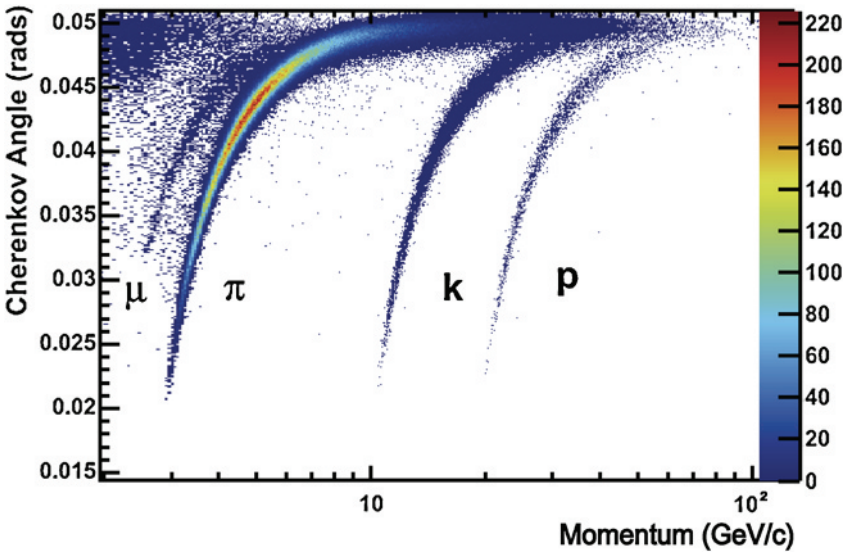

Figure 2.15: *Reconstructed Cherenkov angles as a function of track momentum in the C_4F_{10} radiator [97].*

- SPD, PS and ECAL are divided into three regions of inner, middle and outer with the cell width of 40.4 mm, 60.6 mm and 121.2 mm, respectively.
- The HCAL is composed of only two regions, named as inner and outer regions.

A schematic overview of these subdivisions is shown in Fig. 2.17.

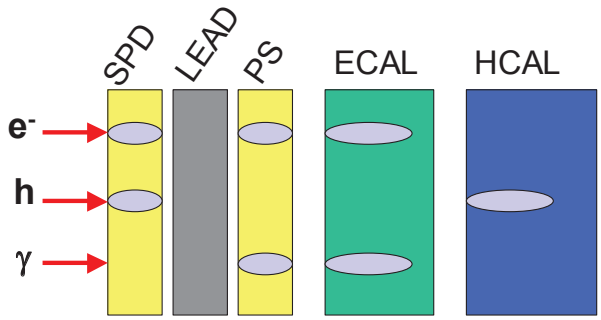

Figure 2.16: *Energy deposited in the different parts of the calorimeter by an electron (e), a hadron (h) and a photon (γ) [80].*

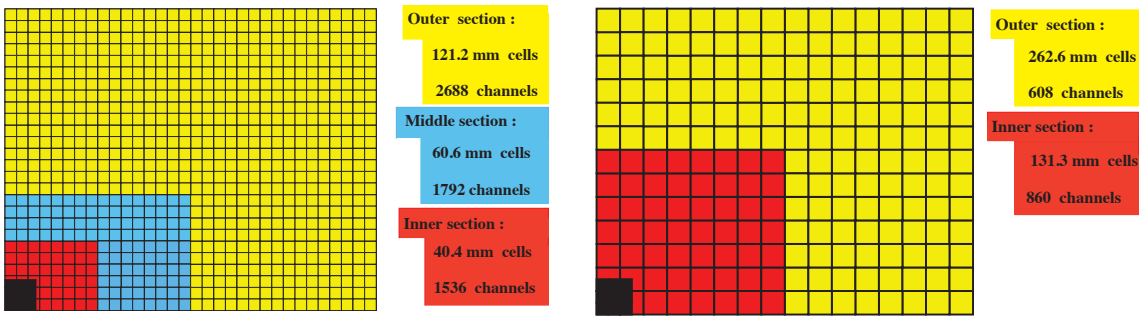

Figure 2.17: *Left: frontal view of the SPD/PS and ECAL detectors, where the three regions mentioned in the text are shown. Right: frontal view of the HCAL where there are only two regions [80].*

At this level, suppose that we have a media with mass number A and atomic number Z. For this media, we could define a distance for an electron over which the electron will lose its energy by a factor e through radiating in that medium [99]. This distance is called radiation length of electron, and it is derived as follows:

$$X_0 = \frac{A \cdot 716.4}{Z(Z+1)\ln(287/\sqrt{Z})}\ g/\mathrm{cm}^2$$

As it is shown in Fig. SPD and PS are installed before the electromagnetic calorimeter(ECAL), and they play a supplementary role for it. In addition to that, both of the SPD and PS are formed by scintillator plane with the thickness of 15 mm. Moreover, in design of calorimeter, SPD and PS are separated by a lead plate whose thickness is 2.5 times of radiation length. This measure is determined in a way that it provides the possibility for the electron to initiate the electromagnetic shower in the plate which can be detected by PS and ECAL which are installed after it. The SPD sector can determine whether it hit by a charged particle or a neutral one. As a matter of fact, when a charge particle passes through the scintillator material, it produces light while the neutral particle does not have such ability. The light emitted by the scintillator material is collected by wavelength-shifting optical fibers (WLS) and emitted light from them are headed toward the multi-anode photomultipliers, installed outside the detector, by using another set of clear fibers. It is through this mechanism that SPD can distinguish between the charged and neutral tracks. Furthermore, the PS determines whether the reconstructed hit belongs to the category of electron/photon or not. In other words, it can provide an information related to the electromagnetic characteristics of the particle.

In general, Shashlik is a layout in any sampling calorimeter comprises several layers of absorber and scintillator materials. The ECAL sector of LHCb as a sampling calorimeter is using this technology as well. The absorber material for ECAL is the Lead, and it includes 66 plates with the thickness of 2 mm. Moreover, as the second component of

the Shashlick technology, plastic scintillator layers are installed between the lead layers. The thickness of these scintillator layers are about 4 mm. Then by installing the WLS optical fibers across this module and in a longitudinal direction, the produced light by scintillation process are transferred toward the read-out photomultipliers. In the design of the ECAL two proportions were respected for determining its size:

- Nuclear interaction length,
- Radiation length.

The former refers to the mean distance through a medium which is required for a relativistic charged particle in order to reduce its energy by factor e and the latter is mentioned before. This quantity is proportional to $A^{1/2}$ where A is the atomic number of the medium. According to these parameters, ECAL was designed to be 1.1 times larger than the interaction length, and it should be 25 times larger than the radiation length. Furthermore, as it is shown in Fig. 2.18 the submodules of the ECAL divided into three types, each of which is being used in specific region. Those submodules installed in the outer region has the dimension of 12cm $\times$ 12cm, the middle region was covered by submodule of 6cm $\times$ 6cm and the size of the submodule corresponds to the inner region is 4cm $\times$ 4cm. Noted that the installed module in the inner, middle and outer regions of the ECAL have nine, four and single read-out channels, respectively.

The last sector of the LHCb calorimeter was devoted to the energy measurement for the hadronic showers. The information of this subdetector is used, along with other information, in order to perform a L0 trigger for tracks. In the design of HCAL, the absorber layer has chosen to be iron plates. The thickness of these plates are 6 mm and 4 mm while scintillating medium is placed between them. The modules of the HCAL are divided into two main categories with respect to the region and dimensions of them. The inner module whose dimension is 13cm $\times$ 13cm, while the other one covers the outer region and its dimension is 26cm $\times$ 26cm.

Although, pre data taking tests have determined the performance of both ECAL and HCAL, during the LHCb run, their resolutions are limited due to pile-up effects. According to these tests, The energy resolutions of the ECAL has been measured to be $\frac{\sigma(E)}{E} = \frac{(8.5-9.5)\%}{\sqrt{E}} \oplus 0.8\%$ while the resolution of HCAL is determined as $\frac{\sigma(E)}{E} = \frac{(69\pm5)\%}{\sqrt{E}} \oplus (9 \pm 2)\%$ [100].

The calibration process can be done for the ECAL by considering the resonances that can decay into two photons. As an instance, the decay of $\pi^0 \to \gamma\gamma$ can be considered as the calibrations samples. In the meanwhile, in order to calibrate the HCAL, the energy which is measure in calorimeter should be considered next to the corresponding momentum which is determined by tracking system. These two measured values in LHCb can provide a ratio which is used for this calibration.

2.4.3 The muon system

The final part of the LHCb detector is the muon system, which provides the identification of muons. Muons are present as final decay products in different fundamental LHCb

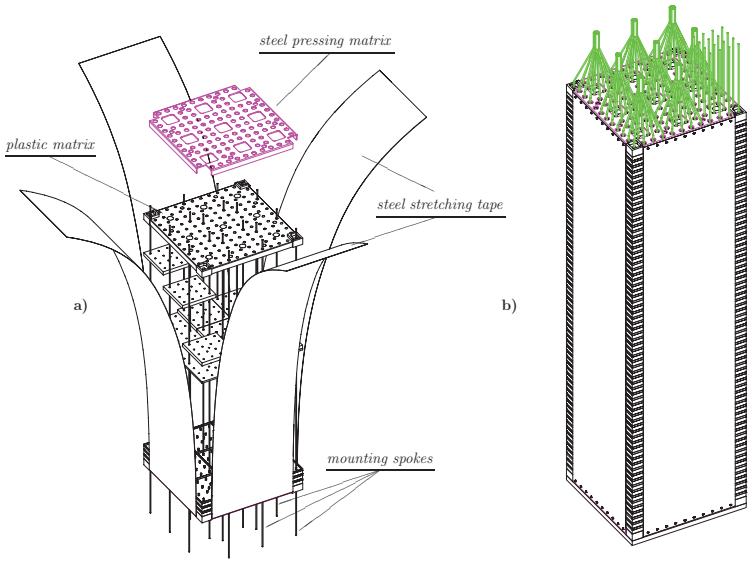

Figure 2.18: *Left: picture of an ECAL module during the assembly phase, the lead/scintillator layers are also shown. Right: representation of an assembled ECAL module of the inner region, the green lines represent the optical fibers conveying the light to photo-multipliers.*

measurements such as $B^0 \to K^{*0}\mu^+\mu^-$ [101], $B_s^0 \to J/\psi(\mu^+\mu^-)\phi$ [102] or $B_s \to \mu^+\mu^-$ [103, 104].

The muon system [105] (see Fig. 2.19) is made of five stations (M1 to M5) covering an angular acceptance of ±300 mrad in the horizontal plane and ±200 mrad in the vertical plane. This corresponds to a geometrical efficiency of approximately 46% for the detection of muons arising from B hadrons. The first muon station, M1, is placed before the calorimeters in order to avoid possible multiple scattering effects that could modify the particle trajectory. The remaining stations, M2 to M5, are placed after the calorimeter system, at the end of the LHCb detector, and are separated by iron planes 80 cm thick. Each muon station is divided into four regions (R1-R4) as shown in Fig. 2.20. The R1 region is the closest to the beam-pipe and has the most dense segmentation, while the R4 region is the farthest. The segmentation defined per region is such that the charged particle occupancy is expected to be approximately the same in each region. All the muon chambers are composed by Multi-Wire Proportional Chambers, except for the inner region of the M1 station, which exploits three gas electron multiplier foils sandwiched between anode and cathode planes (GEM detectors). In total, the muon system consist of 1368 MWPC and 12 GEM detectors.

2.4.4 Multivariate PID methods

The particle identification (PID) in LHCb is achieved by combining the information coming from the various sub-detectors. The RICH detectors, the calorimeters and the

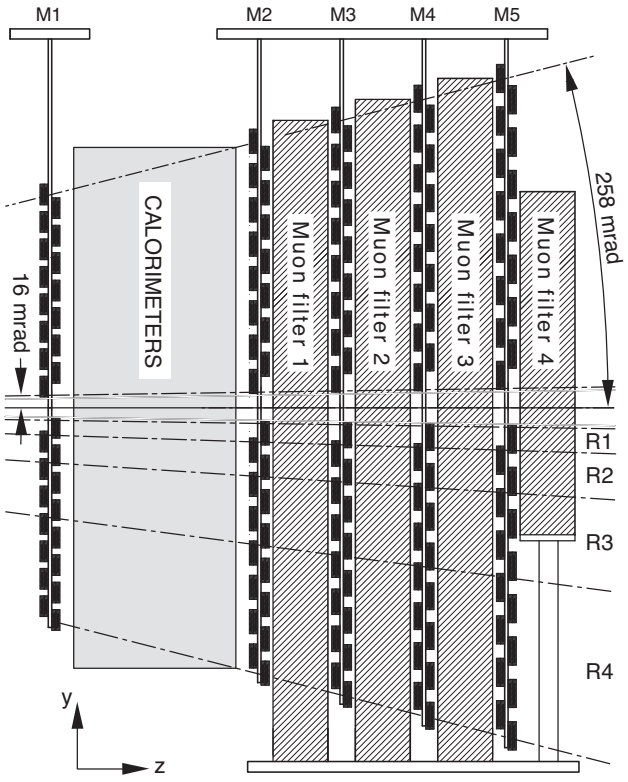

Figure 2.19: *Side view of the LHCb muon system [80].*

muon stations are used for the identification of charged particles (e, μ, π, K and p), while photons (γ) and neutral pions (π^0) are identified using the calorimeter system.

For each particle the available PID information is elaborated from two variables of different nature, but with the same purpose: the log-likelihood difference (DLL) and the ProbNN variable which has been introduced later in the collaboration.

The first variable, the DLL, is defined as the difference between a given PID hypothesis (x) and the pion hypothesis as

$$DLL_{x\pi} = \ln \mathcal{L}_x - \ln \mathcal{L}_\pi = \ln \left(\frac{\mathcal{L}_x}{\mathcal{L}_\pi} \right) \ , \tag{2.6}$$

where each likelihood function $\mathcal{L}_i$ ($i = x$ or π) combines the information coming from the various PID sub-detectors. The higher the variable $DLL_{x\pi}$ is, the higher the probability of the candidate is to be π[‡].

[‡]The $DLL_{x\pi}$ is a special case of $DLL_{xy} = \ln \left(\frac{\mathcal{L}_x}{\mathcal{L}_\pi} \right)$ variable which relates any particle hypotheses x and y. Through this definition, the higher value of DLL_{xy} denoted the higher probability for the candidate to be identified as x and the lower the DLL_{xy} the higher probability of candidate to be y

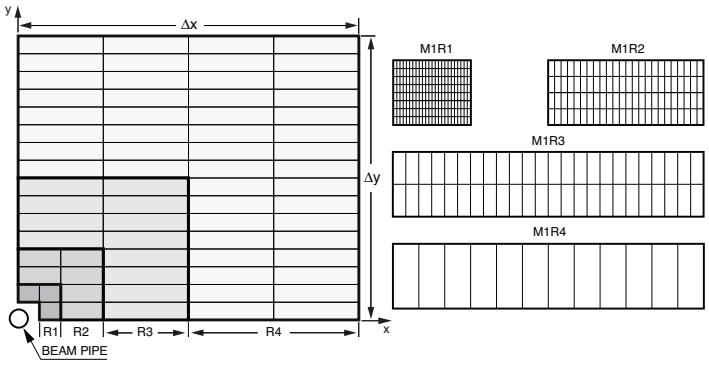

Figure 2.20: *Left: front view of a quadrant of a muon station, each rectangle represents a chamber. Right: segmentation of the four types of chambers corresponding to the four region of M1. In M2, M3 (M4, M5), the number of columns per cell is double (half) with respect to M1, while the number of rows is the same.*

The second kind of variable, the ProbNN, is built by running multivariate analysis tools (in particular Neural Networks [106]) based on the detector PID information. Differently from the likelihood functions, the multivariate analyses take into account the correlations between the information coming from the different detectors. However, an extra training section is mandatory to train these multivariate tools.

The ProbNN variables produced as output are defined between 0 and 1, as a probability would be, and can be used to separate between different tracks' hypothesis. In particular, they are referred to as ProbNNx according to the particle hypothesis x which is tested. where x can be π, K, p, e and μ.

In the analysis presented in this thesis, ProbNN variables are used to distinguish between charged hadrons (kaon, pion and protons). For what concerns the identification of neutral particles, which is very important in analyses involving radiative decays, this is achieved using dedicated PID variables described in detail in Ref. [107].

2.5 The LHCb trigger

The pp bunch crossing at LHC is 40 MHz while the rate of the inelastic collision at LHCb point is around 15 MHz for RunI and around 30 MHz in RunII [108] Therefore, recording the full data stream requires certain technologies and expenditure, which is limited. As an instance, at the time of design of LHCb, it was impossible to store all data at the rate of production.

Even though the production cross-section of the $b\bar{b}$ is high, it is still much smaller than

the *pp* inelastic cross-section [78]. Thus, even at the level of not limiting by available resources and technology, it is not efficient to store all these data because only a fraction of those produced events are the matter of interest. Due to these limitations, a devoted data flow was designed in order to optimally select the interesting events and rejects most of the background events.

This process is called triggering and in order to achieve the best performance(*i.e.* fastest buffering and throughput while having a maximally efficient data taking) the whole process and data flow is separated into three main levels, consecutively. The Fig. 2.21 demonstrates the output of each level with more details.

The three aforementioned stages of LHCb trigger system can also be categorized into two main classes:

- Hardware trigger, which is known as Level-0 or L0 trigger.
- Software trigger which comprise two other trigger levels:
  - High Level Trigger 1 (HLT1)
  - High Level Trigger 2 (HLT2)

In the following each of these triggering levels will be discussed in details.

2.5.1 Hardware Trigger

Hardware or Level-0 trigger (known as L0 trigger) is the primary level of data flow and designed to reduce the rate of data flow to 1 MHz. This reduction is based on the basic selection by using a custom design of electronics. This trigger step was performed based on the result coming from *Level 0 Decision Unit* (L0DU) where L0 algorithms are running. To perform these decision, this unit uses information coming from the calorimeters, the muon chambers and also pile-up sensors in VELO sectors. The decisions out of this information are mainly categorized into two main classes: calorimeter trigger and muon trigger.

2.5.1.1 L0 Calorimeter trigger

The calorimeter trigger is based on provided information by SPD, PS, ECAL and HCAL. In the previous section it has been mentioned how the segmentation was designed for each of the modules (plates) or subsections and why they are denser as we go toward the beam pipe.

To fire an L0 trigger related to any specific decision(*i.e* `L0Hadron`, `L0Electron` and `L0Photon`), first the ECAL is considered as a cluster of transverse energy of 2×2 cells. The output of the ECAL can be achieved by having the energy of the cell i as E_i. Thus, the position of this cell's center and the average point of the *pp* interaction can be determined. Then using these two points, a line can be determined and angle θ can be defined between the axis(toward the beam pipe) and this line. Finally, using this defined angle, the transverse deposited energy E_T can be deduced as $E_i \sin\theta_i$. Furthermore, by summing

up, the E_T of each cluster can be determined. Those cluster with highest E_T is selected and assigned to either, hadron, photon or electrons. Then, using the following logic the calorimeter system distinguish between hadrons, electron and photons:

- The same process is applied on HCAL and if the event also corresponds to the highest E_T in HCAL, it is defined as hadron.
- if the track does not hit the SPD while at least one PS cell was hit and the deposited energy in PS is higher than 5 Minimum Ionizing Particle (MIP) threshold, it is defined as photons.
- The track is defined as electron if the photon conditions were fulfilled, while having at least one hit in SPD sector.

Since processing of high multiplicity events raised the computational costs for the software trigger levels, it would be better to remove such events at hardware triggers. Therefore, the calculated total number of hits in SPD was used to extract such events from data flow. In Run-I this threshold was determined to be 600 and in Run-II it is decreased to 450.

2.5.1.2 Muon Trigger

In order to fire a trigger for muon track by L0DU, it is required to reconstruct the muon track separately. This reconstruction is done based on searching the hit in five muon sectors and considering the origin of the hits to be the interaction point. Then, using this reconstructed track and its slope, the transverse momentum of muon is determined. In case that we have several candidates for an event, only the one with the highest transverse momentum is used for trigger decision. It should be noted that the p_T determination at this level is done by approximate resolution between 20 and 25 percent.

2.5.2 Software trigger

The software trigger, also known as High Level Trigger (HLT), is based on applying the set of modifiable requirements on the data to deliver it to the LHCb mass storage with an acceptable rate of 5KHz (for RunI) and 12.5 KHz (for Run-II). The reason behind this increase is that as the energy of center of mass increase we should expect to have a higher rate of interesting events. To perform HLT, the corresponding C++ package is run on the Event Filter Farm (EFF). This farm comprises over 29000 CPU cores to implement over 26000 copies of this application. During the execution, certain set of requirement devoted to each group of analysis are applied on the data. these set of requirement are called *trigger lines*. Each set of these requirements were chosen optimally to extract a specific class of events. Due to the computational power of the aforementioned resources, the required time per each event processing for the Run-I data, was estimated about 30 ms. Concerning the timing for such computations, the Software triggers were designed to be done in two sublevels: Level-1, which is known as HLT1 and level-2 which is named as HLT2.

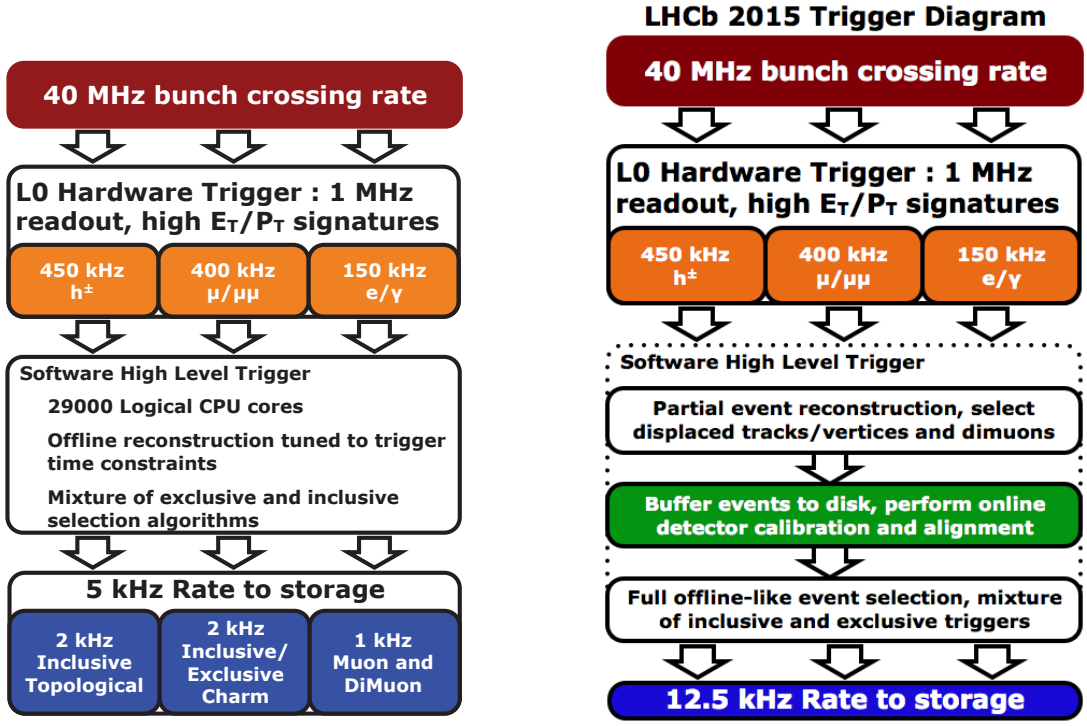

Figure 2.21: *Flow-diagram of the different trigger stages in Run 1 (left) and Run 2 (right). Software High Level Trigger indicates HLT1 and HLT2 stages.*

2.5.2.1 High Level Trigger 1 (HLT1)

The main propose of this level is to decrease the 1MHz rate of input (coming from L0 trigger) while selecting events related to beauty and charm decays. Also, the events which required higher computational time were determined and rejected in order to no waste the CPU power. As an instance, the events whose OT occupancy is larger than 20% would require to take more than 25 ms to process. Therefore, rejecting these events will help us to do the remaining process faster. In the next step, and using the remaining events, we perform a reconstruction. In this level, the information from tracking system is used in order to select the events whose tracks are originated in primary vertices (PV) and their corresponding p_T is high. Furthermore, the reconstructed tracks were required to have the IP larger than 125 μm with respect to any PV while their momentum is larger than 12.5 GeV/c and their transverse momentum to be at least 1.8 GeV/c. In case that the events passed the `L0Photon` and `L0ElECTRONS`, the requirement become looser and the p_T for such events is considered to be bigger than 0.8 GeV/c.

2.5.2.2 High Level Trigger 1 (HLT1)

Thanks to the selection in HLT1 the HLT2 can be done as a (semi) full event reconstruction. In the ideal circumstance, if we have a detector which is perfectly calibrated and fully aligned, we could perform a full event reconstruction. However, due to these imperfections

in our LHCb detector, we required to constantly calibrate the detector and align it as well. These process is changing between the fills and each time need to be optimized. In Run-I data taking period, no parallel process was considered for such calibration and alignment. Instead, during the data taking, so called online, only a simplified version of reconstruction was used in order to process the data in time and then in another step after HLT2, so called offline, the data were reprocessed. At the end of the run-I the HLT was optimized and this optimization increased the saved amount of events in the disk by 20%. This new strategy enables to lower the threshold of p_T for the reconstruction algorithm and using the devoted algorithm for the reconstruction of long-lived particle tracks as well [109]. Fortunately, in RunII data taking period, this optimization in HLT is accompanied by the EFF upgrade and as a result it allows the full event reconstruction for HLT2. At the same time, the HLT1 performed parallelly for the RunII and its results saved in to 5PB buffer. This allows us to have a fully online alignment and calibration for the detector while being able to apply HLT2 on top of HLT1, between the fills, to the data that kept in the buffer. Therefore, due to this upgrade and optimized method, the Run-II samples were significantly outperformed the online reconstruction results of Run-I.

2.5.3 Trigger decision categories

So far, we discussed how trigger system is using an algorithm to perform a decision and apply it on track. These algorithms can be combined with their selection parameters. To each of these ensembles of requirements we could assign a unique key which is known and Trigger Configuration Key (TCK). According to the trigger, the events in each sample can be divided into three main classes:

Trigger On Signal (TOS) These are related to the type of event for which the presence of the signal is sufficient to fire the trigger

Trigger independent of Signal (TIS) The presence of events other than signal is enough in order to fire the trigger.

TIS and TOS the events which belongs to both TIS and TOS simultaneously.

2.6 LHCb Software

The LHCb experiment's softwares are divided into around 20 packages. Each of them is kept in its own Git repository on CERN's GitLab instance. The names and dependencies of most applications are shown in Figure 2.22

The LHCb software framework is based on the `Gaudi` framework [110]. This framework is independent, and it provides generic implementations of services and interfaces which are necessary for processing events in HEP experiments. For instance, `LHCb` and `Lbcom` are two libraries which were built up on this framework and their LHCb dedicated classes are used for many tasks such as detector geometry.

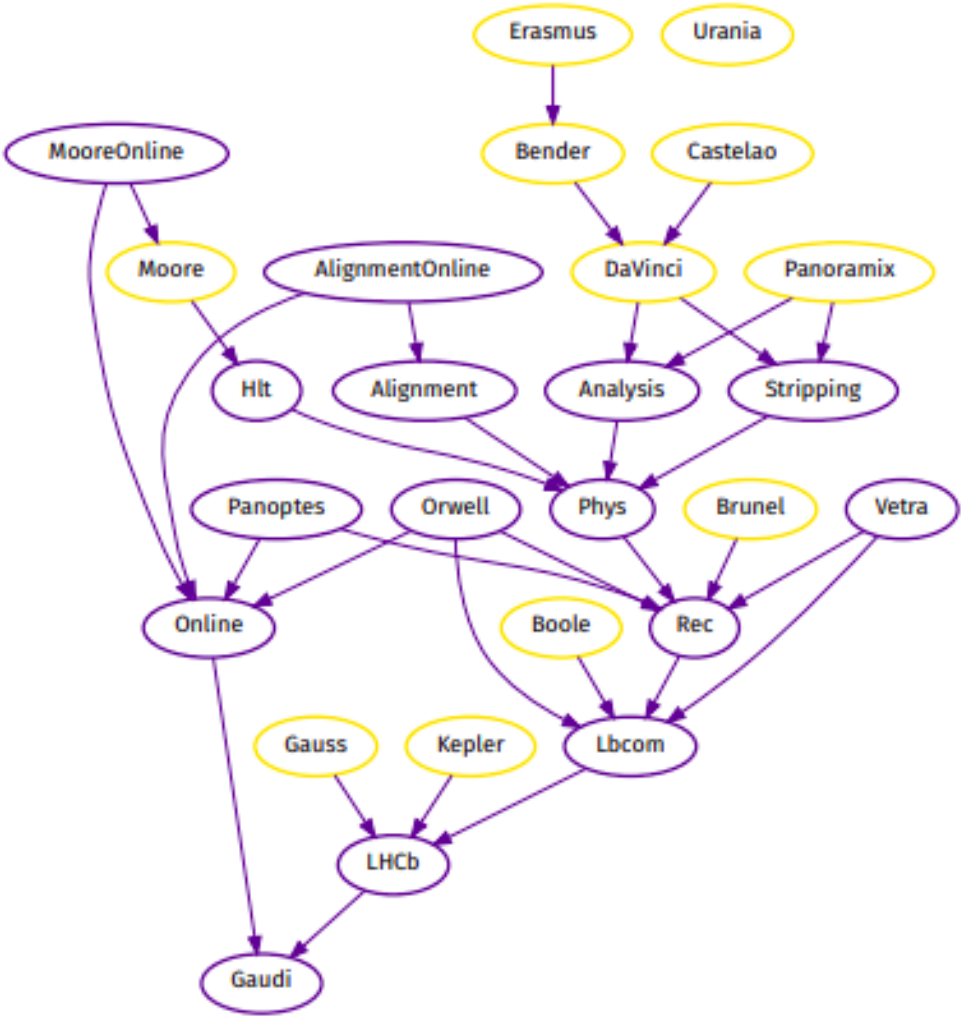

Figure 2.22: *The key software packages maintained by the LHCb collaboration. The yellow color emphasized the set of the more frequently used environments.*

In order to use the Worldwide LHC Computing Grid and perform offline reconstruction as part of centralized processing campaigns, a high level application was design which is called `Brunel` [111]. Since Run-II `Moore`, which is the high-level trigger application in LHCb, conducts the same reconstruction. To let this happened, another independent library is used to share the reconstructed events between `Moore` and `Brunel`. This code is called `Rec`. `Phys` and `Analysis` are two other libraries which contain software to implement physics data objects in analyses. They contain data objects such as vertices and particles and mainly utilized via `Davinci` and `Moore` software applications.

`Stripping` is the process of filtering data which is reconstructed by `Brunel`. This process of filtering is centralized through `Davinci` to produce `ROOT` [112] files containing

the information regarding the signal candidates and their properties in the form of `TTree` data structure. Direct manipulation of stripping output is restricted to a small group of the users. In order to work with these output files more conveniently, the `Bender` software application can be used.

2.7 Simulation at LHCb

Monte Carlo Simulation is one of the inevitable steps for each analysis in high energy physics. These types of inputs enable to acquire the information that is hard to access through real data. Such generations for each LHC experiment is done through a dedicated package. This process in LHCb can be divided into four main phases, which are integrated in the `Gaudi` framework. in the following, these steps are briefly discussed.

1st phase

In the first phase, the physical events and their interaction with LHCb detector is simulated by `Gauss` framework. It is through this software package that the generations of pp collision events and simulation of detector responses to these products are governed. For this purpose, `PYTHIA 8` [113] with LHCb specific configuration [114] is being used to generate the events. Then the hadronic decays and their states are simulated using `EvtGen` [115] and the modeling of final states for radiation is done using `PHOTOS` [116].

Moreover, `Gauss` simulates the running conditions such as smearing of the interaction zones related to the proton bunch transverse and longitudinal sizes, and the luminosity changes during a fill which is caused by the finite beam lifetime. As a result, pp collisions are generated related to the required running luminosity. The next step in `Gauss`'s processes of simulation is related to the propagation of the generated states in LHCb detector. As discussed in reference [117], through this step, interactions and detector effects are simulated using the `GEANT4` package [118].

For each simulation there is a python file which is called job option configuration. Due to the details mentioned in this piece of code, the `GEANT4` simulation is controlled. In order to study the detector responses and generation process, we normally use reference decay channels which are the samples of pure dataset. Thus, we provide a so-called tuning in the MC production related to these differences in order to match the data.

2nd phase

The second phase is governed by `Boole` package. Through this step, hits in subdetectors are digitized, and raw datasets are modelled. During the second steps, in order to decrease the required amount of CPU and disk space, we use a set of requirement which is called "generator-level cuts". These requirements are made in order to veto out the events which will not be reconstructed by the LHCb. In other words, the events out of the LHCb acceptance is vetoed-out using these cuts.

3rd and 4th Phases

The third phase of LHCb process is dedicated to the tracks' reconstruction, which is deduced by `Brunel` software package. The fourth and final step is related to the offline analysis requirements. During this step, by using the `Davinci` package, the reconstructed tracks are utilized to build further physical variables. The `DaVinci` software controls the production of physical objects such as tracks from `Gauss` output or detector responses to real-time data-taking. It includes tools for tagging particle flavor and refitting the events by considering sets of constraints such as masses and vertices. One should take into account that in implementation and set up of the `DaVinci` package, treating the MC and real data in the same way is the main consideration.

Chapter 3

MVA tools for PID selection

3.1 Overview

The reconstruction of the $B^0_{d,s} \to K^0_S h^\pm h'^\mp$ candidates relies on the correct identification of the nature of the particles in the final state.

In the following chapter, the algorithms used in order to extract PID information from the LHCb sub-detectors measurements are first discussed.

Then the novel `PIDCorr` method, aimed at correcting the imperfections of the simulated PID responses in MC samples, is reviewed. This method allows preserving the correlations of PID variables within the process of corrections.

Finally, a novel tool making use of multivariate classifiers is introduced. This tool is employed to discriminate optimally signal candidates, in the spectrum of interest, from cross-feeding candidates. These cross-feeding candidates result from other spectra by misidentification of one or several final-state particles.

3.2 PID Variables

3.2.1 PID Variables in LHCb

Every sub-detectors at LHCb provide a collective set of information that can be used by various algorithms to provide variables (also called "feature" in Machine Learning context) about reconstructed objects in the experiment. First, each sub-detector gather a unique set of information corresponding to each of its recorded hits. Then, these information are combined by using various algorithms to extract the aforementioned features. These features are used in order to understand further properties of the reconstructed objects.

Particle identification as one of these complex tasks in LHCb is achieved by using the same rationale. It is important to provide this information to distinguish between exclusive final states of a B decays and reduce the background. Concerning the charge properties of the particles, we have two main categories for them: charged particles and neutral ones. To implement particle identification for charged particles such as e, μ, π, K and

p, readout information from muon chambers, calorimeter detectors and RICH detectors are collected and used, whereas in case of having neutral particle such as photons (γ) and neutral pions (π^0) the corresponding algorithms are implemented on the information of calorimeter system (ECAL and HCAL) next to the Scintillating Pad Detector (SPD) and the PreShower (PS) detectors. For instance, in case an energy deposit is found in the ECAL while there is no signature of deposit energy in the HCAL and no track associated to it, the object is identified as photon.

In the LHCb collaboration, the PID information is projected on two types of multivariate discriminators:

- The log-likelihood difference (DLL)
- The ProbNN variables

These two methods to derive the PID variables were discussed with details in section2.4.4.

3.2.2 PID variables in $B^0_{d,s} \to K^0_S h^\pm h'^\mp$

In the study presented in this thesis, the charmless decay of neutral B^0 or B_s mesons to the final states $K^0_S h^+ h'^-$ have been investigated. In this family of decays, each of h and h' can be either pion or kaon. Therefore, the $B_{d,s} \to K^0_S h^+ h'^-$ decay family comprises 4 different decays which can be distinguished by the knowledge of the nature of h and h' (PID identification as pion or kaon).

At the reconstruction level for the events, we first reconstruct the tracks, then identify them using the particle identification techniques and finally based on these tracks and their information we reconstruct the events (decay). For instance, based on π^+, π^- and K^0_S tracks and their information we can reconstruct the B^0 or B_s and we reconstruct the decay of $B^0 \to K^0_S \pi^+ \pi^-$ or $B_s \to K^0_S \pi^+ \pi^-$. It is possible that during the identification process, one of the tracks (with nature A) is misidentified as another one (with nature B). Thus, instead of having the correct reconstruction, we will reconstruct this decay as it belongs to another category. Let's come back to our $B^0 \to K^0_S \pi^+ \pi^-$ example. In this case, if the π^+ is identified as K^+ then the reconstructed event would be $B^0 \to K^0_S K^+ \pi^-$ instead of the original one. The type of background coming from this misidentification is denoted signal cross-feeds.

In order to fight against this type of backgrounds, we should use an ensemble of PID variables and control the level of contamination by cross-feeds through their corresponding cuts. This ensemble can be very simple, by using only few cuts, or it can be as complex as Multivariate analysis tools. In the latter case, the nonlinearity of the tool will help us to use the correlation between the PID variables in order to enhance the performance of this classification.

In this study, `ProbNN` variables are used to distinguish between charged hadrons which are kaon, pion and protons. In our samples it is denoted as `ProbNNh` where h can either

denote a pion, kaon or proton. Figs. 3.1 and 3.2 show the distributions of these variables for 2012b and 2018 Down-Down* Monte-Carlo samples, respectively.

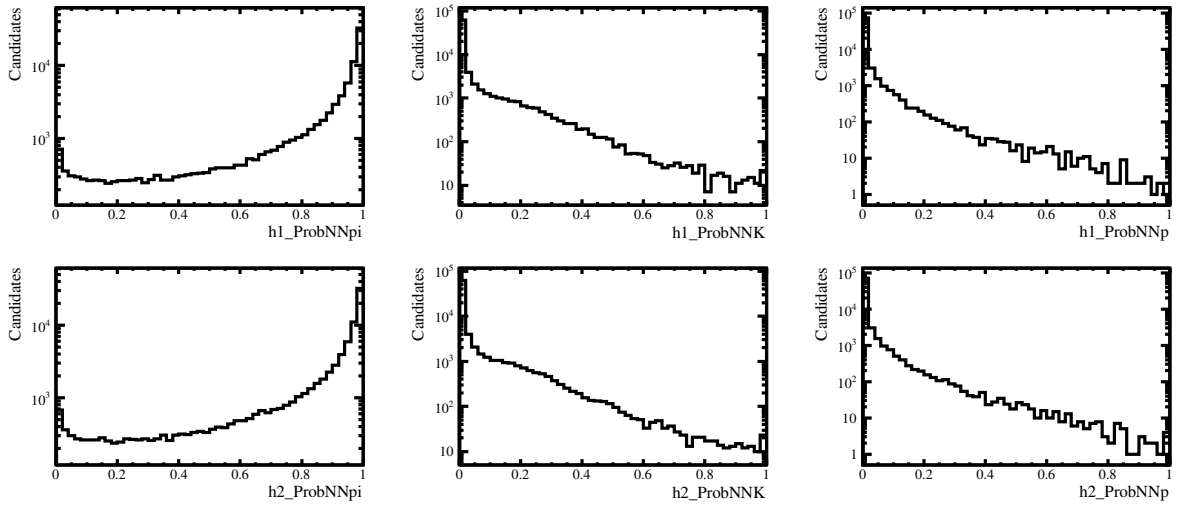

Figure 3.1: Distributions of `ProbNNh` for 2012b $B^0 \to K^0_S \pi^+ \pi^-$ Down-Down K^0_S MC sample. The top (resp. bottom) row shows the distribution for hadron 1 (resp. 2).

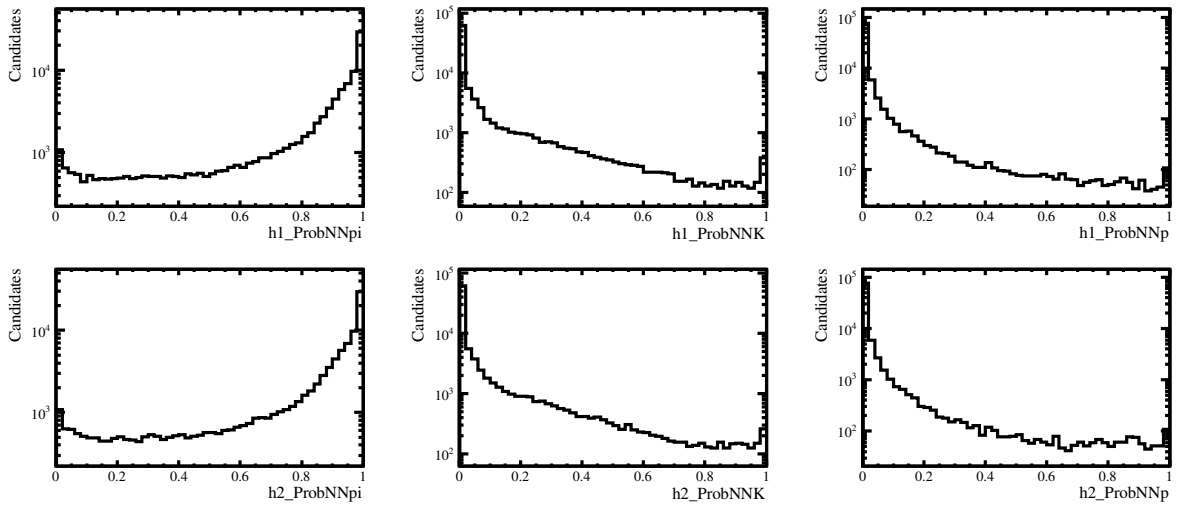

Figure 3.2: Distributions of `ProbNNh` for 2018 $B^0 \to K^0_S \pi^+ \pi^-$ Down-Down K^0_S MC samples. The top (resp. bottom) row shows the distribution for hadron 1 (resp. 2).

*By anticipation of the details given in Chapter 4, Down-Down (Long-Long) K^0_S reconstructed candidates are formed from the combinationof two Downstream (Long) tracks.

3.3 PID Calibration

The purpose of Monte Carlo (MC) simulations production is that we could mimic the behavior of data for our samples. To provide a perfect reflection of real data in our MC samples, correct calculation of detector responses to a passing particle is essential; and computing these responses requires modelling of the kinematics of the particle and the occupancy of the detectors. In spite of the fact that the simulations provide an acceptable description for the decay kinematics, some discrepancies can be found between the real data and their relevant MC samples [119]. Therefore, in order to perform a estimation based on the provided information by these MC samples (e.g. determining the efficiencies) we need to correct the corresponding variables of MC at first and then provide those estimations. The term "correction" in this context means that, providing a set of weights based on some kinematic properties of the (reconstructed) track such as momentum and pseudorapidity; and by applying those weights to the MC samples the correction matches the behavior of MC samples to the data ones.

One of the crucial information in most of the analysis in LHCb is particle identification (PID). To do so, each analysis required the measurement of the selection efficiencies involving PID. The common point about all of them is to use data-driven techniques to measure such efficiencies. Therefore, one of the most important corrections to be considered is related to PID responses in MC samples. There are several ways to provide these calibrations (corrections). These calibration approaches are relying on the set of calibration samples which were collected during the data taking. The details of these high-purity samples can be found in [120, 121]. Table.3.1 represents some of the most common samples which are used for the calibration purpose in RunI and RunII. The systematic related to the size of the samples (purity of them) is studied in section 5.2.2

Species	Decay Modes	Momentum Coverage		Stripping Line	Signal Yield[$\times 10^3$]	purity[%]
		Low	High			
$\pi^{\pm}$	$D^0 \to K^-\pi^+$ from $D^{*+} \to D^0\pi^+$		✓	D02KPiTag π^-	20004 ± 5	68.364 ± 0.010
			✓	D02KPiTag π^+	19582 ± 5	67.805 ± 0.010
	$K^0_S \to \pi^+\pi^-$	✓		Ks2PiPiLL	8889.9 ± 3.4	74.565 ± 0.013
$K^{\pm}$	$D^0 \to K^-\pi^+$ from $D^{*+} \to D^0\pi^+$		✓	D02KPiTag π^-	20004 ± 5	68.364 ± 0.010
			✓	D02KPiTag π^+	19582 ± 5	67.805 ± 0.010
	$\phi \to K^+K^-$ from $D^{*+} \to \phi\pi^+$	✓		Ds2PiPhiKKNegTagged	4492.7 ± 2.7	52.991 ± 0.019
		✓		Ds2PiPhiKKPosTagged	4491.4 ± 2.6	52.613 ± 0.018
		✓		Ds2PiPhiKKUnbiased	6488.5 ± 3.2	28.498 ± 0.008
$p, \bar{p}$	$\Lambda_0 \to p\pi^-$		✓	Lambda2PPiLLhighPT p^+	11020.5 ± 3.4	96.446 ± 0.007
			✓	Lambda2PPiLLhighPT p^-	10776.3 ± 3.4	96.335 ± 0.007
			✓	Lambda2PPiLLveryhighPT p^+	3552.9 ± 2.0	86.100 ± 0.016
			✓	Lambda2PPiLLveryhighPT p^-	3274.1 ± 1.9	86.072 ± 0.017
		✓	✓	Lambda2PPiLL p^+	7145.2 ± 2.8	93.757 ± 0.009
		✓	✓	Lambda2PPiLL p^-	6758.5 ± 2.7	93.121 ± 0.010
	$\Lambda_c^+ \to pK^-\pi^+$ from $\Lambda_b^0 \to \Lambda_c^+\mu^-$		✓	Lb2LcMuNu	149.1 ± 0.5	17.61 ± 0.04
$\mu^{\pm}$	$J/\psi \to \mu^+\mu^-$		✓	DetJPsiMuMuNegTagged	3469.2 ± 2.8	22.552 ± 0.014
			✓	DetJPsiMuMuPosTagged	3488.1 ± 2.8	22.924 ± 0.014
	$J/\psi \to \mu^+\mu^-$ from $B^+ \to J/\psi K^+$	✓		B2KJPsiMuMuNegTagged	90.29 ± 0.31	60.00 ± 0.06
		✓		B2KJPsiMuMuPosTagged	90.81 ± 0.32	60.34 ± 0.06
$e^{\pm}$	$J/\psi \to e^+e^-$ from $B^+ \to J/\psi K^+$	✓	✓	B2KJPsiEENegTagged	13.44 ± 0.13	57.93 ± 0.22
		✓	✓	B2KJPsiEEPosTagged	13.33 ± 0.13	57.94 ± 0.22

Table 3.1: Calibration Samples for PID in LHCb. Low and high momentum region coverage in this table are 2 - 15 GeV/c and 15–100 GeV/c, respectively.

3.3.1 Corrections with PIDCalib

In the former analysis, the `PIDCalib` method from the PIDCalib package [119] was used. Through this approach, efficiency tables and performance histograms can be delivered (according to the corresponding calibration samples) by considering any arbitrary set of PID requirements.

In fact, this method relies on the technique which is called tag-and-prob, which requires clean data samples. In order to provide these clean samples, first a mass fit is applied to the whole calibration sample and then using the $s\mathcal{P}lot$ technique [122] the background is statistically subtracted. Tight requirements are applied to a track to ensure its correct identification, and we call it a *tag* particle. The second track, which is called *prob*, is subsequently used to determine the PID efficiency, by counting the number of events before and after applying the aforementioned cuts.

The PID response depends on the kinematical properties of the track (momentum, transverse momentum, pseudorapidity) and the track multiplicity in the event. The efficiency is therefore templated in the space of these quantities. Note that two out of the three kinematical variables are enough to fully describe the particle kinematics. The performance of the correction method will depend on the choice of the binning.

If the binning was chosen too coarse, the efficiency would not be constant within a bin, while choosing too fine binning or too many variables lead to large statistical uncertainties. A systematic uncertainty is therefore estimated to quantify the effect of the choice of the binning. Moreover, using this approach ignores the existing correlation between the PID variables per events and, hence, does not preserve them after the corrections. It is known that for the same track, PID variables are strongly correlated[†], and these correlations could be used very efficiently by means of multivariate analysis tool. However, after using `PIDCalib` method these correlations do not preserve, and implication of MVA on the PID variables is meaningless.

3.3.2 PIDCorr : a new tool for corrections

Recently, there is a new approach added to the PIDCalib package which is known as `PIDCorr`. Contrary to the former method, in this method we use an unbinned approach to provide the correction for the MC samples. In order to do that, a four-dimensional calibration PDF is made out of the transverse momentum, pseudorapidity, track multiplicity and PID variable of the correcting track. This PDF is calculated using a method which is known as kernel density estimation (KDE) and the corresponding package for implementing KDE algorithm is called Meerkat [123, 124].

To explain further the KDE method, lets consider a random set of values y_i which represent a vector of variables y. In general this vector is multidimensional, however for the sake of simplicity we just consider a one dimensional case. This variable has a true

[†]As an example, we could indicate the negative correlations between the `ProbNNpi` and `ProbNNK`. In other words, if we have a particle (reconstructed track) which is pion-like, it is less kaon-like at the same time.

PDF $P_t(y)$ and we have a data set $\{y_i|i = 1..N\}$ whose values are sampled from our true PDF. Therefore, our $P_t(y)$ estimator [125, 126] is,

$$P_{KDE}(y) = \frac{1}{N}\sum_{1=1}^{N} K(y - y_i), \tag{3.1}$$

where $\int K(y)dy = 1$. The kernel $K(y)$ can be written in variety of forms. Here we use Epanechnikov form [127, 128]:

$$K(y) = \begin{cases} \frac{3}{4\sigma}(1 - \frac{y^2}{\sigma^2}) & \text{for } y \in (-\sigma, \sigma), \\ 0 & \text{otherwise,} \end{cases} \tag{3.2}$$

in which σ is the kernel width.

The advantage of this method is to provide an event-by-event correction for the MC samples. In addition, contrary to the `PIDCalib` method, it can preserve the aforementioned correlations between the variables of a track and hence the resulting variable by this method can be used by MVA tools to perform further complex PID tasks. In the following, the detail of this transformation technique will be discussed. Figs. 3.3 and 3.4 represents the result of this correction for a collection of PID variables for $B^0 \to K^0_S\pi^+\pi^-$ samples of 2018 and 2012b related to the DownDown K^0_S reconstruction and the rest is presented in Appendix A

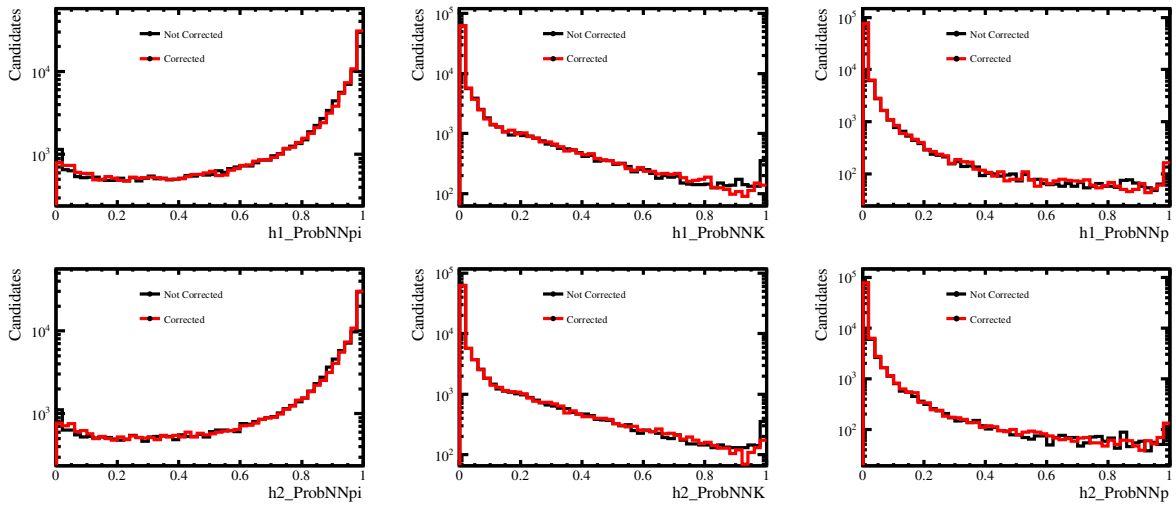

Figure 3.3: Comparison between the Corrected (Red) and Non-corrected (Black) for $B^0 \to K^0_S\pi^+\pi^-$ samples of 2018 *MagDown* for Down-Down K^0_S reconstructions. The Top (resp. Bottom) row denotes the distributions for h1 (resp. h2) hadrons. The plots are shown in logarithmic scale.

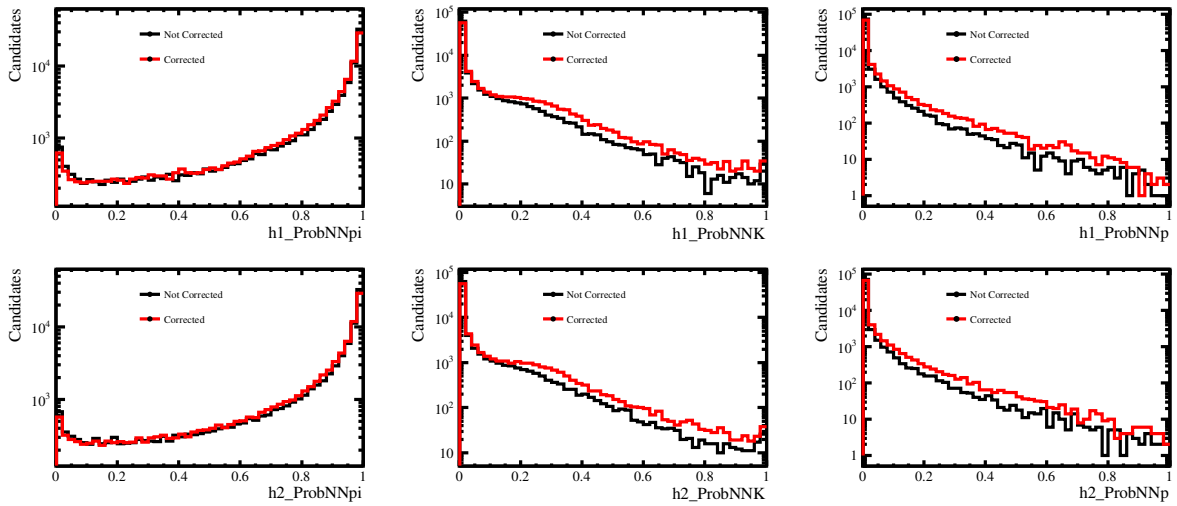

Figure 3.4: Comparison between the Corrected (Red) and Non-corrected (Black) for $B^0 \to K^0_S\pi^+\pi^-$ samples of 2012b *MagDown* for Down-Down K^0_S reconstructions. The Top (resp. Bottom) row denotes the distributions for h1 (resp. h2) hadrons. The plots are shown in logarithmic scale.

3.3.3 PID Transformation

As it was mentioned, `PIDCorr` is a method which transforms the distribution of the PID variables in MC, using the calibration samples, in order to correct the imperfections of the simulation. This transformation technique is done by using the method of inverse transform sampling, which is also known as "inverse transformation method" and "Smirnov transform" [124].

The PDF of a given PID variable is determined from the calibration samples as a function of p_T, η and N_{tracks} and the nature of the particle. Let's write it as $p_{\text{exp}}(x|p,\eta,N_{\text{track}})$ where x is the PID variable to be corrected. Based on this PDF, we could define the cumulative distribution function in the following form

$$P_{\text{exp}}(x|p,\eta,N_{track}) = \int_{-\infty}^{x} p_{\text{exp}}(y|p,\eta,N_{track})dy. \tag{3.3}$$

Since our PID variable distributions are normalizable, one could define ξ as the normalized P_{exp}, in the following form,

$$\xi = \frac{\int_{x_{min}}^{x_{corr}} p_{\text{exp}}(x|p,\eta,N_{track})dx}{\int_{x_{min}}^{x_{max}} p_{\text{exp}}(x|p,\eta,N_{track})dx} \quad , \quad x_{corr} \in (x_{min}, x_{max}) \tag{3.4}$$

Fig. 3.5 shows a schematic view of normalized cumulative distribution function $\xi(x)$ which is deduced for an arbitrary normalizable distribution function $p(x)$.

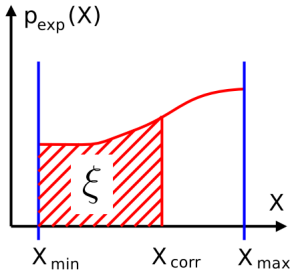

Figure 3.5: The schematic view of cumulative distribution function out of an arbitrary normalizable distribution function $p(x)$.The figure is taken from Ref. [124]

It is obvious that $\xi \in (0,1)$ and is monotonous. Therefore, as a consequence of Smirnov Transformation Theorem, by using the Inverse transform sampling we could find the inverse transformation $P^{-1}_{\rm exp}(\xi|p,\eta,N_{track}) = x$ such that the random variable $x \in p_{\rm exp}(x|p,\eta,N_{track})$. We can do the same procedure for another random variable $x_{\rm MC} \in p_{\rm MC}(x)$. Now we can deduce two monotonous functions by providing the normalized cumulative distribution function from $p_{\rm exp}(x)$ and $p_{\rm MC}$. Then using the one-to-one correspondence between the two monotonous functions, we can define a transformation between the two which can transform each $x_{\rm MC} \in p_{\rm MC}(x)$ to $x_{\rm corr} \in p_{\rm exp}$. Schematic view of this procedure is shown by Fig. 3.6.

Now, with respect to the above explanation, if we take the ξ function from the MC PID distribution then we have,

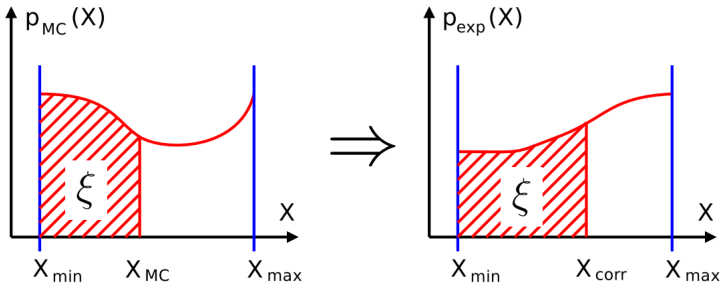

Figure 3.6: The schematic view of two normalized cumulative distribution functions. As it is presented, the value of the $\xi(x = x_{\rm MC})$ for $p_{MC}(x)$ and $\xi(x = x_{\rm corr})$ is equal. Also since ξ in both cases are monotonous, it allows us to define a transformation between these two distributions.

$$\xi = \frac{\int_{x_{min}}^{x_{MC}} p_{MC}(x|p,\eta,N_{track})dx}{\int_{x_{min}}^{x_{max}} p_{MC}(x|p,\eta,N_{track})dx} = \frac{\int_{x_{min}}^{x_{corr}} p_{\rm exp}(x|p,\eta,N_{track})dx}{\int_{x_{min}}^{x_{max}} p_{\rm exp}(x|p,\eta,N_{track})dx}. \tag{3.5}$$

Thus we could define a variable transformation of the following form,

$$x_{corr} = f(x_{MC}|p,\eta,N_{track}) = P^{-1}_{\rm exp}(P_{MC}(x_{MC}|p,\eta,N_{track})|p,\eta,N_{track}) \tag{3.6}$$

In other words by using this method we could find a map between the MC distribution of a PID variable and the data distribution of it. What is so important in here is that using this method x_{MC} and x_{corr} are still sharing the same event properties and as a result the correlations between the variables in the MC Sample are preserved.

3.4 PID selection Tool

In order to fight against the cross-feed backgrounds and discriminate between signal and this type of background, we should use the PID variables related to the reconstructed objects of each event. They can be used in various ways. The first and easiest way is to apply a set of simple cuts to the PID variables for which the PID variables are used independently of the each other. The second method is to use rectangular cut by using two PID variables and determine an optimize cut on its basis. In contrast to the first method, we consider a relation between two variables(see Eq.3.7). The third and most efficient method is to use a multivariate analysis tool in order to remove the cross feeds. The reason that the third method is more powerful than the other two approaches is that the MVA provides a nonlinear method to use the existing strong correlations between the PID variables of a single track while using the correlations between the tracks as well. Thus, as a result of application of this extra information, it could be more discriminant than the other two methods. To provide MVA, there exist many possibilities. After implementing several algorithms and comparison of their results and performances, it is decided to train our classifier based on the python Scikit-learn package [129]. Among the available algorithms inside this library, XGBoost algorithm [130] is chosen to be used for our classification task. For each year and specific decay mode, we trained an individual classifier. In order to be sure that the correct signal and cross-feed events were introduced to the tools, the MC-matched events were used among signal and cross-feed background samples. Also, the same physical requirements are applied to both samples by applying the trigger, stripping and preselection requirements to both of them. Among the PID variables, the `ProbNN`s for hadrons (protons, kaons and pions) are chosen as input variables. Thus, this classifier is based on 6 different variables of `h1_ProbNNpi`, `h1_ProbNNK`, `h1_ProbNNp`, `h2_ProbNNpi`, `h2_ProbNNK`, `h2_ProbNNp` as input variables. In order to demonstrate the discrimination power of these input variables for the Run I(II), the histograms of their distributions for the signal and cross-feed samples are presented in Figs. 3.7 and 3.8 for $B^0 \to K^0_{\mathrm{S}}\pi^+\pi^-$ decay mode of the 2012b and 2018, respectively.

3.5 Training and Validation of PID tool

After providing the appropriate input data, one of the most important parts in training an MVA tool is hyper-parameter tuning of the classifier. Among the hyper parameters of the XGBoost algorithm , `n_estimator` which indicate the number of tree and `max_depth` which defines the maximum tree depth for base learners are the parameters with the most

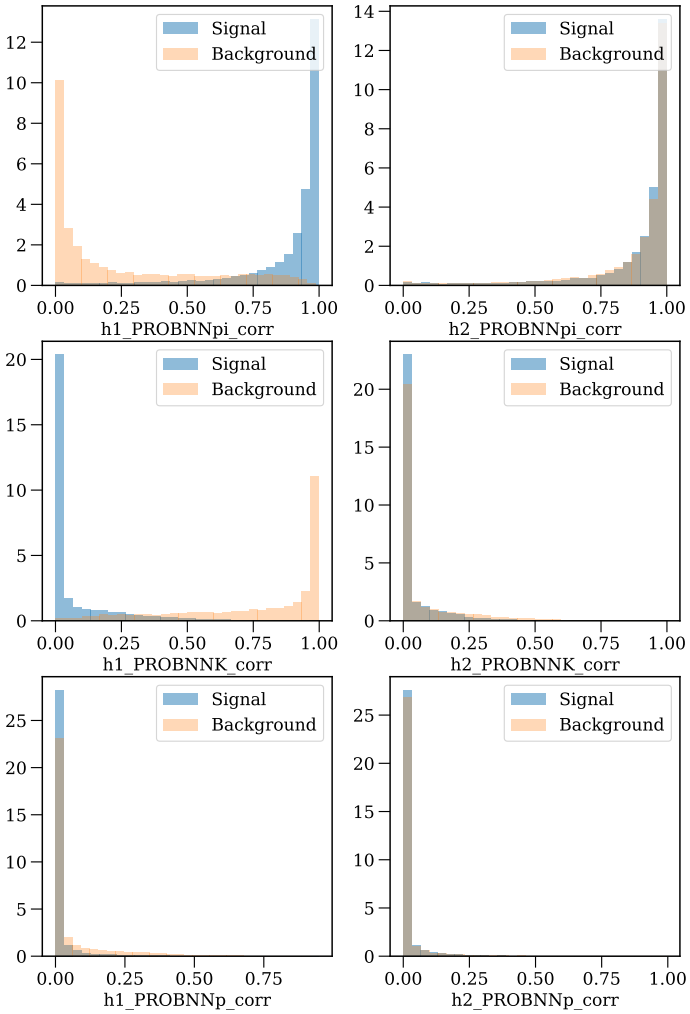

Figure 3.7: Distributions of `ProbNNh` used in the PID XGBoost for 2012b Down-Down K^0_S. The cross-feed MC of $B^0 \to K^0_S \pi^+ \pi^-$ is used as the background. For the sake of simplicity, the plots which consist of cross-feed for h1 (K misidentification as π) are shown.

impact on the results and the tuning is done with respect to them. The table 3.2shows the final value of these hyper parameters related to each trained classifier.

This tuning can be monitored toward several measures to determine the optimized values for a set hyper-parameters. In our analysis, the measure which we choose for this propose is the area of the ROC curve. The ROC curve itself will indicate how much of the

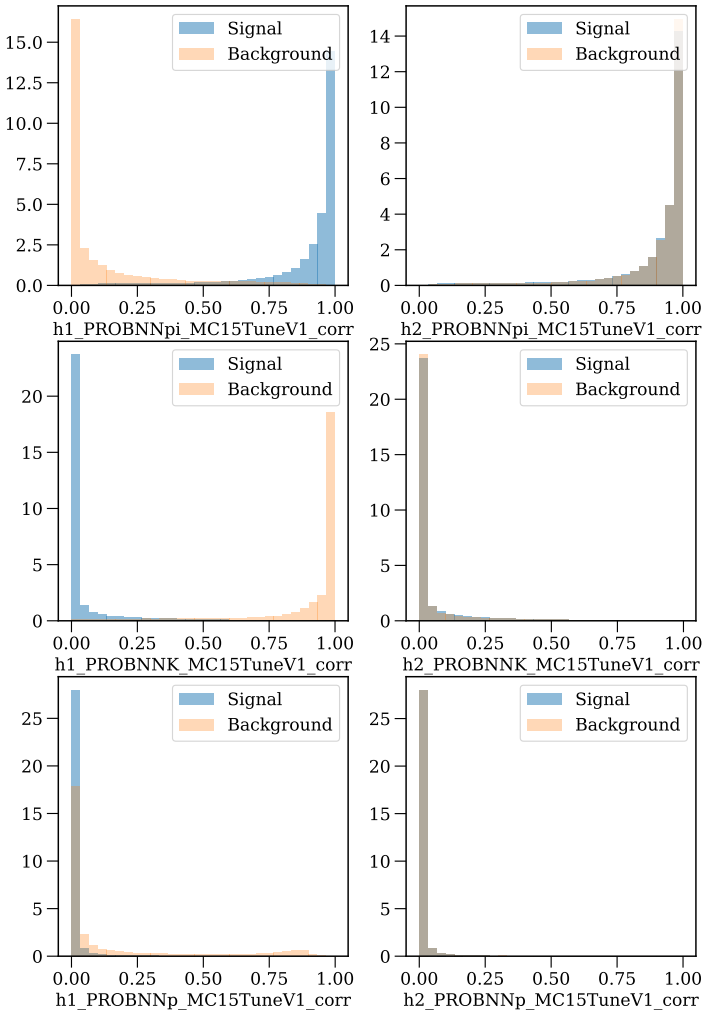

Figure 3.8: Distributions of `ProbNNh` used in the PID XGBoost for 2018 Down-Down K^0_S. The cross-feed MC of $B^0 \to K^0_S \pi^+ \pi^-$ is used as the background. For simplicity only the plots which consist of cross-feed for h1 (K misidentification as π) is shown.

background will be rejected at a specific acceptance for the signal. Thus, the area of this curve would be 1 in an ideal situation where all the signal events were accepted while all the background is rejected. The Fig. 3.9 will show the ROC curve of the classifier for the selected optimal hyper-parameter of 2012b and 2018 $B^0 \to K^0_S \pi^+ \pi^-$ samples.

The second most important concern in MVA is to avoid biasing the training. In order to

year	K^0_S	Hyper parameter	$B^0_{d,s} \to K^0_S\pi^+\pi^-$	$B^0_{d,s} \to K^0_S K^+\pi^-$	$B^0_{d,s} \to K^0_S\pi^+K^-$	$B^0_{d,s} \to K^0_S K^+K^-$
RunI	DD	`n_estimator`	350	350	350	350
		max_depth	2	2	2	2
	LL	`n_estimator`	250	250	250	250
		`max_depth`	2	2	2	2
RunII	DD	`n_estimator`	700	700	700	700
		`max_depth`	3	3	3	3
	LL	`n_estimator`	550	500	500	600
		`max_depth`	3	3	3	3

Table 3.2: The tuned hyper parameters of the XGBoost classifiers for RunI and RunII.

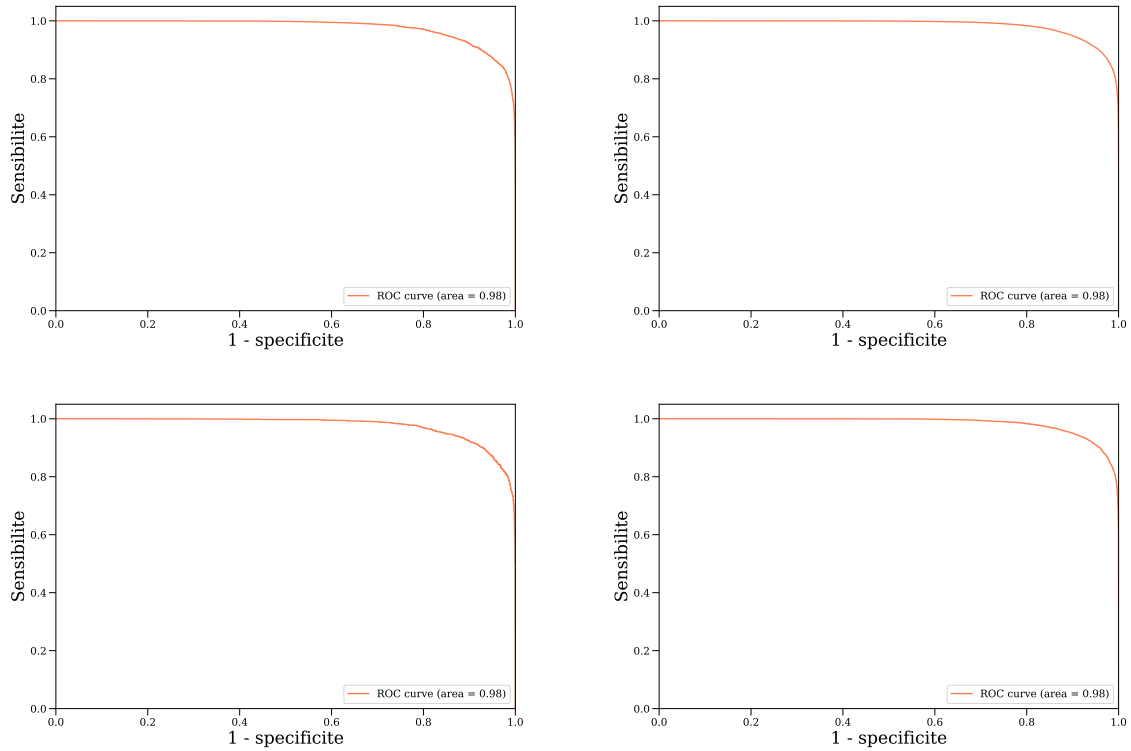

Figure 3.9: The ROC Curve for the PID XGBoost of 2012b (left) and 2018(right) discriminant for the $B^0 \to K^0_S\pi^+\pi^-$ samples and Down-Down (top) and Long-Long (bottom) K^0_S reconstructions. The x axis here shows the true negative (TN) rate which tells how much background is correctly identified while the y axis denotes the true Positive (TP) rate. TP indicates the rate of signal which is labeled correctly.

fulfil this requirement the signal and data samples are randomly split into two sub-samples that are then used as training and validation samples. Thereafter, we calculate the MVA output, using each background and signal sample, in turn, for the training and the testing phase. For this propose and in order to provide a reproducible results, a specific random

seed was used and 70 percents of the events are used in a train sample and the rest is devoted to the validation samples. The PID discriminant response histograms for the $B^0 \to K^0_S \pi^+ \pi^-$ decay mode of the 2012*b* and 2018 are displayed in Fig. 3.10 as an example of implementation of this method for the XGBoost PID. As it is shown in the Fig. 3.10, regardless of difference in details of the training for each year, the shapes of the response are similar.

As the last important concerns, for each MVA tools, the hyperparameters should be optimized up to the level of overtraining. To be sure about this concern as it can be seen in the Fig. 3.10 the outputs of train and test samples are plotted on top of each other whereas Kolmogorov-Smirnov (KS) statistics test has been applied on these two samples. The statistical significance and the assigned p-value of the KS test show that in almost all the cases the assigned p-value is bigger than the statistical significance of the sample and hence no over training occurred. Also the regions of interests (close to the probable final cut) are scrutinized further via the plots and no hint of overtraining is spotted.

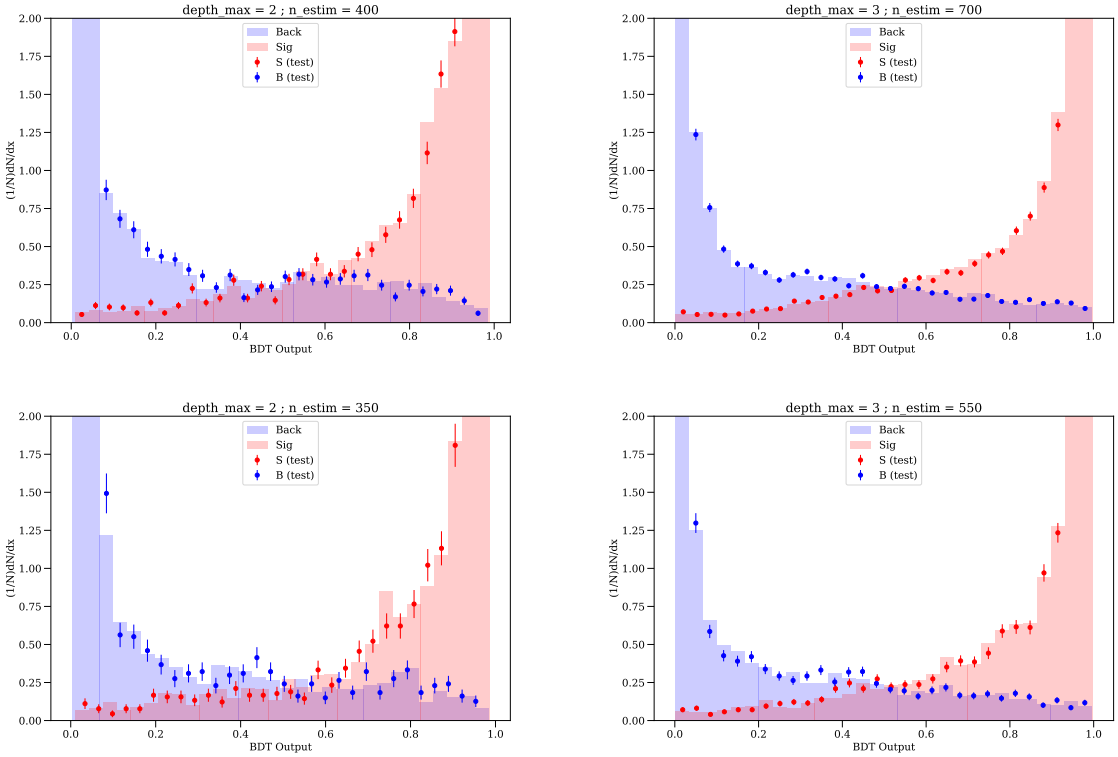

Figure 3.10: Training and validation samples response for the PID XGBoost of 2012b (left) and 2018(right) discriminant for the Down-Down (top) and Long-Long (bottom) K^0_S events.

3.6 Comparison of the methods

So far a new method is introduced in order to provide a PID-based discriminating tool to fight against cross-feed background. In each analysis, depending on the choice of the PID requirement, the results can be studied through the efficiency of the signal and backgrounds (by applying corresponding requirements). Thus, in case of having several methods, these efficiencies can be used as a measure to compare the effectiveness of a method with respect to the other one(s).

In the former $K^0_S h^+ h'^-$ study, due to the choice of correction for PID variables (`PIDCalib`), the correlations of the PID variables are ignored, thus they could only be treated and optimized just by considering the PID variables and simple relation between them. As a result, a rectangular cut of the form,

$$\texttt{h\_ProbNNpi} > \texttt{h\_ProbNNK} + \alpha \tag{3.7}$$

was chosen and the optimized point, is defined by parameter α for rectangular cuts. Since this optimized choices will lead in to PID requirements, there would be an efficiency for signal and cross-feed samples corresponding to them. In order to provide a comparison between the former methods and the current existing choice for the PID purposes, we can use a reference point and compare the performance of former and current approach with respect to that. This reference point can be defined by the following method:

I) We considered the optimal α value in the former analysis.

II) Corresponding to this value, we can determine the Efficiency of the signal and cross-feed samples.

III) Based on the output of the MVA tools on our sample, this signal efficiency corresponds to a specific requirement(MVA cut).

IV) By applying this MVA cut on the the cross-feed sample we retrieve its efficiency. Then, by comparing this value and the one which is deduced previously for the cross-feed (in II) we can determine how much we can purify the data sample.

The Table. 3.3 is showing one example of this comparison for the $B_s \to K^0_S \pi^+ \pi^-$ between the former analysis methods and the current MVA method.

It can be seen in Table. 3.3 that with respect to the proposed comparison we have improvements which are more than factor 2 and up to factor 3 in purifying the samples. Moreover, due to the PID improved performance in RunII, results should be even better for this duration of data taking.

In the current analysis, we apply the deduced MVA model to the signal and cross-feed backgrounds and by this we will provide a new PID variable whose requirement reflects the complex multidimensional nonlinear choices in the six dimensional feature space of `ProbNNh`s. As a matter of fact, this non-linearity plays a central role because it benefits from the existing correlation between `ProbNNh`s to make a better choice in the aforementioned feature space.

year	decay mode	KS reconstruction	alpha (prev ANA)	Efficiency(%)		
				Signal	Cross-Feed	
					rectangular-cut	XGB ProbNN
2012b	Bs2KSpipi	DD	0.22	85.3	21.5	6.4
		LL	0.36	83.6	14.0	5.6
2012a	Bs2KSpipi	DD	0.22	85.6	21.6	7.0
		LL	0.36	82.4	14.6	6.6
2011	Bs2KSpipi	DD	0.25	86.3	21.5	10.6
		LL	0.35	85.7	12.6	8.3

Table 3.3: Comparison between former (rectangular) and current (MVA) PID methods, for $B_s \to K^0_S \pi^+ \pi^-$ sample of the RunI.

Thus far, the development of PID MVA tool is presented in this chapter. In the next chapter, the output of this tool will be utilized next to the output of another MVA tool to perform an optimization in order to find a set of optimal cuts to kill the optimal amount of backgrounds.

Chapter 4

Multichannel $B^0_{d,s} \to K^0_S h^\pm h'^\mp$ study

Among the vast amount of possibilities for decays of neutral B mesons, the charmless three-body decays for which their final states contain a K^0_S particle has shown a specific potential to study the $\mathcal{CP}$ asymmetries. These decays can be listed as six different modes of $B^0_{d,s} \to K^0_S \pi^+ \pi^-$, $B^0_{d,s} \to K^0_S K^+ K^-$ and $B^0_{d,s} \to K^0_S K^\pm \pi^\mp$. The reason we focused on the final states with K^0_S is that the K^0_L particle is a long-lived particle whose lifetime is $(5.116 \pm 0.021) \times 10^{-8}$ s [131], and it cannot be easily identified in LHCb detector. On the contrary, K^0_S mostly decays within the LHCb tracking system and can be reconstructed. For this purpose, two tracks identified as opposite charge pions and originating from the same space point are combined to reconstruct the K^0_S mesons. Each of these (two) pion tracks, itself, can be reconstructed either in the VELO or outside the VELO. In the former case, the pion track is labeled as "long-track" and in the latter one is referred as "downstream-track". Therefore, based on these two types of pions three following reconstructions are possible for the K^0_S candidates:

- Down-Down (DD): This K^0_S candidate is reconstructed from two downstream pion tracks.
- Long-Long (LL): K^0_S candidates in this case are reconstructed from two long tracks pions.
- Long-Down (LD): Few percent of K^0_S reconstructed candidates belong to this category in which the two pions are of different type. However, we are disregarding them in our analysis.

Since the Long-Long K^0_S candidates own the vertex detector information, their momentum is better resolved than those of the Down-Down category. In turn, the invariant-mass resolution of the b-meson signal candidates is better determined. Given the K^0_S lifetime, the Long-Long K^0_S candidate sample is however half the Down-Down K^0_S candidate sample.

The goal of this study is to provide a unique method for data preparation and prepare a unique tool which can be used for time-dependent Dalitz plot analysis(DPA) $B^0 \to K^0_S \pi^+ \pi^-$ and time-integrated DPA of $B^0_{d,s} \to K^0_S \pi^+ \pi^-$ while they can be used for an update on the

branching fraction using the $9\,\text{fb}^{-1}$ integrated luminosity with the goal of observing and measuring the branching fraction of $B_s \to K^0_S K^+ K^-$ state*. However, depending on each of the above proposes, this unique tool will feature different optimal working point.

4.1 Data and Monte Carlo samples

Data samples

This study is done using the data collected by the LHCb experiment during the RunI (2011 and 2012) and RunII (2015 to 2018) pp collision campaigns. The corresponding integrated luminosity is about 9 fb^{-1}. Reconstruction of events is done using devoted versions of the software for each year of data taking period. This is made necessary by the different conditions of machine energy, background level, trigger and detector conditions. The analysis is accordingly performed by splitting the data-taking years in consistent samples. Table 4.1 summarizes the data taking conditions for each year.

Year	c.m. energy	Luminosity	Stripping version
2011	7 TeV	1.10670 fb^{-1}	`Stripping20r1`
2012	8 TeV	2.08198 fb^{-1}	`Stripping20`
2015	13 TeV	0.32822 fb^{-1}	`Stripping24r1`
2016	13 TeV	1.66512 fb^{-1}	`Stripping28r1`
2017	13 TeV	1.71466 fb^{-1}	`Stripping29r2`
2018	13 TeV	2.18561 fb^{-1}	`Stripping34`

Table 4.1: List of the data samples used in this analysis, the data taking conditions and the corresponding stripping versions.

MC simulated samples

In order to study the behavior of signal and backgrounds, specifically in terms of efficiency, Monte Carlo(MC) samples are generated with conditions which are as similar as possible to what we have for data taking. The production of all these samples is done by using `Sim09` with PYTHIA 8 and the production results were saved in DST format† In the MC sample production, the signal events are required to be generated with a uniform distribution in the square Dalitz plane (sqDP). The Table 4.3 is representing the number of events, magnet polarity and year of each generated sample corresponding to RunI and Table 4.4

*Using the $3\,\text{fb}^{-1}$ integrated luminosity (RunI) data set the $B_s \to K^0_S K^+ K^-$ mode is still unobserved [132]

†A DST file is a `ROOT` file which contains the full event information, such as reconstructed objects and raw data. Each event typically takes around 150 kB of disk space in the DST format.

displays the same information for the samples of RunII. Also, Table 4.2 provides the simulation conditions related to each year.

As we discussed in Sec. 2.5 trigger configuration (denoted by TCKs) often changes during the data taking. It is not practical to implement all these configurations in the MC generation. In general, the trigger configuration which is chosen for simulation is the best one in representing the condition in the corresponding data taking year. The only exception is related to the 2012 for which we have two separated TCKs. This is due to the fact that during the technical stop at the end of June 2012, the HLT2 topological lines were faced to significant modification, in order to include the Down-Down category of K^0_S and Λ candidates. These changes had a strong impact on the trigger efficiency and have to be accounted for in simulations. Therefore, for the year 2012, two distinct MC samples have been generated, each one with the most representative TCK corresponding to the pre- or post-June period. In the following, they will be referred to as 2012a and 2012b.

In order to make the best use of the computing resources, some very loose cuts have been set at generator level. Events are retained for the next stages of the simulation only if daughter particles of the decay of interest are generated within the LHCb detector acceptance. The same requirements have been applied to all the decay modes. A complete list of the cuts can be found in Table 4.5.

Year	CONDDB	DDDB	pileup factor ν	TCK	Stripping
2011	sim-20160614-1-vc-m{u,d}100	20170721-1	2.0	0x40760037	Stripping20r1
2012a	sim-20160321-2-vc-m{u,d}100	20170721-2	2.5	0x409f0045	Stripping20
2012b	sim-20160321-2-vc-m{u,d}100	20170721-2	2,5	0x4097003d	Stripping20
2015	sim-20161124-vc-m{u,d}100	20170721-3	1.6	0x411400a2	Stripping24r1
2016	sim-20170721-2-vc-m{u,d}100	20170721-3	1.6	0x6139160F	Stripping28r1

Table 4.2: MC generation conditions for each year.

Mode	Event type	2011 Sim09f		2012a Sim09f		2012b Sim09f	
		Mag. Down	Mag. Up	Mag. Down	Mag. Up	Mag. Down	Mag. Up
$B^0 \to K^0_S\pi^+\pi^-$	11104127	1,145,934	1,024,558	1,118,117	1,260,028	1,009,270	1,000,177
$B^0 \to K^0_S K^+K^-$	11104117	1,097,056	1,393,779	1,093,774	1,029,548	1,000,748	1,001,588
$B^0 \to K^0_S K^\pm\pi^\mp$	11304165	1,090,089	1,232,656	1,009,452	1,181,179	1,005,393	1,002,828
$B_s \to K^0_S\pi^+\pi^-$	13104126	1,381,239	1,086,745	1,107,872	1,025,546	1,035,152	1,029,250
$B_s \to K^0_S K^+K^-$	13104136	1,159,799	1,150,884	1,261,310	1,129,587	1,002,846	1,027,273
$B_s \to K^0_S K^\pm\pi^\mp$	13304106	1,124,732	1,131,317	1,004,502	1,204,447	1,066,764	1,076,761

Table 4.3: Number of MC events generated for each mode according to the year and the magnet polarity (RunI).

Mode	Event type	2015 Sim09e		2016 Sim09e	
		Mag. Down	Mag. Up	Mag. Down	Mag. Up
$B^0 \to K^0_S\pi^+\pi^-$	11104127	2,055,032	2,008,492	2,001,287	2,001,205
$B^0 \to K^0_S K^+K^-$	11104117	2,017,345	2,001,073	2,004,882	2,000,835
$B^0 \to K^0_S K^\pm\pi^\mp$	11304165	2,004,600	2,003,133	2,031,373	2,007,537
$B_s \to K^0_S\pi^+\pi^-$	13104126	2,042,502	2,006,784	2,011,125	2,023,340
$B_s \to K^0_S K^+K^-$	13104136	2,045,297	2,136,559	2,001,293	2,004,224
$B_s \to K^0_S K^\pm\pi^\mp$	13304106	2,002,461	2,004,447	2,013,167	2,003,733

Table 4.4: Number of MC events generated for each mode according to the year and the magnet polarity (RunII).

Candidate	Cut	Description
B	$p_T(B) > 1500\,\text{MeV}$	Transverse momentum of the B candidate
$h^{(\prime)}$	$0.010\text{ rad} < \theta(h^{(\prime)}) < 0.400\text{ rad}$	Charged daughters of the B within detector acceptance.
	$1.8 < \eta(h^{(\prime)}) < 5.0$	Pseudo-rapidity of $h^{(\prime)}$ candidates.
	$3.0\,\text{GeV} < p(h^{(\prime)}) < 150\,\text{GeV}$	Total momentum.
K^0_S	$2 < \eta(K^0_S) < 5$	Pseudo-rapidity of K^0_S candidate.
	`KsTT = GVEV &(GFAEVX(GVZ,1.e+10)<240*centimeter)`	valid K^0_S must decay less than 240 cm downstream of interaction point
K^0_S daughters	$1.6 < \eta_{\pi^\pm} < 5.2$	Pseudo-rapidity of $h^{(\prime)}$
	$2.0\,\text{GeV} < p(\pi^\pm) < 150\,\text{GeV}$	Total momentum.
	`bothPI=2==GNINTREE(('pi+'==GABSID))`	K^0_S must decay to two charged pions

Table 4.5: Cuts applied at MC generator level.

4.2 Event reconstruction and online selection

4.2.1 Trigger

For each analysis, a series of offline trigger selection can be selected from the relevant trigger lines. For the RunI samples, these trigger requirements are selected to be identical to the previous studies [13, 20]. The following LHCb terminology is used through this document:

- `TOS`: As it is mentioned in Sec. 2.5, it refers to the events which are triggered on signal information.
- `TIS`: This refers to the events which are triggered by particles that do not belong to the signal decay. (see Sec. 2.5).
- `Hlt1TrackAllL0Decision`: It reflects that the trigger is fired for the event, based on the displacement from the primary vertex and its transverse momentum[‡]
- `Hlt1TwoTrackMVADecision`: This refers to the trigger, based on an MVA classifier, which searches for the two tracks to make a vertex. This line is added for RunII and makes the HLT1 to be more efficient for hadronic charm and beauty decay.
- `Hlt2TopoNBody(Simple)`: This trigger condition fired based on the output of a classifier which uses topological properties of full reconstructed event for N = 2, 3 or 4 tracks to make a vertex.
- `Hlt2TopoNBodyBBDTDecision`: This trigger is fired based on the output of a Bonsai boosted decision tree [133] by combining topological properties of 2,3 or 4 tracks to make a vertex. For Run II data, the `Hlt2TopoNBodyBBDTDecision` is complemented by a HLT2 line featuring a direct kinematic reconstruction of the signal B candidate. It was observed that about 3 % of the B candidates were recovered, featuring those with low-momentum tracks, hence populating the edges of the DP where the interference between amplitudes are the most probable.

For RunII, apart from using two MVA-decision based trigger lines for HLT1, there is another difference which is coming from the hardware (L0) level. It has been decided not to use `L0Global_TIS` in order to avoid the inclusion of events selected by non-physical trigger lines. Instead, a list of physical triggers is used. In practice, the number of events selected by this list of physical triggers and `L0Global_TIS` differ only by a few tenths of events. Thus, the requirement to pass the L0 stage can be a positive `TOS` decision from the hadron trigger(`L0Hadron_TOS`), positive `TIS` from at least one of the physical triggers, or both.

A summary of the trigger requirements for each year is given in Table 4.6.

[‡]For the transverse momentum, the threshold of 1.6 GeV/c is determined to fire the trigger.

Year	Trigger requirements	HLT1 trigger requirements	HLT2 trigger requirements
2011	B_L0HadronDecision_TOS	B_Hlt1TrackAllL0Decision_TOS	B_Hlt2Topo2BodyBBDTDecision_TOS
	B_L0DiMuonDecision_TIS		B_Hlt2Topo3BodyBBDTDecision_TOS
	B_L0MuonDecision_TIS		B_Hlt2Topo4BodyBBDTDecision_TOS
	B_L0ElectronDecision_TIS		B_Hlt2Topo2BodySimpleDecision_TOS
	B_L0PhotonDecision_TIS		B_Hlt2Topo3BodySimpleDecision_TOS
	B_L0HadronDecision_TIS		B_Hlt2Topo4BodySimpleDecision_TOS
2012	B_L0HadronDecision_TOS	B_Hlt1TrackAllL0Decision_TOS	B_Hlt2Topo2BodyBBDTDecision_TOS
	B_L0DiMuonDecision_TIS		B_Hlt2Topo3BodyBBDTDecision_TOS
	B_L0MuonDecision_TIS		B_Hlt2Topo4BodyBBDTDecision_TOS
	B_L0ElectronDecision_TIS		
	B_L0PhotonDecision_TIS		
	B_L0HadronDecision_TIS		
2015	B_L0HadronDecision_TOS	B_Hlt1TrackMVADecision_TOS	B_Hlt2Topo2BodyDecision_TOS
	B_L0DiMuonDecision_TIS	B_Hlt1TwoTrackMVADecision_TOS	B_Hlt2Topo3BodyDecision_TOS
	B_L0MuonDecision_TIS		B_Hlt2Topo4BodyDecision_TOS
	B_L0ElectronDecision_TIS		
	B_L0PhotonDecision_TIS		
	B_L0HadronDecision_TIS		
	B_L0MuonEWDecision_TIS		
	B_L0MuonNoSPDDecision_TIS		
	B_L0JetElDecision_TIS		
	B_L0JetPhDecision_TIS		
2016	B_L0HadronDecision_TOS	B_Hlt1TrackMVADecision_TOS	B_Hlt2Topo2BodyDecision_TOS
	B_L0DiMuonDecision_TIS	B_Hlt1TwoTrackMVADecision_TOS	B_Hlt2Topo3BodyDecision_TOS
	B_L0MuonDecision_TIS		B_Hlt2Topo4BodyDecision_TOS
	B_L0ElectronDecision_TIS		
	B_L0PhotonDecision_TIS		
	B_L0HadronDecision_TIS		
	B_L0MuonEWDecision_TIS		
	B_L0JetElDecision_TIS		
	B_L0JetPhDecision_TIS		
2017	B_L0HadronDecision_TOS	B_Hlt1TrackMVADecision_TOS	B_Hlt2Topo2BodyDecision_TOS
	B_L0DiMuonDecision_TIS	B_Hlt1TwoTrackMVADecision_TOS	B_Hlt2Topo3BodyDecision_TOS
	B_L0MuonDecision_TIS		B_Hlt2Topo4BodyDecision_TOS
	B_L0ElectronDecision_TIS		
	B_L0PhotonDecision_TIS		
	B_L0HadronDecision_TIS		
	B_L0MuonEWDecision_TIS		
2018	B_L0HadronDecision_TOS	B_Hlt1TrackMVADecision_TOS	B_Hlt2Topo2BodyDecision_TOS
	B_L0DiMuonDecision_TIS	B_Hlt1TwoTrackMVADecision_TOS	B_Hlt2Topo3BodyDecision_TOS
	B_L0MuonDecision_TIS		B_Hlt2Topo4BodyDecision_TOS
	B_L0ElectronDecision_TIS		
	B_L0PhotonDecision_TIS		
	B_L0HadronDecision_TIS		
	B_L0MuonEWDecision_TIS		

Table 4.6: List of L0 trigger requirements used for each year. A logical OR is implied between each line, and a logical AND is implied between the columns.

4.2.2 Stripping

The stripping process is a part of the LHCb data flow that is issued only once centrally to build the candidates relevant to calibration and physics purposes to be used by analysts.

It allows to comply with the affordable computing ressources. The data are sorted into specific streams, by using a set of selections, called the stripping lines. The output files are regrouped into the streams whose selections contain similar stripping lines.

The stripping lines used in this study, also known as B2KShh lines, select the $B_{d,s} \to K^0_S h^+ h'^-$ candidates. They are part of the BnoC lines (suite) that select various charmless B decay modes. Through the stripping process, the whole lines treat the charged hadrons as pions without applying any PID requirement[§]. This is done to avoid duplication in final state.

In order to form the B candidates, K^0_S candidates are combined with two oppositely charged pions. So the categories of K^0_S reconstruction (LL and DD) are important in defining the stripping line. In addition, while the overall structure of stripping lines are kept the same for both RunI and RunII, the details of stripping, *e.g.* the specific cuts, are different in each of these two periods. Therefore, with respect to the period of data taking and K^0_S reconstruction the following stripping lines are applied:

- RunI:

  `StrippingB2KShhDDLine`

  `StrippingB2KShhLLLine`

- RunII:

  `StrippingB2KShh_DD_Run2_OS_Line`

  `StrippingB2KShh_LL_Run2_OS_Line`

Same as previous analysis [134] all these `B2KShh` lines consist of two requirements that retain the events with less than 250 `Long` tracks and more than one primary vertices. The table. 4.7 denoted these cuts.

Selection requirement	Definition of variable
$N_{\text{LongTrack}} < 250$	Number of `Long` tracks per event
$N_{\text{PV}} \geq 1$	Number of primary vertices per event

Table 4.7: Global requirements of stripping

According to the required K^0_S reconstruction, candidates are taken from one of the `StdLooseKsLL` or `StdLooseKsDD` containers[¶].

Then to provide the two oppositely charged pions in RunI the $h^{(\prime)}$ candidates are taken from `StdLoosePions` whereas for RunII they are chosen from `StdAllNoPIDsPions`.

[§]They will be refitted afterwards in the nTuples process with correct mass hypothesis and identities

[¶]The K^0_S candidates in `StdLooseKsLL` container are reconstructed by using the pions which are taken from the `StdLoosePions` and this list is only contains the `Long` Tracks. The `StdLooseKsDD` container take its pions from `StdNoPIDDownPions`list consists of `Downstream` tracks [134].

Note that PID requirements are not applied to neither of the containers' candidates. The difference between `StdLoosePions` and `StdAllNoPIDsPions` are coming from two requirements that exist for the first container (and applied on its candidates) and not for the latter. The first cut states that the tracks are required to have the minimum transverse momentum of 250 MeV ($p_{\rm T}(h^{(\prime)}) > 250\,{\rm MeV}$). The second requirement indicates that the minimum impact parameter χ^2 of pion tracks with respect to the PV should be bigger than four ($\min\chi^2_{\rm IP}$ $(\pi^{\pm})> 4$).

Theses two conditions were removed in the second container for RunII to benefit the future Dalitz plot analysis. This is because the low-$p_{\rm T}$ candidates are populating the corners of the Dalitz plot and hence can be useful for the purpose of amplitude analysis. However, removing these cuts has increased the background level dramatically. Thus, to compensate this effect HLT1 and HLT2 requirements were added to the stripping cuts to kill most of these background events.

In order to meet the bandwidth requirement (agreed) for each stripping line and a fast processing of the events ($<$ 1 ms per event), the relevant cuts are applied sequentially to the daughter particles, the intermediate particles (in our case $K^0_{\rm S}$) and then on their combination to form the candidate. The cuts are using the variables which are related to the topological properties of decay, specifically related to the vertices and their topology. The reason behind this choice is to avoid biasing the Dalitz plane distributions. These variables can be listed as:

- χ^2 of the vertex fit ($\chi^2_{\rm vtx}$)
- Flight distance χ^2 or χ^2 of distance from the PV ($\chi^2_{\rm FD}$)
- The minimum impact parameter (IP) χ^2 of a track with respect to the related PV($\min\chi^2_{\rm IP}$)
- The distance of the closest approach(DOCA)
- The cosine of the direction angle(DIRA)

Tables 4.8 and 4.9 summarize the stripping cuts used for RunI and RunII respectively.

The data and MC tuples related to this study are produced with `Bender` version `32r4p3`. As described above, the charged particles ($h^{(\prime)}$) selected by the stripping lines are considered as pions. Then, during the nTuples filling, identities and mass hypothesis of these hadrons are changed to match the decay final states of $K^0_{\rm S}\pi^+\pi^-$, $K^0_{\rm S}K^{\pm}\pi^{\mp}$, and $K^0_{\rm S}K^+K^-$ and the decay tree is refitted using the `DecayTreeFitter` (DTF) package [135]. As a result all the corresponding variables in the decay tree are updated with respect to these modifications.

Cut step	Candidate(s)	StrippingB2KShhDDLine	StrippingB2KShhLLLine
DaughterCuts	K^0_S	$p(K^0_S) > 6000.0$ MeV $\lvert m_{\pi^+\pi^-} - m^{\rm PDG}_{K^0_S}\rvert < 30.0$ MeV $\chi^2_{\rm vtx}(K^0_S) < 12.0$ $\chi^2_{\rm FD}(K^0_S) > 50.0$	- $\lvert m_{\pi^+\pi^-} - m^{\rm PDG}_{K^0_S}\rvert < 20.0$ idem $\chi^2_{\rm FD}(K^0_S) > 80.0$
	K^0_S daughters	$p(\pi^\pm) > 2.0$ GeV $\min\chi^2_{\rm IP}$ $(\pi^\pm)> 4$ - DOCA χ^2 of K^0_S daughters< 25 - -	idem $\min\chi^2_{\rm IP}$ $(\pi^\pm)> 9$ $p_{\rm T}(\pi^\pm) > 250$ MeV idem track χ^2/ndf < 4.0 track ghost probability < 0.5
	$h^\pm$ $(\pi^\pm)$	track χ^2/ndf < 4.0 track ghost probability < 0.5 $p_{\rm T}(h^\pm) > 250$ MeV $\min\chi^2_{\rm IP}$ $(h^\pm)> 4$	idem idem idem idem
CombinationCut		$p_{\rm T}(B) > 1000.0$ MeV $p_{\rm T}(K^0_S) + p_{\rm T}(h^+) + p_{\rm T}(h^-) > 4200.0$ MeV at least 2 daughters with $p_{\rm T} > 800$ MeV $(4000 < m_{K^0_S h^+ h'^-} < 6200)$ MeV `AVAL_MAX(MIPDV(PRIMARY),PT)>0.05` DOCA χ^2 of any pair of daughters< 5	idem $p_{\rm T}(K^0_S) + p_{\rm T}(h^+) + p_{\rm T}(h^-) > 3000.0$ MeV idem idem idem idem
MotherCut		$p_{\rm T}(B) > 1500.0$ MeV $\chi^2_{\rm vtx}(B) < 12.0$ DIRA$(B)> 0.999$ $\min\chi^2_{\rm IP}$ $(B)< 6.0$ B flight distance w.r.t. any PV > 1.7 mm $\chi^2_{\rm FD}(B) > 50$ $\chi^2_{\rm IP}$ (h^+) + $\chi^2_{\rm IP}$ $(h^-)> 50$	idem idem DIRA> 0.9999 $\min\chi^2_{\rm IP}$ $(B)< 8.0$ B flight distance > 1.0 mm idem -

Table 4.8: Stripping requirements for RunI. As the stripping is applied in different steps, the same cut can appear multiple times. When this happens, only the last occurrence of the cut, the tightest version, is listed in this table.

Cut step	Candidate(s)	StrippingB2KShh_DD_Run2_OS_Line	StrippingB2KShh_LL_Run2_OS_Line
TriggerCuts	HLT1	Hlt1TrackMVADecision	idem
		Hlt1TwoTrackMVADecision	idem
		Hlt1IncPhiDecision (Hlt1PhiIncPhiDecision)	idem
	HLT2	Hlt2Topo{2,3,4}BodyDecision	idem
		Hlt2IncPhiDecision (Hlt2PhiIncPhiDecision)	idem
DaughterCuts	K^0_S	$p(K^0_S) > 6000.0\,\text{MeV}$	-
		$\lvert m_{\pi^+\pi^-} - m^{\text{PDG}}_{K^0_S}\rvert < 30.0\,\text{MeV}$	$\lvert m_{\pi^+\pi^-} - m^{\text{PDG}}_{K^0_S}\rvert < 20.0\,\text{MeV}$
		$\chi^2_{\text{vtx}}(K^0_S) < 12.0$	idem
		$\chi^2_{\text{FD}}(K^0_S) > 50.0$	$\chi^2_{\text{FD}}(K^0_S) > 80.0$
	K^0_S daughters	$p(\pi^\pm) > 2.0\,\text{GeV}$	idem
		$\min\chi^2_{\text{IP}}\ (\pi^\pm) > 4$	$\min\chi^2_{\text{IP}}\ (\pi^\pm) > 9$
		-	$p_{\text{T}}(\pi^\pm) > 250\,\text{MeV}$
		DOCA χ^2 of K^0_S daughters< 25	idem
		track $\chi^2/\text{ndf} < 4.0$	idem
		-	track ghost probability < 0.5
	$h_{1,2}$	track $\chi^2/\text{ndf} < 4.0$	idem
		track ghost probability < 0.5	idem
CombinationCut		$p_{\text{T}}(B) > 1000.0\,\text{MeV}$	idem
		$p_{\text{T}}(K^0_S) + p_{\text{T}}(h^+) + p_{\text{T}}(h^-) > 4200.0\,\text{MeV}$	$p_{\text{T}}(K^0_S) + p_{\text{T}}(h^+) + p_{\text{T}}(h^-) > 3000.0\,\text{MeV}$
		at least 2 daughters with $p_{\text{T}} > 800\,\text{MeV}$	idem
		$(4000 < m_{K^0_S h^+ h'^-} < 6200)\,\text{MeV}$	idem
		DOCA χ^2 between pairs of daughters < 25	idem
MotherCut		$p_{\text{T}}(B) > 1500.0\,\text{MeV}$	idem
		$\chi^2_{\text{vtx}}(B) < 12.0$	idem
		DIRA$(B) > 0.999$	idem
		$\chi^2_{\text{FD}}(B) > 5$	idem
		$Z_{\text{vtx}}(K^0_S) - Z_{\text{vtx}}(B) > 15.0-$	idem
		$\chi^2_{\text{IP}}\ (\pi^\pm) < 6.0$	-
		sum of the χ^2_{IP} of the daughters w.r.t their PV > 50.0	idem

Table 4.9: Stripping requirements for RunII. As the stripping is applied in different steps, the same cut can appear multiple times. When this happens, only the last occurrence of the cut, the tightest version, is listed in this table.

4.3 Offline Preselection

After applying the stripping requirements and before training the Multivariate analysis (MVA) tools, to further reduce the backgrounds' contribution to the data, a set of loose cuts with high efficiency on the signal, is applied on the samples. These cuts are required to minimally bias the Dalitz plane. Thus, their variables need to have the lowest possible correlations with the kinematics of daughter particles. As a result, the devised selection is determined based on topological variables and a set of very loose cuts on the momentum p of the B-meson daughters.

Compared to the previous studies, most of these selections are not modified, except that the lower range of the fiducial cut is decreased from $3\,\mathrm{GeV}/c$ to $2.59\,\mathrm{GeV}/c$. The rationale behind this change is that the new calibration samples for the particle identification response provide particles from a lower momentum threshold. These tracks are useful for the Physics of interest because they are populating preferentially the corners of the Dalitz plane where most of the amplitude interferences do occur. The Table 4.10 indicates a brief overview of this set of cuts and in the following the reason behind their application is discussed:

- `B_STRIP_VTXISOCHI2ONETRACK > 4` : This cut is required to remove partially reconstructed B decays (for which a charged track is missed) as well as a fraction of the combinatorial background while keeping the events with clear isolated B vertex. Indeed, to define this cut, first the difference of a vertex χ^2 ($\Delta\chi^2$) is calculated between the case of having one additional track and the one without it. Then we required it to be greater than 4.

- `KS_ENDVERTEX_Z - B_ENDVERTEX_Z > 30` : During the reconstruction phase, there are a set of K^0_S candidates whose reconstruction point is upstream of the B vertex. In order to remove these events, a 30 mm distance is required between the B and K^0_S vertices (toward the beam direction).

- `h{1,2}_isMuon == 0` : Among the reconstructed events, there might be candidates whose hadrons' track(s) are compatible with muons. These candidates are removed by applying this `!isMuon` cut.

- $2590\,\mathrm{MeV}/c \leq p\ (h^{(\prime)}) \leq 100000\,\mathrm{MeV}/c$: In the PID step, we should deal with the response of the RICH detector. These responses are obtained in a certain range of momentum. Thus, in order to have a set of tracks with appropriate and calibrated RICH information, the momentum of $h^{(\prime)}$ need to be constrained by requiring this fiducial cuts.

- $\mathrm{min}\chi^2_\mathrm{IP}(h^{(\prime)}) > 4$ & $p_\mathrm{T}(h^{(\prime)}) > 250\,\mathrm{MeV}/c$: As was mentioned in Sec. 4.2.2 some requirements in RunI stripping are relaxed in RunII stripping campaigns. Removing these lines has an important consequence, e.g. dramatically exceeding the requirements for the computing resources and storage space. Therefore, reapplying the removed cuts is decided to have a manageable sized nTuples.

Preselection cut	Description
`B_STRIP_VTXISOCHI2ONETRACK` > 4	B vertex isolation variable
`KS_ENDVERTEX_Z` $-$ `B_ENDVERTEX_Z` > 30	K^0_S vertex separation w.r.t. the B vertex
`h{1,2}_isMuon == 0`	Reject $h^{(\prime)}$ candidates compatible with the muon hypothesis
$2590 \leq p\ (h^{(\prime)}) \leq 100000$	Fiducial cut
$\min\chi^2_{\rm IP}\ (h^{(\prime)}) > 4$	Minimum IP χ^2 of the charged daughters with respect to the related PV
$p_{\rm T}(h^{(\prime)}) > 250$ MeV	Minimum transverse momentum of the charged daughters.

Table 4.10: Preselection cuts. Note that, in RunI case, the cuts on the transverse momenta and the $\min(\chi^2_{\rm IP})$ of the candidates are already included in the stripping line, so they are not applied again here.

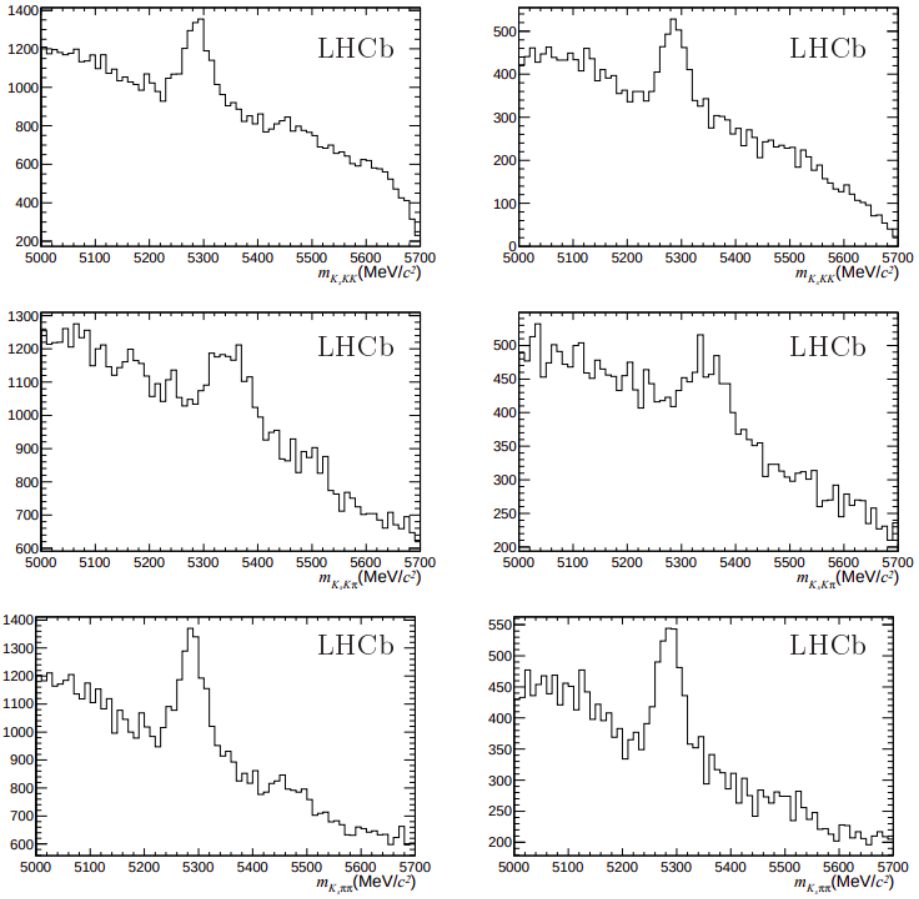

Figure 4.1: Reconstructed B candidates invariant-mass after preselection for (top) $K^0_S K^+ K^-$, (middle) $K^0_S K^\pm \pi^\mp$, (bottom) $K^0_S \pi^+ \pi^-$. The Left and right columns correspond to the Down-Down and Long-Long K^0_S reconstruction, respectively. It is taken from Ref [132]

4.4 Multivariate Analysis

Likewise what we have in many other analyses in LHCb, the $K^0_S h^\pm h'^\mp$ studies are also suffering from several types of background. The most dominant one, which is originated from a combination of random tracks in the detector, is called combinatorial background. The second type of background, known as cross-feed, is caused by misidentification of hadrons in a companion mode of the signal of interest (e.g. the misidentification of K as π in the mode $B_s \to K^0_S K^+\pi^-$ will make it belong to the $K^0_S\pi^+\pi^-$ experimental spectrum). The third type is called partially reconstructed background and will be discussed in details in Sec 6.1.4.

In order to suppress background's contribution of the first and second type, an individual Multivariate analysis (MVA) tool is trained for each of them. The first one which is called "Topological MVA" is devoted to fight against the combinatorial background while "PID MVA" is designed to suppress the cross-feed which is the second dominant contribution of the background. In the following section Topological MVA will be described while the PID MVA was formerly introduced in the Chapter. 3

Topological MVA

As it was mentioned, this tool is designed in order to remove most of the contributions of combinatorial background. This work has been conducted by our collaborators in LHCb following the same approach as in [20] and we just report here the necessary elements. The signal sample consists of MC-matched simulated signal events while the background is taken from the data samples themselves in the right-hand-side-band of the data ($m_{K^0_S\pi^+\pi^-} > 5425$ MeV/c^2). The same requirements such as trigger, stripping, and preselection are applied to both signal and background samples. Moreover, there are significant contributions from b-baryon decays, which are $\Lambda_b \to pK^0_S\pi$ and $\Lambda_c^+ \to pK^0_S$. Since they do not share the attributes of the combinatorics (they behave as signal), they can be removed explicitly by applying appropriate veto cuts (These cuts are discussed with further details in Sec. 4.7.). The reason behind applying the Λ_b veto is that, despite Λ_b mass is below the range of right-hand-side-band, forcing them to be reconstructed with the proton mass hypothesis will push a significant amount of its events toward the upper-mass-band which is predetermined for the background sample.

Similar to what is done for the PID case, the XGBoost algorithm is chosen from the scikit-learn library. To avoid biasing the training, signal and background samples are randomly split into two sub-samples with proportions of 70% and 30%, that are then used as training and testing samples respectively.

Finally, instead of training an individual tool for each $K^0_S h^+ h'^-$ decay mode, a unique one is trained with respect to the $B^0 \to K^0_S\pi^+\pi^-$ samples. This is done because the $K^0_S h^\pm h'^\mp$ decays (*e.g* $K^0_S\pi^+\pi^-$, $K^0_S K^\pm\pi^\mp$ and $K^0_S K^+K^-$) have the same topological characteristics. In contrast, since the reconstruction of each K^0_S category (Long-Long and Down-Down) involves different trigger conditions, separated stripping lines and individual preselection conditions, a separate training phase is devoted to each of them.

Discriminating variables for Topological MVA

Aside from developing a good discriminator, feature selection for such MVA requires further concerns. The MVA is trained using the features (variables) defined as an input for it. The same care brought to choose discriminating variables at stripping and preselection levels that are uncorrelated with the kinematics of the variables applies similarly at the MVA selection level. Thus, same as previous selections on data preparation phase, the variables must mainly belong to the topological category of variables which only provide information on geometry and topology of the vertices. Moreover, they should provide information on separation and quality of vertices, direction angle and flight distance of the B mesons. Next to this set, the variables related to transverse momentum and the pseudo rapidity of the B meson can also be used.

Further than this set of variables, there are new sets of variables which are used in this updated analysis. These variables are defined by concerning an observable α associated with the candidate particle T (either K^0_S or B candidate) and its corresponding asymmetry, which is defined using the following formula

$$\mathrm{asym}_\alpha = \frac{\alpha(T) - \sum_{\mathrm{cone}} \alpha}{\alpha(T) + \sum_{\mathrm{cone}} \alpha} \tag{4.1}$$

where α is an observable such as p, p_{T}, $\Delta\eta$ and $\Delta\phi$, and the quantity $\sum_{\mathrm{cone}} \alpha$ is the sum of all the α of the particles inside a cone with an opening angle θ around the track T. Among the possible values of θ, the one corresponding to $\theta = 1.5$ mrad was chosen. In the former studies [71], $p_{\mathrm{T}}^{\mathrm{asym}}$ of the B was uniquely considered, while in this updated analysis the seven remaining variables are also added to the list of selected features.

The only K^0_S reconstruction specific variable is the flight distance significance of the K^0_S with respect to the PV. This variable exists for the training of the MVA dedicated to the Long-Long sample, while it does not exist for the Down-Down samples. Table 4.11 indicates the full list of all the pre-existed and newly added input variables used in the MVA training. Distributions of these variables in the signal and background samples are shown in Figs. 4.2 and 4.3for 2018 DD and 2012b DD samples, respectively.

Hyper-parameter tuning of Topological MVA

Now same as what we have in the "PID MVA" case, after feature selection and determination of an appropriate algorithm to perform the MVA, a measure is defined to maximize the performance of the algorithm by optimizing its hyperparameters. This measure for the optimization is chosen to be the ROC curve. The Fig. 4.4 has shown the ROC cure of the optimized result for the 2018 and 2012b Down-Down samples.

Moreover, in order to avoid overtraining due to the optimization of hyperparameters, a comparison between the response of training and testing steps is performed. The Fig. 4.5 represent the the training and test sub-sample responses for signal and background. Here, likewise what was done in chapter 3 the overtraining is scrutinized using KS test. This process is done for both signal and background, and no hints of overtraining have been traced.

	Variable	Description
Baseline model	B_PT	B transverse momentum
	B_ETA	B pseudorapidity
	B_IPCHI2_OWNPV	χ^2_{IP} of the B w.r.t its PV
	B_VDCHI2_OWNPV	χ^2_{FD} of the B
	B_DIRA_OWNPV	cosine of the B direction angle
	B_ENDVERTEX_CHI2	χ^2_{vtx} of the B
	B_STRIP_VTXISODCHI2ONETRACK	B vertex isolation variable
	B_STRIP_CONEPTASYM_1_5	p_{T} asymmetry for a cone of radius 1.5 rad around the B-candidate in the η-ϕ plane
	h1_IPCHI2_OWNPV + h2_IPCHI2_OWNPV	sum of the χ^2_{IP} of $h^{(\prime)}$ w.r.t their PV.
	KS_VDCHI2_OWNPV	χ^2_{FD} of the LL K^0_{S}
Additional variables	KS_STRIP_CONEPTASYM_1_5	cone p_{T} asymmetry for the K^0_{S}-candidate
	B_STRIP_CONEPASYM_1_5	cone p asymmetry for the B-candidate
	KS_STRIP_CONEPASYM_1_5	cone p asymmetry for the K^0_{S}-candidate
	B_STRIP_CONEDELTAETA_1_5	cone $\delta\eta$ asymmetry for the B-candidate
	KS_STRIP_CONEDELTAETA_1_5	cone $\delta\eta$ asymmetry for the K^0_{S}-candidate
	B_STRIP_CONEDELTAPHI_1_5	cone $\delta\phi$ asymmetry for the B-candidate
	KS_STRIP_CONEDELTAPHI_1_5	cone $\delta\phi$ asymmetry for the K^0_{S}-candidate

Table 4.11: MVA input variables. Note that KS_VDCHI2_OWNPV is used only in the training of the LL samples.

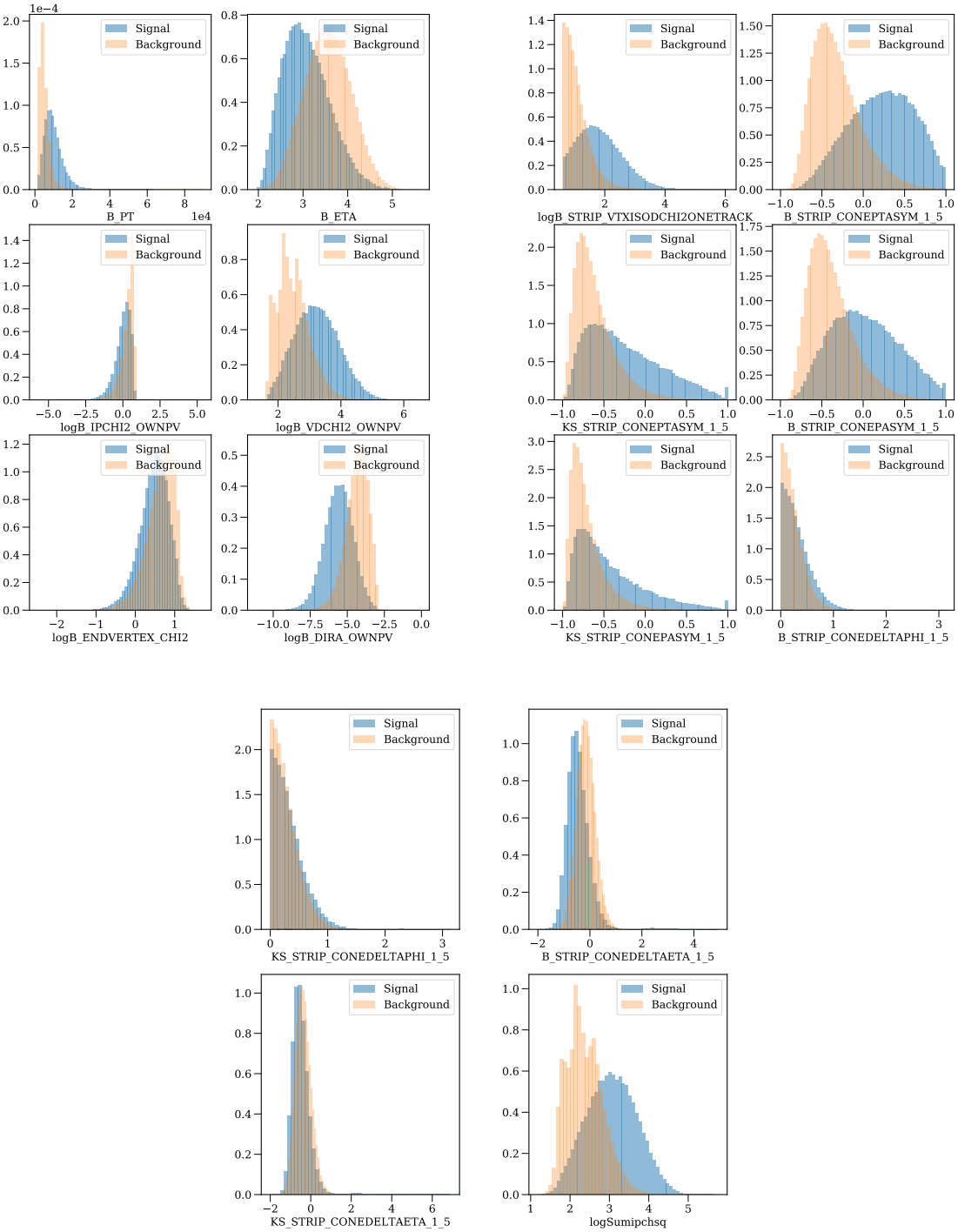

Figure 4.2: Distributions of input variables for topological MVA of 2018 Down-Down.

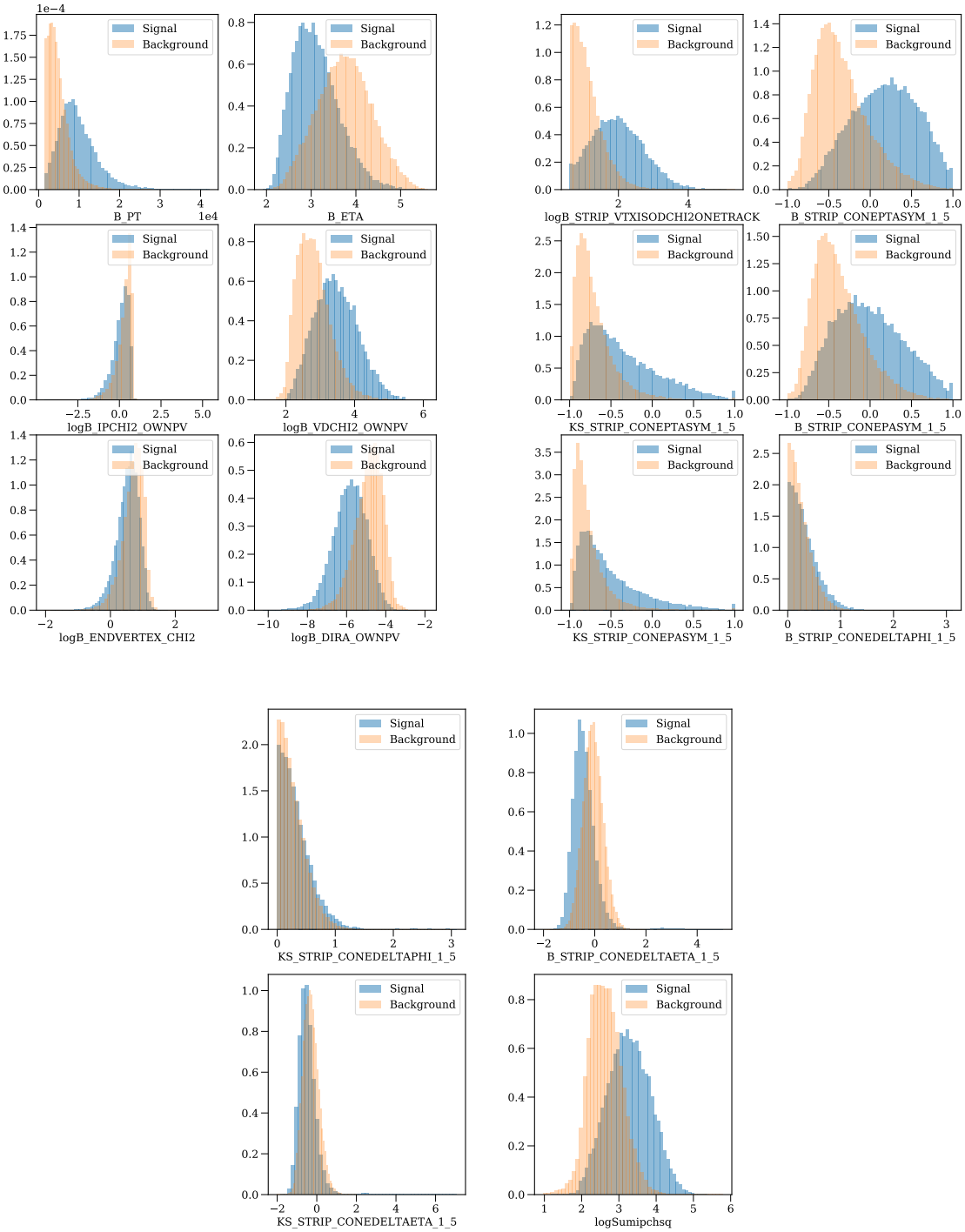

Figure 4.3: Distributions of input variables for topological MVA of 2012b Down-Down.

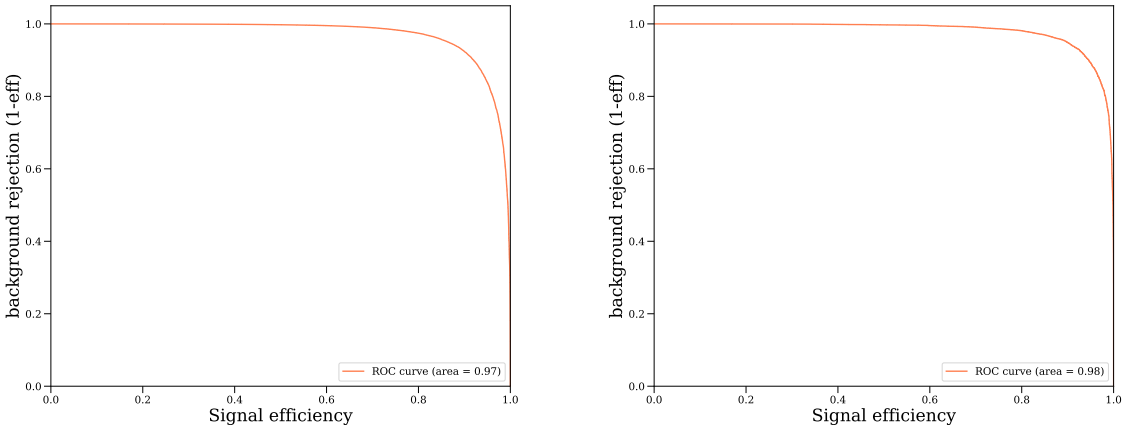

Figure 4.4: Left(right): The ROC curve for topological MVA of 2018(2012b) Down-Down.

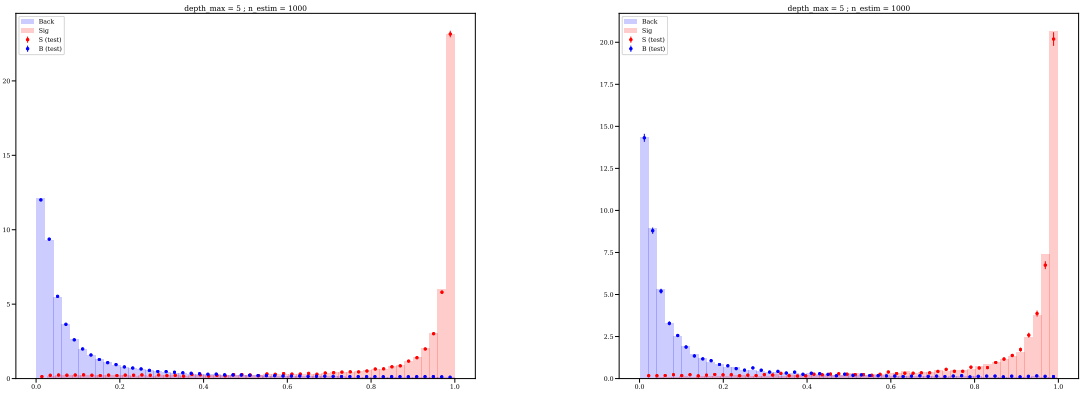

Figure 4.5: Left (right): The comparison between the test and training output of the topological MVA for both signal and background samples of 2018(2012b) Down-Down.

4.5 2D Optimization

The reason behind definition of two different MVA tools for our analysis is to kill two main types of background to the highest possible values while preserving the signal events in its optimal value. To fulfill this requirement, first a 2D surface is deduced using the outputs of MVA tools. Then a 2D optimization is implemented on this 2D manifold to maximize the significance of the signal events for the observed mode and discovery potential of the unobserved mode. In other words, once we have these MVA outputs, we should determine a(n) (optimal) working point, using 2D optimization, which satisfies this requirement.

To do so, first an appropriate figure of merit (FoM) is required. Therefore, following FoM is used for the observed mode,

$$\mathrm{FoM} = \frac{\mathrm{S}}{\sqrt{\mathrm{S}+\mathrm{B}}}\,, \tag{4.2}$$

where S and B are the number of signal and background events, respectively.

However, for the unobserved mode of $B_s \to K^0_{\mathrm{S}} K^+ K^-$, the expected signal is unknown and an appropriate FoM is the so-called Punzi FoM [136] which optimises the upper limit to be determined on the corresponding branching fraction:

$$\mathrm{FoM}_{\mathrm{Punzi}} = \frac{\epsilon_{\mathrm{sig}}}{\frac{\mathrm{a}}{2} + \sqrt{\mathrm{B}}}\,, \tag{4.3}$$

in which ϵ_{sig} is the signal efficiency obtained by counting the MC events passing both MVA cuts, and a corresponds to the significance of the limit, in units of Gaussian standard deviations that one wants to place on the branching fraction. We have chosen $a = 5$.

In order to estimate the number of signal events (S) we have,

$$S = S_0 \times \epsilon_{\mathrm{stripping}} \times \epsilon_{\mathrm{preselection}} \times \epsilon_{\mathrm{veto}} \times \epsilon_{\mathrm{selection}} \times \epsilon_{\mathrm{GLC}}\,, \tag{4.4}$$

in which each ϵ corresponds to efficiency for a requirement (*e.g.* stripping, preselection, veto, selection cuts and the acceptance of the LHCb (generator level cut or GLC)) which is applied on the samples and S_0 is defined in the following form,

$$S_0 = 2 \times \sigma(b\bar{b}) \times \int \mathcal{L}dt \times \mathcal{B}(K^0_{\mathrm{S}} \to \pi^+\pi^-) \times \mathcal{B}(B^0_{d,s} \to K^0_{\mathrm{S}} h^{\pm} h'^{\mp}) \times f_{d,s} \times \epsilon_{\mathrm{GEC}}\,, \tag{4.5}$$

where $\sigma(b\bar{b})$ denotes the cross-section of the $b\bar{b}$ production, $\int \mathcal{L}dt$ indicates the integrated luminosity of a certain year, $\mathcal{B}(K^0_{\mathrm{S}} \to \pi^+\pi^-)$ shows the branching fraction of K^0_{S} decay into two π, $\mathcal{B}(B^0_{d,s} \to K^0_{\mathrm{S}} h^{\pm} h'^{\mp})$ is the branching fraction of $B^0_{d,s}$ to $K^0_{\mathrm{S}} h^{\pm} h'^{\mp}$ where $h^{(\prime)}$ is either π or K, $f_{d,s}$ highlights the hadronization fraction of a b-quark into $B_{d,s}$ mesons and ϵ_{GEC} denotes the efficiency of Global Event Cuts (GEC). The GEC are requirements on the number of Scintillating Pad Detector hits and number of Outer Tracker hits which are imposed at the first level of trigger in order to remove the too large events that the data acquisition can not cope with. Its efficiency is estimated thanks to Mini-bias events for RunI. The simulation improved significantly for the RunII and hence was used for the

GEC efficiency determination in the RunII data. Note that the $\mathcal{B}(B^0_{d,s} \to K^0_S h^\pm h'^\mp)$ is borrowed from previous study [20].

Furthermore, in order to determine the expected number of background events (B) we should consider the two main contributions of combinatorial and cross-feed sources. The contribution of combinatorial background is estimated by using a polynomial fit of the right-hand sideband of the data and its extrapolation into the mass peak region. One should take into account that only events which satisfy the $m_{K^0_S h^+ h'^-} > 5550\text{MeV/c}^2$ criterion are considered. This choice is made to exclude the Λ_b region, where candidates could have similar behaviour as signal events.

Since the second contribution is originated from the misidentification of one of the two hadrons, its number of events is estimated by using S_0 determination while considering an appropriate branching fraction based on the origin of cross-feed events. As an instance, one of the cross-feed samples which enters in the $K^0_S\pi^+\pi^-$ experimental mode can come from the original mode of the $B^0 \to K^0_S K^\pm \pi^\mp$ whose K is misidentified as π. Therefore, the corresponding S_0 for determination of number of these events consists of the branching fraction of $B^0 \to K^0_S K^\pm \pi^\mp$.

Moreover, the efficiency of the selection for the cross-feed must be normalized with respect to the efficiency of the signal event.

The result of the 2D optimization is performed mode by mode for each year. For each decay mode according to the Feynman diagram of the decay modes, the quark transition which occurs through this decay and the probability which determines with respect to the CKM matrix, a probability can be deduced. This probability enables us to determined which decay mode is more probable than the other one. Using this concept, the decay mode which is more probable is called Cabbibo favored and the other one is labeled as Cabbibo suppressed. The table 4.12 is summarising the list of Cabbibo favord and Cabbibo suppressed mode in our analysis.

experimental mode	Cabbibo Favored	Cabbibo suppressed
$K^0_S\pi^+\pi^-$	$B^0 \to K^0_S\pi^+\pi^-$	$B_s \to K^0_S\pi^+\pi^-$
$K^0_S K^\pm\pi^\mp$	$B_s \to K^0_S K^\pm\pi^\mp$	$B^0 \to K^0_S K^\pm\pi^\mp$
$K^0_S K^+K^-$	$B^0 \to K^0_S K^+K^-$	$B_s \to K^0_S K^+K^-$

Table 4.12: Categorization of the analysis decay mode in terms of Cabbibo supressed and Cabbibo favored modes.

The optimization maps of the 2018 and 2012b are presented in the Figs 4.6 to 4.9 and for each year the Cabbibo suppressed and favored maps are shown separately.

In addition, since the Cabbibo favored modes are more probable than the suppressed category, their accumulation in the experimental mode are more significant. Thus, in optimization, their FoM maximises using looser cuts. As a result, the optimize cuts which are derived for Cabbibo favored mode is called Loose cuts and those corresponds to suppressed category of decay mode is called Tight cuts.

Furthermore, tables 4.13 to 4.18 show the deduced optimal points in this optimization. In the presented results, the notion and concept of the cross-feed is reflected as follows. As discussed above, the cross-feed is resulted in misidentification of the decay products (either $h1$ or $h2$) which are used to reconstruct the $B^0_{d,s} \to K^0_S h^+ h^-$ experimental spectrum. Depends on the misidentification of K as π and vice versa, which occurs to h_1 or h_2 the cross-feed is labeled and shown in the tables as CF1 or CF2, respectively. As an instance for the selected decay mode of $B_s \to K^0_S \pi^+ \pi^-$ the CF1 comes from misidentification of K as π for the events which are originally belong to the $B_s \to K^0_S K^+ \pi^-$ and the CF2 results from the same misidentification for the events which originate from $B_s \to K^0_S K^- \pi^+$. The other type of cross-feed samples result from misidentication of p and $\bar{p}$ as π or K for the events which originate from $\Lambda^0_b \to \overset{(-)}{p} K^0_S h^{(+)}_-$ where h is either K or π. These type of cross-feeds are also mentioned in the table as Lb1 and Lb2 which denotes that misidentification is occurred for p and $\bar{p}$, respectively. As an example, for experimental spectrum of $K^0_S \pi^+ \pi^-$, the Lb1 cross-feed comes from the misidentification of p as π^+ in $\Lambda^0_b \to p K^0_S \pi^-$ and Lb2 results from misidentification of $\bar{p}$ as π^- in $\Lambda^0_b \to \bar{p} K^0_S \pi^+$.

The final point about these tables is that in each row in the first five columns the signal mode (with respect to which the maximizing is done) is denoted in terms of the mode, mother particle type(B_s or B^0), and K^0_S reconstruction (Down-Down or Long-Long); the next two columns indicate the optimized cuts and in the rest of the columns mention the corresponding efficiencies (deduced in 2.5 σ window around the PDG B-Mass value) of maximized signal mode and the discussed backgrounds which are used for this optimization.

By applying the optimized cuts, we can determine the efficiency of them in the whole mass range and not only in the region of interest. Tables 4.19 to 4.25 show these efficiencies for the signal and cross-feeds which are resulted by misidentifications of $h^{(\prime)}$ for $B^0_{d,s} \to K^0_S \pi^+ \pi^-$ and $B^0_{d,s} \to K^0_S K^+ K^-$ decay modes of 2018 to 2011, respectively (The results related to the $B^0_{d,s} \to K^0_S K^\pm \pi^\mp$ decay modes are presented in Appendix C). A word of caution is in order. This determination corresponds to a *flat* efficiency in the Squared Dalitz-plane. The efficiency to be considered when evaluating the branching fraction shall consider the actual distribution of the events in the DP. This determination is addressed in the Section 5.1.2.

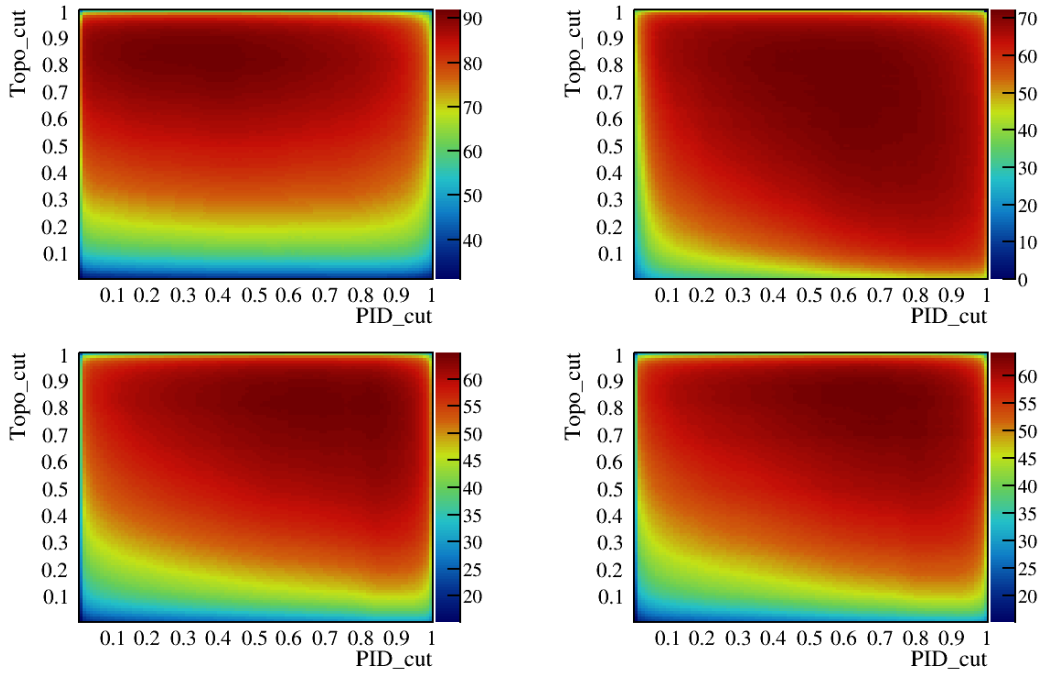

Figure 4.6: The 2D Optimization of Cabbibo favored modes $B^0_{d,s} \to K^0_S h^+ h'^-$ decay for 2018 DD K^0_S reconstruction. Top: left(right) corresponds to the $B^0 \to K^0_S \pi^+ \pi^-$ ($B^0 \to K^0_S K^+ K^-$). Bottom: left(right) corresponds to $B_s \to K^0_S \pi^+ K^-$($B_s \to K^0_S K^+ \pi^-$)

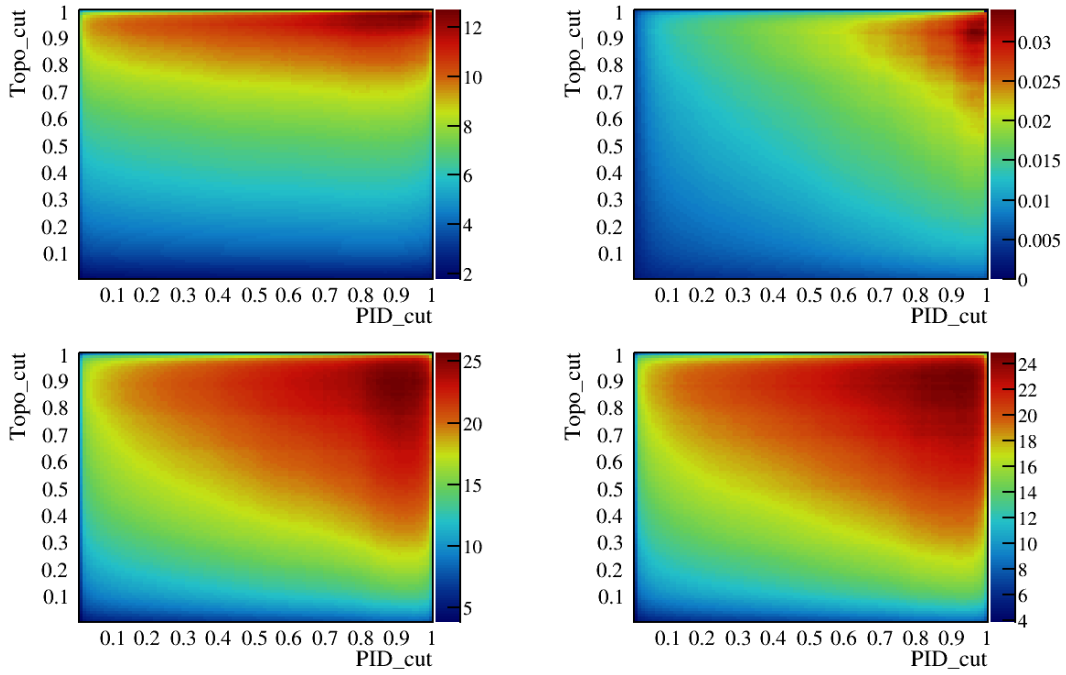

Figure 4.7: The 2D Optimization of Cabbibo suppressed modes $B^0_{d,s} \to K^0_S h^+ h'^-$ decay for 2018 DD K^0_S reconstruction. Top: left(right) corresponds to the $B_s \to K^0_S \pi^+ \pi^-$ ($B_s \to K^0_S K^+ K^-$). Bottom: left(right) corresponds to $B^0 \to K^0_S \pi^+ K^-$($B^0 \to K^0_S K^+ \pi^-$)

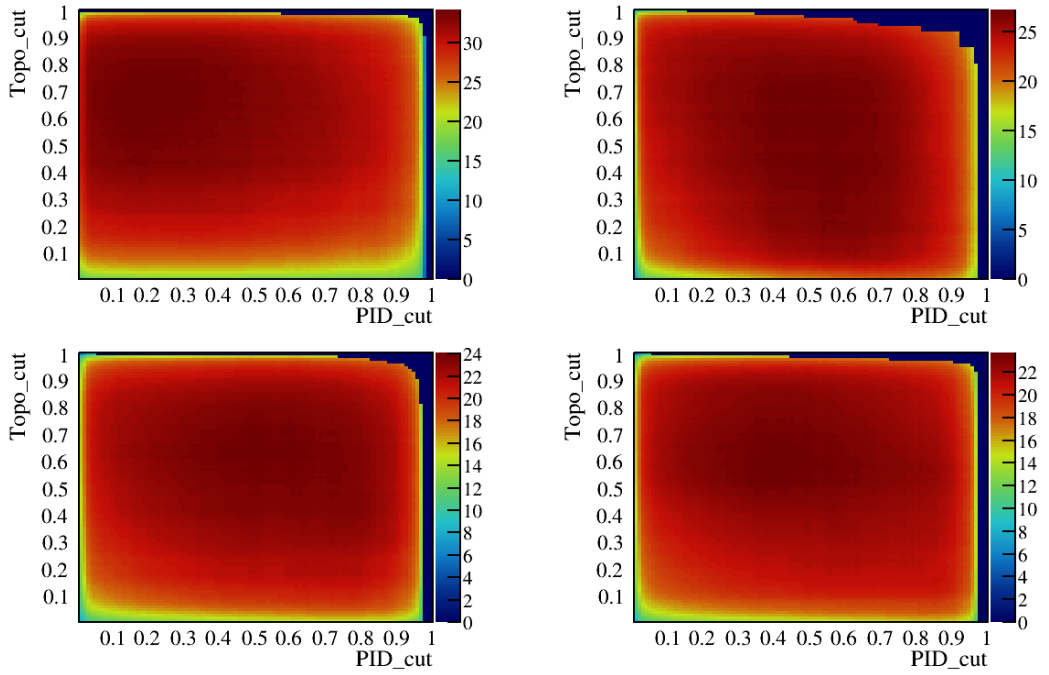

Figure 4.8: The 2D Optimization of Cabbibo favored modes $B^0_{d,s} \to K^0_S h^+ h'^-$ decay for 2012b DD K^0_S reconstruction. Top: left(right) corresponds to the $B^0 \to K^0_S \pi^+ \pi^-$ ($B^0 \to K^0_S K^+ K^-$). Bottom: left(right) corresponds to $B_s \to K^0_S \pi^+ K^-$($B_s \to K^0_S K^+ \pi^-$)

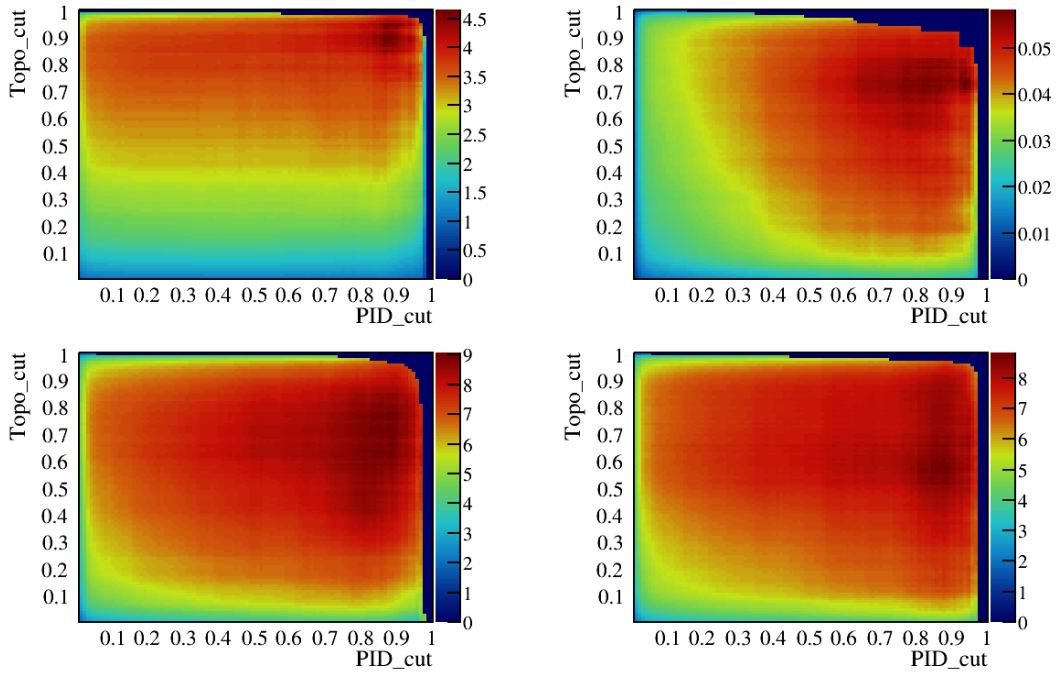

Figure 4.9: The 2D Optimization of Cabbibo suppressed modes $B^0_{d,s} \to K^0_S h^+ h'^-$ decay for 2012b DD K^0_S reconstruction. Top: left(right) corresponds to the $B_s \to K^0_S \pi^+ \pi^-$ ($B_s \to K^0_S K^+ K^-$). Bottom: left(right) corresponds to $B^0 \to K^0_S \pi^+ K^-$($B^0 \to K^0_S K^+ \pi^-$)

Mode	Btype		KSreco		Cut		Efficiency (%)					
	Bd	Bs	DD	LL	Topo	PID	Sig	CF1	CF2	Lb1	Lb2	Comb
pipiKS	✓		✓		0.81	0.4	68.7 (0.2)	3.7 (0.4)	3.5 (0.4)	5.0 (1.0)	5.0 (1.0)	1.26 (0.02)
		✓	✓		0.97	0.94	33.8 (0.2)	0.09 (0.07)	0.08 (0.06)	0.4 (0.3)	0.2 (0.2)	0.066 (0.004)
	✓			✓	0.83	0.28	74.9 (0.2)	5.1 (0.7)	5.0 (0.7)	6.0 (2.0)	6.0 (2.0)	0.74 (0.02)
		✓		✓	0.94	0.93	47.7 (0.3)	0.2 (0.1)	0.1 (0.1)	0.5 (0.5)	0.4 (0.5)	0.132 (0.009)
KpiKS	✓		✓		0.89	0.89	51.5 (0.3)	0.25 (0.09)	0.4 (0.1)	2.0 (1.0)	0.5 (0.5)	0.142 (0.005)
		✓	✓		0.8	0.69	66.8 (0.2)	1.3 (0.2)	1.7 (0.2)	5.0 (1.0)	2.1 (0.6)	0.47 (0.009)
	✓			✓	0.82	0.86	63.4 (0.4)	0.4 (0.2)	0.7 (0.2)	3.0 (2.0)	0.5 (0.8)	0.174 (0.009)
		✓		✓	0.77	0.75	70.5 (0.4)	1.0 (0.3)	1.5 (0.3)	3.0 (1.0)	2.0 (0.9)	0.27 (0.01)
piKKS	✓		✓		0.91	0.92	47.6 (0.3)	0.2 (0.08)	0.3 (0.1)	0.2 (0.3)	2.0 (1.0)	0.121 (0.004)
		✓	✓		0.83	0.69	64.8 (0.2)	1.2 (0.2)	1.9 (0.2)	2.5 (0.7)	4.0 (1.0)	0.418 (0.008)
	✓			✓	0.84	0.92	57.8 (0.4)	0.2 (0.1)	0.4 (0.2)	0.2 (0.5)	2.0 (2.0)	0.126 (0.008)
		✓		✓	0.77	0.64	73.6 (0.3)	1.8 (0.4)	2.2 (0.4)	1.9 (0.9)	5.0 (2.0)	0.37 (0.01)
KKKS	✓		✓		0.73	0.64	70.4 (0.2)	2.0 (0.4)	2.0 (0.4)	5.0 (2.0)	4.0 (2.0)	0.351 (0.008)
		✓	✓		0.91	0.96	44.3 (0.2)	0.2 (0.1)	0.11 (0.09)	1.4 (0.6)	1.2 (0.6)	0.038 (0.003)
	✓			✓	0.64	0.6	77.6 (0.2)	2.5 (0.7)	2.2 (0.7)	4.0 (2.0)	5.0 (2.0)	0.34 (0.01)
		✓		✓	0.91	0.94	52.3 (0.3)	0.3 (0.2)	0.3 (0.2)	2.0 (1.0)	2.0 (1.0)	0.035 (0.004)

Table 4.13: Results of 2D optimization for 2018 $B^0_{d,s} \to K^0_S h^+ h'^-$ samples. In each row, the first 5 columns define the signal mode (The optimization designed to maximize it) in terms of decay mode, mother particle type(B_s or B^0), and K^0_S reconstruction (Long-Long or Down-Down). The next two columns denote the optimal cuts.The rest of the columns represent the efficiencies of signal, cross-feeds and combinatorial background species. The reported efficiencies and their corresponding uncertainty (in parenthesis) are in percentage.

Mode	Btype		KSreco		Cut		Efficiency (%)					
	Bd	Bs	DD	LL	Topo	PID	Sig	CF1	CF2	Lb1	Lb2	Comb
pipiKS	✓		✓		0.85	0.35	66.8 (0.2)	3.6 (0.4)	3.6 (0.4)	5.0 (1.0)	5.0 (1.0)	1.09 (0.02)
		✓	✓		0.97	0.94	35.1 (0.2)	0.11 (0.07)	0.11 (0.07)	0.8 (0.3)	0.2 (0.2)	0.069 (0.004)
	✓			✓	0.83	0.32	74.5 (0.2)	4.2 (0.7)	4.2 (0.6)	4.0 (2.0)	6.0 (2.0)	0.68 (0.02)
		✓		✓	0.95	0.9	50.4 (0.3)	0.3 (0.2)	0.2 (0.2)	0.5 (0.4)	0.9 (0.6)	0.101 (0.009)
KpiKS	✓		✓		0.83	0.92	54.4 (0.2)	0.16 (0.07)	0.29 (0.09)	2.0 (1.0)	0.2 (0.3)	0.208 (0.006)
		✓	✓		0.73	0.69	69.8 (0.2)	1.3 (0.2)	1.8 (0.2)	4.3 (0.9)	5.0 (0.7)	0.58 (0.01)
	✓			✓	0.89	0.91	57.2 (0.4)	0.2 (0.1)	0.3 (0.2)	2.0 (2.0)	0.3 (0.5)	0.095 (0.008)
		✓		✓	0.77	0.66	74.2 (0.3)	1.5 (0.3)	2.0 (0.3)	7.0 (2.0)	9.0 (1.0)	0.35 (0.01)
piKKS	✓		✓		0.92	0.91	48.6 (0.2)	0.14 (0.07)	0.4 (0.1)	0.2 (0.3)	2.0 (1.0)	0.116 (0.005)
		✓	✓		0.8	0.77	64.6 (0.2)	0.8 (0.1)	1.2 (0.2)	1.2 (0.4)	5.1 (0.9)	0.46 (0.01)
	✓			✓	0.87	0.85	64.2 (0.4)	0.5 (0.2)	0.8 (0.2)	0.5 (0.7)	3.0 (2.0)	0.13 (0.009)
		✓		✓	0.81	0.62	73.3 (0.3)	1.6 (0.3)	2.0 (0.4)	3.0 (0.9)	5.0 (2.0)	0.33 (0.01)
KKKS	✓		✓		0.74	0.66	70.5 (0.2)	1.8 (0.3)	2.0 (0.4)	5.0 (1.0)	5.0 (1.0)	0.349 (0.008)
		✓	✓		0.94	0.99	32.0 (0.2)	0.02 (0.04)	0.02 (0.03)	0.4 (0.3)	0.5 (0.3)	0.01 (0.001)
	✓			✓	0.67	0.65	76.9 (0.2)	1.9 (0.6)	2.0 (0.6)	5.0 (2.0)	5.0 (2.0)	0.32 (0.01)
		✓		✓	0.96	0.98	39.9 (0.3)	0.1 (0.1)	0.06 (0.09)	1.2 (0.8)	1.1 (0.8)	0.011 (0.003)

Table 4.14: Results of 2D optimization for 2017 $B^0_{d,s} \to K^0_S h^+ h'^-$ samples. In each row, the first 5 columns define the signal mode (The optimization designed to maximize it) in terms of decay mode, mother particle type(B_s or B^0), and K^0_S reconstruction (Long-Long or Down-Down). The next two columns denote the optimal cuts. The rest of the columns represent the efficiencies of signal, cross-feeds and combinatorial background species. The reported efficiencies and their corresponding uncertainty (in parenthesis) are in percentage.

Mode	Btype		KSreco		Cut		Efficiency (%)					
	Bd	Bs	DD	LL	Topo	PID	Sig	CF1	CF2	Lb1	Lb2	Comb
pipiKS	✓		✓		0.85	0.45	64.7 (0.2)	2.7 (0.3)	2.7 (0.3)	5.0 (1.0)	5.0 (1.0)	0.95 (0.01)
		✓	✓		0.96	0.97	33.3 (0.2)	0.05 (0.04)	0.04 (0.04)	0.03 (0.08)	0.02 (0.06)	0.081 (0.004)
	✓			✓	0.83	0.35	74.5 (0.2)	3.8 (0.6)	3.6 (0.6)	5.0 (2.0)	7.0 (2.0)	0.61 (0.02)
		✓		✓	0.96	0.91	48.5 (0.3)	0.2 (0.1)	0.2 (0.1)	1.0 (0.7)	1.1 (0.8)	0.065 (0.006)
KpiKS	✓		✓		0.88	0.9	52.0 (0.2)	0.21 (0.08)	0.4 (0.1)	2.0 (1.0)	0.7 (0.6)	0.158 (0.005)
		✓	✓		0.8	0.66	66.6 (0.2)	1.4 (0.2)	1.7 (0.2)	4.0 (1.0)	5.6 (0.9)	0.49 (0.01)
	✓			✓	0.93	0.91	56.0 (0.4)	0.2 (0.1)	0.3 (0.2)	2.0 (2.0)	0.4 (0.7)	0.061 (0.005)
		✓		✓	0.83	0.72	71.2 (0.3)	1.1 (0.3)	1.4 (0.3)	5.0 (2.0)	2.0 (1.0)	0.23 (0.01)
piKKS	✓		✓		0.85	0.94	50.7 (0.2)	0.1 (0.06)	0.23 (0.08)	0.1 (0.2)	2.0 (1.0)	0.165 (0.006)
		✓	✓		0.77	0.7	67.3 (0.2)	1.0 (0.2)	1.6 (0.2)	2.0 (0.6)	5.0 (1.0)	0.54 (0.01)
	✓			✓	0.91	0.87	60.3 (0.4)	0.4 (0.2)	0.6 (0.2)	0.3 (0.7)	3.0 (2.0)	0.076 (0.006)
		✓		✓	0.84	0.63	71.7 (0.3)	1.4 (0.3)	2.0 (0.3)	2.0 (1.0)	6.0 (2.0)	0.22 (0.01)
KKKS	✓		✓		0.61	0.71	72.5 (0.1)	1.6 (0.3)	1.6 (0.3)	5.0 (2.0)	5.0 (2.0)	0.53 (0.01)
		✓	✓		0.94	0.98	36.2 (0.2)	0.03 (0.04)	0.03 (0.04)	0.8 (0.5)	0.7 (0.5)	0.015 (0.002)
	✓			✓	0.8	0.58	74.5 (0.2)	2.1 (0.6)	2.2 (0.6)	5.0 (2.0)	5.0 (3.0)	0.25 (0.01)
		✓		✓	0.98	0.98	35.4 (0.3)	0.1 (0.1)	0.03 (0.07)	1.0 (1.0)	1.0 (1.0)	0.006 (0.002)

Table 4.15: Results of 2D optimization for 2016 $B^0_{d,s} \to K^0_S h^+ h'^-$ samples. In each row, the first 5 columns define the signal mode (The optimization designed to maximize it) in terms of decay mode, mother particle type(B_s or B^0), and K^0_S reconstruction (Long-Long or Down-Down). The next two columns denote the optimal cuts. The rest of the columns represent the efficiencies of signal, cross-feeds and combinatorial background species. The reported efficiencies and their corresponding uncertainty (in parenthesis) are in percentage.

Mode	Btype		KSreco		Cut		Efficiency (%)					
	Bd	Bs	DD	LL	Topo	PID	Sig	CF1	CF2	Lb1	Lb2	Comb
pipiKS	✓		✓		0.63	0.17	77.9 (0.3)	9.0 (1.0)	9.0 (1.0)	9.0 (2.0)	9.0 (2.0)	3.4 (0.1)
		✓	✓		0.89	0.86	42.9 (0.4)	0.4 (0.2)	0.4 (0.2)	1.8 (0.7)	1.0 (0.6)	0.4 (0.04)
	✓			✓	0.42	0.2	83.6 (0.3)	9.0 (2.0)	9.0 (2.0)	10.0 (2.0)	9.0 (3.0)	6.3 (0.3)
		✓		✓	0.78	0.95	28.6 (0.5)	0.0 (0.01)	0.0 (0.1)	0.1 (0.2)	0.1 (0.3)	0.22 (0.07)
KpiKS	✓		✓		0.7	0.88	49.2 (0.5)	0.3 (0.2)	0.6 (0.2)	2.0 (2.0)	0.7 (0.7)	0.35 (0.03)
		✓	✓		0.61	0.6	72.3 (0.4)	3.7 (0.6)	4.2 (0.6)	5.0 (1.0)	12.0 (1.0)	1.05 (0.06)
	✓			✓	0.67	0.81	60.8 (0.7)	1.0 (0.5)	1.3 (0.6)	2.0 (3.0)	1.0 (2.0)	0.48 (0.09)
		✓		✓	0.58	0.66	72.6 (0.6)	2.4 (0.8)	3.3 (0.9)	5.0 (3.0)	8.0 (2.0)	1.1 (0.1)
piKKS	✓		✓		0.56	0.87	54.0 (0.5)	0.4 (0.2)	0.8 (0.3)	0.7 (0.7)	1.0 (2.0)	0.66 (0.05)
		✓	✓		0.58	0.35	78.7 (0.3)	7.2 (0.7)	6.7 (0.7)	15.0 (1.0)	7.0 (2.0)	1.79 (0.08)
	✓			✓	0.67	0.88	51.7 (0.8)	0.2 (0.3)	0.6 (0.4)	1.0 (2.0)	1.0 (3.0)	0.29 (0.07)
		✓		✓	0.34	0.65	77.8 (0.6)	2.5 (0.8)	3.6 (0.9)	12.0 (2.0)	5.0 (3.0)	2.4 (0.2)
KKKS	✓		✓		0.42	0.53	79.1 (0.3)	4.8 (0.9)	5.2 (0.9)	4.0 (2.0)	3.0 (2.0)	0.89 (0.05)
		✓	✓		0.73	0.92	42.4 (0.4)	0.3 (0.2)	0.2 (0.2)	0.7 (0.6)	0.9 (0.6)	0.1 (0.02)
	✓			✓	0.43	0.6	79.2 (0.4)	3.0 (1.0)	4.0 (1.0)	3.0 (4.0)	4.0 (4.0)	0.8 (0.1)
		✓		✓	0.56	0.84	59.8 (0.5)	0.9 (0.7)	1.4 (0.8)	2.0 (2.0)	3.0 (2.0)	0.16 (0.05)

Table 4.16: Results of 2D optimization for 2012b $B^0_{d,s} \to K^0_S h^+ h'^-$ samples. In each row, the first 5 columns define the signal mode (The optimization designed to maximize it) in terms of decay mode, mother particle type(B_s or B^0), and K^0_S reconstruction (Long-Long or Down-Down). The next two columns denote the optimal cuts. The rest of the columns represent the efficiencies of signal, cross-feeds and combinatorial background species. The reported efficiencies and their corresponding uncertainty (in parenthesis) are in percentage.

Mode	Btype		KSreco		Cut		Efficiency (%)					
	Bd	Bs	DD	LL	Topo	PID	Sig	CF1	CF2	Lb1	Lb2	Comb
pipiKS	✓		✓		0.56	0.22	75.9 (0.2)	7.9 (0.9)	7.5 (0.9)	8.0 (3.0)	9.0 (3.0)	5.5 (0.3)
		✓	✓		0.84	0.88	38.4 (0.3)	0.1 (0.1)	0.2 (0.2)	0.6 (0.7)	0.6 (0.7)	0.5 (0.09)
	✓			✓	0.58	0.18	82.1 (0.3)	9.0 (2.0)	9.0 (2.0)	9.0 (4.0)	8.0 (4.0)	2.7 (0.3)
		✓		✓	0.8	0.85	51.1 (0.6)	0.3 (0.4)	0.4 (0.5)	2.0 (2.0)	7.0 (3.0)	0.4 (0.1)
KpiKS	✓		✓		0.72	0.89	45.4 (0.4)	0.2 (0.1)	0.4 (0.2)	1.0 (2.0)	1.0 (1.0)	0.27 (0.06)
		✓	✓		0.47	0.48	76.8 (0.3)	4.9 (0.6)	5.3 (0.6)	6.0 (2.0)	15.0 (2.0)	2.5 (0.2)
	✓			✓	0.59	0.93	41.8 (0.8)	0.1 (0.2)	0.1 (0.2)	0.0 (2.0)	0.1 (0.8)	0.28 (0.08)
		✓		✓	0.64	0.44	79.3 (0.6)	0.4 (0.3)	18.3 (0.9)	5.0 (3.0)	13.0 (3.0)	1.0 (0.2)
piKKS	✓		✓		0.53	0.88	53.4 (0.4)	0.3 (0.2)	0.5 (0.2)	1.0 (1.0)	1.0 (2.0)	1.1 (0.1)
		✓	✓		0.53	0.38	77.6 (0.3)	5.7 (0.6)	6.7 (0.6)	16.0 (2.0)	7.0 (2.0)	3.1 (0.2)
	✓			✓	0.48	0.94	40.5 (0.8)	0.1 (0.2)	0.0 (0.1)	0.2 (0.8)	1.0 (2.0)	0.36 (0.09)
		✓		✓	0.58	0.44	79.9 (0.6)	5.0 (1.0)	6.0 (1.0)	13.0 (3.0)	6.0 (3.0)	1.3 (0.2)
KKKS	✓		✓		0.42	0.51	79.5 (0.2)	4.7 (0.8)	4.6 (0.8)	4.0 (3.0)	4.0 (3.0)	1.6 (0.1)
		✓	✓		0.73	0.87	49.7 (0.3)	0.7 (0.3)	0.6 (0.3)	1.0 (1.0)	1.0 (1.0)	0.16 (0.05)
	✓			✓	0.3	0.47	84.6 (0.4)	6.0 (2.0)	5.0 (2.0)	4.0 (5.0)	3.0 (5.0)	1.3 (0.2)
		✓		✓	0.19	0.83	66.6 (0.5)	1.4 (0.8)	1.5 (0.9)	2.0 (2.0)	2.0 (2.0)	0.7 (0.1)

Table 4.17: Results of 2D optimization for 2012a $B^0_{d,s} \to K^0_S h^+ h'^-$ samples. In each row, the first 5 columns define the signal mode (The optimization designed to maximize it) in terms of decay mode, mother particle type(B_s or B^0), and K^0_S reconstruction (Long-Long or Down-Down). The next two columns denote the optimal cuts. The rest of the columns represent the efficiencies of signal, cross-feeds and combinatorial background species. The reported efficiencies and their corresponding uncertainty (in parenthesis) are in percentage.

Mode	Btype		KSreco		Cut		Efficiency (%)					
	Bd	Bs	DD	LL	Topo	PID	Sig	CF1	CF2	Lb1	Lb2	Comb
pipiKS	✓		✓		0.5	0.17	80.9 (0.2)	9.3 (0.9)	8.9 (0.9)	9.0 (2.0)	9.0 (2.0)	6.1 (0.3)
		✓	✓		0.91	0.93	30.6 (0.3)	0.1 (0.1)	0.06 (0.09)	0.6 (0.6)	0.4 (0.5)	0.19 (0.05)
	✓			✓	0.6	0.25	80.4 (0.3)	8.0 (1.0)	7.0 (1.0)	9.0 (3.0)	9.0 (3.0)	3.6 (0.4)
		✓		✓	0.77	0.91	47.1 (0.5)	0.1 (0.2)	0.2 (0.2)	0.5 (0.9)	1.0 (1.0)	0.7 (0.2)
KpiKS	✓		✓		0.41	0.85	60.6 (0.4)	0.6 (0.2)	1.1 (0.3)	2.0 (2.0)	2.0 (2.0)	1.1 (0.1)
		✓	✓		0.4	0.49	80.2 (0.3)	5.2 (0.6)	5.1 (0.5)	6.0 (2.0)	15.0 (2.0)	2.6 (0.2)
	✓			✓	0.62	0.8	63.7 (0.6)	0.6 (0.4)	1.5 (0.6)	2.0 (4.0)	2.0 (3.0)	0.8 (0.2)
		✓		✓	0.41	0.57	80.1 (0.5)	3.2 (0.8)	4.1 (0.8)	5.0 (3.0)	14.0 (3.0)	2.3 (0.3)
piKKS	✓		✓		0.51	0.86	57.0 (0.4)	0.4 (0.2)	0.9 (0.3)	2.0 (2.0)	2.0 (2.0)	0.9 (0.1)
		✓	✓		0.37	0.55	78.6 (0.3)	4.4 (0.5)	4.9 (0.5)	14.0 (2.0)	5.0 (2.0)	2.9 (0.2)
	✓			✓	0.21	0.87	61.7 (0.6)	0.3 (0.3)	0.9 (0.4)	1.0 (2.0)	2.0 (4.0)	1.5 (0.2)
		✓		✓	0.47	0.55	79.7 (0.5)	4.0 (0.8)	4.3 (0.8)	16.0 (2.0)	6.0 (3.0)	1.7 (0.2)
KKKS	✓		✓		0.38	0.33	84.0 (0.2)	6.6 (0.9)	6.6 (0.9)	4.0 (3.0)	4.0 (3.0)	1.6 (0.1)
		✓	✓		0.45	0.9	52.9 (0.3)	0.5 (0.3)	0.4 (0.2)	1.0 (1.0)	1.0 (1.0)	0.39 (0.06)
	✓			✓	0.12	0.47	87.5 (0.2)	5.0 (1.0)	5.0 (1.0)	4.0 (5.0)	5.0 (4.0)	3.1 (0.3)
		✓		✓	0.1	0.91	54.2 (0.5)	0.2 (0.3)	0.1 (0.2)	2.0 (2.0)	2.0 (2.0)	1.0 (0.2)

Table 4.18: Results of 2D optimization for 2011 $B^0_{d,s} \to K^0_S h^+ h'^-$ samples. In each row, the first 5 columns define the signal mode (The optimization designed to maximize it) in terms of decay mode, mother particle type(B_s or B^0), and K^0_S reconstruction (Long-Long or Down-Down). The next two columns denote the optimal cuts. The rest of the columns represent the efficiencies of signal, cross-feeds and combinatorial background species. The reported efficiencies and their corresponding uncertainty (in parenthesis) are in percentage.

Decay Mode	KS	Optimization	Signal_s	Signal_d	CrossFeed_d	CrossFeed_s
pipiKS	DD	Loose	0.760(0.002)	0.749(0.002)	0.085(0.0007)	0.0845(0.0007)
pipiKS	DD	Tight	0.399(0.002)	0.387(0.002)	0.0055(0.0003)	0.0052(0.0003)
pipiKS	LL	Loose	0.821(0.002)	0.823(0.002)	0.121(0.002)	0.125(0.002)
pipiKS	LL	Tight	0.476(0.003)	0.478(0.003)	0.0059(0.0005)	0.0054(0.0005)
KKKS	DD	Loose	0.758(0.002)	0.745(0.002)	0.047(0.0007)	0.049(0.0007)
KKKS	DD	Tight	0.466(0.002)	0.461(0.002)	0.0033(0.0002)	0.0031(0.0002)
KKKS	LL	Loose	0.829(0.002)	0.825(0.002)	0.057(0.001)	0.055(0.001)
KKKS	LL	Tight	0.549(0.003)	0.553(0.003)	0.0055(0.0004)	0.006(0.0005)

Table 4.19: Efficiency results based on the 2D optimized cuts for 2018 Monte Carlo samples. These MC samples consist of $B^0_{d,s} \to K^0_S\pi^+\pi^-$(resp. $K^0_S K^+K^-$) signal and their corresponding cross-feed samples related to the $B^0_{d,s} \to K^0_S K^\pm\pi^\mp$ samples whose π or K is misidentified.

Decay Mode	KS	Optimization	Signal_s	Signal_d	CrossFeed_d	CrossFeed_s
pipiKS	DD	Loose	0.743(0.001)	0.731(0.002)	0.086(0.0007)	0.086(0.0007)
pipiKS	DD	Tight	0.381(0.002)	0.360(0.002)	0.0023(0.0001)	0.0029(0.0002)
pipiKS	LL	Loose	0.816(0.002)	0.819(0.002)	0.103(0.001)	0.101(0.001)
pipiKS	LL	Tight	0.580(0.003)	0.580(0.003)	0.0116(0.0006)	0.0114(0.0006)
KKKS	DD	Loose	0.756(0.001)	0.748(0.002)	0.0438(0.0007)	0.0434(0.0006)
KKKS	DD	Tight	0.321(0.002)	0.308(0.002)	0.0003(6e-05)	0.00034(6e-05)
KKKS	LL	Loose	0.813(0.002)	0.815(0.002)	0.046(0.001)	0.046(0.001)
KKKS	LL	Tight	0.419(0.003)	0.425(0.003)	0.001(0.0002)	0.0009(0.0001)

Table 4.20: Efficiency results based on the 2D optimized cuts for 2017 Monte Carlo samples. These MC samples consist of $B^0_{d,s} \to K^0_S\pi^+\pi^-$(resp. $K^0_S K^+K^-$) signal and their corresponding cross-feed samples related to the $B^0_{d,s} \to K^0_S K^\pm\pi^\mp$ samples whose π or K is misidentified.

Decay Mode	KS	Optimization	Signal_s	Signal_d	CrossFeed_d	CrossFeed_s
pipiKS	DD	Loose	0.711(0.001)	0.706(0.002)	0.062(0.0007)	0.062(0.0007)
pipiKS	DD	Tight	0.408(0.002)	0.400(0.002)	0.0029(0.0002)	0.0036(0.0002)
pipiKS	LL	Loose	0.813(0.002)	0.817(0.002)	0.09(0.001)	0.091(0.001)
pipiKS	LL	Tight	0.532(0.003)	0.526(0.003)	0.006(0.0004)	0.0066(0.0004)
KKKS	DD	Loose	0.774(0.001)	0.770(0.001)	0.0365(0.0006)	0.0355(0.0006)
KKKS	DD	Tight	0.380(0.002)	0.378(0.002)	0.001(0.0001)	0.001(0.0001)
KKKS	LL	Loose	0.797(0.002)	0.792(0.002)	0.05(0.001)	0.051(0.001)
KKKS	LL	Tight	0.372(0.003)	0.382(0.003)	0.0014(0.0002)	0.0011(0.0002)

Table 4.21: Efficiency results based on the 2D optimized cuts for 2016 Monte Carlo samples. These MC samples consist of $B^0_{d,s} \to K^0_S\pi^+\pi^-$(resp. $K^0_S K^+K^-$) signal and their corresponding cross-feed samples related to the $B^0_{d,s} \to K^0_S K^\pm\pi^\mp$ samples whose π or K is misidentified.

Decay Mode	KS	Optimization	Signal_s	Signal_d	CrossFeed_d	CrossFeed_s
pipiKS	DD	Loose	0.777(0.001)	0.770(0.001)	0.0695(0.0007)	0.07(0.0007)
pipiKS	DD	Tight	0.397(0.002)	0.390(0.002)	0.0049(0.0003)	0.004(0.0002)
pipiKS	LL	Loose	0.859(0.002)	0.859(0.002)	0.109(0.002)	0.116(0.002)
pipiKS	LL	Tight	0.533(0.003)	0.533(0.003)	0.0032(0.0003)	0.0035(0.0004)
KKKS	DD	Loose	0.799(0.001)	0.795(0.001)	0.041(0.0007)	0.0434(0.0007)
KKKS	DD	Tight	0.363(0.002)	0.363(0.002)	0.0012(0.0001)	0.0012(0.0001)
KKKS	LL	Loose	0.796(0.002)	0.802(0.002)	0.0215(0.0007)	0.02(0.0007)
KKKS	LL	Tight	0.669(0.003)	0.672(0.003)	0.0134(0.0007)	0.0117(0.0006)

Table 4.22: Efficiency results based on the 2D optimized cuts for 2015 Monte Carlo samples. These MC samples consist of $B^0_{d,s} \to K^0_S\pi^+\pi^-$(resp. $K^0_S K^+K^-$) signal and their corresponding cross-feed samples related to the $B^0_{d,s} \to K^0_S K^\pm\pi^\mp$ samples whose π or K is misidentified.

Decay Mode	KS	Optimization	Signal_s	Signal_d	CrossFeed_d	CrossFeed_s
pipiKS	DD	Loose	0.834(0.003)	0.844(0.003)	0.228(0.003)	0.229(0.003)
pipiKS	DD	Tight	0.462(0.003)	0.462(0.004)	0.0096(0.0007)	0.0089(0.0006)
pipiKS	LL	Loose	0.905(0.003)	0.906(0.003)	0.224(0.004)	0.225(0.004)
pipiKS	LL	Tight	0.454(0.005)	0.462(0.005)	0.01(0.001)	0.007(0.0007)
KKKS	DD	Loose	0.848(0.003)	0.838(0.003)	0.115(0.002)	0.114(0.002)
KKKS	DD	Tight	0.447(0.003)	0.439(0.004)	0.0073(0.0006)	0.0073(0.0006)
KKKS	LL	Loose	0.818(0.004)	0.830(0.004)	0.092(0.003)	0.091(0.003)
KKKS	LL	Tight	0.631(0.005)	0.641(0.005)	0.027(0.002)	0.027(0.001)

Table 4.23: Efficiency results based on the 2D optimized cuts for 2012b Monte Carlo samples. These MC samples consist of $B^0_{d,s} \to K^0_S\pi^+\pi^-$(resp. $K^0_S K^+K^-$) signal and their corresponding cross-feed samples related to the $B^0_{d,s} \to K^0_S K^\pm\pi^\mp$ samples whose π or K is misidentified.

Decay Mode	KS	Optimization	Signal_s	Signal_d	CrossFeed_d	CrossFeed_s
pipiKS	DD	Loose	0.832(0.002)	0.823(0.002)	0.198(0.003)	0.207(0.002)
pipiKS	DD	Tight	0.401(0.003)	0.402(0.003)	0.0058(0.0005)	0.0056(0.0005)
pipiKS	LL	Loose	0.887(0.004)	0.894(0.003)	0.235(0.005)	0.244(0.005)
pipiKS	LL	Tight	0.573(0.006)	0.597(0.005)	0.019(0.001)	0.017(0.001)
KKKS	DD	Loose	0.844(0.002)	0.839(0.002)	0.113(0.002)	0.117(0.002)
KKKS	DD	Tight	0.524(0.003)	0.513(0.003)	0.0155(0.0007)	0.018(0.0007)
KKKS	LL	Loose	0.893(0.003)	0.893(0.004)	0.129(0.004)	0.143(0.004)
KKKS	LL	Tight	0.744(0.005)	0.729(0.005)	0.044(0.002)	0.054(0.003)

Table 4.24: Efficiency results based on the 2D optimized cuts for 2012a Monte Carlo samples. These MC samples consist of $B^0_{d,s} \to K^0_S\pi^+\pi^-$(resp. $K^0_S K^+K^-$) signal and their corresponding cross-feed samples related to the $B^0_{d,s} \to K^0_S K^\pm\pi^\mp$ samples whose π or K is misidentified.

Decay Mode	KS	Optimization	Signal_s	Signal_d	CrossFeed_d	CrossFeed_s
pipiKS	DD	Loose	0.873(0.002)	0.874(0.002)	0.238(0.003)	0.238(0.003)
pipiKS	DD	Tight	0.420(0.003)	0.400(0.003)	0.0067(0.0005)	0.0061(0.0005)
pipiKS	LL	Loose	0.869(0.003)	0.870(0.003)	0.2(0.004)	0.189(0.004)
pipiKS	LL	Tight	0.616(0.004)	0.608(0.005)	0.018(0.001)	0.016(0.001)
KKKS	DD	Loose	0.893(0.002)	0.890(0.002)	0.164(0.002)	0.168(0.002)
KKKS	DD	Tight	0.507(0.003)	0.507(0.003)	0.0076(0.0005)	0.0067(0.0005)
KKKS	LL	Loose	0.929(0.002)	0.926(0.002)	0.132(0.003)	0.131(0.003)
KKKS	LL	Tight	0.599(0.005)	0.607(0.005)	0.0105(0.0007)	0.009(0.0007)

Table 4.25: Efficiency results based on the 2D optimized cuts for 2011 Monte Carlo samples. These MC samples consist of $B^0_{d,s} \to K^0_S\pi^+\pi^-$(resp. $K^0_S K^+K^-$) signal and their corresponding cross-feed samples related to the $B^0_{d,s} \to K^0_S K^\pm\pi^\mp$ samples whose π or K is misidentified.

4.6 Mutual exclusivity

Our analysis consists of a simultaneous mass-fit of four different spectra of $K^0_S h^+ h'^-$ where $h^{(\prime)}$ is either π or K. In the case that each event in the $K^0_S h^+ h'^-$ selection enters a unique spectrum, it can be claimed that the selected samples is mutually exclusive. Since the difference between the spectra is caused by the $h^{(\prime)}$ particle identification, the mutual exclusiveness of the samples can be examined through the nature of h and h'. Given the PID XGBoost, one can check that mutual exclusivity is realized by applying the optimized PID cut

To do so, for each decay mode, next to the main trained PID model, we apply the model in which $h^{(\prime)}$ belongs to the other hadron type. Then, by requiring the optimal cut, we can determine how many events in each MC and Data samples passed both (MVA)PID cuts and can be assigned to more than one spectrum. The tables 4.26 - 4.28 has shown the result of mutual exclusivity evaluation for 2018 samples as the sample with the highest statistics. Note that in the tables, the cases in which no event passed the cuts (hence the sample is completely mutual exclusive) are not mentioned. This result shows that the considered samples have a statistical overlap up to $O(10^{-3})$ for the MC samples (with low statistics) and $O(10^{-5})$ for our data samples. The cross-contamination of the samples is therefore negligible and we will consider that mutual exclusivity of the samples is fully realised.

decay	Data	MC	DD	LL	cuts	Total entries	Passed	Efficiency
Bd2pipiKS		✓	✓		PID_pipi $\geq$ 0.4 & PID_Kpi $\geq$ 0.89	72762	54	0.0007(0.0001)
		✓	✓		PID_pipi $\geq$ 0.4 & PID_Kpi $\geq$ 0.89 & Topo $\geq$ 0.81	72762	50	0.0007(0.0001)
		✓	✓		PID_pipi $\geq$ 0.4 & PID_piK $\geq$ 0.92	72762	6	8e-05(3e-05)
		✓	✓		PID_pipi $\geq$ 0.4 & PID_piK $\geq$ 0.92 & Topo $\geq$ 0.81	72762	5	7e-05(3e-05)
	✓		✓		PID_pipi $\geq$ 0.4 & PID_Kpi $\geq$ 0.89	1833183	598	0.00033(1e-05)
	✓		✓		PID_pipi $\geq$ 0.4 & PID_Kpi $\geq$ 0.89 & Topo $\geq$ 0.81	1833183	52	2.8e-05(4e-06)
	✓		✓		PID_pipi $\geq$ 0.4 & PID_piK $\geq$ 0.92	1833183	107	5.8e-05(6e-06)
	✓		✓		PID_pipi $\geq$ 0.4 & PID_piK $\geq$ 0.92 & Topo $\geq$ 0.81	1833183	13	7e-06(2e-06)
		✓		✓	PID_pipi $\geq$ 0.28 & PID_Kpi $\geq$ 0.89	26749	132	0.0049(0.0004)
		✓		✓	PID_pipi $\geq$ 0.28 & PID_Kpi $\geq$ 0.89 & Topo $\geq$ 0.83	26749	125	0.0047(0.0004)
		✓		✓	PID_pipi $\geq$ 0.28 & PID_piK $\geq$ 0.92	26749	38	0.0014(0.0002)
		✓		✓	PID_pipi $\geq$ 0.28 & PID_piK $\geq$ 0.92 & Topo $\geq$ 0.83	26749	38	0.0014(0.0002)
	✓			✓	PID_pipi $\geq$ 0.28 & PID_Kpi $\geq$ 0.89	575493	123	0.00021(6e-05)
	✓			✓	PID_pipi $\geq$ 0.28 & PID_Kpi $\geq$ 0.89 & Topo $\geq$ 0.83	575493	82	0.00014(2e-05)
	✓			✓	PID_pipi $\geq$ 0.28 & PID_piK $\geq$ 0.92	575493	200	0.00035(2e-05)
	✓			✓	PID_pipi $\geq$ 0.28 & PID_piK $\geq$ 0.92 & Topo $\geq$ 0.83	575493	20	3.5e-05(8e-06)
Bs2pipiKS	✓		✓		PID_pipi $\geq$ 0.9 & PID_Kpi $\geq$ 0.69	1833183	48	2.6e-05(4e-06)
	✓		✓		PID_pipi $\geq$ 0.9 & PID_Kpi $\geq$ 0.69 & Topo $\geq$ 0.97	1833183	2	1.1e-06(8e-07)
	✓		✓		PID_pipi $\geq$ 0.9 & PID_piK $\geq$ 0.62	1833183	53	2.9e-05(4e-06)
		✓		✓	PID_pipi $\geq$ 0.91 & PID_piK $\geq$ 0.64	29197	2	7e-05(5e-05)
		✓		✓	PID_pipi $\geq$ 0.91 & PID_piK $\geq$ 0.64 & Topo $\geq$ 0.94	29197	2	7e-05(5e-05)
	✓			✓	PID_pipi $\geq$ 0.91 & PID_Kpi $\geq$ 0.59	575493	8	1.4e-05(5e-06)
	✓			✓	PID_pipi $\geq$ 0.91 & PID_piK $\geq$ 0.64	575493	130	0.00023(2e-05)
	✓			✓	PID_pipi $\geq$ 0.91 & PID_piK $\geq$ 0.64 & Topo $\geq$ 0.94	575493	4	7e-06(3e-06)

Table 4.26: Results of Mutual Exclusivity study for $B^0_{d,s} \to K^0_S\pi^+\pi^-$ samples.

decay	Data	MC	DD	LL	cuts	Total entries	Passed	Efficiency
Bd2KpiKS		✓	✓		PID_Kpi $\geq$ 0.89 & PID_pipi $\geq$ 0.4	38787	75	0.0019(0.0002)
		✓	✓		PID_Kpi $\geq$ 0.89 & PID_pipi $\geq$ 0.4 & Topo $\geq$ 0.89	38787	64	0.0017(0.0002)
	✓		✓		PID_Kpi $\geq$ 0.89 & PID_KK $\geq$ 0.64	2246635	137	6.1e-05(5e-06)
	✓		✓		PID_Kpi $\geq$ 0.89 & PID_KK $\geq$ 0.64 & Topo $\geq$ 0.89	2246635	2	9e-07(6e-07)
	✓		✓		PID_Kpi $\geq$ 0.89 & PID_pipi $\geq$ 0.4	2246635	701	0.00031(1e-05)
	✓		✓		PID_Kpi $\geq$ 0.89 & PID_pipi $\geq$ 0.4 & Topo $\geq$ 0.89	2246635	53	2.4e-05(3e-06)
		✓		✓	PID_Kpi $\geq$ 0.89 & PID_pipi $\geq$ 0.28	13901	265	0.019(0.001)
		✓		✓	PID_Kpi $\geq$ 0.89 & PID_pipi $\geq$ 0.28 & Topo $\geq$ 0.89	13901	220	0.016(0.001)
	✓			✓	PID_Kpi $\geq$ 0.89 & PID_KK $\geq$ 0.6	726305	4	6e-06(3e-06)
	✓			✓	PID_Kpi $\geq$ 0.89 & PID_pipi $\geq$ 0.28	726305	135	0.00019(5e-05)
	✓			✓	PID_Kpi $\geq$ 0.89 & PID_pipi $\geq$ 0.28 & Topo $\geq$ 0.89	726305	88	0.00012(1e-05)
Bs2KpiKS	✓		✓		PID_Kpi $\geq$ 0.69 & PID_pipi $\geq$ 0.9	2246635	53	2.4e-05(3e-06)
	✓		✓		PID_Kpi $\geq$ 0.69 & PID_pipi $\geq$ 0.9 & Topo $\geq$ 0.8	2246635	6	3e-06(1e-06)
	✓			✓	PID_Kpi $\geq$ 0.59 & PID_pipi $\geq$ 0.91	726305	10	1.4e-05(4e-06)

Table 4.27: Results of Mutual Exclusivity study for $B^0_{d,s} \to K^0_S\ K^+\pi^-$ samples.

decay	Data	MC	DD	LL	cuts	Total entries	Passed	Efficiency
Bd2KKKS		✓	✓		PID_KK $\geq$ 0.64 & PID_piK $\geq$ 0.92	71404	1	1e-05(1e-05)
	✓		✓		PID_KK $\geq$ 0.64 & PID_Kpi $\geq$ 0.89	2198411	17	8e-06(2e-06)
	✓		✓		PID_KK $\geq$ 0.64 & PID_Kpi $\geq$ 0.89 & Topo $\geq$ 0.73	2198411	1	5e-07(5e-07)
	✓			✓	PID_KK $\geq$ 0.6 & PID_Kpi $\geq$ 0.89	729881	6	8e-06(3e-06)

Table 4.28: Results of Mutual Exclusivity study for $B^0_{d,s} \to K^0_S\ K^+K^-$samples.

4.7 Background studies

The background structure for the charmless decays of $B^0_{d,s} \to K^0_S h^\pm h'^\mp$ consists of four main categories. The full description of these backgrounds were given in Ref. [137]. In summary, they are:

- Decays with identical final state which proceed through charm or charmonium states such as D^0, D^+, D^+_s, Λ^+_c, or J/ψ. These are removed with vetoes on the invariant masses of various two-body combinations. Table 4.29 shows the vetoes that we apply on both data and the simulated samples.

Inv. Mass	Charm mesons	Chamed Baryons	Chamonia
$K^0_S\pi^+\pi^-$	$D^\pm \to K^0_S\pi^\pm$, $D^\pm_s \to K^0_S\pi^\pm$, $D^\pm \to K^0_S K^\pm$, $D^\pm_s \to K^0_S K^\pm$ $D^0 \to K^\mp\pi^\pm$	Λ^+_c $(\overline{\Lambda}^-_c) \to K^0_S p\overline{p}$	$J/\psi \to \pi^+\pi^-$ $\chi_{c0} \to \pi^+\pi^-$
$K^0_S K^\pm\pi^\mp$	$D^\pm \to K^0_S\pi^\pm$, Dpm$\to K^0_S K^\pm$, $D^0 \to K^\mp\pi^\pm$	Λ^+_c $(\overline{\Lambda}^-_c) \to K^0_S p\overline{p}$	
$K^0_S K^+K^-$	$D^\pm \to K^0_S K^\pm$, $D^\pm_s \to K^0_S K^\pm$, $D^0 \to K^\mp\pi^\pm$	Λ^+_c $(\overline{\Lambda}^-_c) \to K^0_S p\overline{p}$	$J/\psi \to \pi^+\pi^-$ $\chi_{c0} \to \pi^+\pi^-$

Table 4.29: Summary of vetoes on charmed intermediary states. Vetoes on charmed mesons and baryons are defined as a $\pm 30 MeV/c^2$ window around the known value of the resonance mass. Vetoes on charmonia are defined as a $\pm 48 MeV/c^2$ window around the known value of the mass. Vetoes that contain a mis-identified particle are applied using the corresponding mass hypothesis.

- Partially reconstructed backgrounds, for which a pion or a photon is not reconstructed. These backgrounds populate mainly the left sideband of the B-candidate invariant-mass. They are studied using simulated samples and modelled in the mass fit.

- Cross feeds from other signal modes. As it is described in chapter 3, a misidentification may occur for our decay products and our candidate will be reconstructed in the wrong spectrum. These backgrounds are first reduced by using a dedicated PID tool and the remaining of their contribution must be explicitly modeled in the mass fit.

- Combinatorial background which consists of random combinations of tracks, mostly originating before any cut from the primary vertex. The multivariate selection described in section 4.4 is designed specifically to reduce this background as much as possible, while retaining a reasonable signal efficiency. The residual contribution from this background is also modeled in the mass fit.

Apart from the cross-feed background source, another possibility of mis-identification comes from the reconstruction of K^0_S. In this case, p tracks can be mis-identified as π

and therefore we have $\Lambda \to p\pi$ reconstructed as $K^0_S \to \pi\pi$. In order to see whether we need to model it in our mass fit or we can veto these events, we reconstruct the Λ events. Then, in order to determine the mass window of Λ, a simple Gaussian fit is applied on the reconstructed events. As a result, the mass window is determined to be $\|M_{p\pi} - 1115.5\| \geq 6.8\,\mathrm{MeV}/c^2$.

Thereafter, this mass cut is applied on the signal MC events to determine its efficiency on the data samples. Tables 4.30 and 4.31 are summarising the obtained values for 2018 and 2012b samples, respectively. Given its high efficiency, this new line is added to the veto cuts of the analysis.

dkmode	BType		KSreco		Lambda veto Efficiency(%)
	Bd	Bs	DD	LL	
$\pi^+\pi^-$		✓	✓		0.9792(0.0005)
		✓		✓	0.9827(0.0008)
	✓		✓		0.9794(0.0005)
	✓			✓	0.9832(0.0008)
K^+K^-		✓	✓		0.9796(0.0005)
		✓		✓	0.9829(0.0008)
	✓		✓		0.9797(0.0005)
	✓			✓	0.9828(0.0008)
$K^+\pi^-$		✓	✓		0.9786(0.0007)
		✓		✓	0.984(0.001)
	✓		✓		0.9804(0.0007)
	✓			✓	0.982(0.001)
π^+K^-		✓	✓		0.9798(0.0007)
		✓		✓	0.983(0.001)
	✓		✓		0.9801(0.0007)
	✓			✓	0.984(0.001)

Table 4.30: Table of Efficiency for Λ veto for 2018 samples.

dkmode	BType		KSreco		Lambda veto Efficiency(%)
	Bd	Bs	DD	LL	
$\pi^+\pi^-$		✓	✓		0.982(0.0009)
		✓		✓	0.983(0.001)
	✓		✓		0.982(0.001)
	✓			✓	0.983(0.001)
K^+K^-		✓	✓		0.9817(0.0009)
		✓		✓	0.988(0.001)
	✓		✓		0.981(0.001)
	✓			✓	0.985(0.001)
$K^+\pi^-$		✓	✓		0.983(0.001)
		✓		✓	0.985(0.002)
	✓		✓		0.983(0.001)
	✓			✓	0.985(0.002)
π^+K^-		✓	✓		0.98(0.001)
		✓		✓	0.989(0.002)
	✓		✓		0.983(0.001)
	✓			✓	0.986(0.002)

Table 4.31: Table of Efficiency for Λ veto for 2012b samples.

Chapter 5

Efficiencies and systematic study $B^0_{d,s} \to K^0_S h^\pm h'^\mp$

In previous chapters, the requirements such as stripping, triggering, vetoes and preselection cuts were elaborated. In addition, the strategies to fight against two most important types of backgrounds were explained and the MVA tools which were used for this purpose were briefly discussed.

These strategies were implemented in a way to provide the best working point for branching fraction studies while providing the same tools for further studies of Dalitz plot Analysis (DPA) and $\mathcal{CP}$ measurement of $B^0_{d,s} \to K^0_S \pi^+ \pi^-$ and $B^0 \to K^0_S K^+ K^-$. As each of these requirements and selections has an impact on the Dalitz plane, we should study how these patterns affect the efficiencies.

Furthermore, these efficiencies are evaluated by using the MC samples. As we discussed before, the MC might not be able to mimic the data behavior perfectly and need to be corrected with respect to the calibration samples.

Finally, due to the methods which are used for efficiency correction and determination, we assign one or various sources of systematic uncertainties to the determined values of efficiency.

In this chapter first we introduce these efficiency patterns in the Square Dalitz plane (sqDP) and then we determine their average values. Then, we explain the systematic studies regarding each sources of bias to our analysis.

5.1 Signal Efficiency patterns over the Dalitz plane

In an ideal world, the efficiency of signal events is flat across the Dalitz plane and events would be selected equally from any part of the phase space. However, selection cuts, geometrical acceptance and trigger efficiency decreased the number of events in certain regions of the Dalitz plane more than other regions. As a result, considering such non-uniformity is crucial when we fit to data, because it causes a distortion to the distribution of signal events across the Dalitz plane. It is decided to study and analyze the contributions

from distinct sources independently in order to have a better understanding of the efficiency and its fluctuation across the phase space of the decay. Therefore the total efficiency ϵ^{tot} is given by,

$$\epsilon^{\text{tot}} = \epsilon^{\text{geom}} \times \epsilon^{\text{sel|geom}} \times \epsilon^{\text{PID|Sel\&geom}} \tag{5.1}$$

where,

- ϵ^{geom} is the geometrical and generator level cut efficiency. This efficiency is determined by using MC samples and will be discussed in Sec 5.1.1.
- $\epsilon^{\text{sel|geom}}$ is the selection efficiency which consists of the trigger, stripping and offline selection. This efficiency is also determined from the MC sample. Note that at this level, MC samples require to be corrected regarding to the discrepancies between the data and MC for tracking and trigger efficiencies. This part is explained in details in Sec 5.1.2.
- $\epsilon^{\text{PID|Sel\&geom}}$ is the efficiency of particle identification. This one is also determined by using the output of the PID tool (which was discussed in chapter 3) on MC samples and its efficiency pattern will be explained in Sec 5.1.3.

Another advantage of this individual study of efficiency is that it enables us to investigate the possible systematic biases. This study will also be presented in Sec 5.2. Although we split these individual sources of efficiency, one should take into account that in our further applications (such as Dalitz plots or measurement of branching fractions) the only parameter which will be used is the total efficiency which is deduced by multiplication of the corresponding value of each contribution at the given point in Dalitz plane.

5.1.1 Acceptance of the Generator level cut

In order to save the computational resources utilized in each analysis simulation, a set of cuts is applied to retain the events whose final particles are (generated) inside the detector acceptance. In this analysis, the tightest generator level cuts used in LHCb are employed. This ensemble of cuts is presented in table 4.5. To model this acceptance, one should consider a θ parameter which defines the angle between each track and the (z) axes and take into account that $\theta \in [0.01, 0.4]$ rad. Section 2.7 explains the principles of the generator level cuts.

Normally we measure the geometrical efficiency, ϵ^{geom} from generator-level MC samples created without any cuts on the daughter particles, (Gauss configured with `NoCuts` option). Here, using the Laura++ [138] we generate events approximately flat in the sqDP. Then, using the fraction of these events for which all daughter tracks passed these cuts, we determine this efficiency. One should consider here that we do not need to distinguish between triggers or the K^0_S Long-Long and Down-Down categories, because this efficiency is solely determined by the detector geometry and kinematics of the B^0. However, because the B^0 kinematics differ among years of data taking due to the difference in beam energy, it

is important to treat each year individually. Fig 5.1 represent the ϵ^{geom} for $B^0 \to K^0_S\pi^+\pi^-$ samples for 2012b and 2018 as an instance of RunI and RunII.

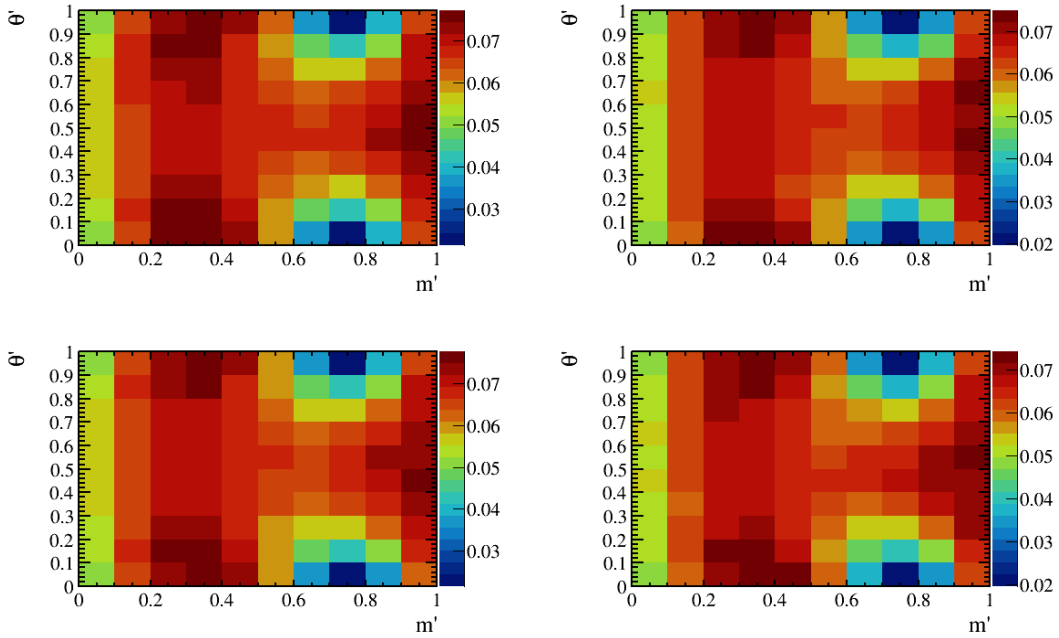

Figure 5.1: *Right(Left)* ϵ^{geom} *across the DP for 2018(2012b)* $B^0 \to K^0_S\pi^+\pi^-$ *samples. Top (Low) row is related to the Up (Down) magnetic separations.*

5.1.2 Selection Efficiency

To determine selection efficiency, whose requirements consist of trigger, stripping and topological MVA (derived by 2D optimization) cuts; the full simulation MC samples are generated with `sqDalitz,TightCut` options and these selection requirements are applied on it. Since both stripping and multivariate topological selections were defined with the goal of minimal efficiency variation across the Dalitz plane, the most significant contribution to the stiff variation of selection efficiency comes from the trigger selection.

One should take into account that other than what is discussed for the PID correction, there are other sources of discrepancies between MC and data samples related to the tracking and L0 trigger which are discussed in the following.

5.1.2.1 Data/MC tracking efficiency correction

Following the conventional technique as stated in [139], tracking corrections are made to the selection efficiency to account for the discrepancies in long tracking efficiency for MC and data. The reconstruction efficiency map, for the long tracks, according to the

calibration data sample is made by Tracking group. This map, which is also known as tracking correction table is made in two bins of pseudorapidity η(1.9-3.2, 3.2-4.9) and five bins of momentum p (5-10, 10–20, 20-40, 40-100, 100-200 GeV/c^2).

In order to produce the Dalitz plane correction map, first the MC events which the ensemble of cuts of the selection but the PID are selected. The reason to exempt the PID cut is that the PID has many corrections per itself and since PID depends on the kinematics (and hence tracking reconstruction efficiencies), it is better to factor it out and the tracking efficiency it corrected before getting to the PID. Then for each event the corresponding p, η, m' and θ' of each B^0-daughter track (except K^0_S daughters) are determined. According to p and η, an efficiency value is selected from tracking correction table. Then using the corresponding m' and θ' this efficiency is associated to a certain bin of sqDP and by multiplying the existing values in that bin, we provide its weight that can be used as a correction factor.

In Fig. 5.2, the total tracking efficiency correction corresponding to 2018 and 2012b samples, which are calculated by multiplying the corrections for each track event by event, is given together with their associated uncertainty.

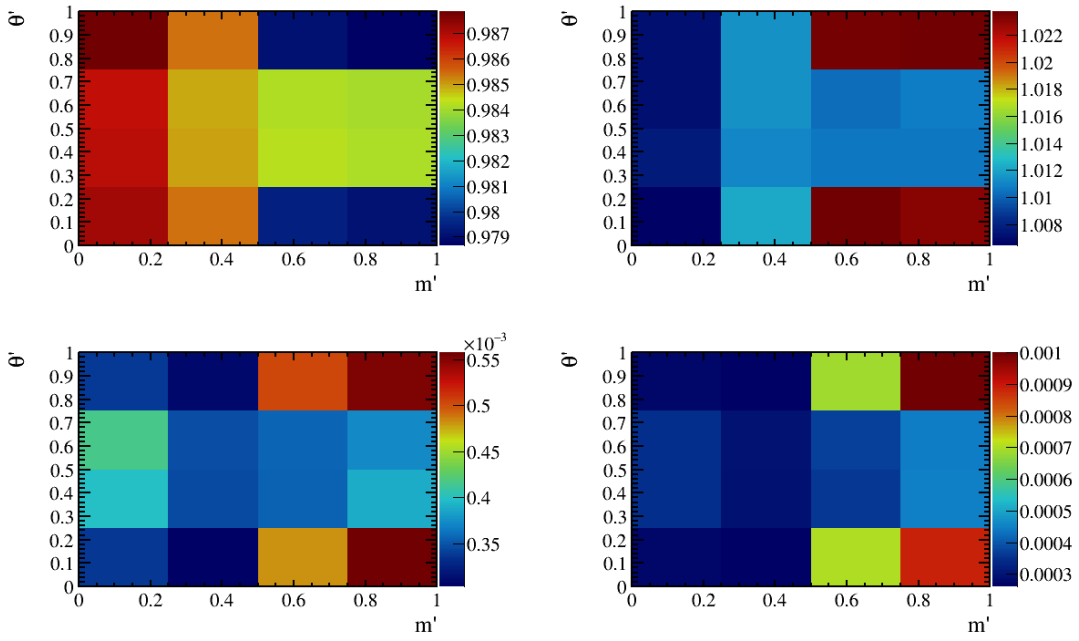

Figure 5.2: *Right(Left) long tracks correction across the Dalitz plane for 2018(2012b) $B^0 \to K^0_S\pi^+\pi^-$ samples. Top and Low rows are related to the corrected efficiency and their systematic biases, respectively.*

5.1.2.2 Data/MC L0Hadron_TOS trigger efficiency correction

At this level, a strategy is set to tackle the observed differences between the L0Hadron_TOS trigger efficiency of MC and data samples and provide an efficiency correction according to that strategy. To do so, one should split each samples into TOS and TIS&!TOS sub-samples.

For the RunI samples, we pursue the standard method to obtain the L0Hadron_TOS efficiency as it is indicated in Ref [140]. Using this method, one can find the relevant efficiency on data rather than data/MC corrections. The data efficiency is calculated using calibration data samples for each track, which are based on the particle type, magnet polarity, calorimeter hit region, and amount of deposited transverse energy. This can be separately evaluated for each individual track among the four tracks of the B^0 simulated candidates which passes the L0Hadron_TOS. To do so, we assign a probability to the possibility of firing trigger for each cluster i with respect to its transverse energy $E_{T,i}$ as $p(E_{T,i})$. As a result, the total efficiency of L0Hadron_TOS can be defined as:

$$\epsilon_{\text{data}}^{\text{TOS}} = 1 - \prod_{i}^{N_{\text{daught}}} (1 - p(E_{T,i})) \tag{5.2}$$

while the efficiencies for trigger of L0Hadron_TIS & !L0Hadron_TOS is,

$$\epsilon_{\text{data}}^{\text{TIS\&!TOS}} = \prod_{i}^{N_{\text{daught}}} (1 - p(E_{T,i})). \tag{5.3}$$

Therefore, the efficiency of B^0 is calculated as the probability whether at least one of the four products of its decay passes the L0Hadron_TOS requirement. Then by evaluating the average efficiency per each bin of the SqDP, we can provide such efficiency distribution for the data.

Now, to determine data/MC correction, we evaluate the efficiency of MC and then their ratio determines the corrections. It is obvious that the relevant distribution for the MC samples can be determined by the ratio of the events which pass the L0Hadron_TIS & L0Hadron_TOS requirement to those were obtained by applying the L0Hadron_TIS solely. Furthermore, we can also provide the correction for the complementary part of the events which belongs to the category of L0Hadron_TIS & !L0Hadron_TOS. For these candidates, the data efficiency can be calculated by determining the probability for the condition in which none of the tracks have passed the L0Hadron_TOS requirements (see Eq.5.3). Finally, in order to provide the correction factor, we have,

$$f_{\text{L0Corr}}^{\text{TOS(TIS\&!TOS)}} = \frac{\epsilon_{\text{data}}^{\text{TOS(TIS\&!TOS)}}}{\epsilon_{\text{MC}}^{\text{TOS(TIS\&!TOS)}}} \tag{5.4}$$

in which $\epsilon_{\text{MC}}^{\text{TOS(TIS\&!TOS)}}$ is the corresponding efficiency for the MC samples.

For the RunII more accurate tables have been added to account for the effects that were neglected when creating and using the RunI tables, such as the overlap between the

tracks, occupancy and calibration effects. These tables were made with respect to the year, magnet polarity, charge and particle species of the samples. Moreover, for each sample, there is one efficiency table as a function of transverse energy per HCAL region (inner or outer) and in order to provide these tables for the π and K, the D^* calibration samples have been used. Further details about these tables can be found in Ref [141].

To provide L0 correction for our RunII samples, we had one major problem. Due to the new stripping for these samples, the HLT lines have already applied on our samples, and we could not provide the correct version of the L0 correction using the MC sample which is already triggered. In order to tackle that problem, we used a set of unfiltered MC samples for which the stripping does not contain the HLT lines. For these unfiltered MC the stripping version is different, however since the stripping were designed to be flat in the SqDP, then using these MC samples causes negligible variation with respect to the main.

Figs.5.3 and 5.4 show the distribution of L0 correction factors for `L0Hadron_TOS` and `L0Hadron_TIS & !L0Hadron_TOS` for 2018 and 2012b $K^0_S\pi^+\pi^-$ Down-Down samples.

5.1.3 PID efficiency

In order to determine PID efficiency $\epsilon^{\text{PID|sel\&geom}}$, we are using the outputs of the PID MVA tool on the signal MC samples. We have discussed in Chapter 3 on how our variables are corrected using `PIDCorr` package and how we train our MVA tool. Here by applying the PID requirement which is devised by the 2D optimization method (working point) we will derive the PID efficiency over the SqDP. Note that the denominator of efficiency is derived from the MC samples which already passed the selection and LHCb acceptance requirements. Thanks to the `PIDCorr` method that we used for PID correction, we can assign multiple sources of systematic, which will be described in details in Sec.5.2.2

5.1.4 Total efficiency

The total efficiency can be evaluated by the product of all individual contributions, that are discussed formerly. Fig. 5.6 and 5.5 show these maps next to their corresponding statistical uncertainties for 2012b and 2018 samples, respectively.

5.2 Systematic study of efficiencies

In this section, we will study the determination of systematic uncertainties related to the signal efficiency across the sqDalitz plane. It has been mentioned that one of the main reasons behind splitting the signal efficiency into individual sources is that we can determine their corresponding systematic and then combine in quadrature to produce the systematic related to the signal efficiencies across the sqDP.

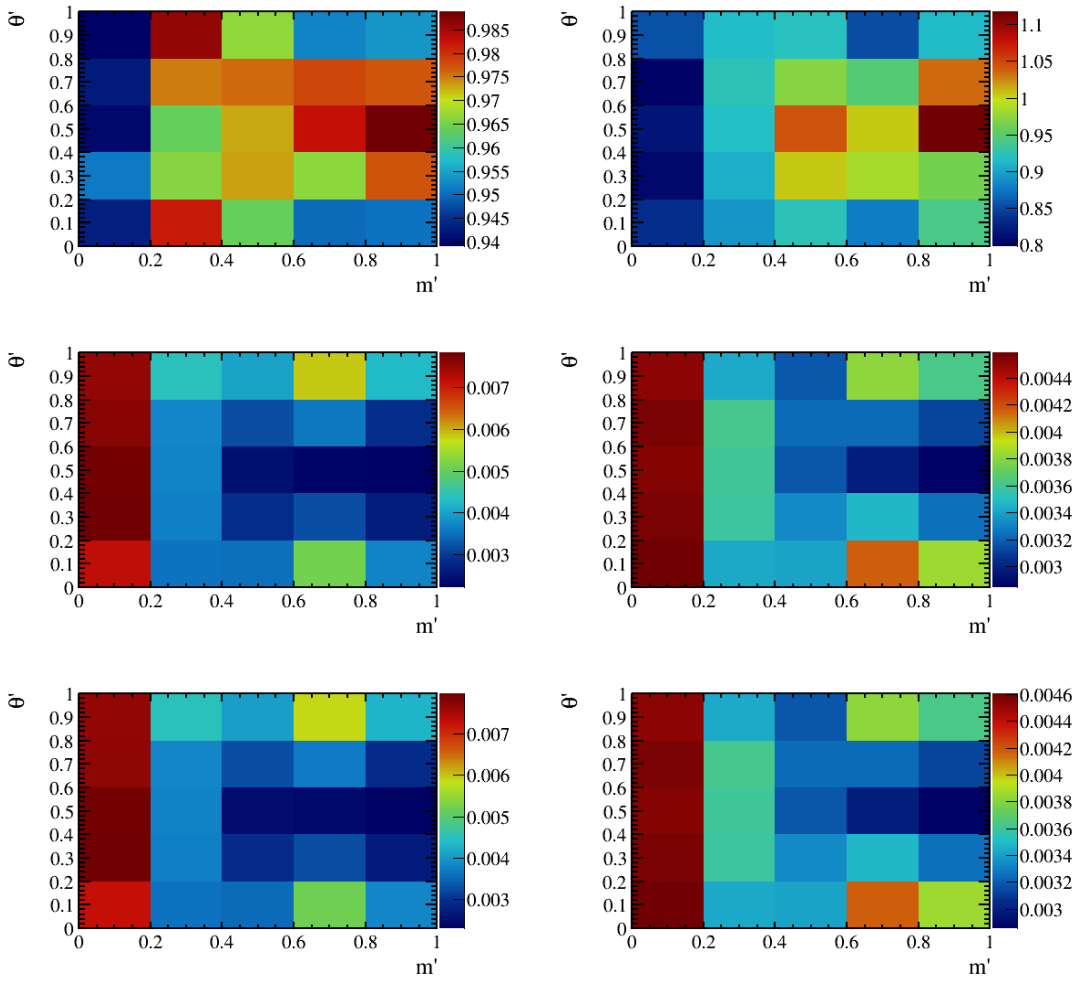

Figure 5.3: *Right(Left)* $\epsilon_{data}^{\text{L0TOS|sel\&geom}}/\epsilon_{MC}^{\text{L0TOS|sel\&geom}}$ *across the DP for 2018(2012b)* $B^0 \to K_S^0\pi^+\pi^-$ *samples and for the DD* K_S^0 *reconstruction and downward magnetic direction. Top, middle and Low rows are related to the corrected efficiency and the upper and lower uncertainties for the histogram bins, respectively.*

5.2.1 Selection efficiencies

5.2.1.1 Tracking Efficiencies

The LHCb tracking performance group advises to apply a relative systematic uncertainty on the tracking corrections of 0.4% and 0.8% for the RunI and RunII, respectively. This systematic is related to the fraction of hadrons that undergoes hadronic interaction before the T station ($z \simeq 9000mm$). Further details about the `TrackCalib` package and the systematic determination are given in [139] and [142]. The Fig.5.7 displays this systematic pattern over the sqDP.

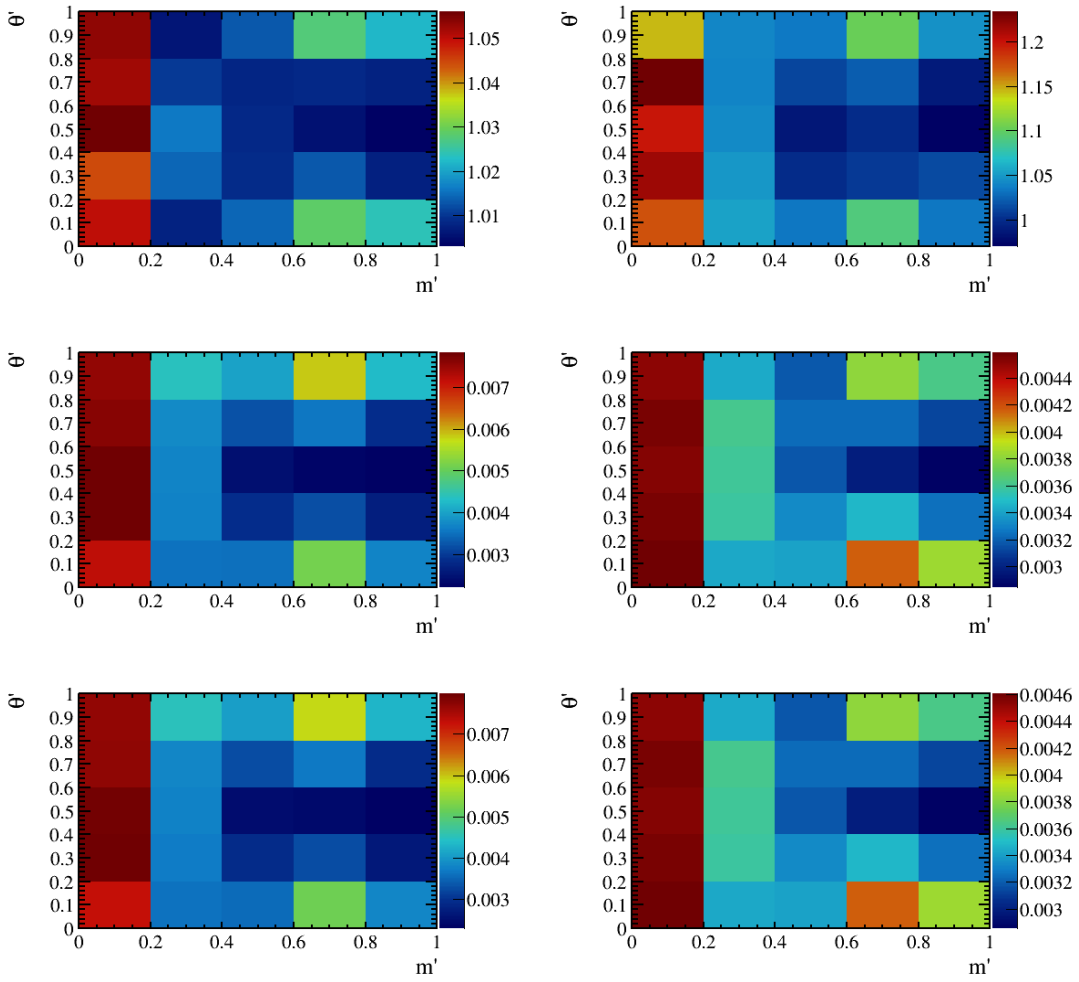

Figure 5.4: *Right(Left)* $\epsilon^{\text{!L0TOS|sel\&geom}}_{data}/\epsilon^{\text{!L0TOS|sel\&geom}}_{MC}$ *across the DP for 2018(2012b)* $B^0 \to K^0_S\pi^+\pi^-$ *samples and for the DD* K^0_S *reconstruction and downward magnetic direction. Top, middle and Low rows are related to the corrected efficiency and the upper and lower uncertainties for the histogram bins, respectively.*

5.2.1.2 Triggering

The L0 trigger efficiencies were calculated in Sec.5.1.2.2. The L0 trigger corrections are provided with dedicated uncertainties. These uncertainties have been propagated to the efficiency determination to determine the high and lower bounds for the estimated error in each bins of sqDP. The Figures 5.8 and 5.9 show the systematic uncertainty corresponding to the L0 correction for both `TOS` and `!TOS` event categories.

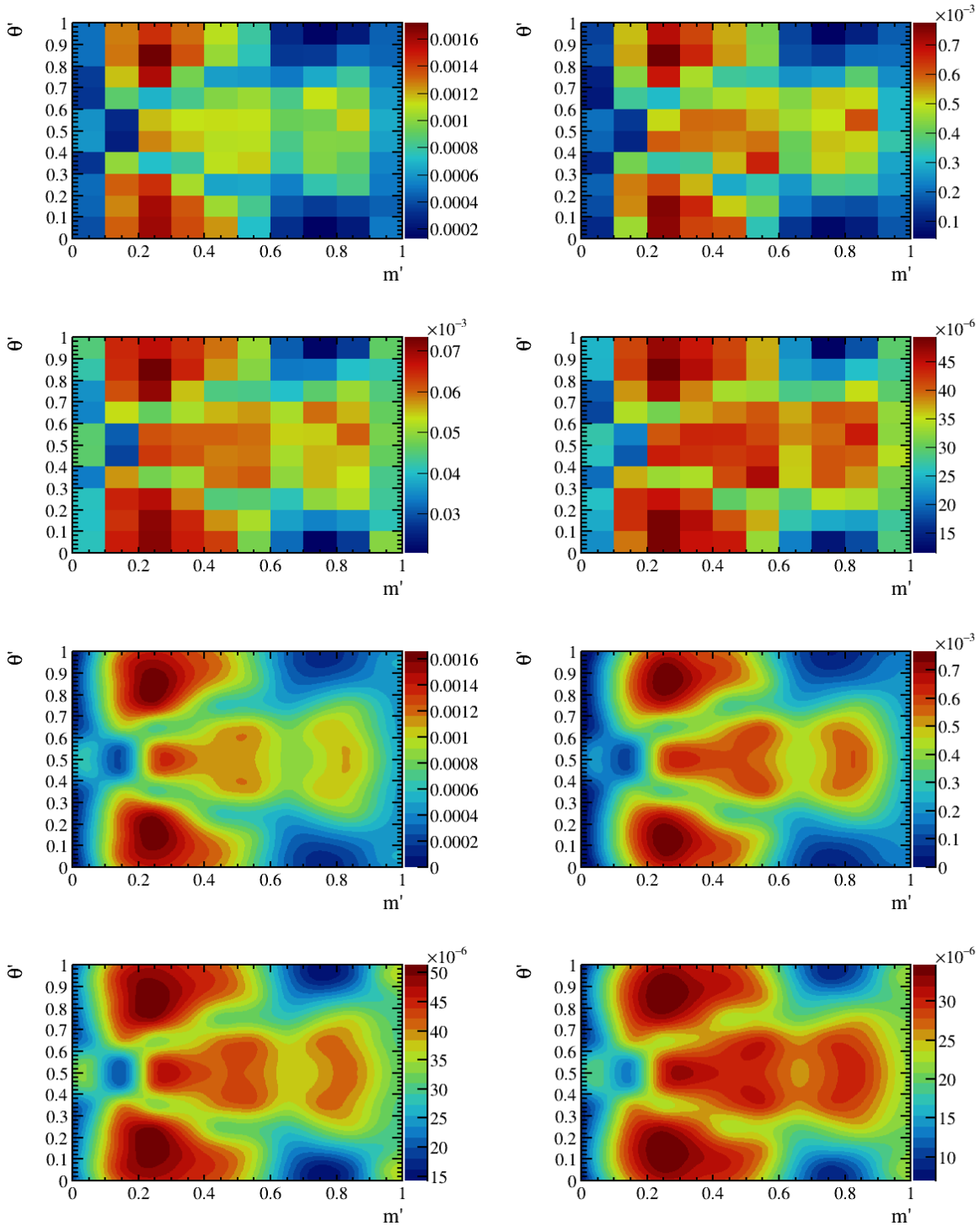

Figure 5.5: Left(Right) column represents ϵ^{tot} across the Dalitz plane for Loose (Tight) selection of 2018 $B^0 \to K^0_S \pi^+ \pi^-$ samples for the DD K^0_S reconstruction and downward magnetic direction. The first and third rows denote the total efficiency in the binned and smoothed format, and the second and fourth rows denote the statistical uncertainty in the binned and smoothed format, respectively. The binned patterns were smoothed using the 2D cubic splined techniques

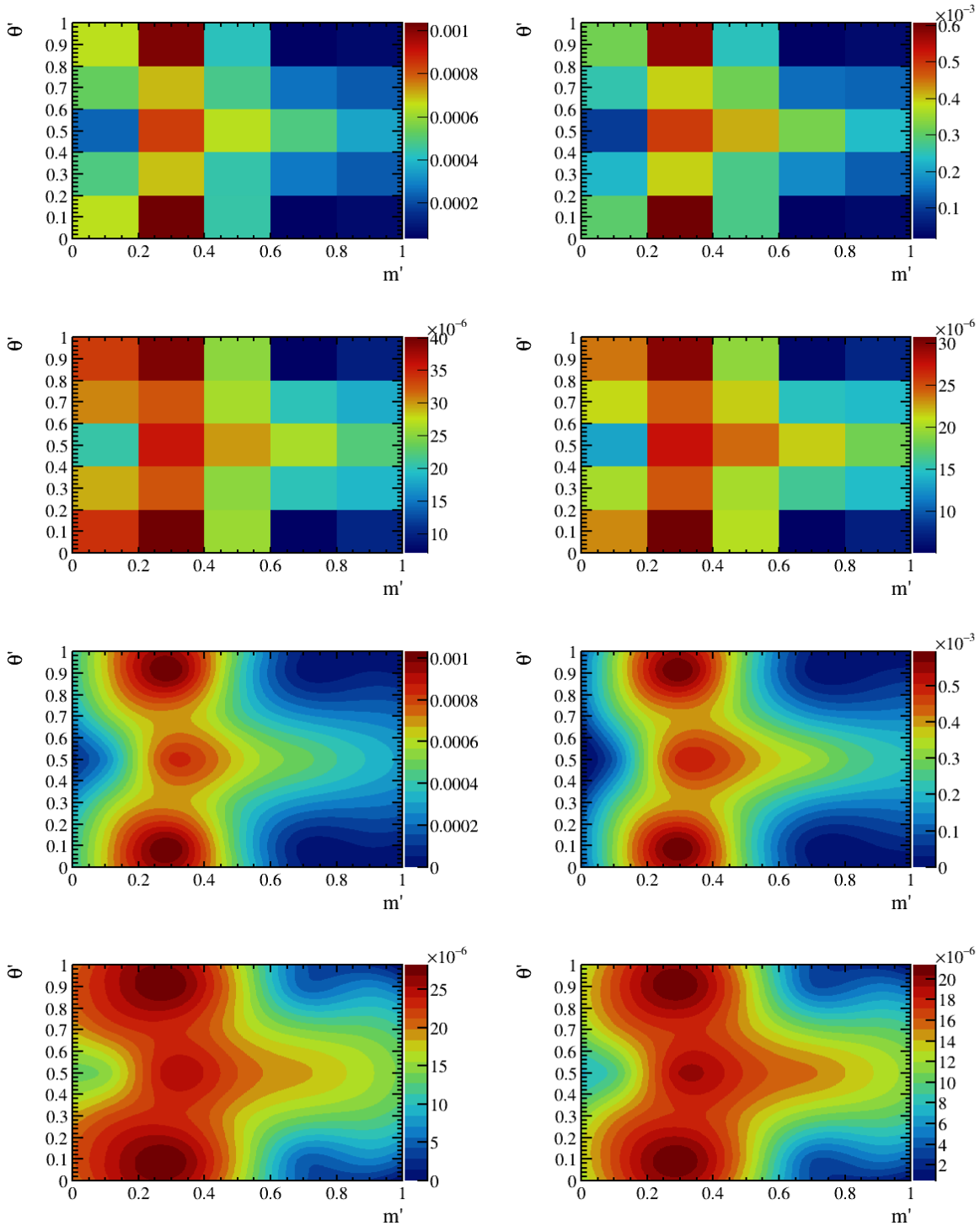

Figure 5.6: Left(Right) column represents ϵ^{tot} across the Dalitz plane for Loose (Tight) selection of 2012b $B^0 \to K^0_S \pi^+ \pi^-$ samples for the DD K^0_S reconstruction and downward magnetic direction. The first and third rows denote the total efficiency in the binned and smoothed format, and the second and fourth rows denote the statistical uncertainty in the binned and smoothed format, respectively. The binned patterns were smoothed using the 2D cubic splined techniques

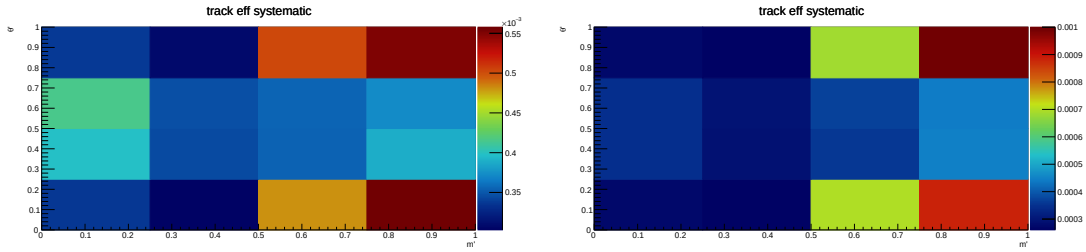

Figure 5.7: *Right(Left) Systematic corresponding to the Tracking correction across the DP for 2018(2012b)* $B^0 \to K^0_S\pi^+\pi^-$ *samples.*

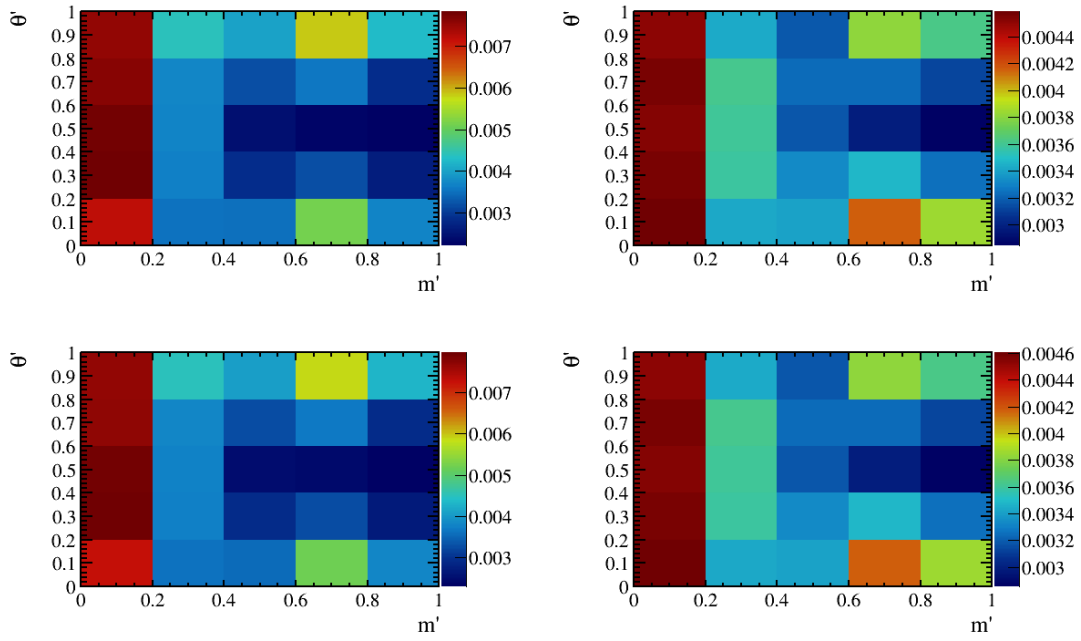

Figure 5.8: *Right(Left resp.): The systematic uncertainty related to the* $\epsilon^{\text{L0TOS|sel\&geom}}_{data}$ *determination across the DP for 2018(2012b resp.)* $B^0 \to K^0_S\pi^+\pi^-$ *samples and for the DD* K^0_S *reconstruction and downward magnetic direction. the Top and Low rows show upper and lower bounds of the uncertainty, respectively.*

5.2.2 PID correction and PID efficiencies

So far, the method of PID correction using the `PIDCorr` package was explained in details (see Chapter 3). The most important effects that can cause biases to the correction method are divided into two main categories:

- 1) PID MC sampling: Since `PIDCorr` uses the MC samples that are much smaller than the data calibration samples, this finite statistics causes a source of systematic.

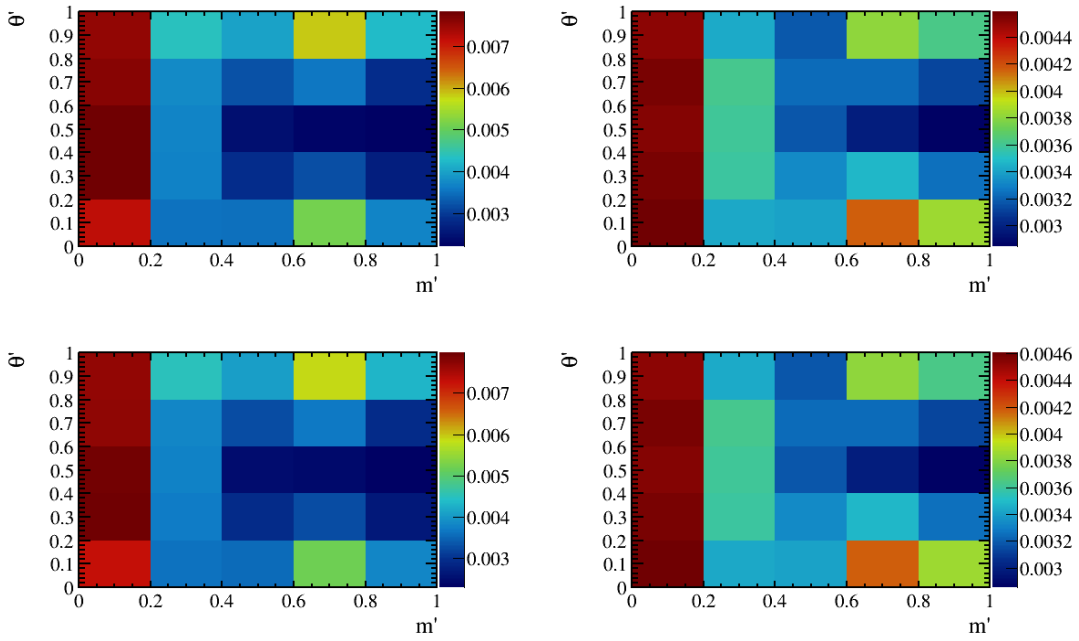

Figure 5.9: *Right(Left resp.): The systematic of* $\epsilon_{data}^{\text{!L0TOS|sel\&geom}}$ *determination across the DP for 2018(2012b resp.)* $B^0 \to K^0_S\pi^+\pi^-$ *samples and for the DD* K^0_S *reconstruction and downward magnetic direction. The upper and lower bounds of of this systematic are shown in the Top and Low rows, respectively.*

- 2)PID control sample parametrization: Since `PIDCorr` is an unbinned correction method, it uses the Kernel density instead of the histograms. Thus, any variation in this kernel can produce another PID response, and thus it is considered as a further source of systematic uncertainties.

The bias related to first source, can be determined by using different PID templates, produced by bootstrapped [143] samples, centrally generated by the PID group and accounting for the year of data taking and magnet polarities. In order to determine the corresponding systematic, first the PID variables of MC samples are corrected with respect to each of those samples. Then, mass vetoes, trigger, preselection and MVA models are applied to them and the $\epsilon_{bootstrapped}^{\text{PID|sel\&geom}}$ are determined for each of the corrected samples. Thereafter, a set of systematic $\{\delta\epsilon_{l,ij}^{\text{PID|sel\&geom}} | l = 1, .., N\}$ is provided by calculating the difference between efficiency of each of the N bootstrapped samples and the main one for the bin (i, j) of the sqDP. Now, the systematic related to this source for each bin of the sqDP is derived as,

$$\delta\epsilon_{MCCalib,i}^{\text{PID|sel\&geom}} = \frac{|\max_{\{l\in N\}}\{\delta\epsilon_{l,ij}^{\text{PID|sel\&geom}}\}| + |\min_{\{l\in N\}}\{\delta\epsilon_{l,ij}^{\text{PID|sel\&geom}}\}|}{2} \tag{5.5}$$

where $\max_{\{l\in N\}}\{\delta\epsilon_{l,i}^{\text{PID|sel\&geom}}\}$ and $\min_{\{l\in N\}}\{\delta\epsilon_{l,ij}^{\text{PID|sel\&geom}}\}$ are maximum and minimum

values of aforementioned set in the bin (i, j) of sqDP. The Fig.5.10 shows this pattern over the sqDP for $B^0 \to K^0_S \pi^+ \pi^-$ samples of 2018 and 2012b data taking periods.

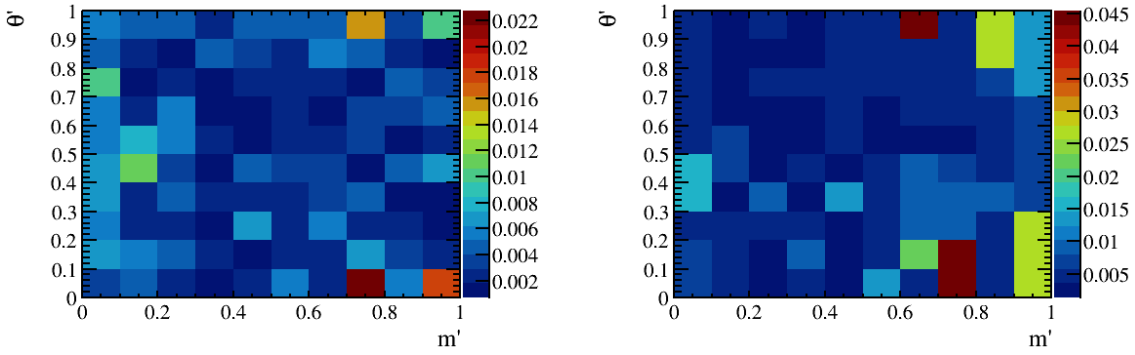

Figure 5.10: *Right(Left) the systematic of* $\epsilon^{\text{PID|sel\&geom}}_{MCCalib}$ *across the sqDP for 2018(2012b)* $B^0 \to K^0_S \pi^+ \pi^-$ *samples and for the DD* K^0_S *reconstruction and downward magnetic direction.*

The second source of systematic uncertainty is estimated by first producing a template prepared with a modified kernel. Using this template thePID correction can be performed on our MC samples and apply experimental requirements (trigger, mass vetoes and preselection cuts) to them. Then same as above, MVA models are applied to this new corrected MC samples, and we can derive the $\epsilon^{\text{PID|sel\&geom}}$. At this stage, the difference between the efficiency that comes from the main template correction and the current one determines the influence of Kernel Density Estimation procedure and its corresponding bias. The Fig.5.11 showed relevant systematic across the sqDP.

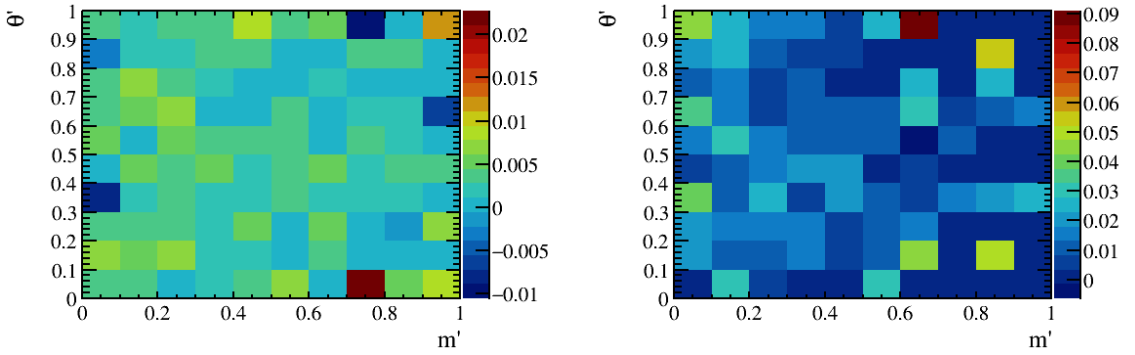

Figure 5.11: *Left(Right resp.) The systematic of* $\epsilon^{\text{PID|sel\&geom}}_{\text{ControlSample}}$ *determination across the DP for 2018(2012b resp.)* $B^0 \to K^0_S \pi^+ \pi^-$ *samples and for the DD* K^0_S *reconstruction and downward magnetic direction are shown.*

5.2.3 binning scheme

In the measurement of branching fractions of $K^0_S h^+ h'^-$ analysis it will be needed to average the efficiency over the bins of sqDP and we will come back to it in the next chapter. By anticipating the determination of average efficiencies, on top of the selection and PID systematic uncertainties, there is another source of systematic that has to be considered further. This is the choice of the binning and it can be determined by varying the binning across each of the θ' and m' axes of sqDP. Each axis is re-binned from 2 to 10 bins; and the amplitude of the average efficiency variation over the sqDP determines the level of uncertainty which is induced by the variation of binning scheme. Although the finer granularity in the binning will result into more accurate estimation of the efficiency in the data, the statistics of our MC samples does not allow us to go higher than 10×10 binning, to avoid empty bins. This choice of the binning will come with an uncertainty at the moment of determining the actual average efficiency weighted by the Dalitz plane. The only thing to say here is that several maps have been prepared in view of determining this efficiency that will happen in the latest stage of branching fraction measurements.

Chapter 6

Efficiency, mass fit and their correspondence

The results presented in the former chapters were mostly focused on the training the multivariate analysis tools (XGBoost classifier) and the determination of the efficiencies of the designed set of cuts, such as trigger, stripping and offline selection (based on the optimization which is performed on the output of trained MVA tools). These studies, designs and outputs are deduced by using Monte Carlo samples.

Through this chapter, after applying the devised optimal cuts (Topological and PID) to the MC and real data and performing the simultaneous mass-fit, we study how the novel method (training of two MVA tools and 2d optimization) results into the enhancement compared to previous analyses [132, 134]. Then, using final results and efficiency map, we verify the consistency between the efficiencies and the mass-fit results. The mass-fit technique has been introduced in the publication [20] and further developed for this update by the Paris collaborators [144]. The essential ingredients of the mass fitter will be shortly described.

6.1 MassFit

One of the most common method in fitting parameters of the model to the data is Maximum-likelihood estimation. This method enabled us to create a model for a variable x through definition of a function $f(x, \theta)$ in which θ is the parameter of the model. Therefore, considering N measurements for our variable x_i, the likelihood function associated to the defined model is

$$\mathcal{L}(\theta) = \prod_{i=1}^{N} f(x_i, \theta) \tag{6.1}$$

Now by maximizing this likelihood, the estimators of the model parameters $\hat{\theta}$ can be derived. For the sake of simplicity, it is mostly preferred to implement the logarithm of likelihood and determine the estimator by maximizing $\mathbf{L}(\theta) = \ln \mathcal{L}(\theta)$ Therefore, by considering

- N_i as number of events corresponding to each species,
- $N_{0,i}$ as the observed number of event parameter for a Poisson distribution,

the log-likelihood can be easily extended as follows,

$$-\mathbf{L}(\theta; N_i) = N + \sum_{i=1}^{N_0} \ln f(x_i, \theta; N_i) \tag{6.2}$$

where $N = \sum_i N_i$ and $N_0 = \sum_i N_{0,i}$. Further detail of this extension is mentioned in Ref. [145].

It is necessary for our study to constrain some of the parameters of the likelihood model. This is realised by extending the likelihood with penalties following a Gaussian expression, $\mathcal{L}(\theta) \times \exp(-\frac{(\theta-\theta_0)^2}{2\sigma_\theta^2})$ in which we consider a central value for our estimator θ_0 and its corresponding uncertainty σ_θ

In the following of this section, we briefly discuss the models which are used in our mass fit. The mass fit consists of an unbinned extended maximum likelihood fit to the invariant-mass distribution (models) of $K^0_S\pi^+\pi^-$, $K^0_S K^\pm\pi^\mp$ and $K^0_S K^+K^-$ to determine various modes' yields. To do so, the following remarks are considered in this simultaneous fit:

- Signal models are determined from corresponding simulated samples.
- Partially-reconstructed background are parameterized using fast MC samples (for further details see chapter 3 of reference [145]). Moreover, their yields are constrained by signal yields, relative branching fraction and adequate efficiencies. Further details of it is mentioned in Ref [132, 134]
- Fully simulated samples are used in order to model the cross-feed backgrounds. The yields of these contributions are constrained to the varying signal yields, their relative branching fraction and their selection efficiencies.
- The combinatorial background is modelled for each spectrum, by positive-definite Bernstein polynomials [146].

6.1.1 Signal models for B^0 and B_s

In order to provide a Signal model, the sum of two Crystal Ball (CB) distributions [147] is implemented whose mean μ and width σ are identical. The CB function itself is made by considering a Gaussian distribution with a radiative tail together*. Taking into account the contribution of two aforementioned signals per spectrum, some parameters are required

*The CB distribution is determined by following function,

$$F(x) = \begin{cases} \exp(-\frac{x-\mu}{2\sigma^2}) & \texttt{if}\ \frac{x-\mu}{\sigma} > -\alpha, \\ (\frac{n}{|\alpha|})^n (\frac{n-\alpha^2}{|\alpha|} - \frac{x-\mu}{\sigma})^{-n} \exp(-\frac{\alpha^2}{2}) & \texttt{if}\ \frac{x-\mu}{\sigma} \leq -\alpha, \end{cases}$$

to be constrained. To do so, a simultaneous fit was done, using the fully simulated MC samples of the signals. Through this fit, the models with the following remarks are used:

- The tail parameter n_0 and turnover point α_0 that are used for modeling the left-hand side of the distribution are different with respect to the spectrum and data-taking taking period, whereas being identical for both of signals and K^0_S reconstructions (Down-Down and Long-Long).

- Considering the tracking effects and their possible links to the right-hand side tails, and having the similar kinematics(at first order) for all the modes, led us to set universal values for right hand side parameters n_1 and α_1 for all samples.

- The fraction of CB distribution with the tail on the left is determined by parameter f. In the model, it is assumed to be the same for both mesons and K^0_S reconstructions. However, they can be different for each reconstruction modes. This parameter is left free in the fit to the MC samples.

- The mean value μ of both signal are set to be free and identical for all reconstruction modes.

- The width(σ)s of all signal modes are determined from fits to the MC simulated samples. These values will be subsequently used in the mass-fit to the data as Gaussian constrains by relating any signal width to the only varying one in the mass fit ($B^0 \to K^0_S \pi^+ \pi^-$)

The simultaneous fit to MC simulated events is performed after the application of the whole selection requirements. The Fig. 6.1 shows the result of this simultaneous fit for 2018 $B^0_{d,s} \to K^0_S h^\pm h'^\mp$ MC samples for K^0_S Down-Down reconstruction.

6.1.2 Cross-feed models

As it is discussed in chapter 3, the misidentification of h'' as h' for the $B^0_{d,s} \to K^0_S h^\pm h''^\mp$ has caused a cross-feed contribution to the $K^0_S h^\pm h'^\mp$ spectrum. To model this contribution, two CB distributions are utilized (same as signal events' distribution) and the means and widths of both of them are set to be identical. Also, in our cross-feed model, both K^0_S reconstructions' parameters are considered to be identical. Moreover, same type of mis-ID shares the same parameter except their mean value[†].

Since cross-feed contributions appear close to the signal peak, they have the possibility of getting absorbed in the tail of the signal distribution, and bias the result of the fit.

in which μ and σ are the mean and width of Gaussian distribution; and α and n denoted the shape and place of radiative tail. For instance, the sign of α determines whether the tail is situated on the right or left side of the Gaussian distribution. Here, that the variable x is the reconstructed mass.

[†]In our h'' as h' mis-ID example, no matter what is the main spectrum, only the mis-ID process is considered to determine the samples whose model parameters can be shared. However, since they belong to a different spectrum, their mean values required to be unique. Thus, it is the only parameter which is not shared between them.

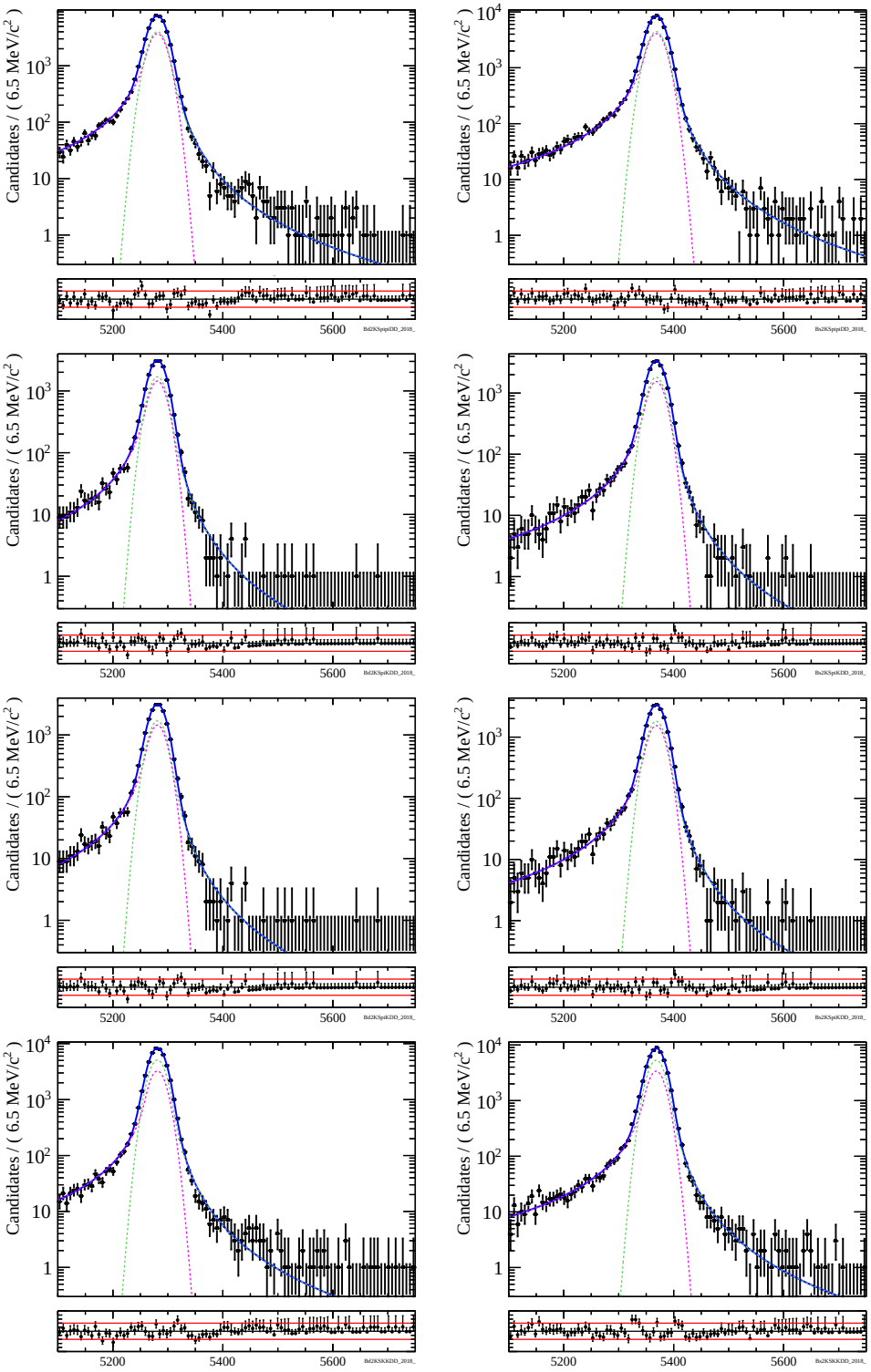

Figure 6.1: Simultaneous fit results for the reconstructed mass of the MC for 2018 samples with K^0_S Down-Down reconstruction. The $K^0_S\pi^+\pi^-$, $K^0_S K^\pm\pi^\mp$ and $K^0_S K^+K^-$ are shown in consecutive rows, while B^0 and B_s relevant plots are shown in left and right columns.

To solve this problem, first we need to perform a simultaneous fit on MC samples for all categories of each spectrum[‡] Fixing the shape of the cross-feed contributions using the values which are extracted from MC fit is not sufficient and constraining the cross-feed yield is inevitable. To do so, A Gaussian is defined using central values that are taken from MC efficiencies and the widths, which are determined from the relevant efficiencies. Then, this Gaussian is implemented to constrain the rate of misidentified signals to their well-identified counterparts.

6.1.3 Combinatorial Background model

The most significant contribution among the backgrounds in $K^0_S h^+ h'^-$ data samples belong to the category which is produced by random combination of tracks from several decays, and as such it is called combinatorial background. There is no dedicated MC samples to study such contribution and extract the model shapes from them. To model this contribution, the right-hand side of the mass spectrum can be used, where the reconstructed mass is above 5550 MeV. This restriction is necessary to remove the candidates $\Lambda_b \to K^0_S ph$, with properties different from the combinatorial background. It is observed that in this region the combinatorial background can be well described by a first order polynomial. The Bernstein polynomial is a convenient choice for a probability density function thanks to its positiveness definition.

6.1.4 Partially reconstructed models

Through this study, in order to model the partially reconstructed background, the same path was paved as the former analysis [132]. These types of background in $B^0_{d,s} \to K^0_S h^+ h'^-$ decays are composed of four types:

- Two of them are charmless radiative decays whose γ is missing. For instance, in $K^0_S \pi^+\pi^-$ reconstruction these types of background consists of $B^0 \to K^0_S \eta'(\to \rho^0(\to \pi^+\pi^-)\gamma)$ and $B^0 \to K^0_S \pi^+\pi^-\gamma$ (which is non-resonant). These types of background have been considered for other modes of $K^0_S h^+ h'^-$ reconstruction, but their contribution was negligible.

- Charmless and open-charm decays, whose $\pi^{\pm,0}$ is missing, comprised the other two type of partially reconstructed background.

To model these contributions, the shape of each is modelled with a Gaussian convoluted Argus function. This distribution is defined by considering a slope s, curvature c and a threshold mass m_t in the following form,

$$f(m; c, s, m_t) = \frac{m}{m_t}\left(1 - (\frac{m}{m_t})^2\right)^c \times \exp\left(-\frac{1}{2}s^2(1 - (\frac{m}{m_t})^2)\right), \tag{6.3}$$

[‡]This means that a simultaneous fit is performed on all the years, hadronization and K^0_S reconstructions samples for each channel.

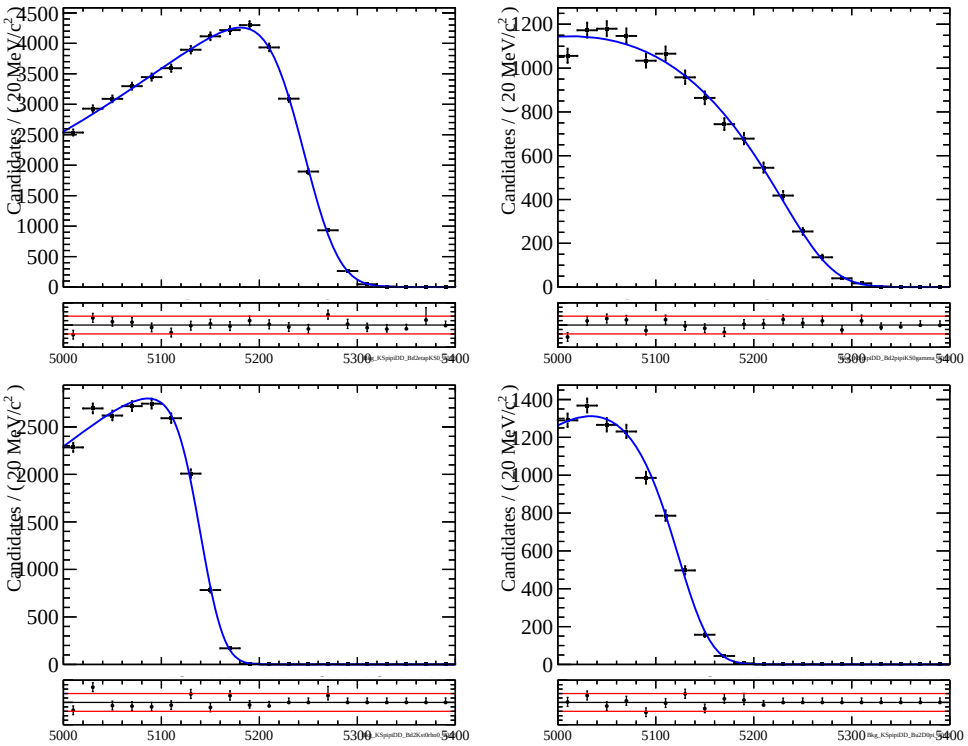

Figure 6.2: Simultaneous fit results for the reconstructed mass of the partially-reconstructed decays (Down-Down K^0_S reconstruction). On the top the two radiative charmless decays (resonant on the left, non-resonant on the right). On the bottom the two decays where π is not reconstructed(charmless on the left, from B to open charm decays on the right).

where the threshold parameter for each contribution is determined by considering the physical threshold of that specific partially-reconstructed decay. For instance, for a decay with missing π, $m_t = m_B - m_\pi$ and in case of radiative decay whose γ is missing, $m_t = m_B$. Thereafter, in order to extract the other parameters, Fast MC samples are used. Moreover, for all categories of partially reconstructed backgrounds of all decay modes[§], the curvature and slope parameters are considered to be identical to those of the $K^0_S\pi^+\pi^-$ mode. The only difference between the shapes is coming from the difference of the B-mass and how it changes the threshold mass. Finally, the width of the Gaussian resolution is fixed to that measured for the well-identified signal decays. The fig. 6.2 shows the result of fit to the MC samples. One should take into account that in the fit to the data, the yields of these contributions are constrained. These constraints are Gaussian, in which we consider the efficiencies of the fully simulated samples and the inclusive branching fraction of them when it is not known well. Thus, the contribution of a partial reconstruction background (PRB) to the decay mode (DM) is given by the following formula,

$$N(\mathrm{PRB}) = N(\mathrm{DM}) \times \mathcal{BF}(\mathrm{PRB}) \times f_\mathrm{G}(\mathrm{PRB}, \mathrm{DM}) \tag{6.4}$$

[§]For all B_s, B^0, both K^0_S reconstructions.

where $f_{\mathrm{G}}(\mathrm{PRB},\mathrm{DM}) = \frac{\epsilon(\mathrm{PRB})}{\mathcal{BF}(\mathrm{DM})\times\epsilon(\mathrm{DM})}$ is the aforementioned Gaussian constraint.

6.1.5 Fit Results and Comparison of Run I

After the shape (parameter) extraction and determining the constraints, the simultaneous fit is done on the samples. The Figs 6.3 to 6.6 represent the simultaneous fit results for 2018 and 2012b as an instance of the fit results for RunI and RunII.

As the fit and its residual show, A satisfactory agreement is obtained for all spectra between the model and the data.

In Chapter 3, we examined based on MC simulated events how much the novel PID selection would improve the signal yields. We are now in position to actually and quantitatively check the level of improvement on the real data by comparing the outcomes of the previous and current fits on RunI data. This improvement in purifying data samples in both tight and loose optimization are illustrated in figs. 6.7- 6.9 by comparing the fit results of the $B^0_{d,s} \to K^0_{\mathrm{S}}\pi^+\pi^-$ of former and the current analysis. In general, when there is a data sample with large statistics (see fig. 6.7) what is observed in the tight optimization is an increase in signal efficiency and decrease in cross-feed and combinatorics with respect to the former study. As far as low statistics data samples are concerned (see fig. 6.9), the signal purity is always improved, while the signal yields might not be enhanced. The novel PID tool (in particular), developed for this updated analysis allows to get rid of almost all background sources.

6.2 Fits and Average Efficiencies comparison

Till this step, the impact of the novel selection method was studied through the comparisons of performance with the former selection with simulated events and the quantitative assessment of the improvement in signal yields and purity with the data samples.

In order to check the correctness of the selection tools and their efficiency determination, one can provide a consistency comparison that would not assume the knowledge of the branching fractions of the mode of interest.

Through the following section the method of this consistency check is presented.

6.2.1 Corrected efficiency maps

In Chapters 3and 5 we presented the corrections applied to the MC samples, in order to improve the accuracy of the simulation description.

The Figures 5.5 and 5.6 show the corrected efficiency for 2018 and 2012b samples as an instance for the RunII and RunI.

6.2.2 *sWeights* and averaging the Efficiencies

The MC samples that we use in this study are generated assuming that the events are distributed evenly in the square Dalitz plane. The actual distribution is not known for

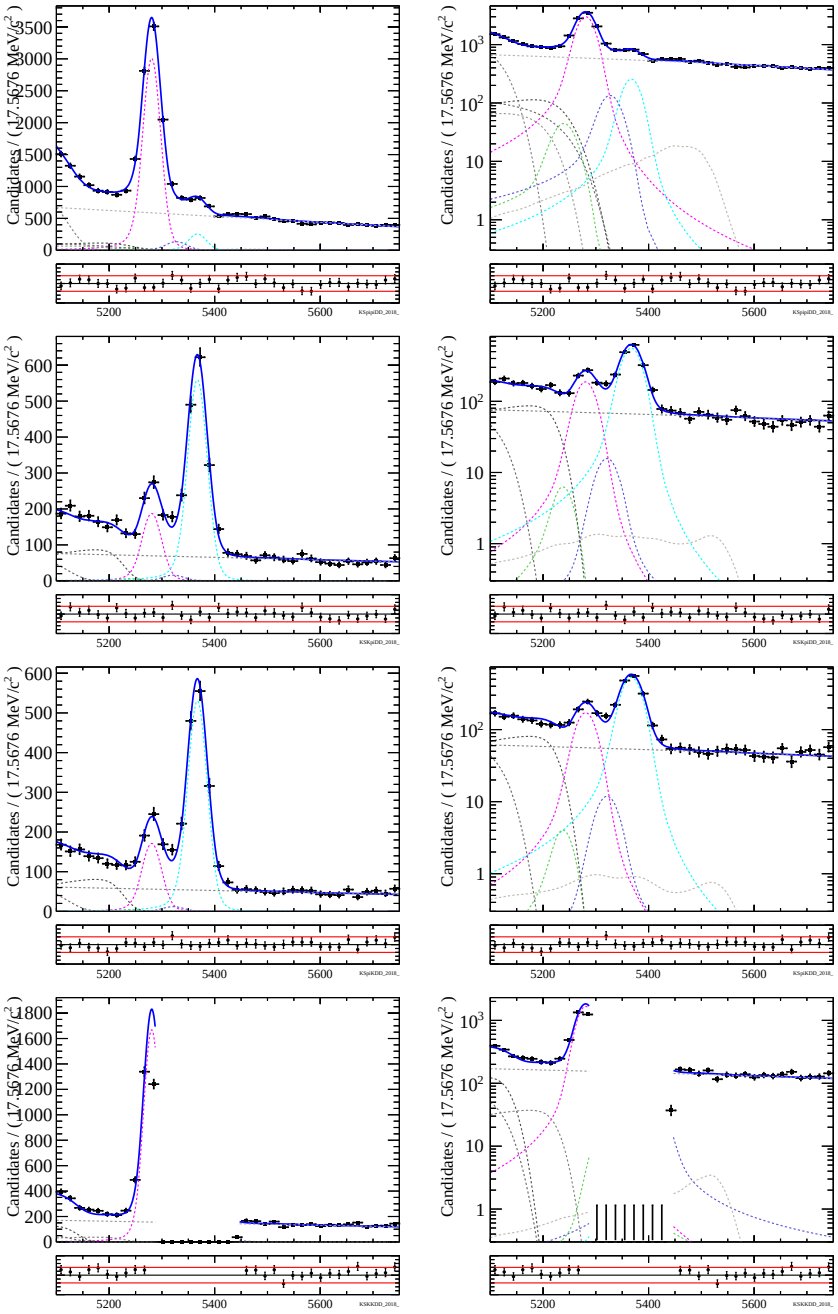

Figure 6.3: Simultaneous fit results as reported in reference [144] for 2018 data samples with K^0_S Down-Down reconstruction using the loose optimization cut (work in progress). The $K^0_S\pi^+\pi^-$, $K^0_S K^\pm\pi^\mp$ and $K^0_S K^+K^-$ were shown in consecutive rows. The left column shows the result on a linear scale and the right one shows in logarithmic scale. On each plot, the total PDF is shown with solid blue and the individual components are shown as dashed lines: The B^0_d and B^0_s signals are in magenta and cyan, respectively. The cross-feed backgrounds from B^0_d is in green and from B^0_s is in purple. The Λ^0_b cross-feed background is shown in brown and peaking above 5400 MeV. The combinatorial background is displayed with the straight dashed line. In the left region of each plot, the gray dashed lines show the partially reconstructed background. In the $K^0_S K^+K^-$ spectra, the region around the B^0_s signal (5320-5450 MeV) is blinded.

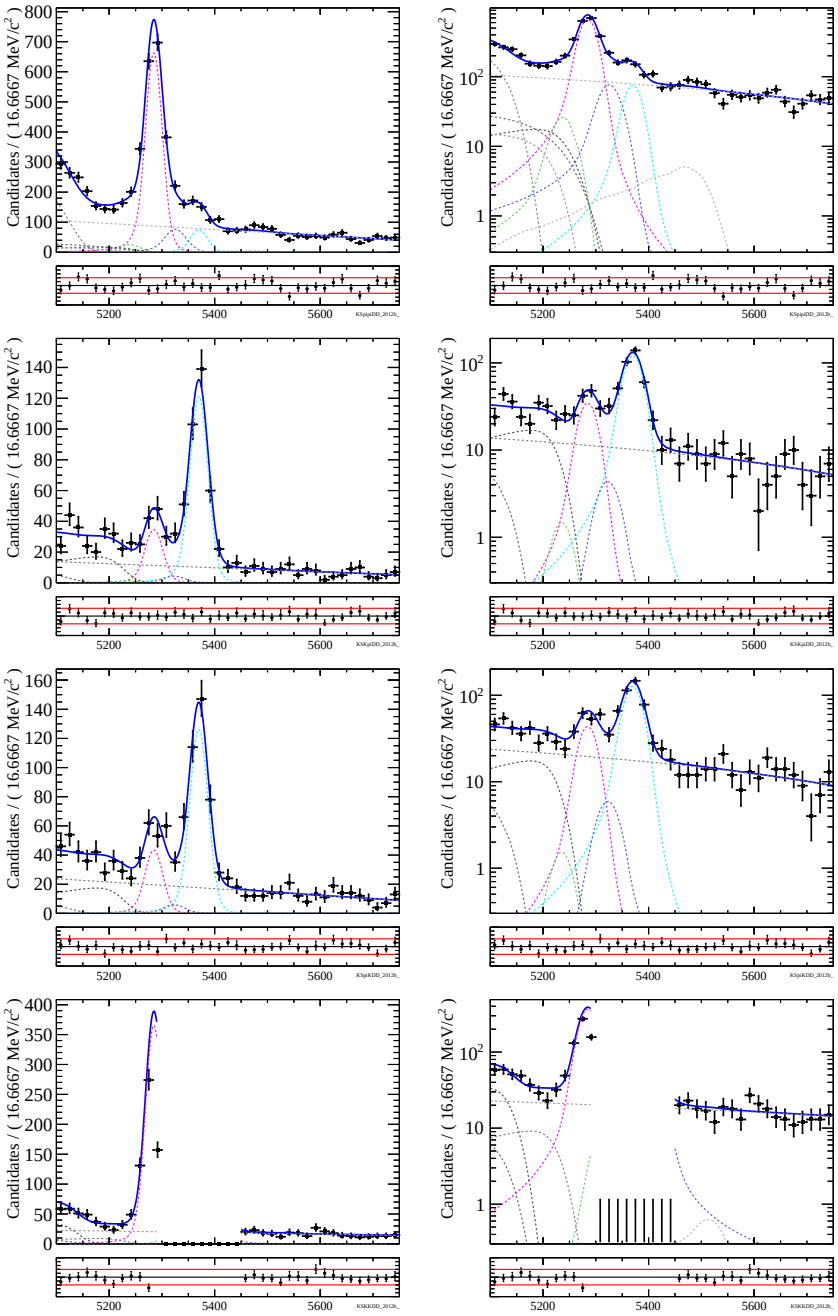

Figure 6.4: Simultaneous fit results as reported in reference [144] for 2012b data samples with K^0_S Down-Down reconstruction using the loose optimization cut (work in progress). The $K^0_S\pi^+\pi^-$, $K^0_S K^\pm\pi^\mp$ and $K^0_S K^+K^-$ were shown in consecutive rows. The left column shows the result on a linear scale and the right one shows in logarithmic scale. On each plot, the total PDF is shown with solid blue and the individual components are shown as dashed lines: The B^0_d and B^0_s signals are in magenta and cyan, respectively. The cross-feed backgrounds from B^0_d is in green and from B^0_s is in purple. The Λ^0_b cross-feed background is shown in brown and peaking above 5400 MeV. The combinatorial background is displayed with the straight dashed line. In the left region of each plot, the gray dashed lines show the partially reconstructed background. In the $K^0_S K^+K^-$ spectra, the region around the B^0_s signal (5320-5450 MeV) is blinded.

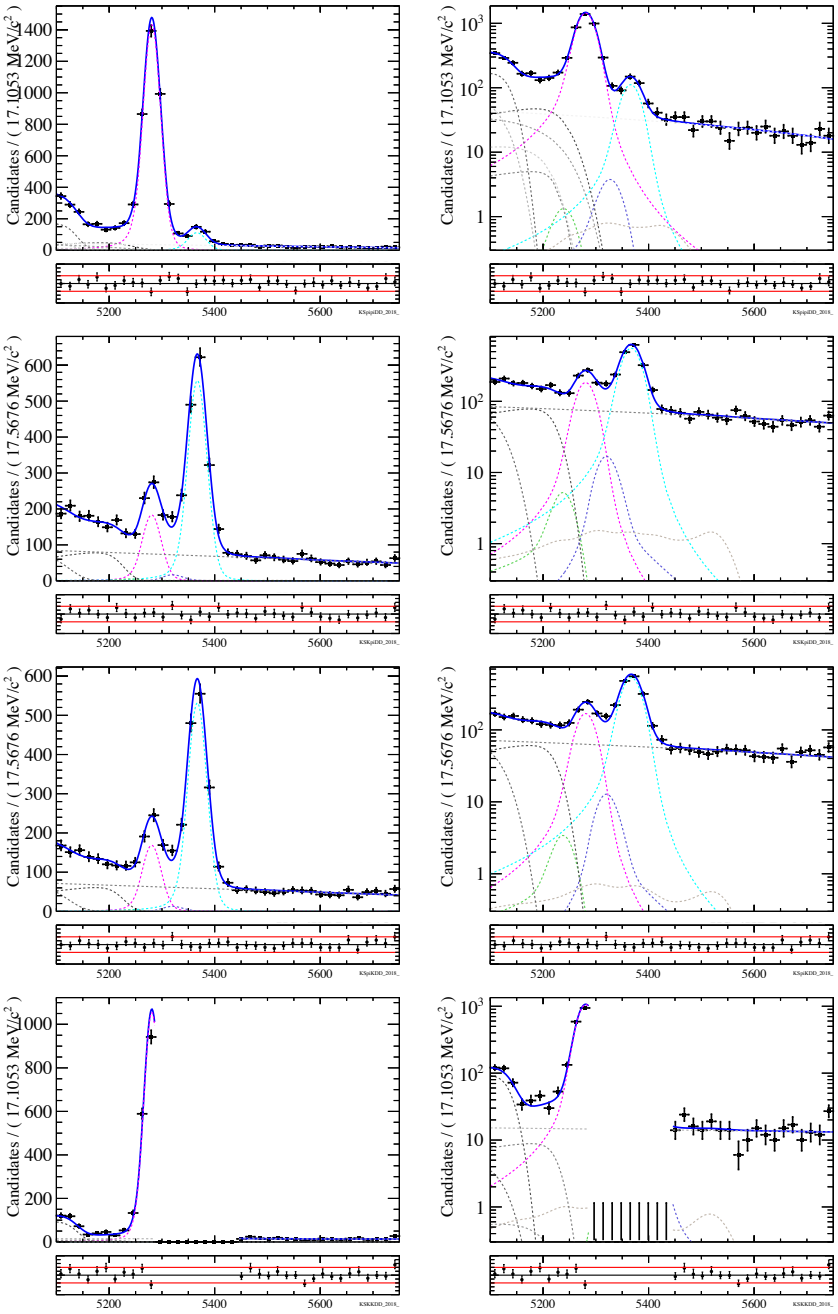

Figure 6.5: Simultaneous fit results as reported in reference [144] for 2018 data samples with K^0_S Down-Down reconstruction using the tight optimization cut (work in progress). The $K^0_S\pi^+\pi^-$, $K^0_S K^\pm\pi^\mp$ and $K^0_S K^+K^-$ were shown in consecutive rows. The left column shows the result on a linear scale and the right one shows in logarithmic scale. On each plot, the total PDF is shown with solid blue and the individual components are shown as dashed lines: The B^0_d and B^0_s signals are in magenta and cyan, respectively. The cross-feed backgrounds from B^0_d is in green and from B^0_s is in purple. The Λ^0_b cross-feed background is shown in brown and peaking above 5400 MeV. The combinatorial background is displayed with the straight dashed line. In the left region of each plot, the gray dashed lines show the partially reconstructed background. In the $K^0_S K^+K^-$ spectra, the region around the B^0_s signal (5320-5450 MeV) is blinded.

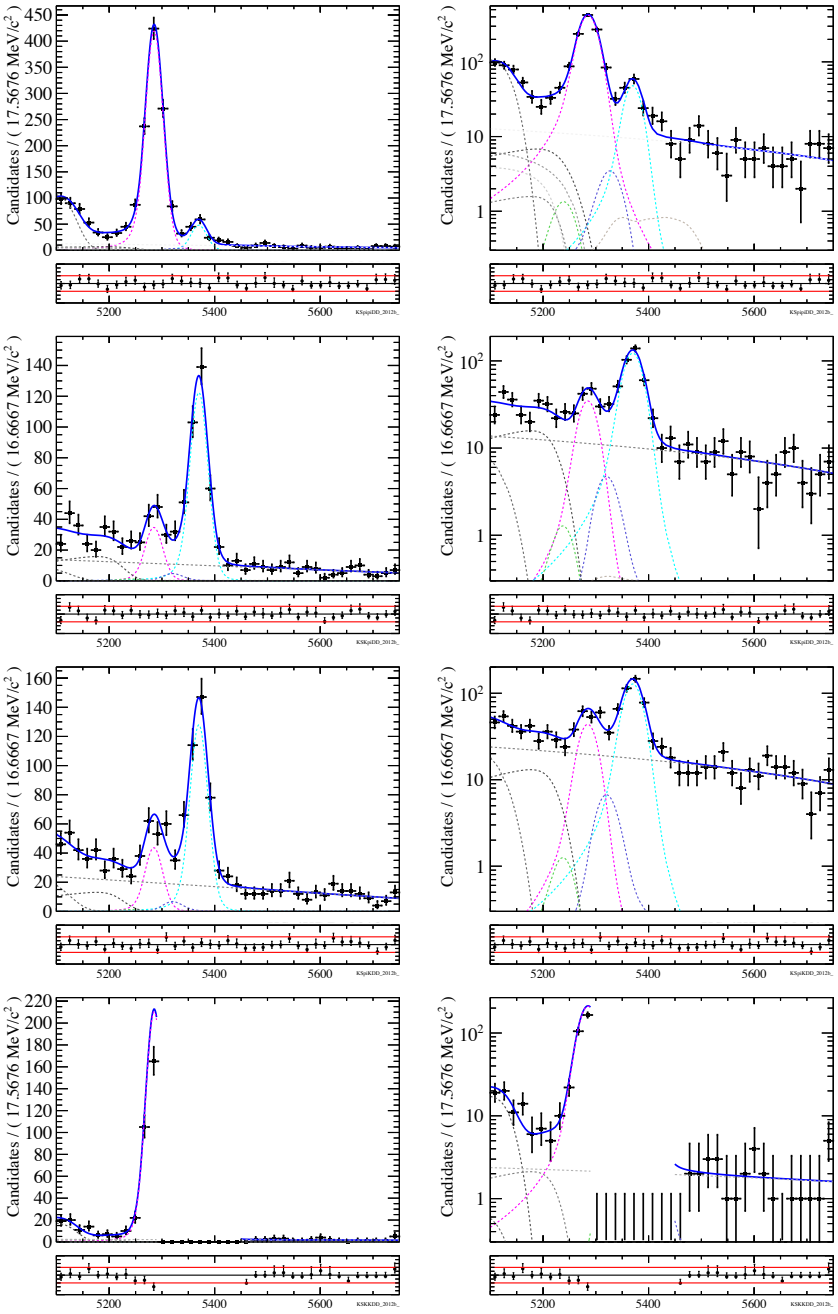

Figure 6.6: Simultaneous fit results as reported in reference [144] for 2012b data samples with K^0_S Down-Down reconstruction using the tight optimization cut (work in progress). The $K^0_S\pi^+\pi^-$, $K^0_S K^\pm\pi^\mp$ and $K^0_S K^+K^-$ were shown in consecutive rows. The left column shows the result on a linear scale and the right one shows in logarithmic scale. On each plot, the total PDF is shown with solid blue and the individual components are shown as dashed lines: The B^0_d and B^0_s signals are in magenta and cyan, respectively. The cross-feed backgrounds from B^0_d is in green and from B^0_s is in purple. The Λ^0_b cross-feed background is shown in brown and peaking above 5400 MeV. The combinatorial background is displayed with the straight dashed line. In the left region of each plot, the gray dashed lines show the partially reconstructed background. In the $K^0_S K^+K^-$ spectra, the region around the B^0_s signal (5320-5450 MeV) is blinded.

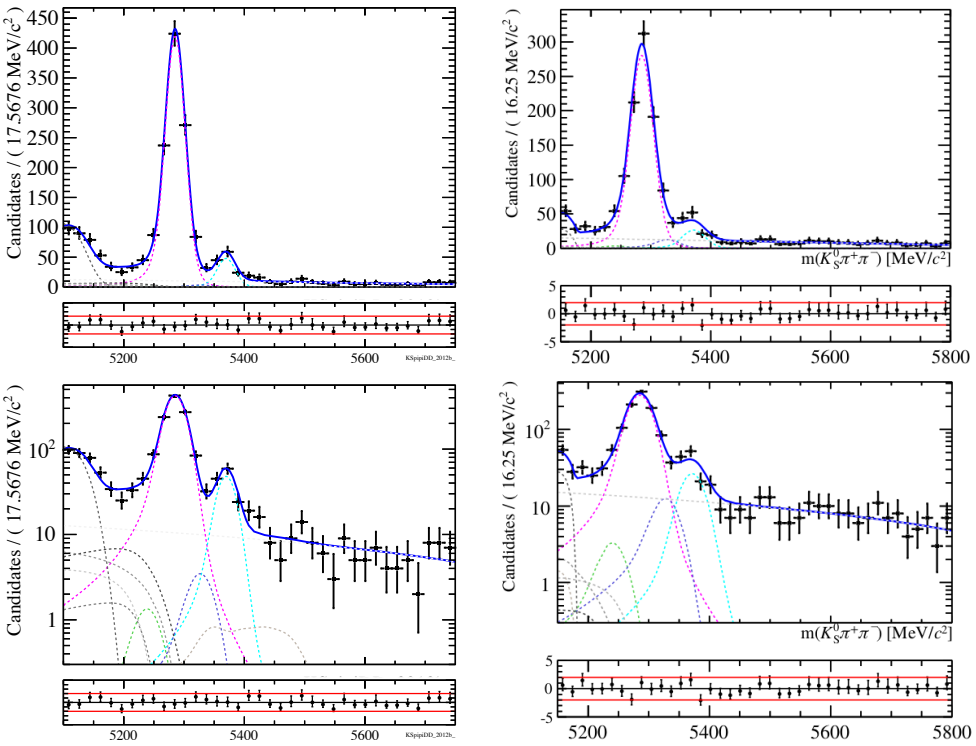

Figure 6.7: Comparison of Simultaneous fit results between the current(left) and former analysis (right) for 2012b data samples with K^0_S Down-Down reconstruction using the tight optimization cut. The top row shows the linear scale while the bottom row dedicated to logarithmic scale. On each plot, the total PDF is shown with solid blue and the individual components are shown as dashed lines: The B^0_d and B^0_s signals are in magenta and cyan, respectively. The cross-feed backgrounds from B^0_d is in green and from B^0_s is in purple. The Λ^0_b cross-feed background is shown in brown and peaking above 5400 MeV. The combinatorial background is displayed with the straight dashed line. In the left region of each plot, the gray dashed lines show the partially reconstructed background.

most of the modes of the interest; its knowledge is however required to estimate the average efficiency on the data.

There are several approaches which can be used to subtract the background from the data in physics analysis and determine the places where accumulated by signal events. The method employed here follows the previous works on the subject [132], the *sPlot* [122] technique, based on the likelihood theorem, and designed to determine individually the various components of a fitted distribution. Let's recall here the essential features. The discriminative variable is the invariant mass of the candidates. The yields of the signals and the combinatorics are the only floating variables in the sFit, all other parameters of the invariant-mass model being fixed to their measured values in the generic mass-fit. The control variables are the squared Dalitz plane variables, which have been proven to be negligibly correlated to the invariant-mass of the B candidates [145].

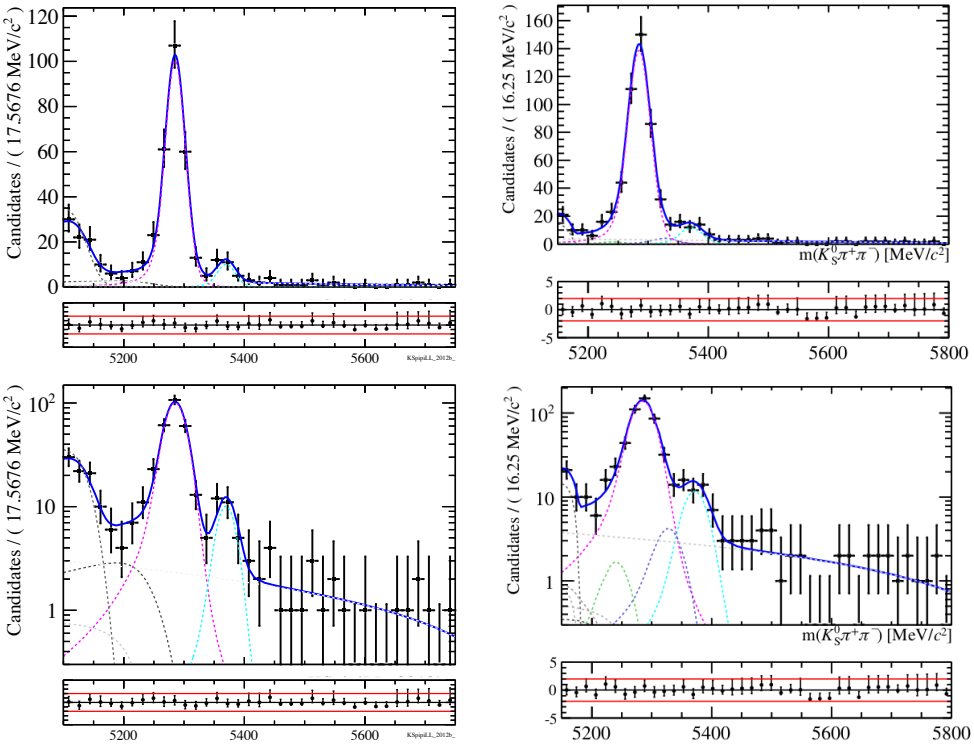

Figure 6.8: Comparison of Simultaneous fit results between the current (left) and former analysis (right) for 2012b data samples with K^0_S Long-Long reconstruction using the tight optimization cut. The top row shows the linear scale while the bottom row dedicated to logarithmic scale. On each plot, the total PDF is shown with solid blue and the individual components are shown as dashed lines: The B^0_d and B^0_s signals are in magenta and cyan, respectively. The cross-feed backgrounds from B^0_d is in green and from B^0_s is in purple. The Λ^0_b cross-feed background is shown in brown and peaking above 5400 MeV. The combinatorial background is displayed with the straight dashed line. In the left region of each plot, the gray dashed lines show the partially reconstructed background.

The result of this sFit is therefore the *sWeighted* map of the sqDP variables, which represent the actual physics of the decays embodying the selection efficiency. Now, in order to project the aforementioned nontrivial variations across the Dalitz plane (in data) on the MC sample and provide the correction per bin for such non-uniform patterns, the efficiencies across the phase space is weighted by using these data-driven *sWeights*. As a result, the number of events entering in the sqDP (the denominator in the efficiency expression) can be weighted by considering the efficiency in the Dalitz plane bin which contain the event i and the event based signal *sWeight* w_i in the following form:

$$N^{\text{weighted}}_{\text{sig}} = \sum_i \frac{w_i}{\epsilon_i} \tag{6.5}$$

Taking into account of this correction, and the fact that the sum of the *sWeights* are equal to the number of signal events ($N_{sig} = \sum_i w_i$), the average efficiency over the Dalitz

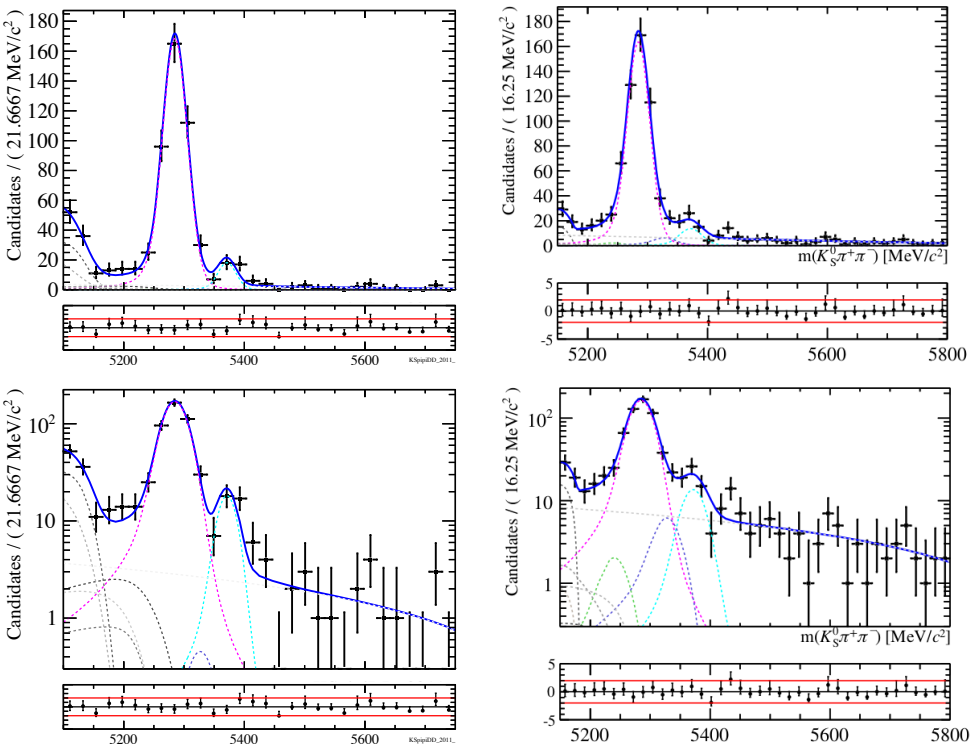

Figure 6.9: Comparison of Simultaneous fit results between the current(left) and former analysis (right) for 2011 data samples with K^0_S Down-Down reconstruction using the tight optimization cut. The top row shows the linear scale while the bottom row dedicated to logarithmic scale. On each plot, the total PDF is shown with solid blue and the individual components are shown as dashed lines: The B^0_d and B^0_s signals are in magenta and cyan, respectively. The cross-feed backgrounds from B^0_d is in green and from B^0_s is in purple. The Λ^0_b cross-feed background is shown in brown and peaking above 5400 MeV. The combinatorial background is displayed with the straight dashed line. In the left region of each plot, the gray dashed lines show the partially reconstructed background.

plane can be determined through the following formula,

$$\bar{\epsilon} = \frac{N_{sig}}{N^{\text{weighted}}_{\text{sig}}} = \frac{\sum_i w_i}{\sum_i \frac{w_i}{\epsilon_i}}. \tag{6.6}$$

6.2.3 fit-efficiency comparison

Since the results of simultaneous mass-fit and signal efficiency maps are going to be used in measurement of branching fraction and Dalitz Plot analysis, it is good to provide a consistency check which does not require the knowledge of branching fractions by using the averaged efficiencies and the yields of signal components.

First, the ratio of the yields $R^{DD/LL}_{\text{Yield}}$ and the ratio of the efficiencies $R^{DD/LL}_{\epsilon}$ are computed. The reason we use these ratios between Down-Down and Long-Long is that

we factor out the branching fractions. One computes their difference and divide by the quadratic sum of their uncertainties in order to express the consistency in terms of a naive statistical significance, that one can interpret straightforwardly. We consider that the results are consistent if this significance is less than 2.5σ.

The results of such comparison for RunII samples are presented in tables 6.1-6.3. Although the results of the RunII do not show any significant problem, the study is still ongoing for the RunI result.

Mode	Mag	Fit_type	DD				LL				$R_\epsilon^{DD/LL}$	$\delta R_\epsilon^{DD/LL}$	$R_{\text{Yield}}^{DD/LL}$	$\delta R_{\text{Yield}}^{DD/LL}$	$\text{dist}_{\epsilon-\text{Yield}}$
			ϵ	$\delta_\epsilon^{\text{stat.}}$	Yield	$\delta_{\text{Yield}}^{\text{stat.}}$	ϵ	$\delta_\epsilon^{\text{stat.}}$	Yield	$\delta_{\text{Yield}}^{\text{stat.}}$					
Bd2KSpipi	MD	Loose	0.000879	9.065E-06	8037.16	121.189	0.000331	5.85008E-06	3170.67	69.7651	2.656771	0.054372	2.5348	0.0676	-1.41
Bd2KSpipi	MU	Loose	0.000849	9.12047E-06	8037.16	121.189	0.000327	5.84456E-06	3170.67	69.7651	2.595859	0.054126	2.5348	0.0676	-0.70
Bd2KSKpi	MD	Tight	0.000365	7.51414E-06	455.79	32.3343	0.000151	5.05149E-06	208.98	21.0994	2.411882	0.0947	2.1810	0.2691	-0.81
Bd2KSKpi	MU	Tight	0.000372	6.87177E-06	455.79	32.3343	0.000141	6.03698E-06	208.98	21.0994	2.64231	0.12324	2.1810	0.2691	-1.56
Bd2KSpiK	MD	Tight	0.000338	5.73236E-06	459.55	30.3386	0.000148	5.97309E-06	203.73	20.1886	2.274496	0.099355	2.2557	0.2686	-0.07
Bd2KSpiK	MU	Tight	0.00034	5.68738E-06	459.55	30.3386	0.000154	6.60461E-06	203.73	20.1886	2.202669	0.101153	2.2557	0.2686	0.18
Bd2KSpipi	MD	Tight	0.000418	7.32367E-06	3784.82	68.0352	0.000212	5.64104E-06	2002.86	49.7834	1.973652	0.062903	1.8897	0.0580	-0.98
Bd2KSpipi	MU	Tight	0.000418	6.67158E-06	3784.82	68.0352	0.000208	4.87054E-06	2002.86	49.7834	2.006505	0.056845	1.8897	0.0580	-1.44
Bd2KSKpi	MD	Loose	0.000458	7.95868E-06	531.71	48.6124	0.000165	5.12404E-06	235.98	25.4178	2.774218	0.098779	2.2532	0.3183	-1.56
Bd2KSKpi	MU	Loose	0.000459	7.77137E-06	531.71	48.6124	0.000158	5.36305E-06	235.98	25.4178	2.913138	0.11078	2.2532	0.3183	-1.96
Bd2KSpiK	MD	Loose	0.000447	7.49794E-06	582.98	47.3406	0.000208	8.8916E-06	215.1	28.6063	2.146798	0.098471	2.7103	0.4223	1.30
Bd2KSpiK	MU	Loose	0.000453	7.73234E-06	582.98	47.3406	0.000217	1.12441E-05	215.1	28.6063	2.082818	0.113512	2.7103	0.4223	1.43
Bs2KSpipi	MD	Loose	0.000847	1.12184E-05	717.78	62.3733	0.000363	1.33869E-05	290.07	32.4886	2.336833	0.091678	2.4745	0.3508	0.38
Bs2KSpipi	MU	Loose	0.000834	1.1481E-05	717.78	62.3733	0.000357	1.62489E-05	290.07	32.4886	2.332855	0.110808	2.4745	0.3508	0.39
Bs2KSKpi	MD	Tight	0.000358	6.03112E-06	1496.31	45.587	0.000143	6.8459E-06	683.34	30.032	2.496399	0.126468	2.1897	0.1171	-1.78
Bs2KSKpi	MU	Tight	0.000357	5.57685E-06	1496.31	45.587	0.000141	4.78226E-06	683.34	30.032	2.529618	0.094286	2.1897	0.1171	-2.26
Bs2KSpiK	MD	Tight	0.000329	5.40652E-06	1458.48	44.0958	0.000136	3.60354E-06	648.84	28.9024	2.426601	0.075767	2.2478	0.1210	-1.25
Bs2KSpiK	MU	Tight	0.000334	5.10132E-06	1458.48	44.0958	0.000134	3.69917E-06	648.84	28.9024	2.481649	0.078121	2.2478	0.1210	-1.62
Bs2KSpipi	MD	Tight	0.000475	7.62234E-06	321.51	24.4688	0.00023	1.01864E-05	179.14	18.3808	2.061687	0.09694	1.7947	0.2293	-1.07
Bs2KSpipi	MU	Tight	0.000472	7.43626E-06	321.51	24.4688	0.000253	1.13816E-05	179.14	18.3808	1.864634	0.08888	1.7947	0.2293	-0.28
Bs2KSKpi	MD	Loose	0.000438	6.89268E-06	1808.5	59.3522	0.000165	5.58911E-06	762.84	33.9572	2.657497	0.099373	2.3707	0.1311	-1.74
Bs2KSKpi	MU	Loose	0.000441	6.35288E-06	1808.5	59.3522	0.000159	4.65594E-06	762.84	33.9572	2.780434	0.090855	2.3707	0.1311	-2.57
Bs2KSpiK	MD	Loose	0.000435	6.43386E-06	1928.55	59.7066	0.000169	3.96819E-06	784.38	36.5408	2.578108	0.071572	2.4587	0.1375	-0.77
Bs2KSpiK	MU	Loose	0.00044	6.30074E-06	1928.55	59.7066	0.000167	3.80056E-06	784.38	36.5408	2.639508	0.07101	2.4587	0.1375	-1.17

Table 6.1: Fit-efficiency comparison for 2018 $B^0_{d,s} \to K^0_S h^+ h'^-$ samples.

Mode	Mag	Fit_type	DD				LL				$R_\epsilon^{DD/LL}$	$\delta R_\epsilon^{DD/LL}$	$R_{\text{Yield}}^{DD/LL}$	$\delta R_{\text{Yield}}^{DD/LL}$	$\text{dist}_{\epsilon-\text{Yield}}$
			ϵ	$\delta_\epsilon^{\text{stat.}}$	Yield	$\delta_{\text{Yield}}^{\text{stat.}}$	ϵ	$\delta_\epsilon^{\text{stat.}}$	Yield	$\delta_{\text{Yield}}^{\text{stat.}}$					
Bd2KSpipi	MD	Loose	0.000896	9.99402E-06	6455.62	106.736	0.000346	6.60531E-06	2806.37	65.7599	2.590801	0.057327	2.3003	0.0660	-3.32
Bd2KSpipi	MU	Loose	0.000883	1.04872E-05	6455.62	106.736	0.000346	6.30267E-06	2806.37	65.7599	2.551353	0.055477	2.3003	0.0660	-2.91
Bd2KSKpi	MD	Tight	0.000392	7.00617E-06	434.43	32.5519	0.000152	5.93218E-06	152.46	17.5072	2.584666	0.11121	2.8495	0.3907	0.65
Bd2KSKpi	MU	Tight	0.000395	7.00696E-06	434.43	32.5519	0.000158	5.87647E-06	152.46	17.5072	2.493059	0.102474	2.8495	0.3907	0.88
Bd2KSpiK	MD	Tight	0.000362	7.28936E-06	407.94	27.7777	0.000157	1.00781E-05	187.34	19.7609	2.313081	0.155957	2.1775	0.2734	-0.43
Bd2KSpiK	MU	Tight	0.000357	7.23726E-06	407.94	27.7777	0.00019	6.67606E-06	187.34	19.7609	1.875035	0.075914	2.1775	0.2734	1.07
Bd2KSpipi	MD	Tight	0.000448	6.96893E-06	3359.43	63.9265	0.000229	6.01167E-06	1890.1	48.7191	1.950914	0.059456	1.7774	0.0569	-2.11
Bd2KSpipi	MU	Tight	0.000445	8.35607E-06	3359.43	63.9265	0.000233	5.39415E-06	1890.1	48.7191	1.909255	0.056897	1.7774	0.0569	-1.64
Bd2KSKpi	MD	Loose	0.000463	8.71376E-06	531.34	48.3071	0.000208	7.91407E-06	168.37	26.2974	2.228555	0.094604	3.1558	0.5703	1.60
Bd2KSKpi	MU	Loose	0.000481	8.58611E-06	531.34	48.3071	0.000208	7.98282E-06	168.37	26.2974	2.309846	0.097657	3.1558	0.5703	1.46
Bd2KSpiK	MD	Loose	0.000488	9.04996E-06	535.48	43.5286	0.000157	1.70028E-05	211.68	26.1136	3.101101	0.339789	2.5297	0.3737	-1.13
Bd2KSpiK	MU	Loose	0.000481	9.06698E-06	535.48	43.5286	0.000196	6.74645E-06	211.68	26.1136	2.449043	0.096013	2.5297	0.3737	0.21
Bs2KSpipi	MD	Loose	0.000981	1.97612E-05	454.21	52.2761	0.000379	1.32784E-05	244.8	29.3527	2.588475	0.104591	1.8554	0.3084	-2.25
Bs2KSpipi	MU	Loose	0.001007	2.13622E-05	454.21	52.2761	0.000377	1.41928E-05	244.8	29.3527	2.67191	0.115486	1.8554	0.3084	-2.48
Bs2KSKpi	MD	Tight	0.000387	5.91251E-06	1352.75	44.1768	0.000156	4.016E-06	564.4	26.671	2.490157	0.074689	2.3968	0.1377	-0.60
Bs2KSKpi	MU	Tight	0.000391	6.05362E-06	1352.75	44.1768	0.000142	6.31693E-06	564.4	26.671	2.755911	0.129812	2.3968	0.1377	-1.90
Bs2KSpiK	MD	Tight	0.000361	5.96806E-06	1315.91	40.9001	0.000171	4.26491E-06	636.24	28.4145	2.112945	0.06319	2.0683	0.1125	-0.35
Bs2KSpiK	MU	Tight	0.000352	5.91013E-06	1315.91	40.9001	0.000167	5.10409E-06	636.24	28.4145	2.104289	0.073389	2.0683	0.1125	-0.27
Bs2KSpipi	MD	Tight	0.000533	1.03752E-05	259.97	22.0863	0.000269	8.42282E-06	133.66	15.722	1.982415	0.073071	1.9450	0.2822	-0.13
Bs2KSpipi	MU	Tight	0.000555	1.05648E-05	259.97	22.0863	0.000261	9.39421E-06	133.66	15.722	2.12452	0.08648	1.9450	0.2822	-0.61
Bs2KSKpi	MD	Loose	0.000491	6.64135E-06	1673.4	57.78	0.000189	6.03433E-06	700.31	34.2116	2.594755	0.089854	2.3895	0.1429	-1.22
Bs2KSKpi	MU	Loose	0.000492	6.61827E-06	1673.4	57.78	0.000177	7.57395E-06	700.31	34.2116	2.779636	0.124616	2.3895	0.1429	-2.06
Bs2KSpiK	MD	Loose	0.000467	6.73495E-06	1660.96	54.2292	0.000199	4.67187E-06	732.12	33.7222	2.343814	0.064546	2.2687	0.1281	-0.52
Bs2KSpiK	MU	Loose	0.000463	6.6173E-06	1660.96	54.2292	0.000193	4.91229E-06	732.12	33.7222	2.39816	0.069963	2.2687	0.1281	-0.89

Table 6.2: Fit-efficiency comparison for 2017 $B^0_{d,s} \to K^0_S h^+ h'^-$ samples.

Mode	Mag	Fit_type	DD				LL				$R_\epsilon^{DD/LL}$	$\delta R_\epsilon^{DD/LL}$	$R_{\text{Yield}}^{DD/LL}$	$\delta R_{\text{Yield}}^{DD/LL}$	$\text{dist}_{\epsilon-\text{Yield}}$
			ϵ	$\delta_\epsilon^{\text{stat.}}$	Yield	$\delta_{\text{Yield}}^{\text{stat.}}$	ϵ	$\delta_\epsilon^{\text{stat.}}$	Yield	$\delta_{\text{Yield}}^{\text{stat.}}$					
Bd2KSpipi	MD	Loose	0.000951	1.01107E-05	5797.19	101.396	0.000411	6.62203E-06	2710.19	65.4898	2.315508	0.044709	2.1390	0.0638	-2.27
Bd2KSpipi	MU	Loose	0.000964	9.78135E-06	5797.19	101.396	0.000404	6.47588E-06	2710.19	65.4898	2.387767	0.045342	2.1390	0.0638	-3.18
Bd2KSKpi	MD	Tight	0.000434	8.05546E-06	371.9	30.4367	0.000156	6.28947E-06	117.58	16.1335	2.790893	0.12416	3.1630	0.5053	0.72
Bd2KSKpi	MU	Tight	0.000442	8.27898E-06	371.9	30.4367	0.000156	7.1609E-06	117.58	16.1335	2.834382	0.140511	3.1630	0.5053	0.63
Bd2KSpiK	MD	Tight	0.000415	7.26871E-06	349.44	29.9711	0.00018	6.94334E-06	194.53	19.5362	2.312612	0.098138	1.7963	0.2372	-2.01
Bd2KSpiK	MU	Tight	0.000417	7.26751E-06	349.44	29.9711	0.000173	5.27511E-06	194.53	19.5362	2.404157	0.084249	1.7963	0.2372	-2.41
Bd2KSpipi	MD	Tight	0.000504	7.28655E-06	2800.77	59.2542	0.00027	5.37196E-06	1634.29	45.2634	1.869289	0.046031	1.7138	0.0597	-2.06
Bd2KSpipi	MU	Tight	0.000514	7.16092E-06	2800.77	59.2542	0.000267	5.45776E-06	1634.29	45.2634	1.922116	0.047507	1.7138	0.0597	-2.73
Bd2KSKpi	MD	Loose	0.000585	1.09557E-05	431.85	45.763	0.000218	8.58304E-06	147.14	24.5312	2.678122	0.116649	2.9350	0.5798	0.43
Bd2KSKpi	MU	Loose	0.000576	1.12085E-05	431.85	45.763	0.000219	9.49107E-06	147.14	24.5312	2.632196	0.125235	2.9350	0.5798	0.51
Bd2KSpiK	MD	Loose	0.000509	8.58411E-06	457.92	47.4447	0.000213	8.66319E-06	250.9	27.4763	2.389315	0.105213	1.8251	0.2751	-1.92
Bd2KSpiK	MU	Loose	0.000507	8.59669E-06	457.92	47.4447	0.000207	6.14627E-06	250.9	27.4763	2.446389	0.083566	1.8251	0.2751	-2.16
Bs2KSpipi	MD	Loose	0.000967	1.53679E-05	508.64	51.5951	0.000452	1.25926E-05	230.12	30.5535	2.139211	0.068608	2.2103	0.3693	0.19
Bs2KSpipi	MU	Loose	0.000952	1.39287E-05	508.64	51.5951	0.000449	1.52324E-05	230.12	30.5535	2.119235	0.078235	2.2103	0.3693	0.24
Bs2KSKpi	MD	Tight	0.000417	6.29868E-06	1198.74	41.9516	0.000171	4.86414E-06	488.7	25.2132	2.438512	0.078619	2.4529	0.1529	0.08
Bs2KSKpi	MU	Tight	0.0004	6.38092E-06	1198.74	41.9516	0.000178	5.9098E-06	488.7	25.2132	2.245757	0.08265	2.4529	0.1529	1.19
Bs2KSpiK	MD	Tight	0.000412	6.7001E-06	1205.03	41.6569	0.000176	4.48793E-06	602.53	27.7968	2.343884	0.070974	2.0000	0.1153	-2.54
Bs2KSpiK	MU	Tight	0.000402	8.65812E-06	1205.03	41.6569	0.00018	4.35013E-06	602.53	27.7968	2.239889	0.072597	2.0000	0.1153	-1.76
Bs2KSpipi	MD	Tight	0.000477	1.22642E-05	238.86	22.1852	0.000264	8.25879E-06	125.53	15.5166	1.806581	0.073221	1.9028	0.2942	0.32
Bs2KSpipi	MU	Tight	0.000491	1.32651E-05	238.86	22.1852	0.000279	8.71287E-06	125.53	15.5166	1.760406	0.072649	1.9028	0.2942	0.47
Bs2KSKpi	MD	Loose	0.000523	7.27022E-06	1528.69	55.4698	0.000202	6.15054E-06	602.55	31.9588	2.590243	0.086724	2.5370	0.1630	-0.29
Bs2KSKpi	MU	Loose	0.000506	6.96744E-06	1528.69	55.4698	0.000222	6.01167E-06	602.55	31.9588	2.283094	0.069467	2.5370	0.1630	1.43
Bs2KSpiK	MD	Loose	0.000545	7.62279E-06	1574.82	56.8913	0.000204	5.77684E-06	758.11	34.5958	2.668453	0.084235	2.0773	0.1209	-4.01
Bs2KSpiK	MU	Loose	0.000518	8.6832E-06	1574.82	56.8913	0.000207	5.35767E-06	758.11	34.5958	2.497964	0.076891	2.0773	0.1209	-2.94

Table 6.3: Fit-efficiency comparison for 2016 $B^0_{d,s} \to K^0_S h^+ h'^-$ samples.

6.3 Towards Branching Fraction measurements of $B^0_{d,s} \to K^0_S h^\pm h'^\mp$ with RunII data

One of the goals of $K^0_S h^+ h'^-$ studies is determination of branching fraction for the decay modes of B^0 and B_s to $K^0_S h^\pm h'^\mp$ final states in which $h^{(\prime)}$ is either K or π.

As it was mentioned in Sec. 6.2.2 and specifically in Eq. 6.6 the corrected number of signal events in sqDP can be determined by using the signal yield of the mass-fit $N_{\rm sig}$ and the averaged efficiency over the sqDP, $\bar{\epsilon}$. Now this corrected number of signal $N^{\rm weighted}_{\rm sig}$ can be utilized to calculate the dedicated branching fraction of the decay as

$$\mathcal{B}(B^0_{d,s} \to K^0_S h^\pm h'^\mp) = \frac{N^{\rm weighted}_{B^0_{d,s}\to K^0_S h^\pm h'^\mp}}{\mathcal{L}\,\sigma(b\bar{b})\,f_{d,s}}, \tag{6.7}$$

in which $f_{s,d}$, $\sigma(b\bar{b})$ and $\mathcal{L}$ are fragmentation fraction [148](also known as hadronization fraction), cross-section of $p\bar{p} \to b\bar{b}$ and integrated luminosity at LHCb. In this study instead of dealing with direct values of branching fraction, we determine the ratio of branching fractions with respect to $B^0 \to K^0_S \pi^+\pi^-$ branching fraction. Thank to the ratio, the $\sigma(b\bar{b})$ and $\mathcal{L}$ in numerator and denominator are canceling each and the the branching fraction is determined as follows,

$$\frac{\mathcal{B}(B^0_{d,s} \to K^0_S h^\pm h'^\mp)}{\mathcal{B}(B^0 \to K^0_S \pi^+\pi^-)} = \left(\frac{N^{\rm weighted}_{B^0_{d,s}\to K^0_S h^\pm h'^\mp}}{N^{\rm weighted}_{B^0\to K^0_S \pi^+\pi^-}}\right)\left(\frac{f_d}{f_{d,s}}\right) \tag{6.8}$$

where can be rewritten by using the Eq. 6.6 in terms of $N_{\rm sig}$ and $\bar{\epsilon}$ as,

$$\frac{\mathcal{B}(B^0_{d,s} \to K^0_S h^\pm h'^\mp)}{\mathcal{B}(B^0 \to K^0_S \pi^+\pi^-)} = \left(\frac{N_{B^0_{d,s}\to K^0_S h^\pm h'^\mp}\ \bar{\epsilon}_{B^0\to K^0_S\pi^+\pi^-}}{N_{B^0\to K^0_S\pi^+\pi^-}\ \bar{\epsilon}_{B^0_{d,s}\to K^0_S h^\pm h'^\mp}}\right)\left(\frac{f_d}{f_{d,s}}\right). \tag{6.9}$$

Some words of caution are in order before presenting the current estimates. The numbers used as inputs are determined from the simultaneous mass fit to the four experimental spectra of interest on one hand and the average efficiency estimated from simulated signal events adequately corrected (with data calibration samples) for simulation trigger and tracking inaccuracies and weighted by the Dalitz plane distribution of the events in the data. Both types of observables (yields and efficiencies) are still preliminary. In particular, the yields obtained by the fit to the $K^0_S K^+ K^-$ spectrum and are still blinded and the ratio of branching fraction for this mode is not reported. Moreover, though several critical systematic uncertainties have been estimated, not all of them are presently at hand. The purpose of the current derivation is therefore to check the internal consistency of the measurements.

The table 6.4 shows the results of branching fraction ratios obtained for the RunII data. It is first checked that all the Down-Down and Long-Long separated results are consistent. As an example, we report the branching fraction ratio of $B_s \to K^0_S \pi^+\pi^-$ for

Down-Down and Long-Long for the 2018 sample with the highest statistics, which are found to be 0.259 ± 0.022 and 0.244 ± 0.029, respectively.

Then by implementing an inverse-variance weighted averaging [149] between Down-Down and Long-Long category of each mode, the ratio of branching fractions for each RunII year are reported in table 6.4.

Branching Fraction	year		
	2016	2017	2018
$\frac{\mathcal{B}(B_s \to K^0_S \pi^+ \pi^-)}{\mathcal{B}(B^0 \to K^0_S \pi^+ \pi^-)}$	0.300 ± 0.022	0.254 ± 0.018	0.293 ± 0.018
$\frac{\mathcal{B}(B^0 \to K^0_S K^\pm \pi^\mp)}{\mathcal{B}(B^0 \to K^0_S \pi^+ \pi^-)}$	0.140 ± 0.010	0.144 ± 0.009	0.141 ± 0.008
$\frac{\mathcal{B}(B_s \to K^0_S K^\pm \pi^\mp)}{\mathcal{B}(B^0 \to K^0_S \pi^+ \pi^-)}$	1.930 ± 0.064	1.872 ± 0.058	1.837 ± 0.054

Table 6.4: Results of branching fraction ratio measurements of $B_s \to K^0_S \pi^+ \pi^-$,$B^0 \to K^0_S K^\pm \pi^\mp$ and $B_s \to K^0_S K^\pm \pi^\mp$ with respect to the $B^0 \to K^0_S \pi^+ \pi^-$ for RunII data. The numbers are quoted only with the statistical uncertainty related to the mass-fit results.

The branching fraction results are found consistent through the entire RunII. This result supplements the consistency checks which were performed and presented in tables 6.1-6.3.

The obtained preliminary ratio of branching fractions for $B^0 \to K^0_S K^\pm \pi^\mp$ and $B_s \to K^0_S K^\pm \pi^\mp$ are furthermore consistent within statistical uncertainties with the results of former study performed on the RunI samples [20]. It should be noted however that the determined ratio for $B_s \to K^0_S \pi^+ \pi^-$ is departing by more than two statistical standard deviations with the result quoted in [20].

Though the accurate comparison with the former results should come with the actual update of measurements with RunI, it is worth mentioning that a profound revision of the weighting of the efficiency in the Dalitz plane in order to maximally used the information present in the data is ongoing. It consists of using the information of the years with higher statistics in order to determine the average efficiency for the years with lower statistics. The comparison of the different determinations will provide an additional handle to estimate an uncertainty about the efficiency weighting.

Conclusion and outlook

Through this study, we have implemented and developed new methods to provide a common tool to perform optimal selections for the future $B^0_{d,s} \to K^0_S h^\pm h'^\mp$ studies and present the possible correction and systematic which are subject to it.

The PID variables are studied and the existing discrepancy between the MC and real data according to the PID responses is corrected by using `PIDCorr` methods. This method allows us to preserve the correlation between the PID variables during the process of PID correction. Then by selecting the `ProbNNh` variables (h is π , K or p), a new MVA tool is developed by using a XGBoost algorithm to fight against the cross-feed backgrounds.

Another MVA tool (Topological), which is developed in LPNHE `KShh` group, is trained against the combinatorial background. Using the output of two MVAs a 2-dimensional optimization is designed. In this optimization, a measure is defined to determine the set of cuts that maximize the significance of our samples.

Besides PID, other possible corrections (relevant to tracking and L0 Triggering process) to rectify the differences between MC and data are studied and evaluated by using appropriate techniques. In addition, several sources of systematic are introduced and evaluated in bins of Dalitz plane.

Finally, the aforementioned corrections are applied to the MC samples, and the average efficiency of the signal is calculated. Using the results of the mass-fit, a consistency check between the efficiency patterns over the Dalitz plane and the mass-fit results is performed. This check confirms that the developed tools, their optimal cuts, and performed mass-fit on RunII data set are designed and developed properly. Also using preliminary mass-fit and averaged efficiency, an estimation of the ratio of branching fractions is performed by using the RunII data. The results of RunII display a satisfactory consistency through the whole RunII and also the results for the decay modes $B^0 \to K^0_S K^\pm \pi^\mp$ and $B_s \to K^0_S K^\pm \pi^\mp$ are showing a good agreement with respect to the former study results [20]. An acceptable agreement is observed for the measurement of the decay mode $B_s \to K^0_S \pi^+ \pi^-$. Yet a tension at the level of 2-3 statistical standard deviations can be noticed. This might be indicative of limitations in the derivation of the candidate distribution in the Dalitz plane for the modes with lower statistics. This is the subject of ongoing efforts in `KShh` LHCb group.

On top of the addition of RunII data and accessing to the larger data set (which only consist of RunI data), the better performance of the prepared tools (in current updated analysis) enables us to increase the statistics of signal event and be able to perform the following studies: the search of the unobserved decay mode $B_s \to K^0_S K^+ K^-$ and the

update of the branching fraction of the five companion decay modes; the time-dependent Dalitz Plot analyses $B^0 \to K^0_S K^+ K^-$ and $B^0 \to K^0_S \pi^+ \pi^-$; the first amplitude analysis of $B^0 \to K^0_S \pi^+ \pi^-$

Appendix A

PID Corrections

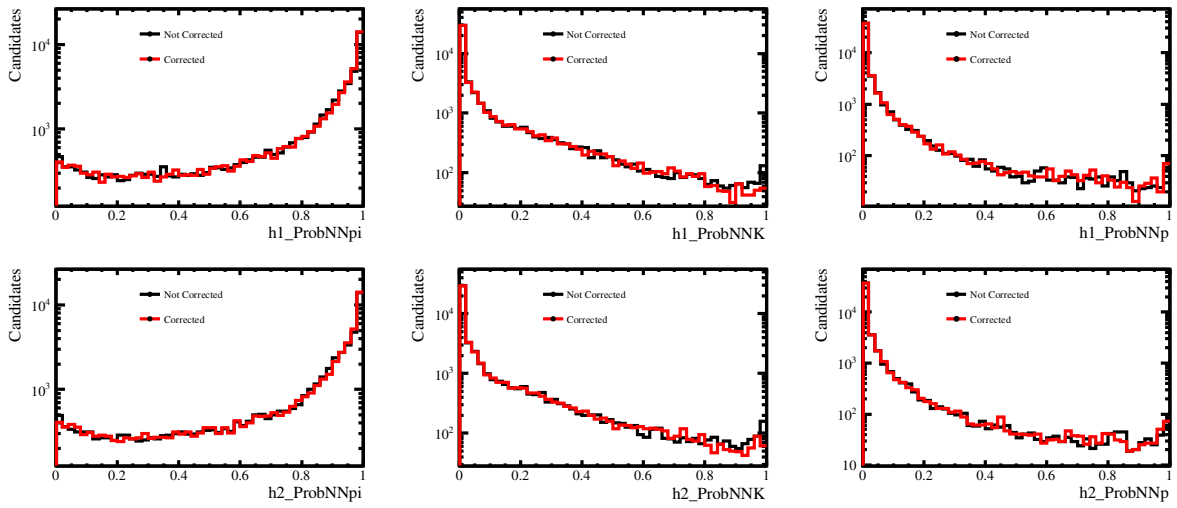

Figure A.1: Comparison between the Corrected (Red) and Non-corrected (Black) for $B^0 \to K^0_S \pi^+ \pi^-$ samples of 2018 *MagDown* for Long-LongK^0_S reconstructions. The Top (Bottom) row denote the distributions for h1 (h2) hadrons. The Plots are shown in logarithmic scale.

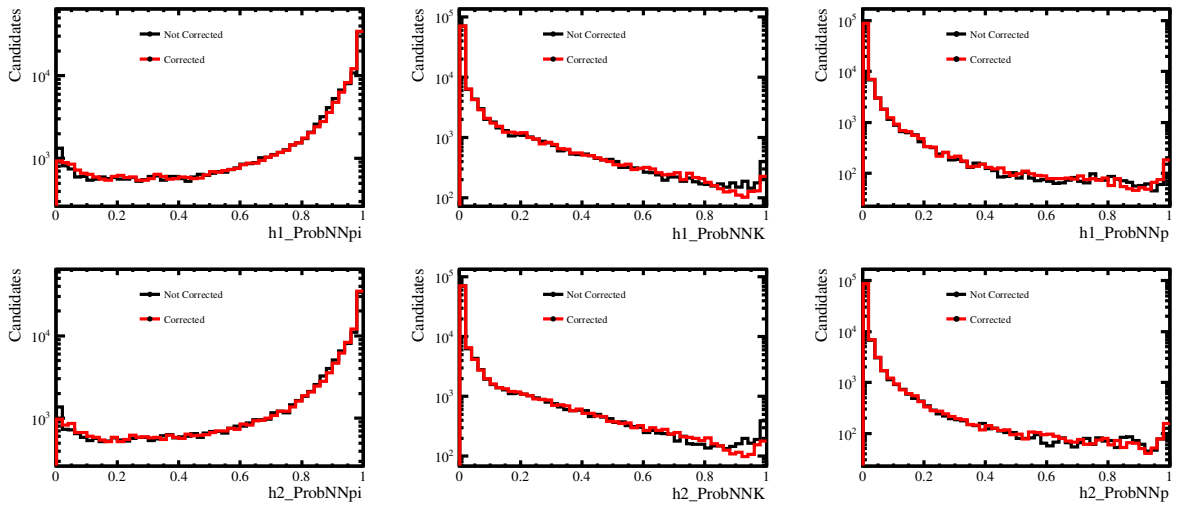

Figure A.2: Comparison between the Corrected (Red) and Non-corrected (Black) for $B_s \to K^0_S \pi^+ \pi^-$ samples of 2018 *MagDown* for Down-DownK^0_S reconstructions. The Top (Bottom) row denote the distributions for h1 (h2) hadrons. The Plots are shown in logarithmic scale.

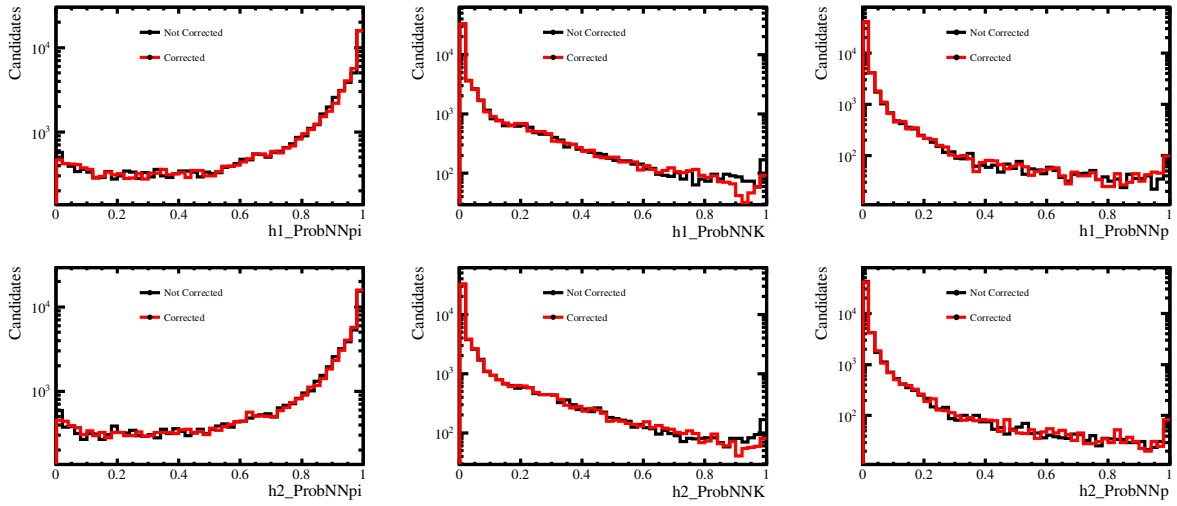

Figure A.3: Comparison between the Corrected (Red) and Non-corrected (Black) for $B_s \to K^0_S \pi^+ \pi^-$ samples of 2018 *MagDown* for Long-LongK^0_S reconstructions. The Top (Bottom) row denote the distributions for h1 (h2) hadrons. The Plots are shown in logarithmic scale.

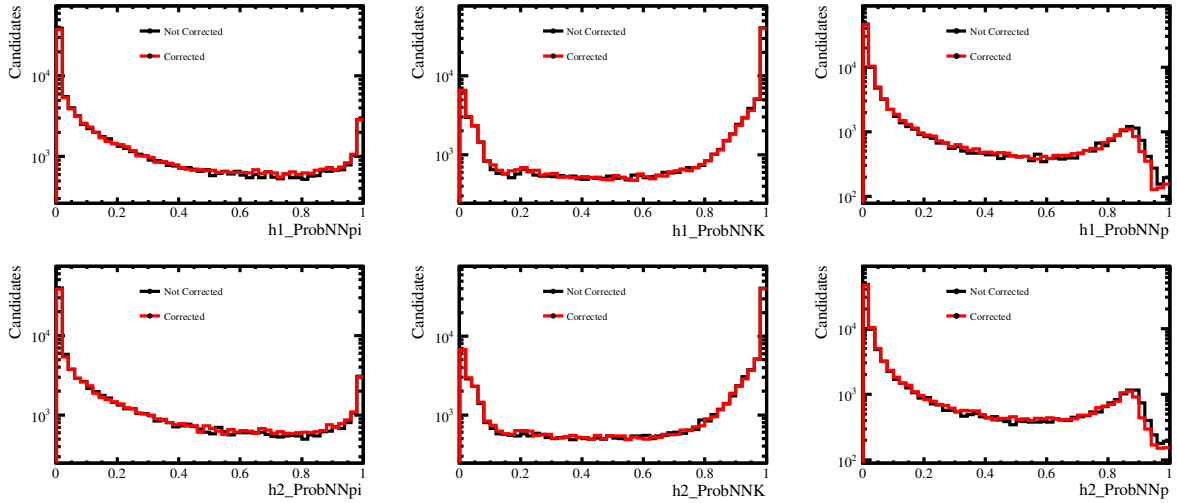

Figure A.4: Comparison between the Corrected (Red) and Non-corrected (Black) for $B^0 \to K^0_S K^+ K^-$ samples of 2018 *MagDown* for Down-DownK^0_S reconstructions. The Top (Bottom) row denote the distributions for h1 (h2) hadrons. The Plots are shown in logarithmic scale.

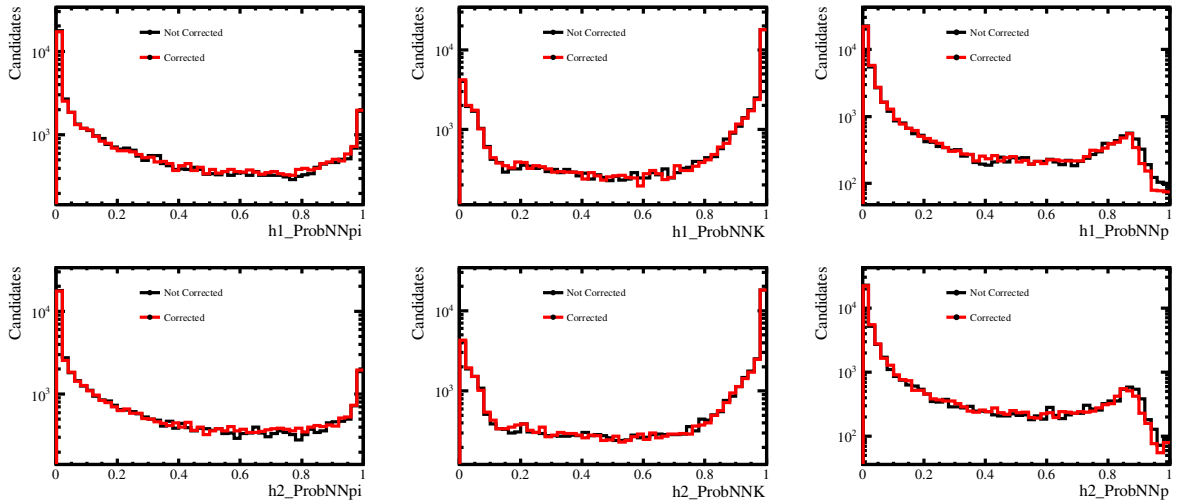

Figure A.5: Comparison between the Corrected (Red) and Non-corrected (Black) for $B^0 \to K^0_S K^+ K^-$ samples of 2018 *MagDown* for Long-LongK^0_S reconstructions. The Top (Bottom) row denote the distributions for h1 (h2) hadrons. The Plots are shown in logarithmic scale.

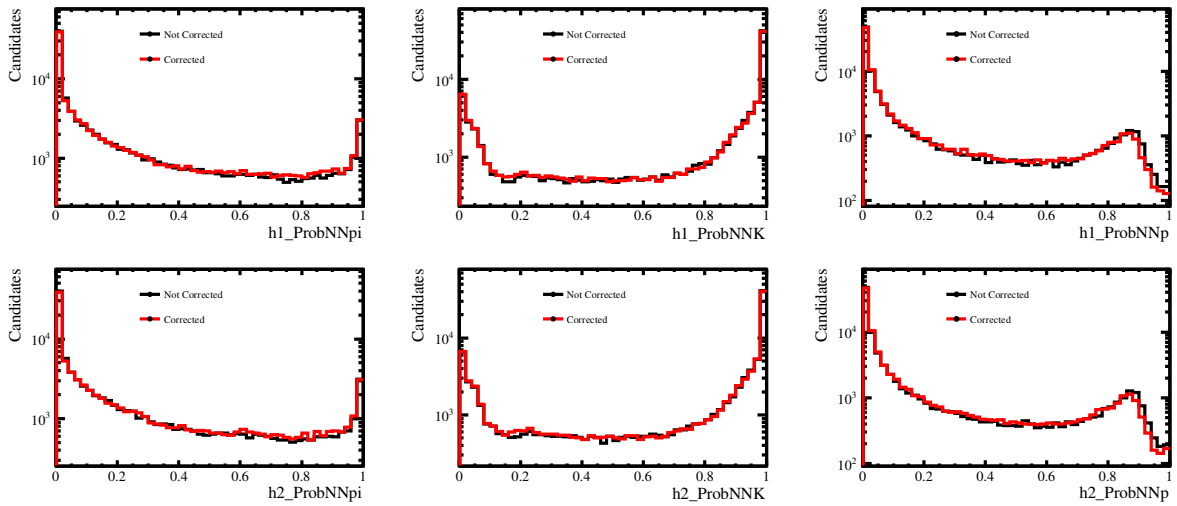

Figure A.6: Comparison between the Corrected (Red) and Non-corrected (Black) for $B_s \to K^0_S K^+ K^-$ samples of 2018 *MagDown* for Down-DownK^0_S reconstructions. The Top (Bottom) row denote the distributions for h1 (h2) hadrons. The Plots are shown in logarithmic scale.

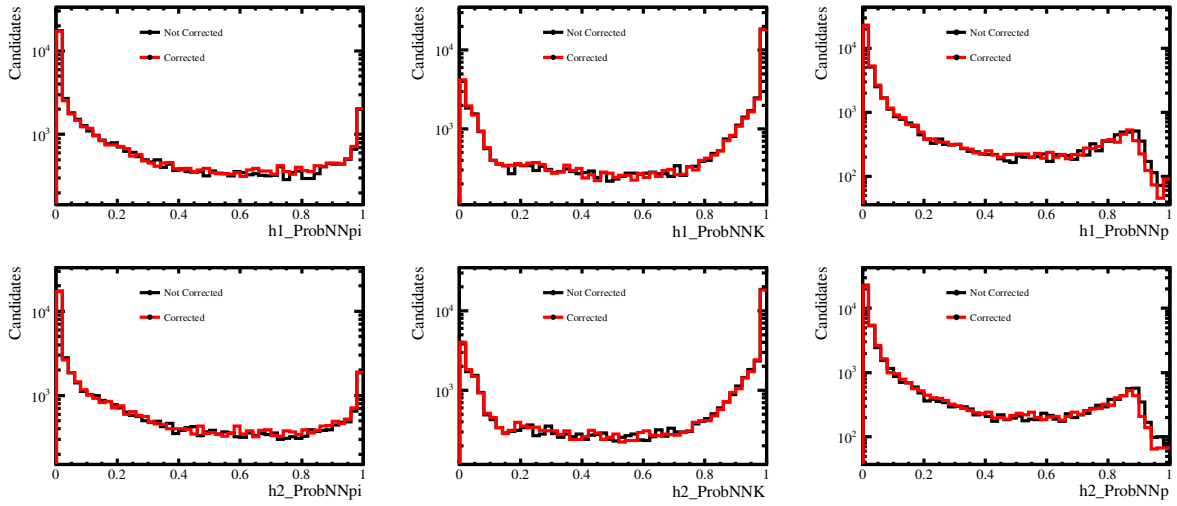

Figure A.7: Comparison between the Corrected (Red) and Non-corrected (Black) for $B_s \to K^0_S K^+ K^-$ samples of 2018 *MagDown* for Long-LongK^0_S reconstructions. The Top (Bottom) row denote the distributions for h1 (h2) hadrons. The Plots are shown in logarithmic scale.

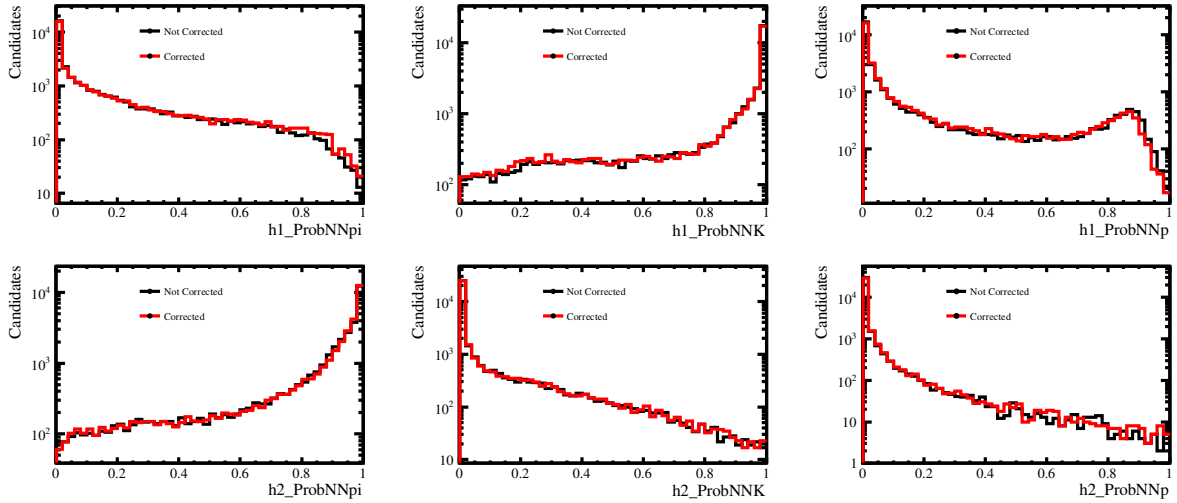

Figure A.8: Comparison between the Corrected (Red) and Non-corrected (Black) for $B^0 \to K^0_S K^+ \pi^-$ samples of 2018 *MagDown* for Down-DownK^0_S reconstructions. The Top (Bottom) row denote the distributions for h1 (h2) hadrons. The Plots are shown in logarithmic scale.

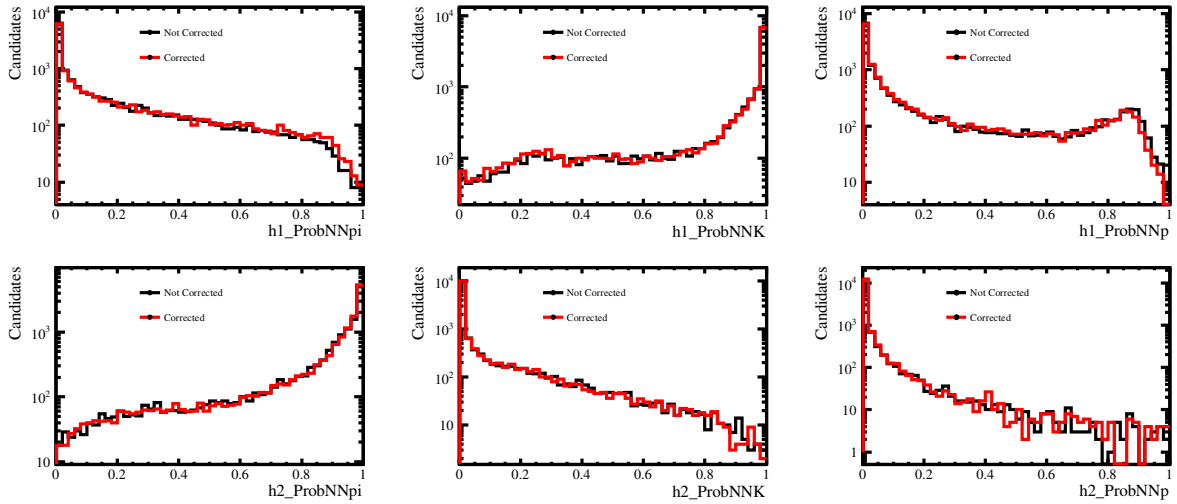

Figure A.9: Comparison between the Corrected (Red) and Non-corrected (Black) for $B^0 \to K^0_S K^+ \pi^-$ samples of 2018 *MagDown* for Long-LongK^0_S reconstructions. The Top (Bottom) row denote the distributions for h1 (h2) hadrons. The Plots are shown in logarithmic scale.

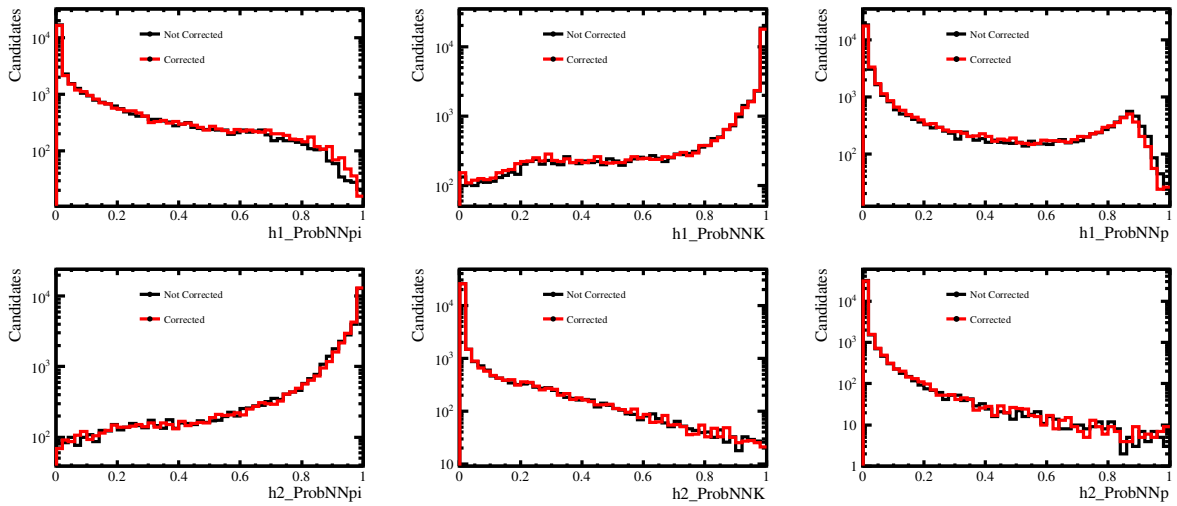

Figure A.10: Comparison between the Corrected (Red) and Non-corrected (Black) for $B_s \to K^0_S K^+ \pi^-$ samples of 2018 *MagDown* for Down-DownK^0_S reconstructions. The Top (Bottom) row denote the distributions for h1 (h2) hadrons. The Plots are shown in logarithmic scale.

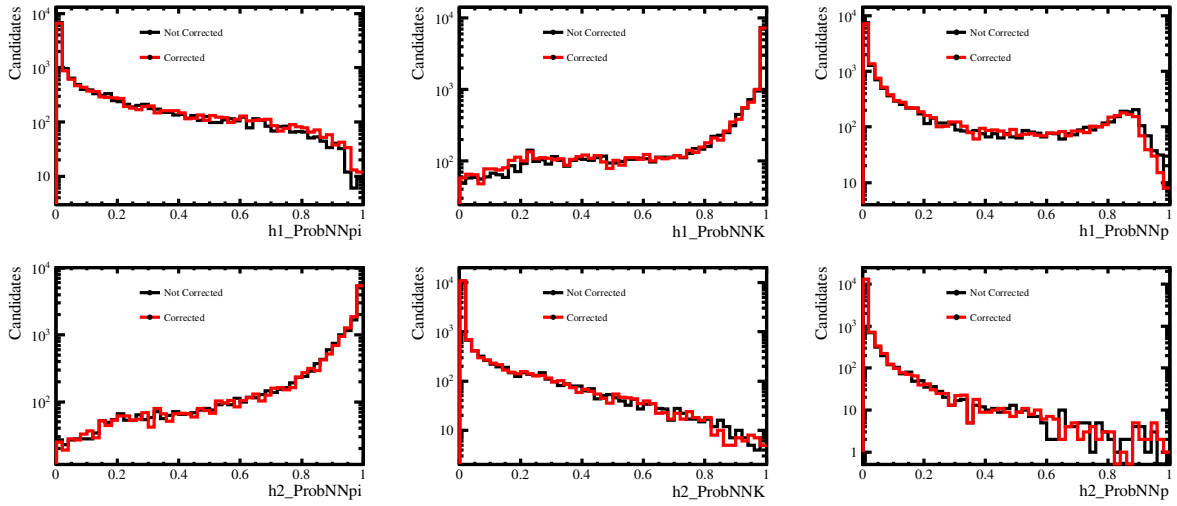

Figure A.11: Comparison between the Corrected (Red) and Non-corrected (Black) for $B_s \to K^0_S K^+ \pi^-$ samples of 2018 *MagDown* for Long-LongK^0_S reconstructions. The Top (Bottom) row denote the distributions for h1 (h2) hadrons. The Plots are shown in logarithmic scale.

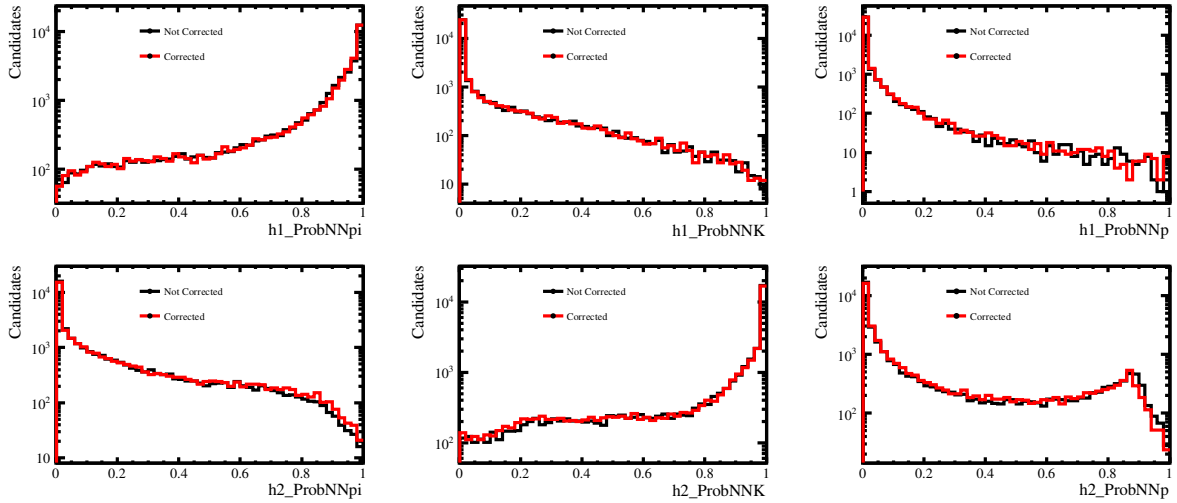

Figure A.12: Comparison between the Corrected (Red) and Non-corrected (Black) for $B^0 \to K^0_S \pi^+ K^-$ samples of 2018 *MagDown* for Down-DownK^0_S reconstructions. The Top (Bottom) row denote the distributions for h1 (h2) hadrons. The Plots are shown in logarithmic scale.

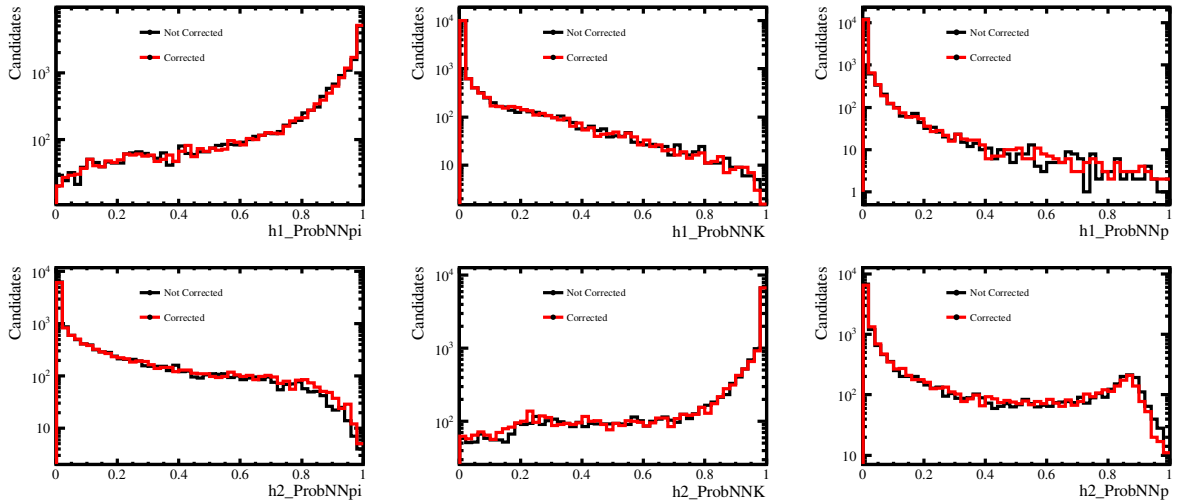

Figure A.13: Comparison between the Corrected (Red) and Non-corrected (Black) for $B^0 \to K^0_S \pi^+ K^-$ samples of 2018 *MagDown* for Long-LongK^0_S reconstructions. The Top (Bottom) row denote the distributions for h1 (h2) hadrons. The Plots are shown in logarithmic scale.

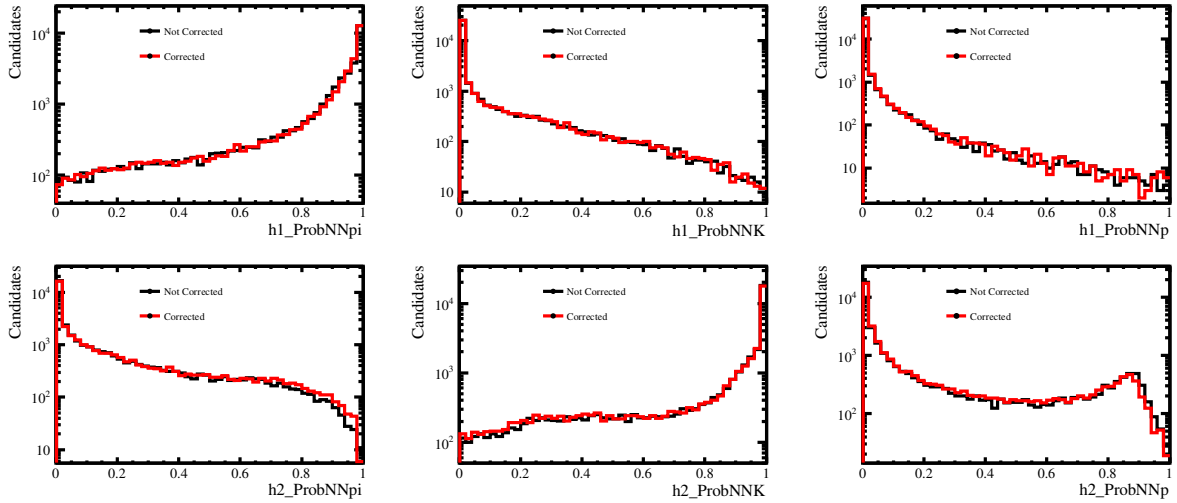

Figure A.14: Comparison between the Corrected (Red) and Non-corrected (Black) for $B_s \to K^0_S \pi^+ K^-$ samples of 2018 *MagDown* for Down-DownK^0_S reconstructions. The Top (Bottom) row denote the distributions for h1 (h2) hadrons. The Plots are shown in logarithmic scale.

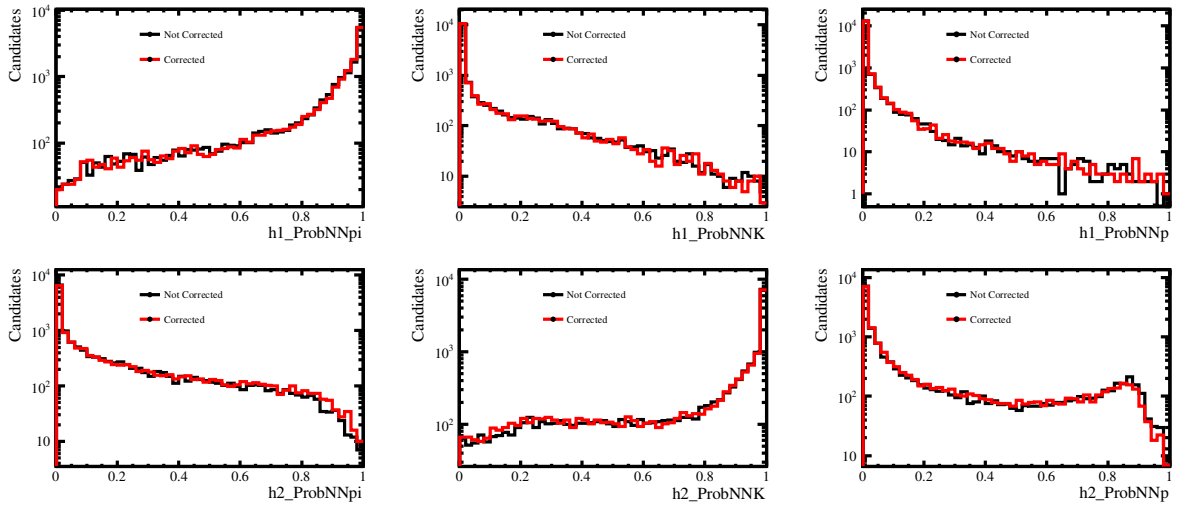

Figure A.15: Comparison between the Corrected (Red) and Non-corrected (Black) for $B_s \to K^0_S \pi^+ K^-$ samples of 2018 *MagDown* for Long-LongK^0_S reconstructions. The Top (Bottom) row denote the distributions for h1 (h2) hadrons. The Plots are shown in logarithmic scale.

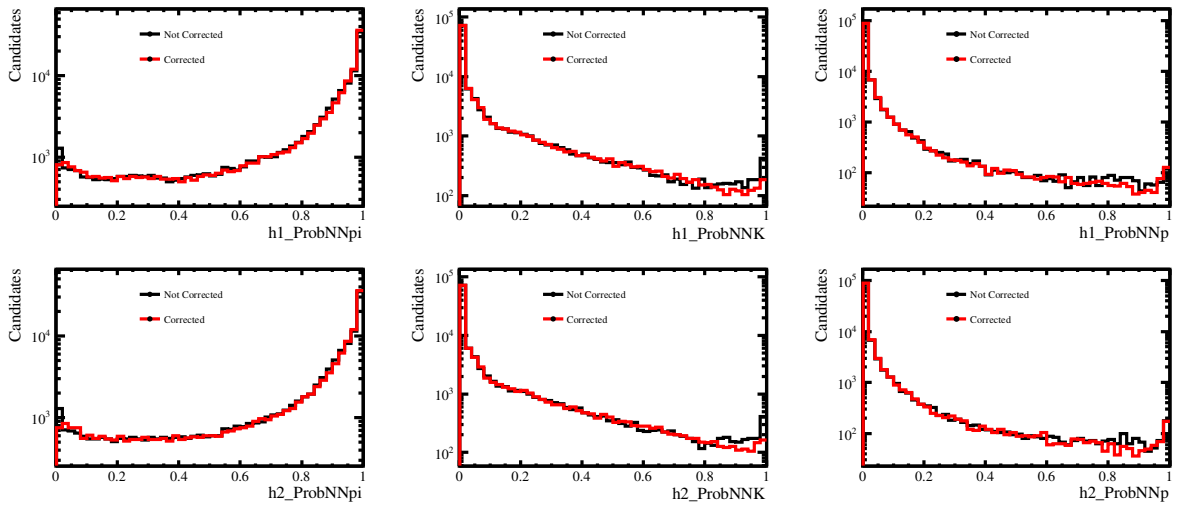

Figure A.16: Comparison between the Corrected (Red) and Non-corrected (Black) for $B^0 \to K^0_S \pi^+ \pi^-$ samples of 2017 *MagDown* for Down-DownK^0_S reconstructions. The Top (Bottom) row denote the distributions for h1 (h2) hadrons. The Plots are shown in logarithmic scale.

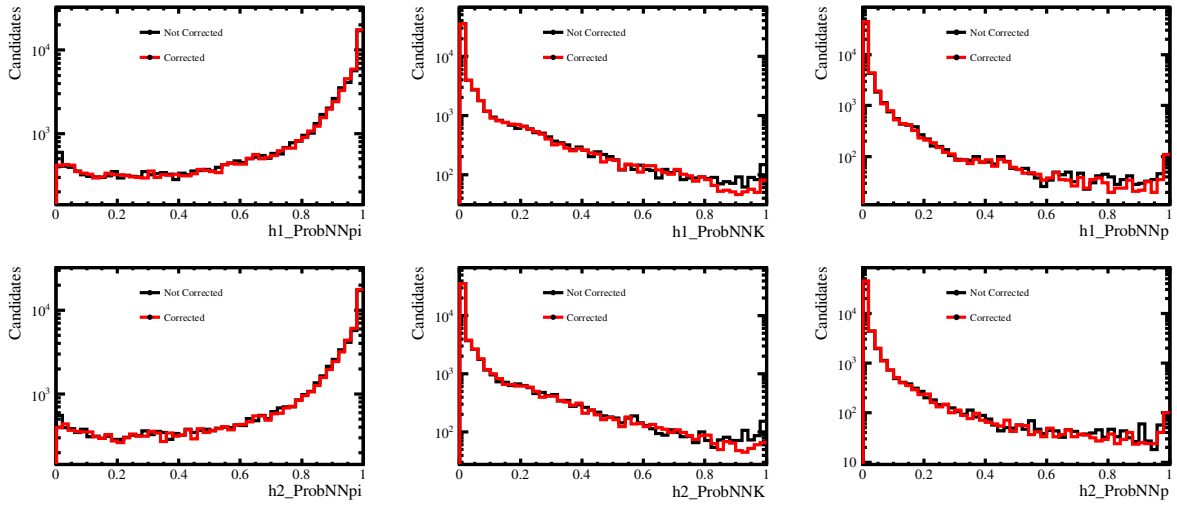

Figure A.17: Comparison between the Corrected (Red) and Non-corrected (Black) for $B^0 \to K^0_S \pi^+ \pi^-$ samples of 2017 *MagDown* for Long-LongK^0_S reconstructions. The Top (Bottom) row denote the distributions for h1 (h2) hadrons. The Plots are shown in logarithmic scale.

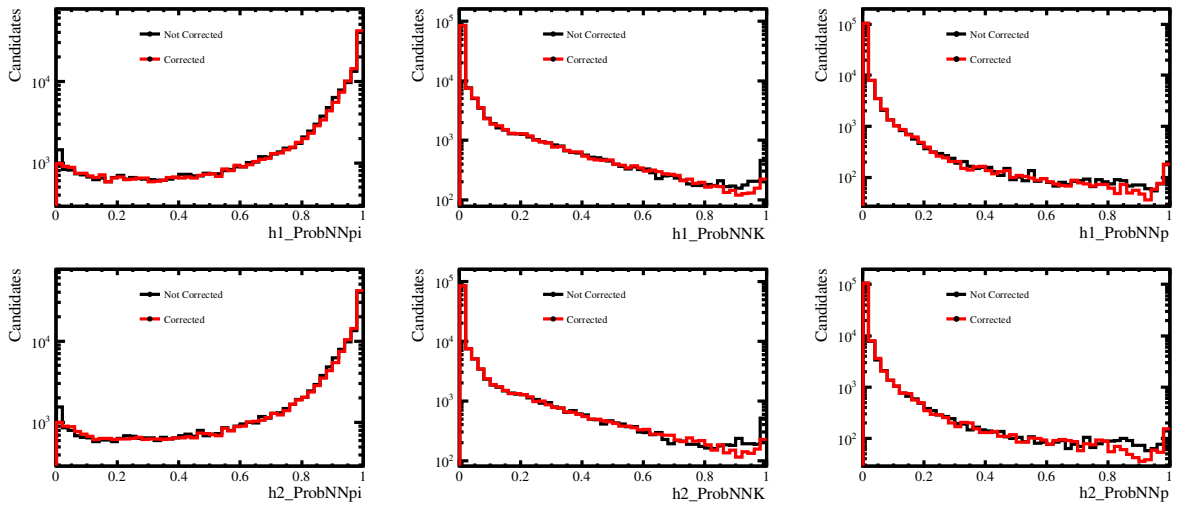

Figure A.18: Comparison between the Corrected (Red) and Non-corrected (Black) for $B_s \to K^0_S \pi^+ \pi^-$ samples of 2017 *MagDown* for Down-DownK^0_S reconstructions. The Top (Bottom) row denote the distributions for h1 (h2) hadrons. The Plots are shown in logarithmic scale.

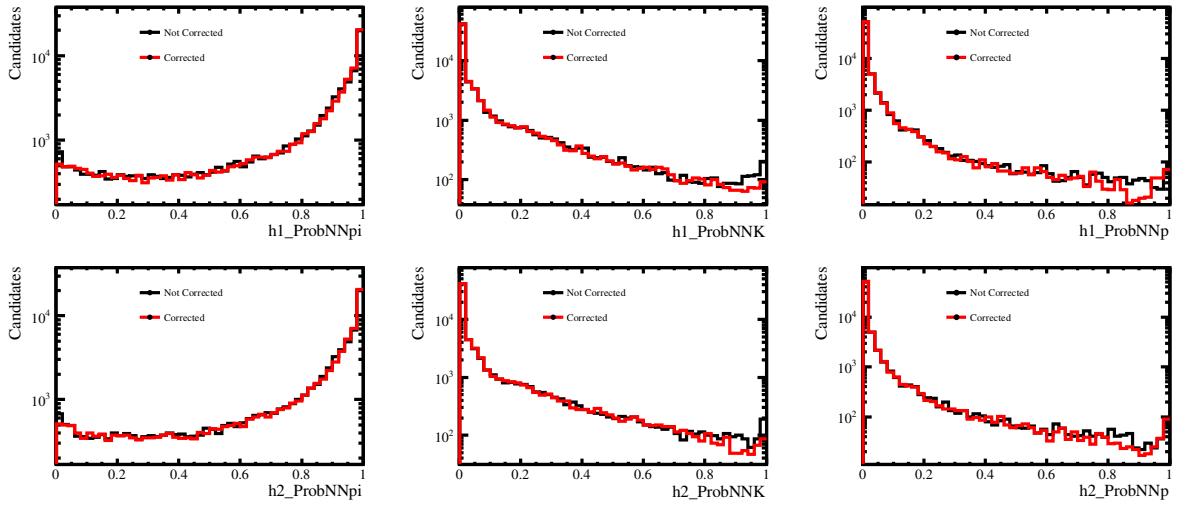

Figure A.19: Comparison between the Corrected (Red) and Non-corrected (Black) for $B_s \to K^0_S \pi^+ \pi^-$ samples of 2017 *MagDown* for Long-LongK^0_S reconstructions. The Top (Bottom) row denote the distributions for h1 (h2) hadrons. The Plots are shown in logarithmic scale.

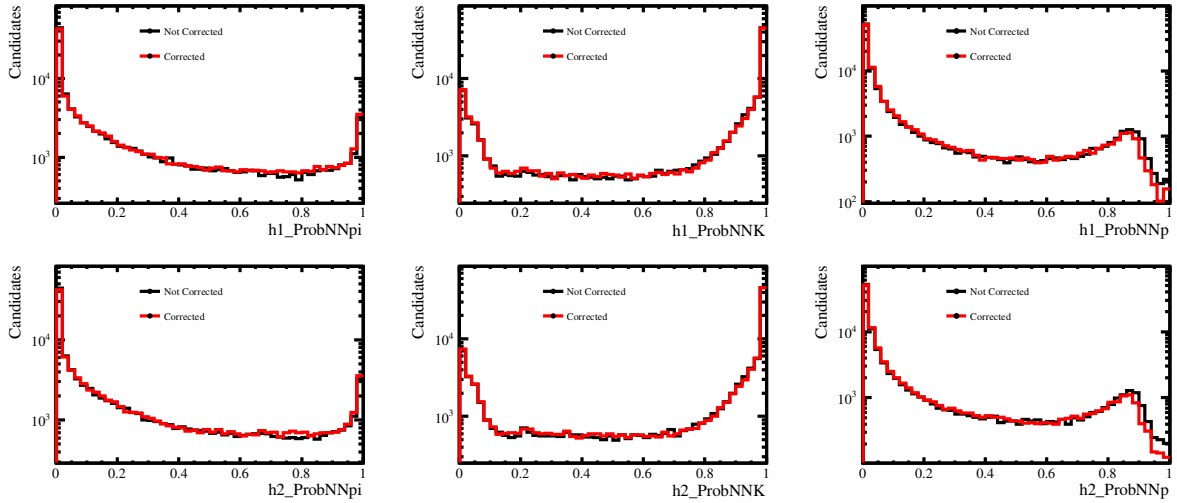

Figure A.20: Comparison between the Corrected (Red) and Non-corrected (Black) for $B^0 \to K^0_S K^+ K^-$ samples of 2017 *MagDown* for Down-DownK^0_S reconstructions. The Top (Bottom) row denote the distributions for h1 (h2) hadrons. The Plots are shown in logarithmic scale.

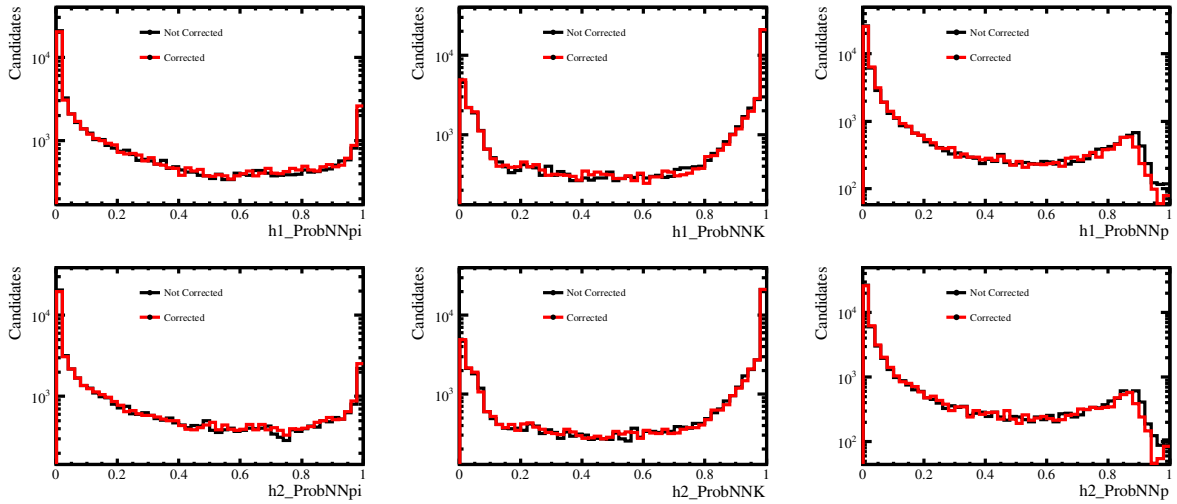

Figure A.21: Comparison between the Corrected (Red) and Non-corrected (Black) for $B^0 \to K^0_S K^+ K^-$ samples of 2017 *MagDown* for Long-LongK^0_S reconstructions. The Top (Bottom) row denote the distributions for h1 (h2) hadrons. The Plots are shown in logarithmic scale.

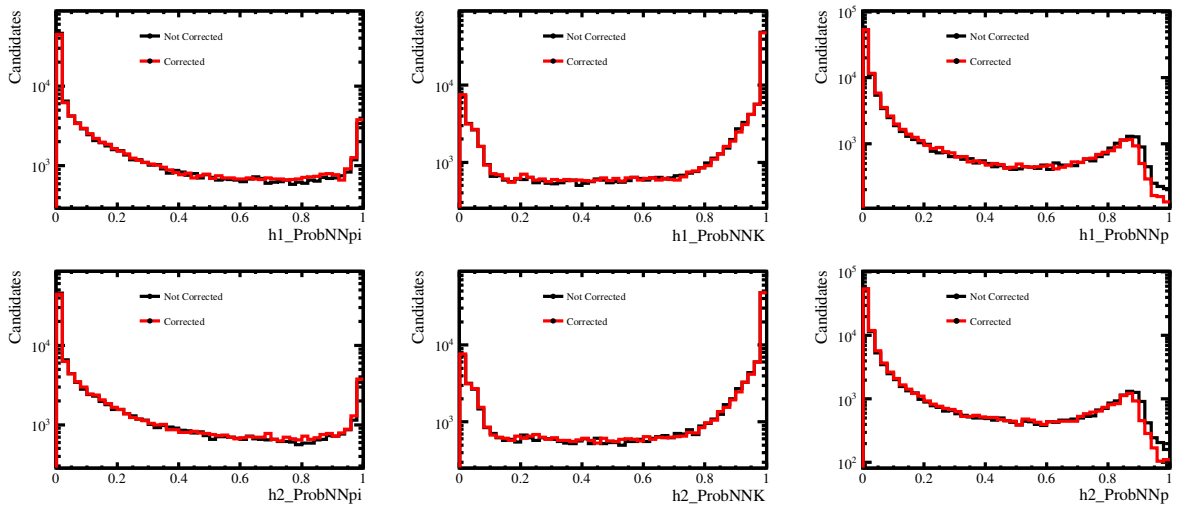

Figure A.22: Comparison between the Corrected (Red) and Non-corrected (Black) for $B_s \to K^0_S K^+ K^-$ samples of 2017 *MagDown* for Down-DownK^0_S reconstructions. The Top (Bottom) row denote the distributions for h1 (h2) hadrons. The Plots are shown in logarithmic scale.

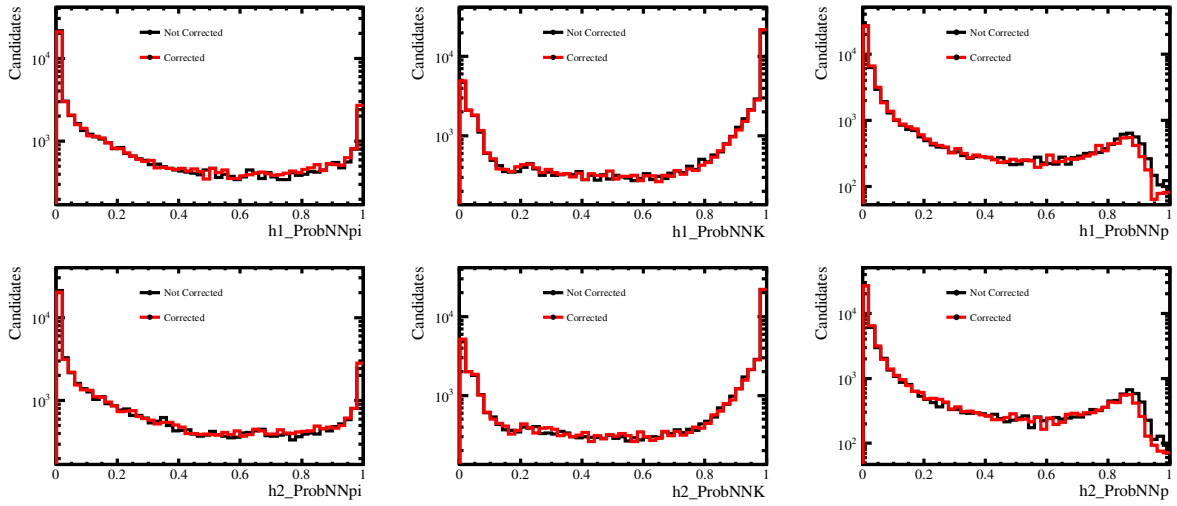

Figure A.23: Comparison between the Corrected (Red) and Non-corrected (Black) for $B_s \to K^0_S K^+ K^-$ samples of 2017 *MagDown* for Long-LongK^0_S reconstructions. The Top (Bottom) row denote the distributions for h1 (h2) hadrons. The Plots are shown in logarithmic scale.

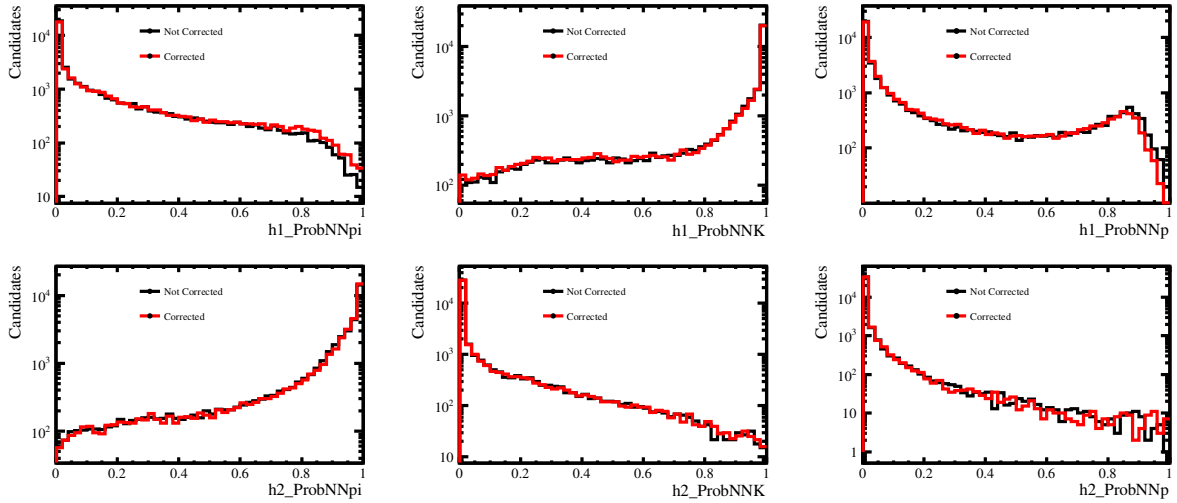

Figure A.24: Comparison between the Corrected (Red) and Non-corrected (Black) for $B^0 \to K^0_S K^+ \pi^-$ samples of 2017 *MagDown* for Down-DownK^0_S reconstructions. The Top (Bottom) row denote the distributions for h1 (h2) hadrons. The Plots are shown in logarithmic scale.

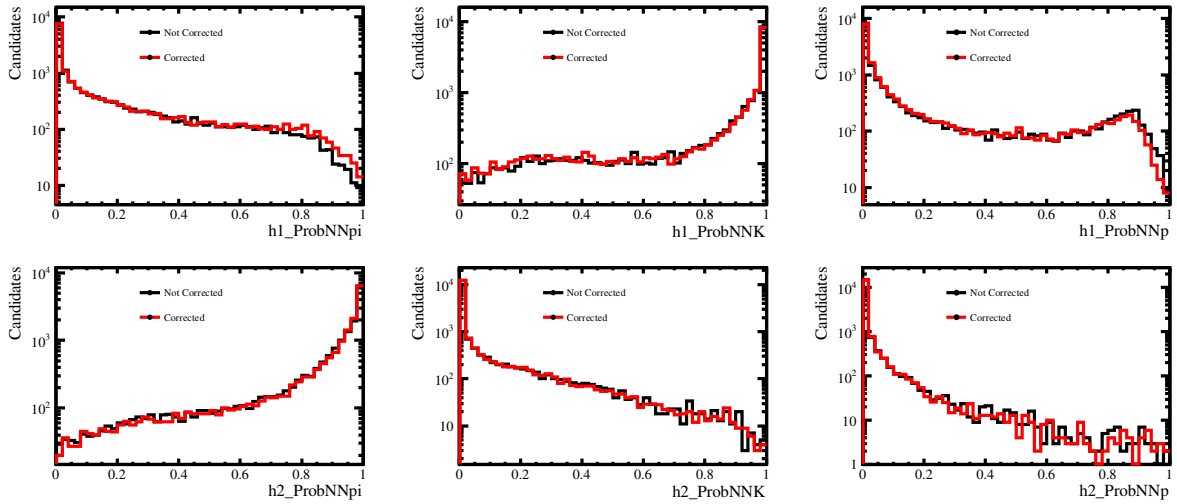

Figure A.25: Comparison between the Corrected (Red) and Non-corrected (Black) for $B^0 \to K^0_S K^+ \pi^-$ samples of 2017 *MagDown* for Long-LongK^0_S reconstructions. The Top (Bottom) row denote the distributions for h1 (h2) hadrons. The Plots are shown in logarithmic scale.

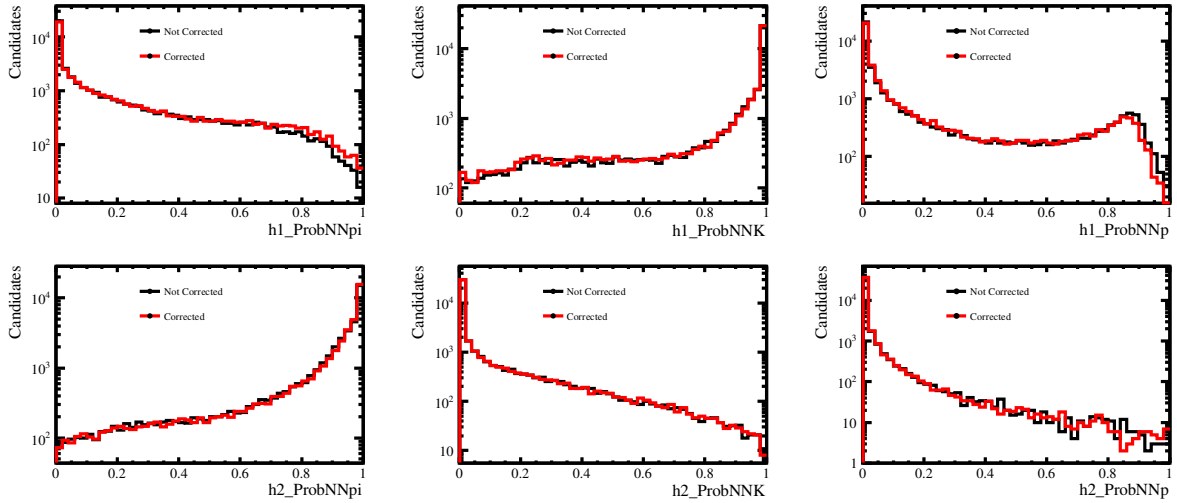

Figure A.26: Comparison between the Corrected (Red) and Non-corrected (Black) for $B_s \to K^0_S K^+ \pi^-$ samples of 2017 *MagDown* for Down-DownK^0_S reconstructions. The Top (Bottom) row denote the distributions for h1 (h2) hadrons. The Plots are shown in logarithmic scale.

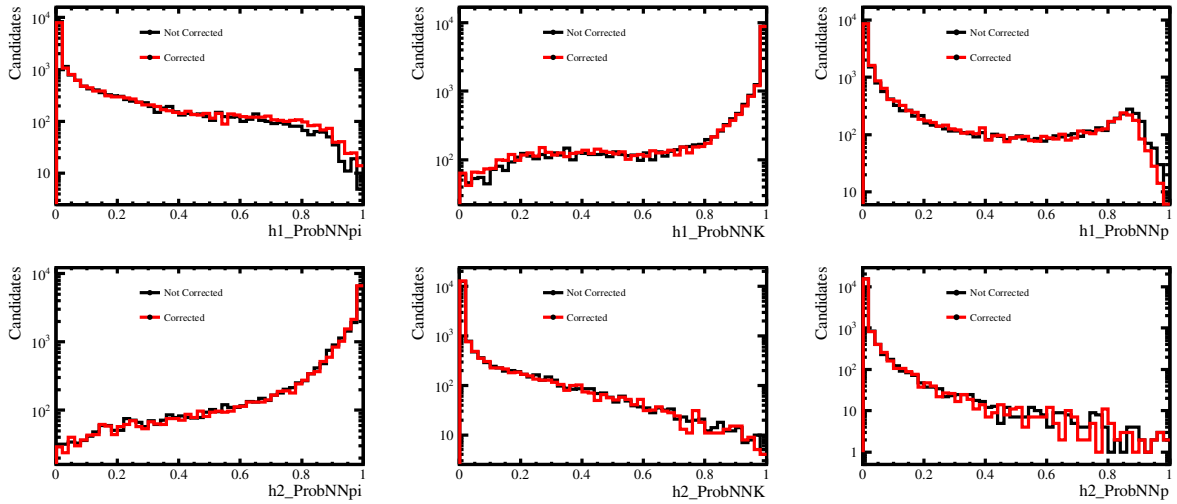

Figure A.27: Comparison between the Corrected (Red) and Non-corrected (Black) for $B_s \to K^0_S K^+ \pi^-$ samples of 2017 *MagDown* for Long-LongK^0_S reconstructions. The Top (Bottom) row denote the distributions for h1 (h2) hadrons. The Plots are shown in logarithmic scale.

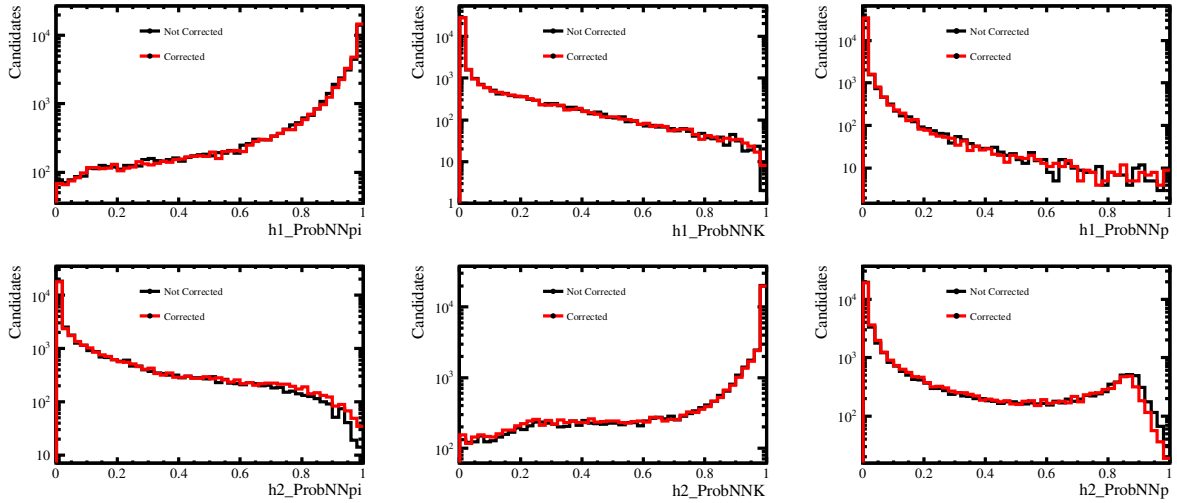

Figure A.28: Comparison between the Corrected (Red) and Non-corrected (Black) for $B^0 \to K^0_S \pi^+ K^-$ samples of 2017 *MagDown* for Down-DownK^0_S reconstructions. The Top (Bottom) row denote the distributions for h1 (h2) hadrons. The Plots are shown in logarithmic scale.

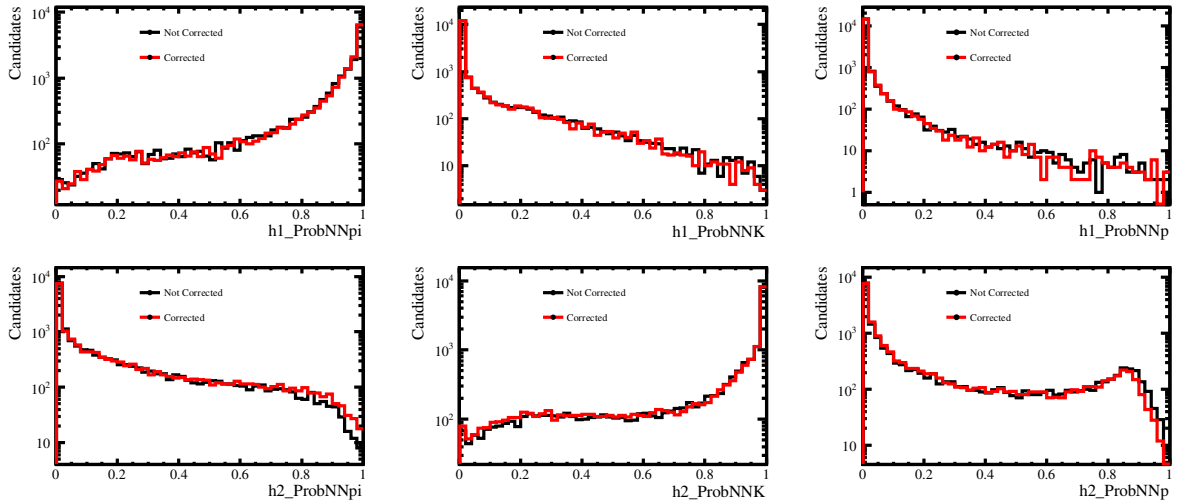

Figure A.29: Comparison between the Corrected (Red) and Non-corrected (Black) for $B^0 \to K^0_S \pi^+ K^-$ samples of 2017 *MagDown* for Long-LongK^0_S reconstructions. The Top (Bottom) row denote the distributions for h1 (h2) hadrons. The Plots are shown in logarithmic scale.

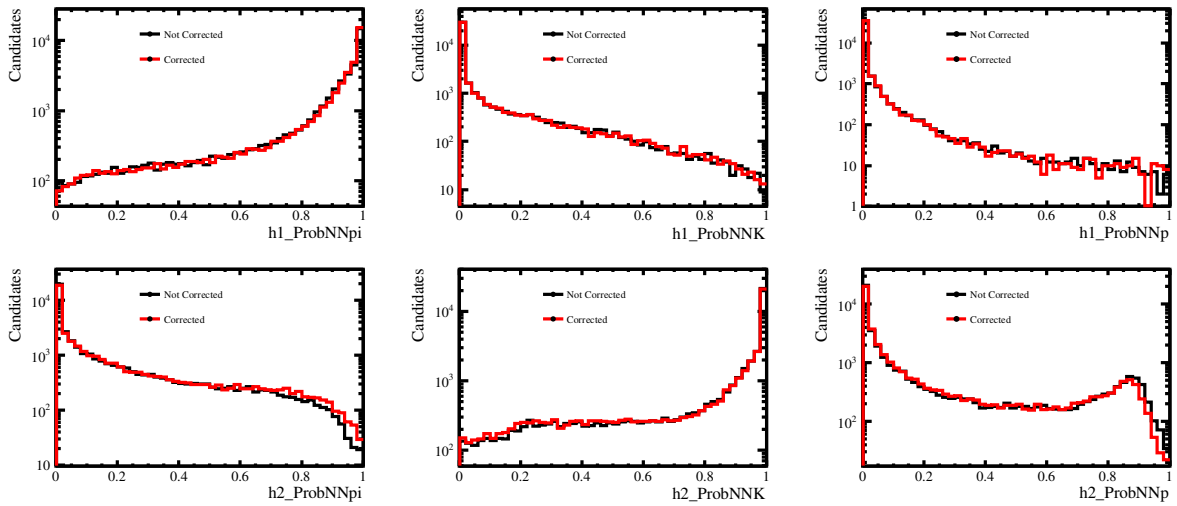

Figure A.30: Comparison between the Corrected (Red) and Non-corrected (Black) for $B_s \to K^0_S \pi^+ K^-$ samples of 2017 *MagDown* for Down-DownK^0_S reconstructions. The Top (Bottom) row denote the distributions for h1 (h2) hadrons. The Plots are shown in logarithmic scale.

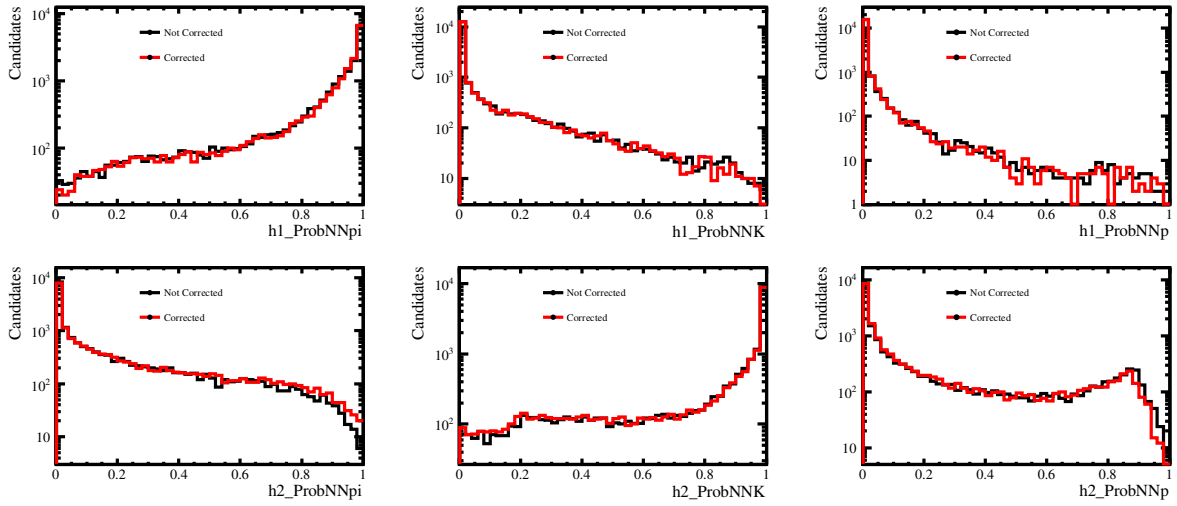

Figure A.31: Comparison between the Corrected (Red) and Non-corrected (Black) for $B_s \to K^0_S \pi^+ K^-$ samples of 2017 *MagDown* for Long-LongK^0_S reconstructions. The Top (Bottom) row denote the distributions for h1 (h2) hadrons. The Plots are shown in logarithmic scale.

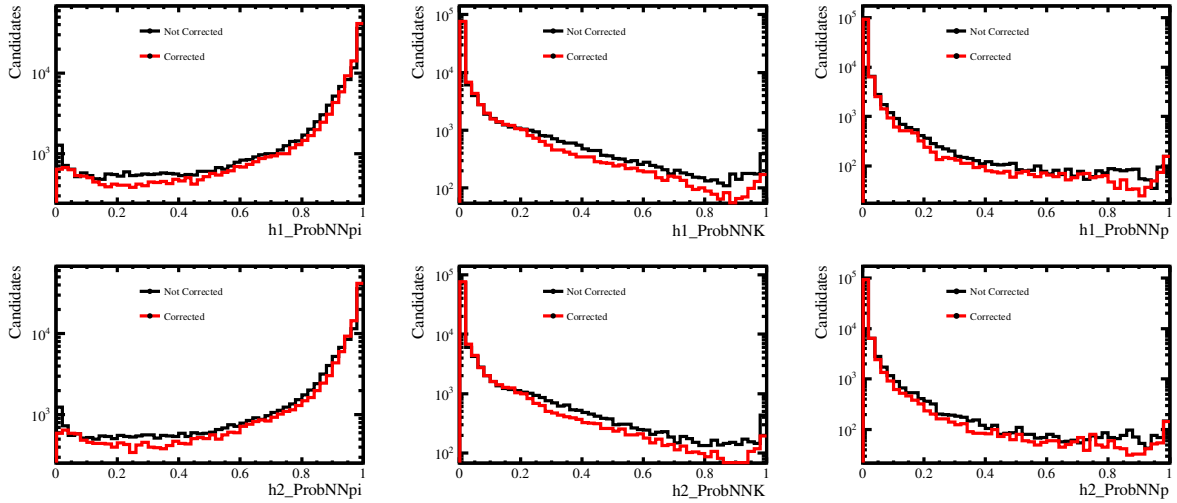

Figure A.32: Comparison between the Corrected (Red) and Non-corrected (Black) for $B^0 \to K^0_S \pi^+ \pi^-$ samples of 2016 *MagDown* for Down-DownK^0_S reconstructions. The Top (Bottom) row denote the distributions for h1 (h2) hadrons. The Plots are shown in logarithmic scale.

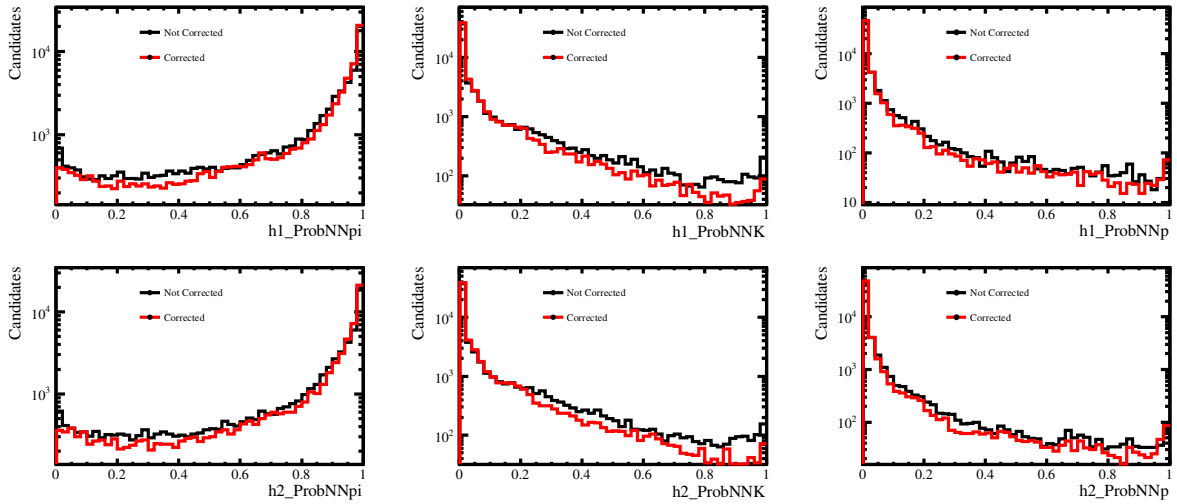

Figure A.33: Comparison between the Corrected (Red) and Non-corrected (Black) for $B^0 \to K^0_S \pi^+ \pi^-$ samples of 2016 *MagDown* for Long-LongK^0_S reconstructions. The Top (Bottom) row denote the distributions for h1 (h2) hadrons. The Plots are shown in logarithmic scale.

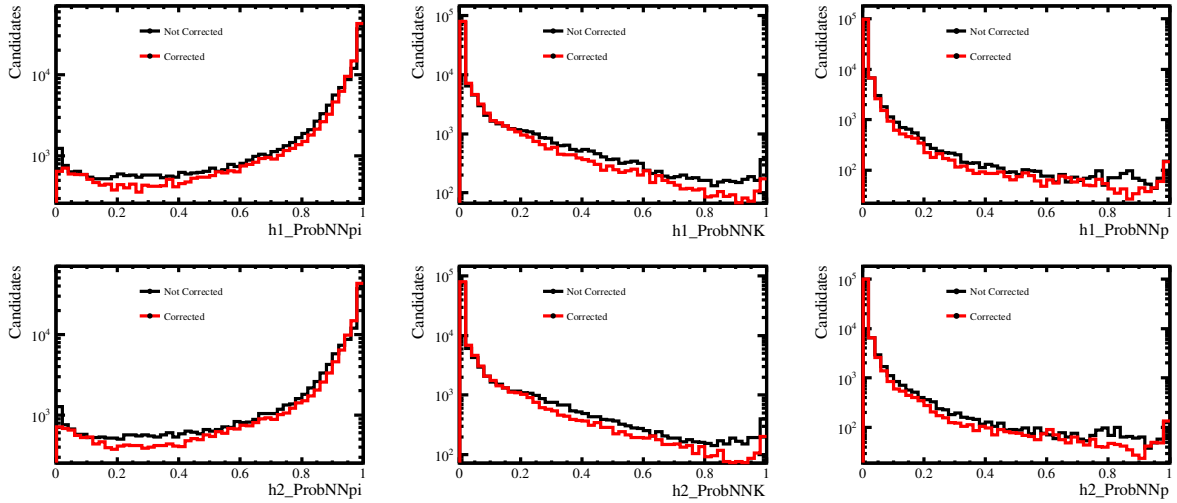

Figure A.34: Comparison between the Corrected (Red) and Non-corrected (Black) for $B_s \to K^0_S \pi^+ \pi^-$ samples of 2016 *MagDown* for Down-DownK^0_S reconstructions. The Top (Bottom) row denote the distributions for h1 (h2) hadrons. The Plots are shown in logarithmic scale.

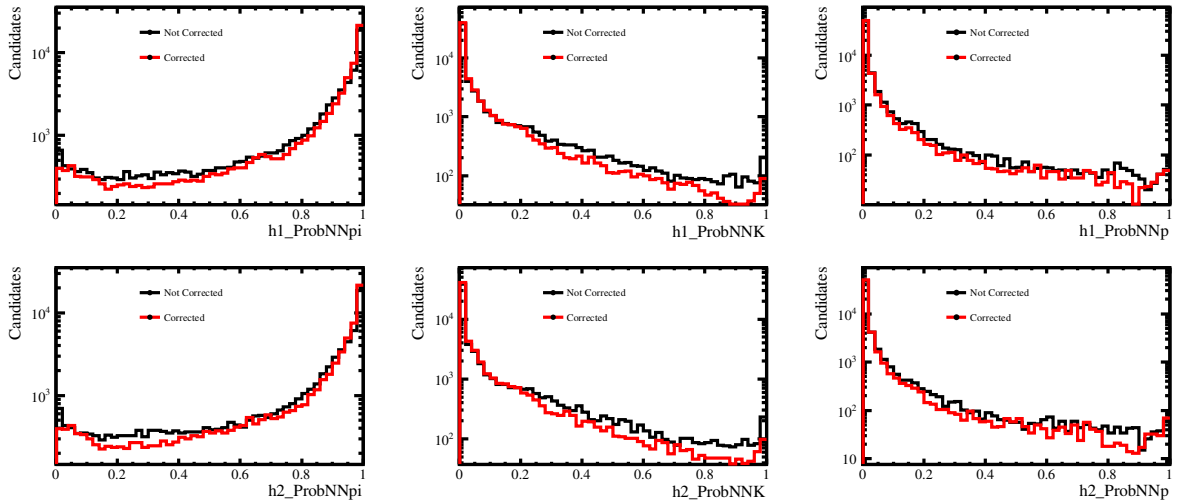

Figure A.35: Comparison between the Corrected (Red) and Non-corrected (Black) for $B_s \to K^0_S \pi^+ \pi^-$ samples of 2016 *MagDown* for Long-LongK^0_S reconstructions. The Top (Bottom) row denote the distributions for h1 (h2) hadrons. The Plots are shown in logarithmic scale.

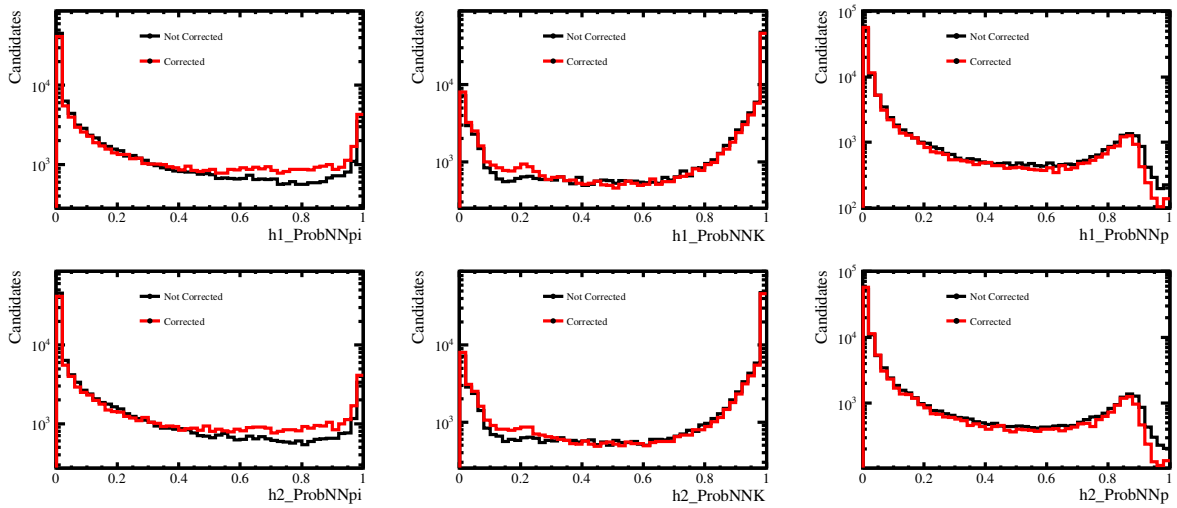

Figure A.36: Comparison between the Corrected (Red) and Non-corrected (Black) for $B^0 \to K^0_S K^+ K^-$ samples of 2016 *MagDown* for Down-DownK^0_S reconstructions. The Top (Bottom) row denote the distributions for h1 (h2) hadrons. The Plots are shown in logarithmic scale.

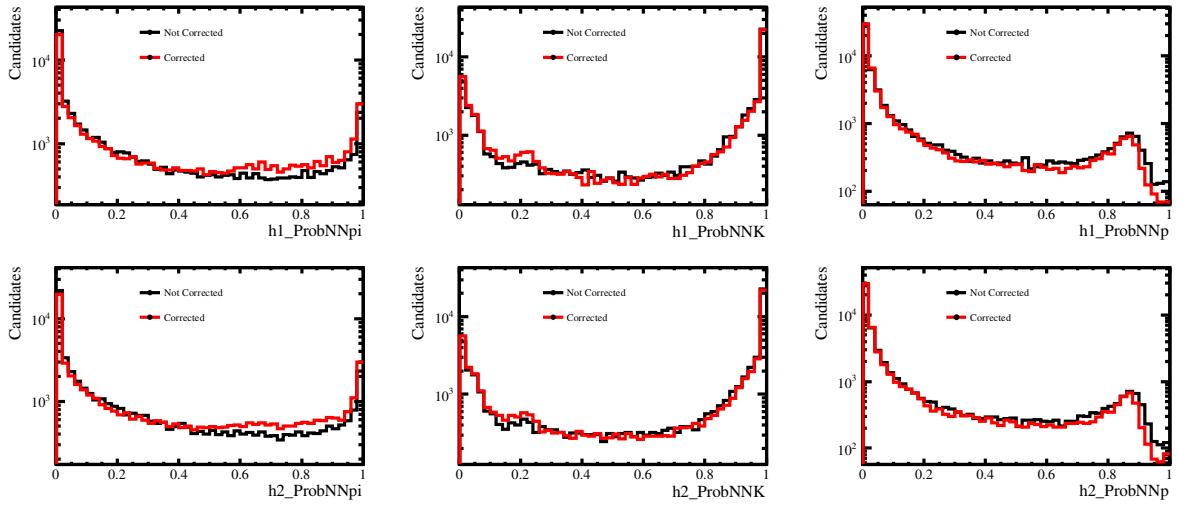

Figure A.37: Comparison between the Corrected (Red) and Non-corrected (Black) for $B^0 \to K^0_S K^+ K^-$ samples of 2016 *MagDown* for Long-LongK^0_S reconstructions. The Top (Bottom) row denote the distributions for h1 (h2) hadrons. The Plots are shown in logarithmic scale.

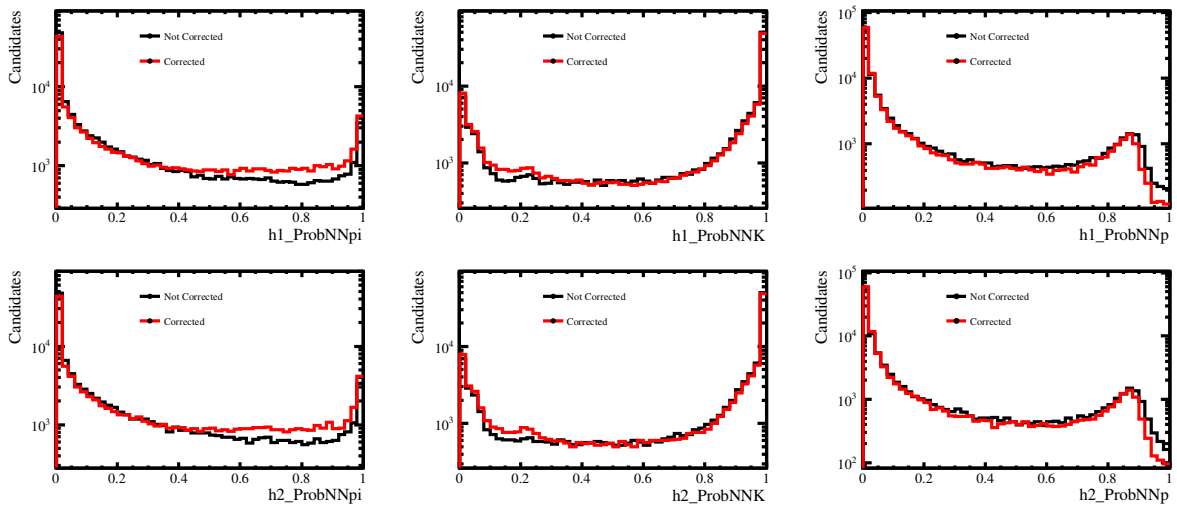

Figure A.38: Comparison between the Corrected (Red) and Non-corrected (Black) for $B_s \to K^0_S K^+ K^-$ samples of 2016 *MagDown* for Down-DownK^0_S reconstructions. The Top (Bottom) row denote the distributions for h1 (h2) hadrons. The Plots are shown in logarithmic scale.

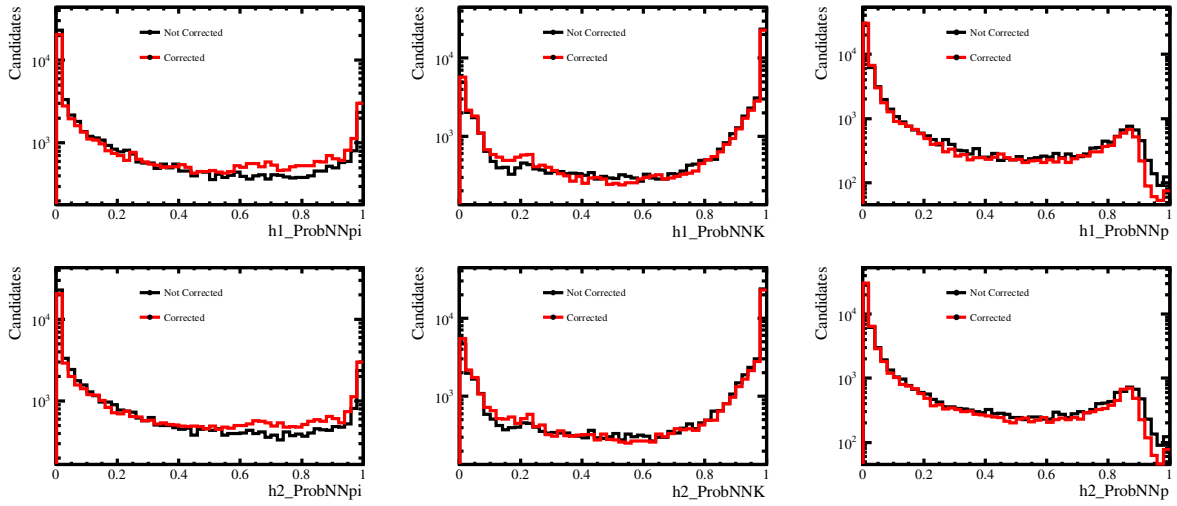

Figure A.39: Comparison between the Corrected (Red) and Non-corrected (Black) for $B_s \to K^0_S K^+ K^-$ samples of 2016 *MagDown* for Long-LongK^0_S reconstructions. The Top (Bottom) row denote the distributions for h1 (h2) hadrons. The Plots are shown in logarithmic scale.

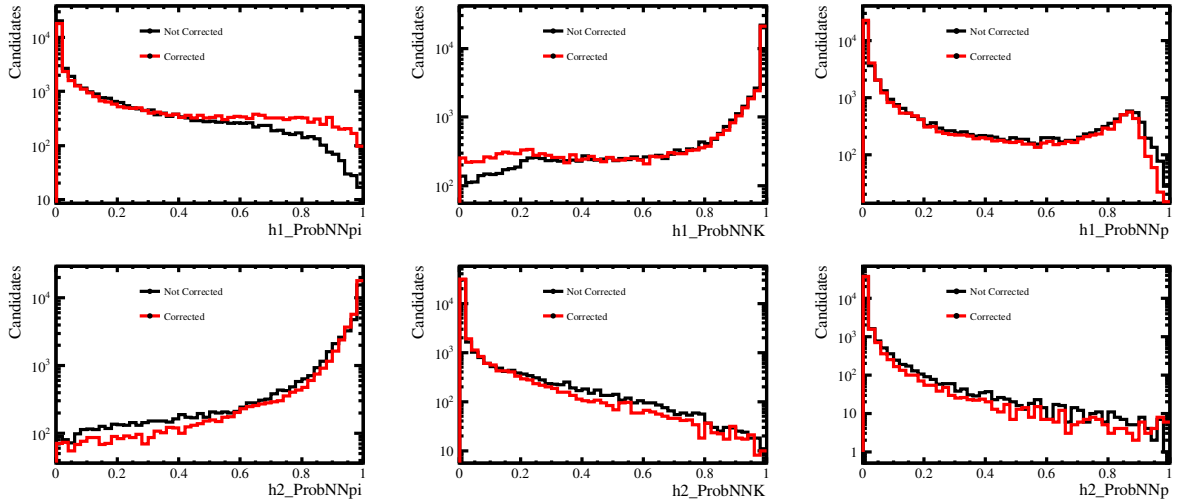

Figure A.40: Comparison between the Corrected (Red) and Non-corrected (Black) for $B^0 \to K^0_S K^+ \pi^-$ samples of 2016 *MagDown* for Down-DownK^0_S reconstructions. The Top (Bottom) row denote the distributions for h1 (h2) hadrons. The Plots are shown in logarithmic scale.

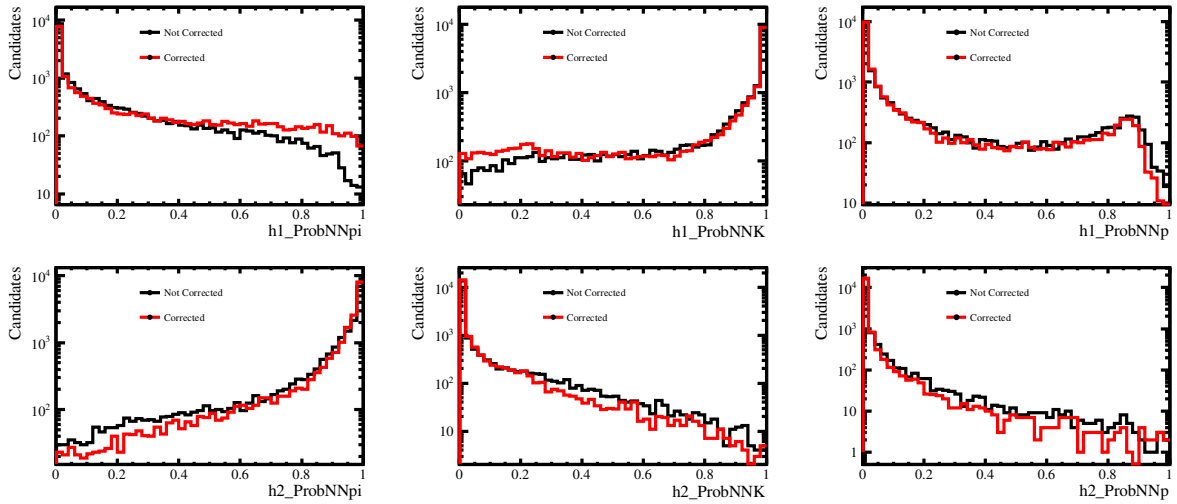

Figure A.41: Comparison between the Corrected (Red) and Non-corrected (Black) for $B^0 \to K^0_S K^+ \pi^-$ samples of 2016 *MagDown* for Long-LongK^0_S reconstructions. The Top (Bottom) row denote the distributions for h1 (h2) hadrons. The Plots are shown in logarithmic scale.

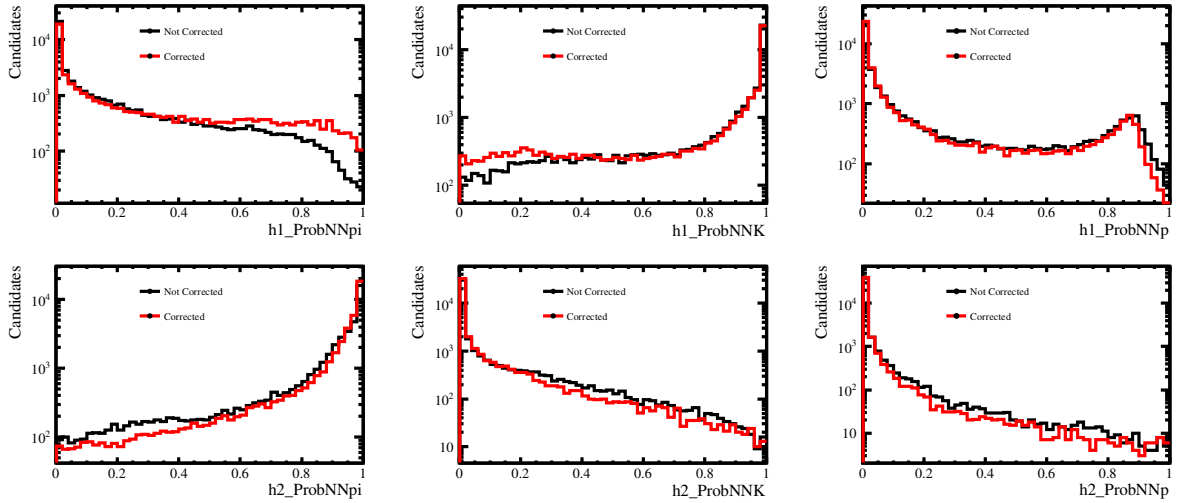

Figure A.42: Comparison between the Corrected (Red) and Non-corrected (Black) for $B_s \to K^0_S K^+ \pi^-$ samples of 2016 *MagDown* for Down-DownK^0_S reconstructions. The Top (Bottom) row denote the distributions for h1 (h2) hadrons. The Plots are shown in logarithmic scale.

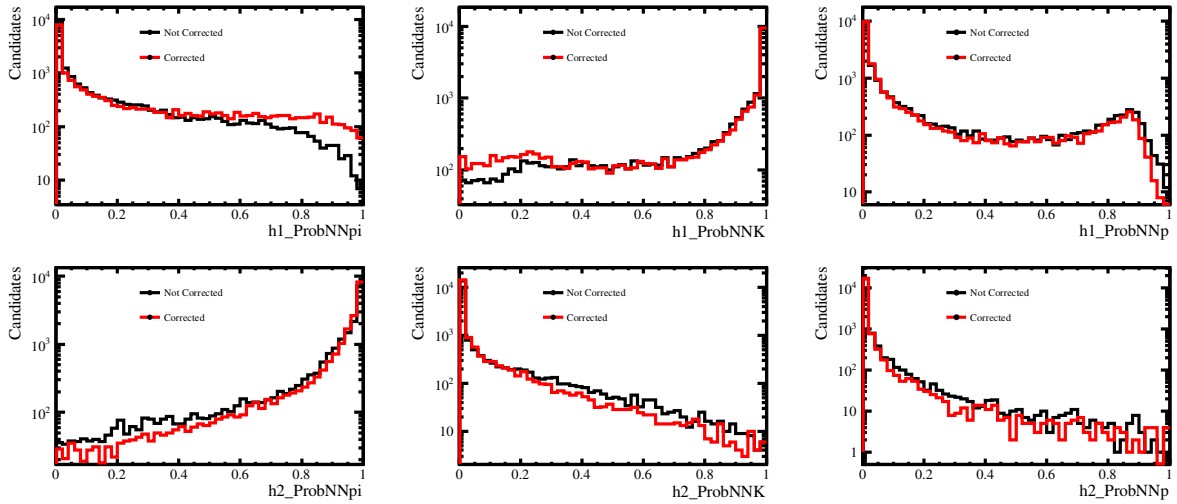

Figure A.43: Comparison between the Corrected (Red) and Non-corrected (Black) for $B_s \to K^0_S K^+ \pi^-$ samples of 2016 *MagDown* for Long-LongK^0_S reconstructions. The Top (Bottom) row denote the distributions for h1 (h2) hadrons. The Plots are shown in logarithmic scale.

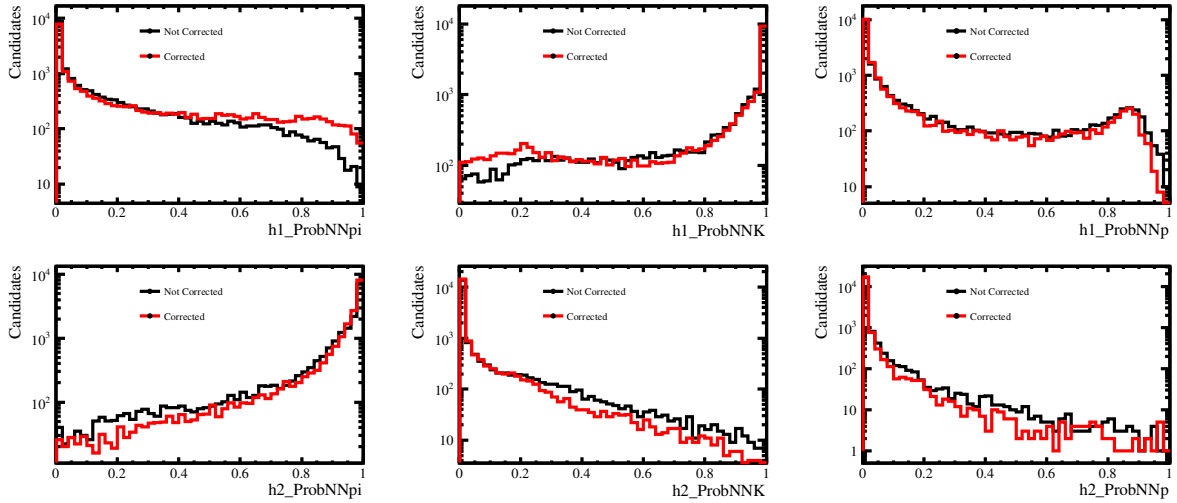

Figure A.44: Comparison between the Corrected (Red) and Non-corrected (Black) for $B_s \to K^0_S K^+ \pi^-$ samples of 2016 *MagUp* for Long-LongK^0_S reconstructions. The Top (Bottom) row denote the distributions for h1 (h2) hadrons. The Plots are shown in logarithmic scale.

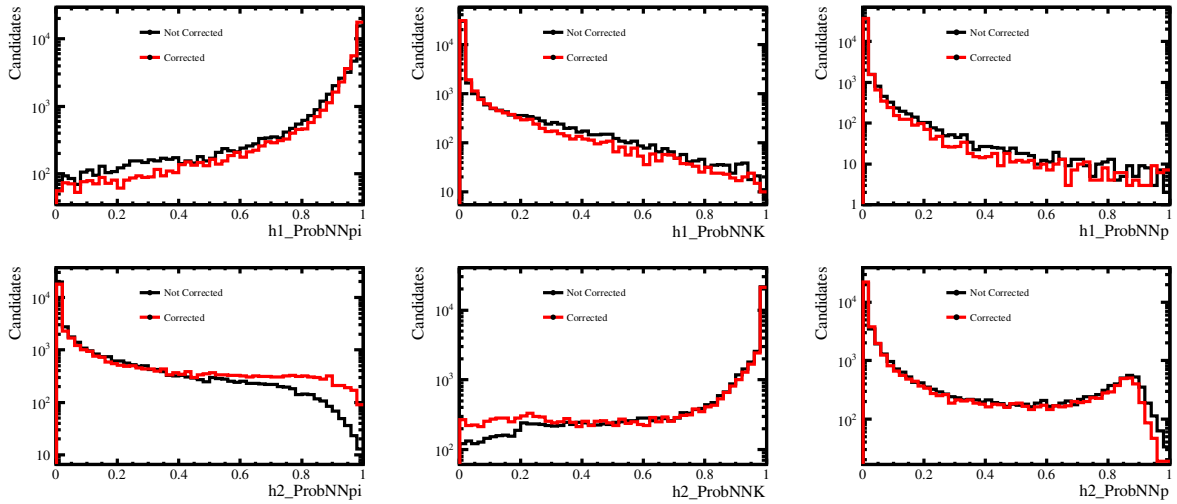

Figure A.45: Comparison between the Corrected (Red) and Non-corrected (Black) for $B^0 \to K^0_S \pi^+ K^-$ samples of 2016 *MagDown* for Down-DownK^0_S reconstructions. The Top (Bottom) row denote the distributions for h1 (h2) hadrons. The Plots are shown in logarithmic scale.

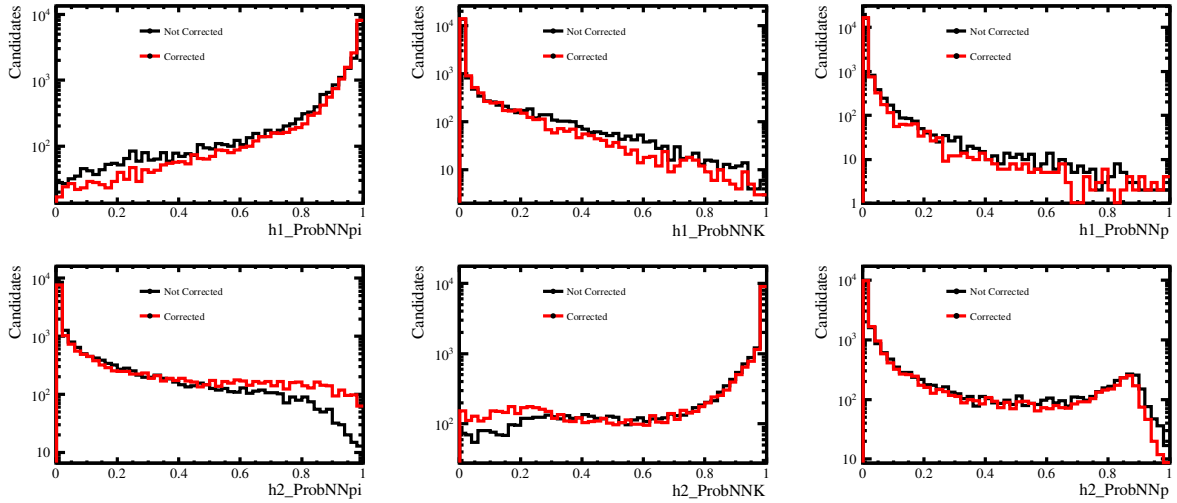

Figure A.46: Comparison between the Corrected (Red) and Non-corrected (Black) for $B^0 \to K^0_S \pi^+ K^-$ samples of 2016 *MagDown* for Long-LongK^0_S reconstructions. The Top (Bottom) row denote the distributions for h1 (h2) hadrons. The Plots are shown in logarithmic scale.

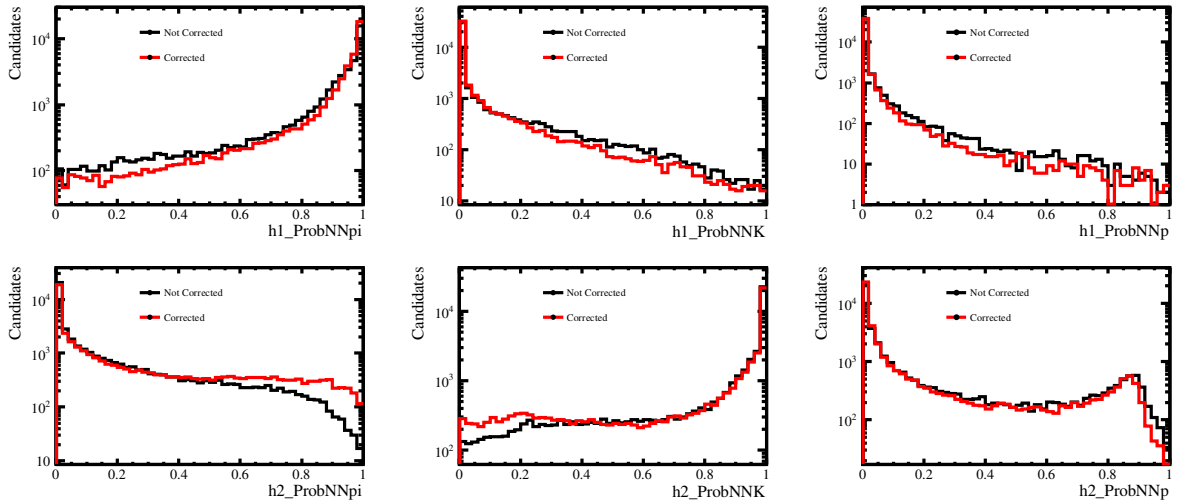

Figure A.47: Comparison between the Corrected (Red) and Non-corrected (Black) for $B_s \to K^0_S \pi^+ K^-$ samples of 2016 *MagDown* for Down-DownK^0_S reconstructions. The Top (Bottom) row denote the distributions for h1 (h2) hadrons. The Plots are shown in logarithmic scale.

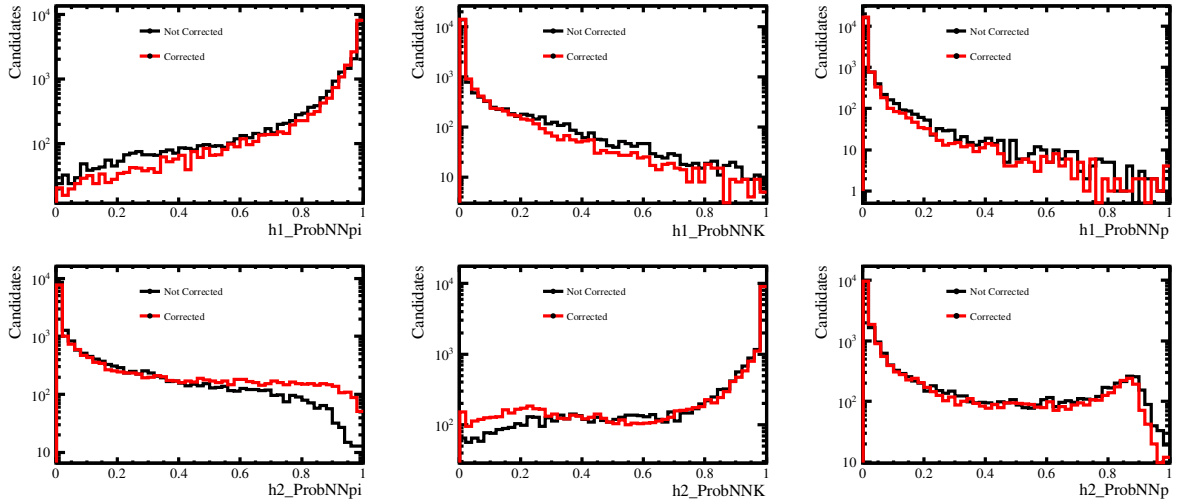

Figure A.48: Comparison between the Corrected (Red) and Non-corrected (Black) for $B_s \to K^0_S \pi^+ K^-$ samples of 2016 *MagDown* for Long-LongK^0_S reconstructions. The Top (Bottom) row denote the distributions for h1 (h2) hadrons. The Plots are shown in logarithmic scale.

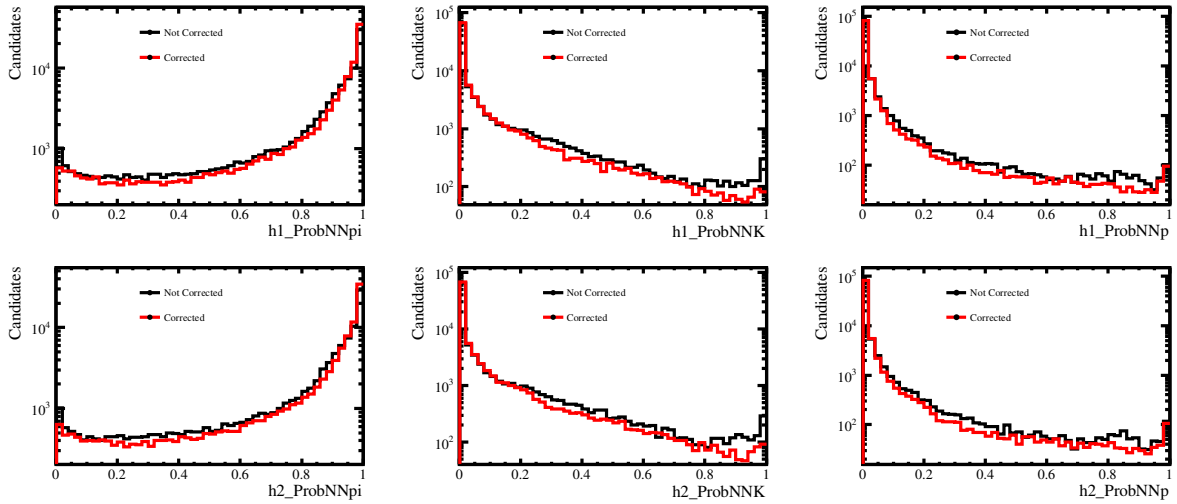

Figure A.49: Comparison between the Corrected (Red) and Non-corrected (Black) for $B^0 \to K^0_S \pi^+ \pi^-$ samples of 2015 *MagDown* for Down-DownK^0_S reconstructions. The Top (Bottom) row denote the distributions for h1 (h2) hadrons. The Plots are shown in logarithmic scale.

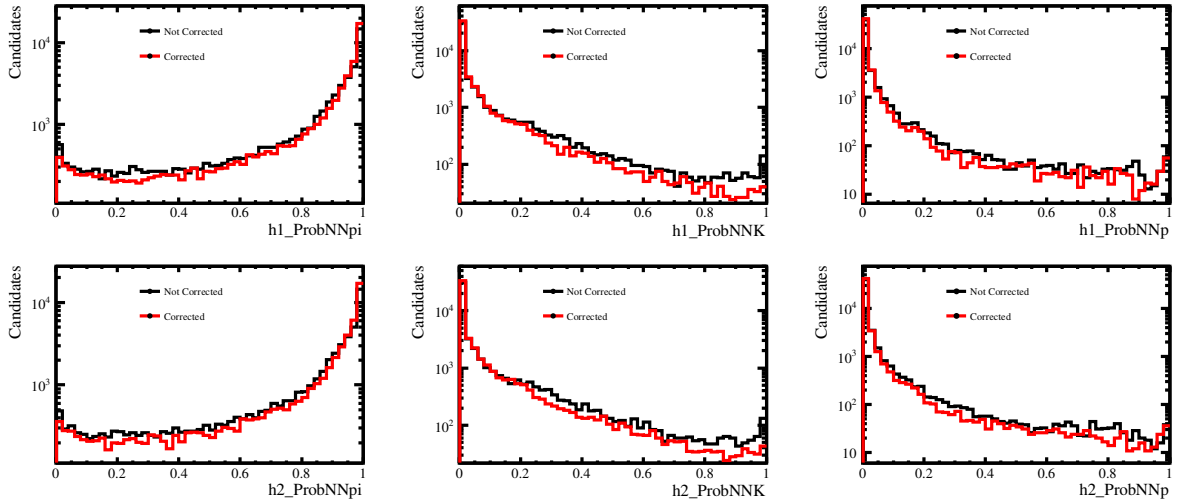

Figure A.50: Comparison between the Corrected (Red) and Non-corrected (Black) for $B^0 \to K^0_S \pi^+ \pi^-$ samples of 2015 *MagDown* for Long-LongK^0_S reconstructions. The Top (Bottom) row denote the distributions for h1 (h2) hadrons. The Plots are shown in logarithmic scale.

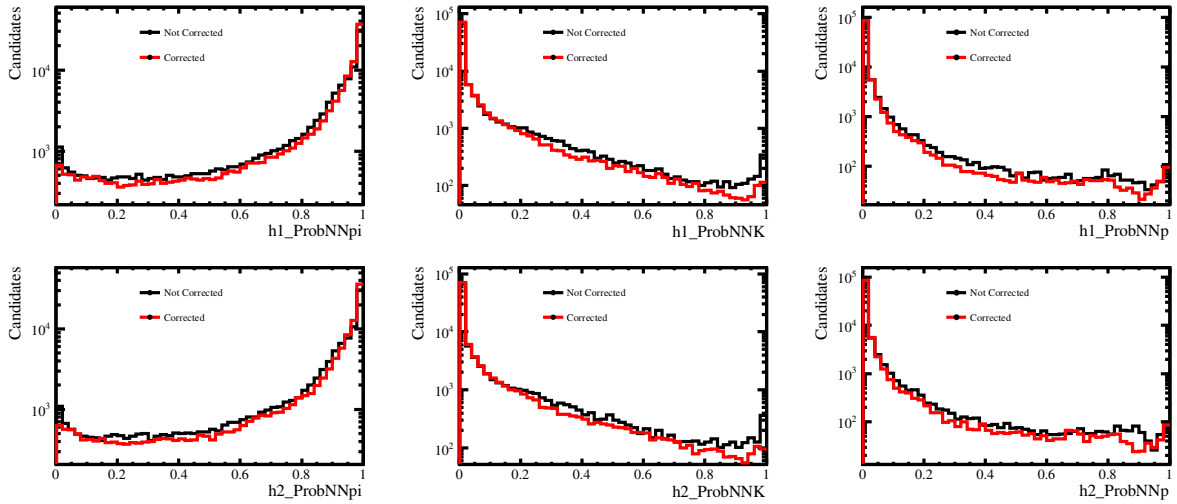

Figure A.51: Comparison between the Corrected (Red) and Non-corrected (Black) for $B_s \to K^0_S \pi^+ \pi^-$ samples of 2015 *MagDown* for Down-DownK^0_S reconstructions. The Top (Bottom) row denote the distributions for h1 (h2) hadrons. The Plots are shown in logarithmic scale.

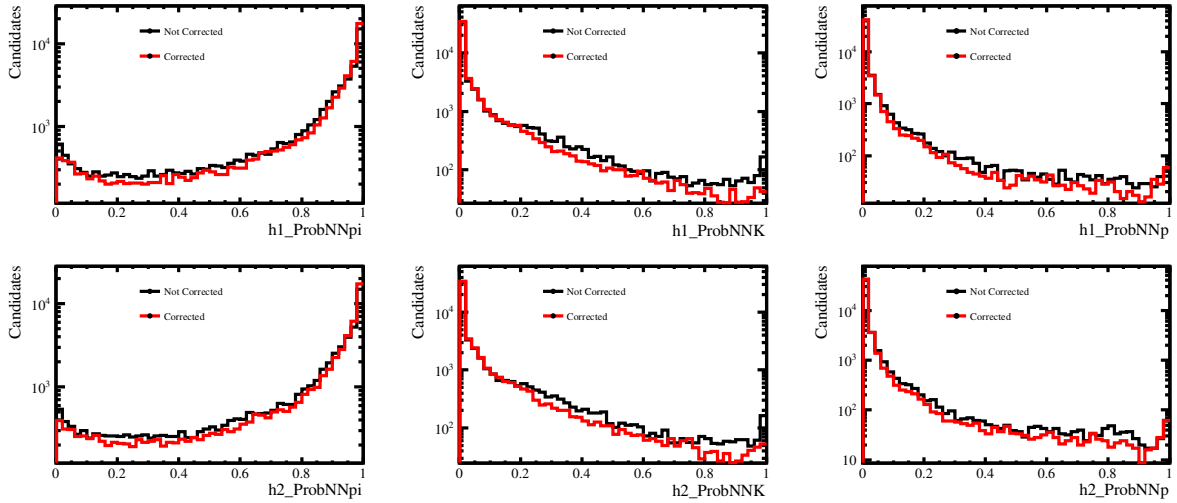

Figure A.52: Comparison between the Corrected (Red) and Non-corrected (Black) for $B_s \to K^0_S \pi^+ \pi^-$ samples of 2015 *MagDown* for Long-LongK^0_S reconstructions. The Top (Bottom) row denote the distributions for h1 (h2) hadrons. The Plots are shown in logarithmic scale.

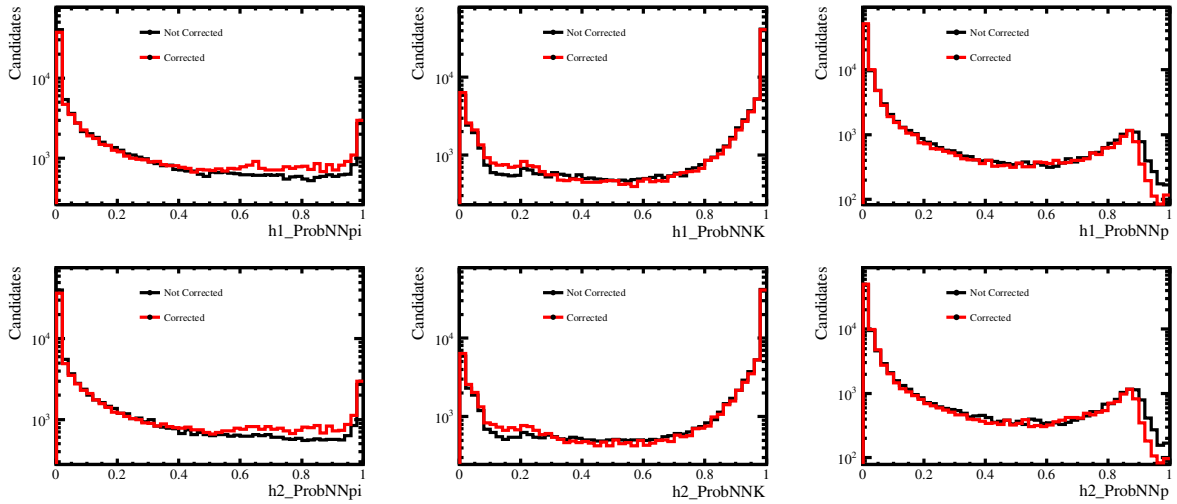

Figure A.53: Comparison between the Corrected (Red) and Non-corrected (Black) for $B^0 \to K^0_S K^+ K^-$ samples of 2015 *MagDown* for Down-DownK^0_S reconstructions. The Top (Bottom) row denote the distributions for h1 (h2) hadrons. The Plots are shown in logarithmic scale.

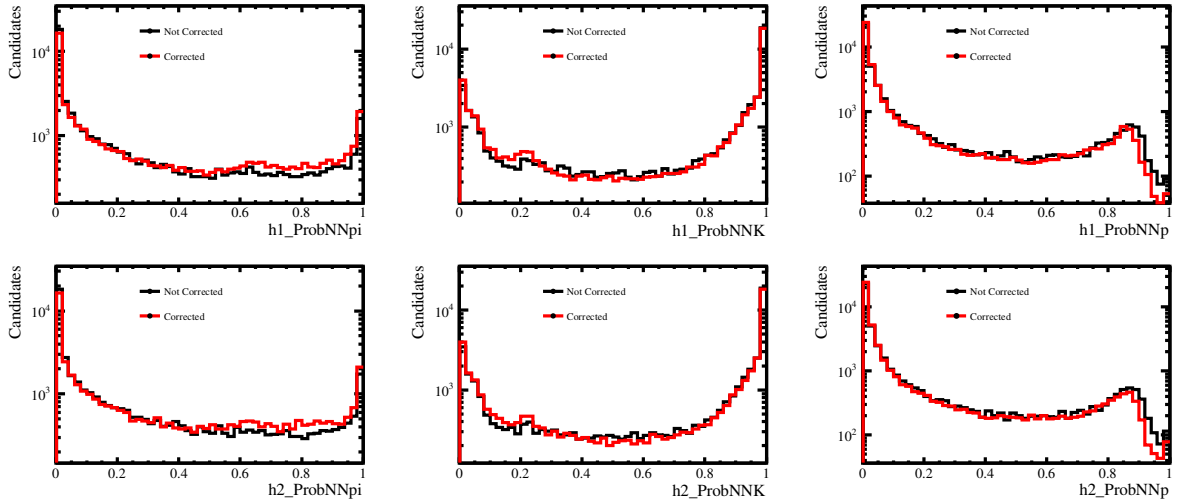

Figure A.54: Comparison between the Corrected (Red) and Non-corrected (Black) for $B^0 \to K^0_S K^+ K^-$ samples of 2015 *MagDown* for Long-LongK^0_S reconstructions. The Top (Bottom) row denote the distributions for h1 (h2) hadrons. The Plots are shown in logarithmic scale.

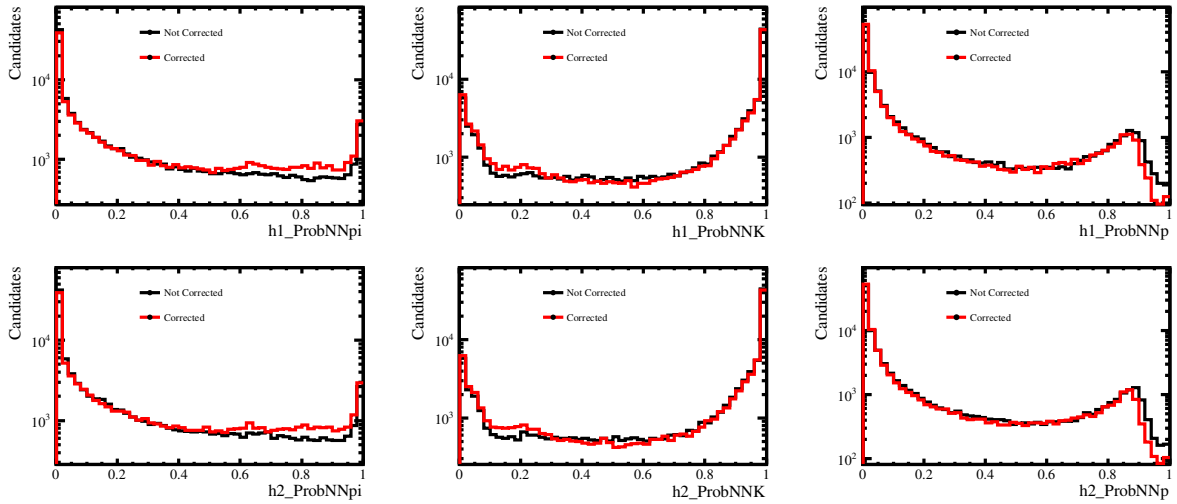

Figure A.55: Comparison between the Corrected (Red) and Non-corrected (Black) for $B_s \to K^0_S K^+ K^-$ samples of 2015 *MagDown* for Down-DownK^0_S reconstructions. The Top (Bottom) row denote the distributions for h1 (h2) hadrons. The Plots are shown in logarithmic scale.

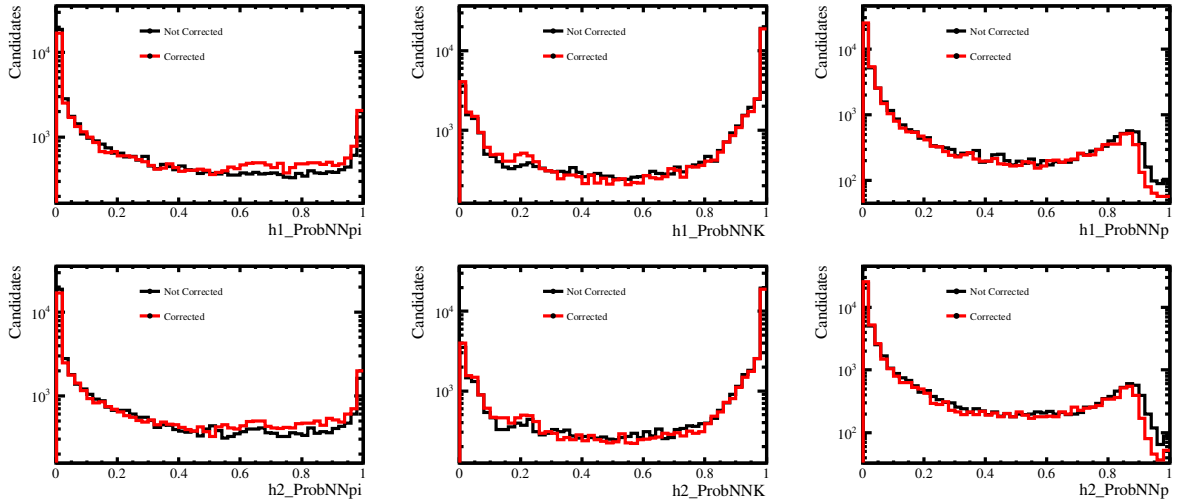

Figure A.56: Comparison between the Corrected (Red) and Non-corrected (Black) for $B_s \to K^0_S K^+ K^-$ samples of 2015 *MagDown* for Long-LongK^0_S reconstructions. The Top (Bottom) row denote the distributions for h1 (h2) hadrons. The Plots are shown in logarithmic scale.

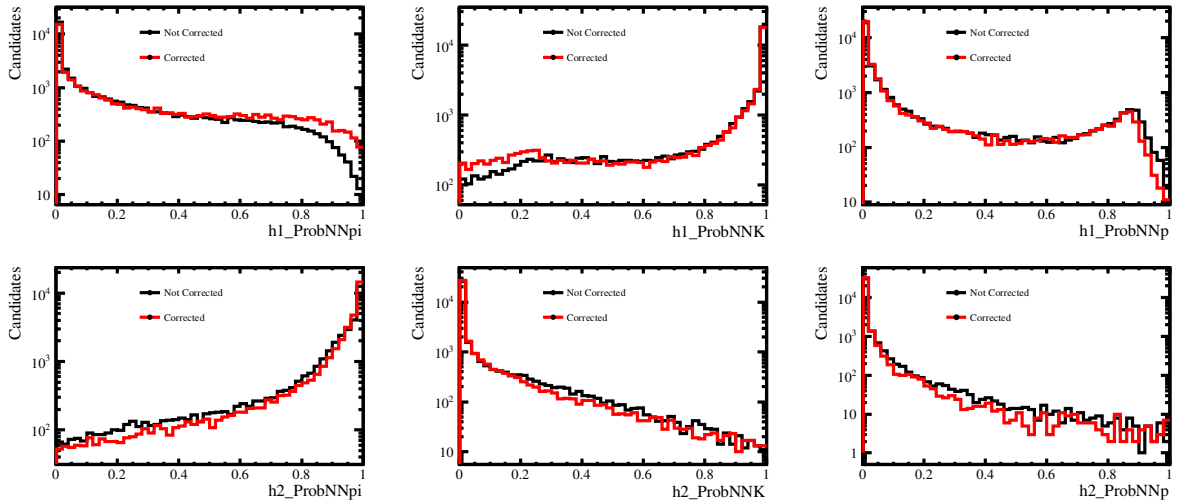

Figure A.57: Comparison between the Corrected (Red) and Non-corrected (Black) for $B^0 \to K^0_S K^+ \pi^-$ samples of 2015 *MagDown* for Down-DownK^0_S reconstructions. The Top (Bottom) row denote the distributions for h1 (h2) hadrons. The Plots are shown in logarithmic scale.

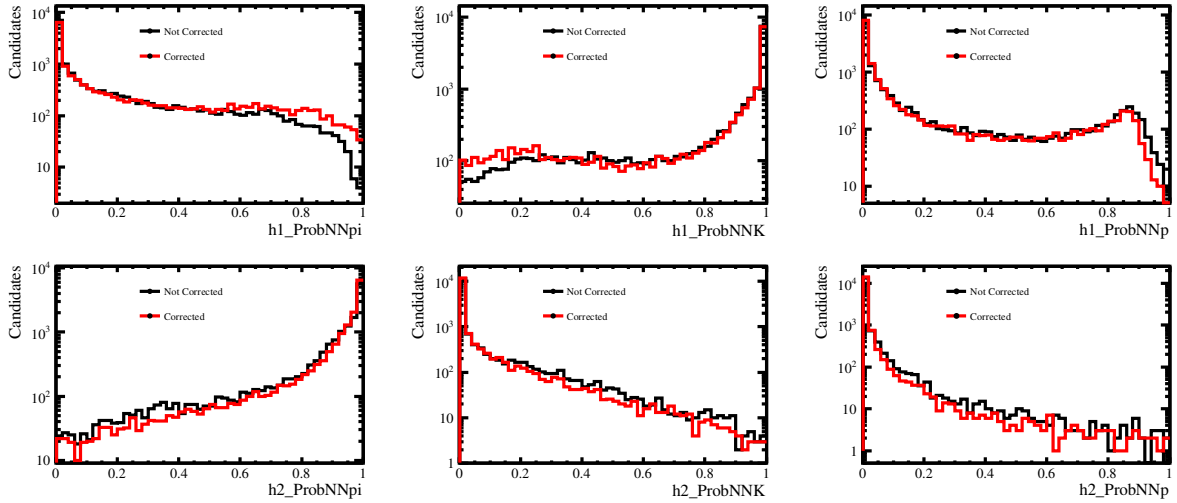

Figure A.58: Comparison between the Corrected (Red) and Non-corrected (Black) for $B^0 \to K^0_S K^+ \pi^-$ samples of 2015 *MagDown* for Long-LongK^0_S reconstructions. The Top (Bottom) row denote the distributions for h1 (h2) hadrons. The Plots are shown in logarithmic scale.

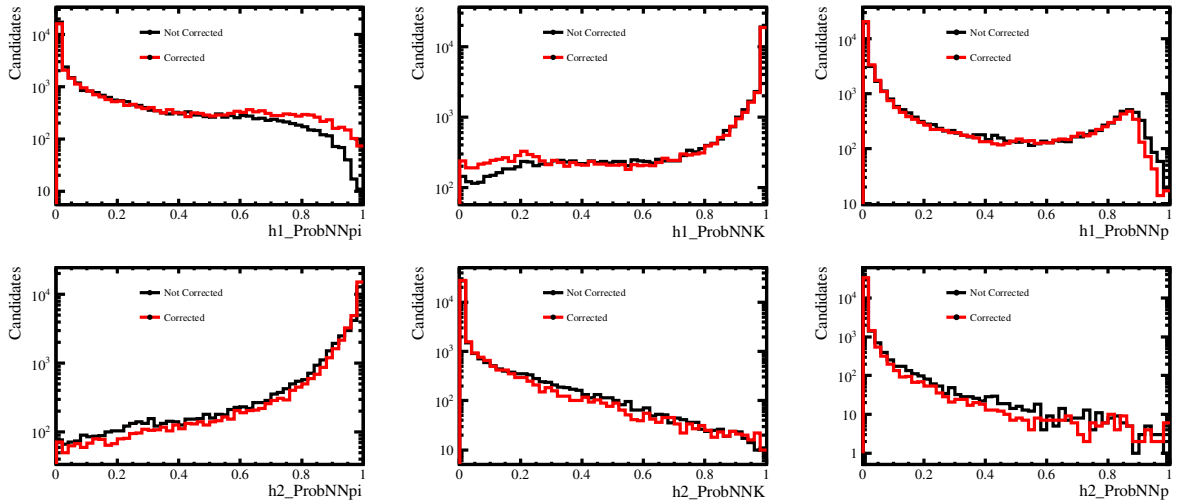

Figure A.59: Comparison between the Corrected (Red) and Non-corrected (Black) for $B_s \to K^0_S K^+ \pi^-$ samples of 2015 *MagDown* for Down-DownK^0_S reconstructions. The Top (Bottom) row denote the distributions for h1 (h2) hadrons. The Plots are shown in logarithmic scale.

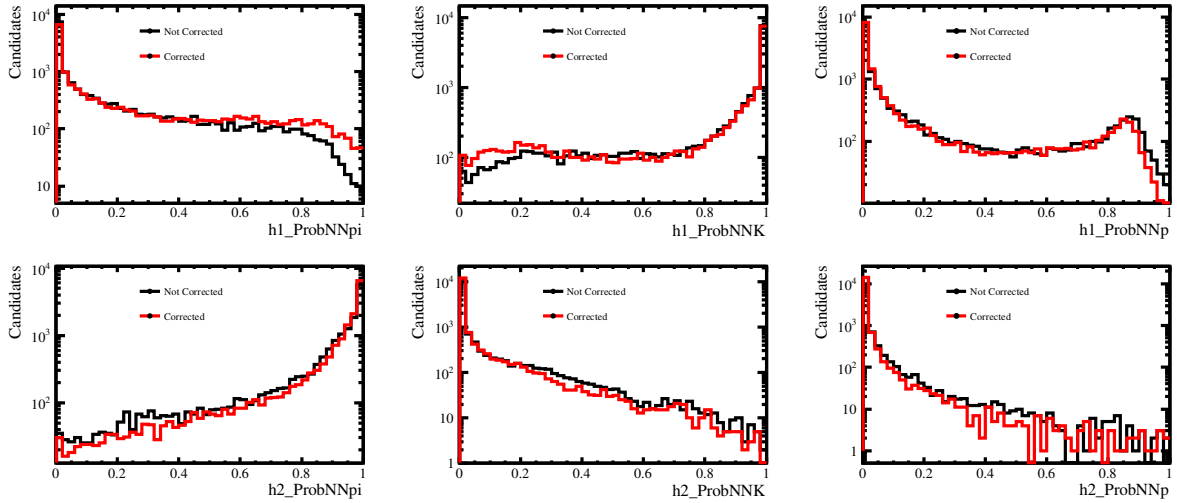

Figure A.60: Comparison between the Corrected (Red) and Non-corrected (Black) for $B_s \to K^0_S K^+ \pi^-$ samples of 2015 *MagDown* for Long-LongK^0_S reconstructions. The Top (Bottom) row denote the distributions for h1 (h2) hadrons. The Plots are shown in logarithmic scale.

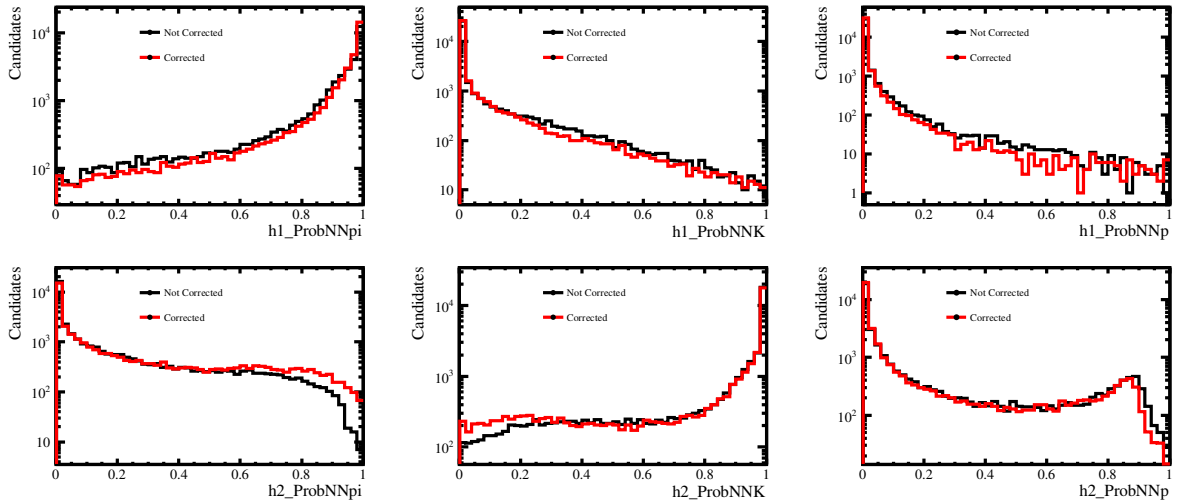

Figure A.61: Comparison between the Corrected (Red) and Non-corrected (Black) for $B^0 \to K^0_S \pi^+ K^-$ samples of 2015 *MagDown* for Down-DownK^0_S reconstructions. The Top (Bottom) row denote the distributions for h1 (h2) hadrons. The Plots are shown in logarithmic scale.

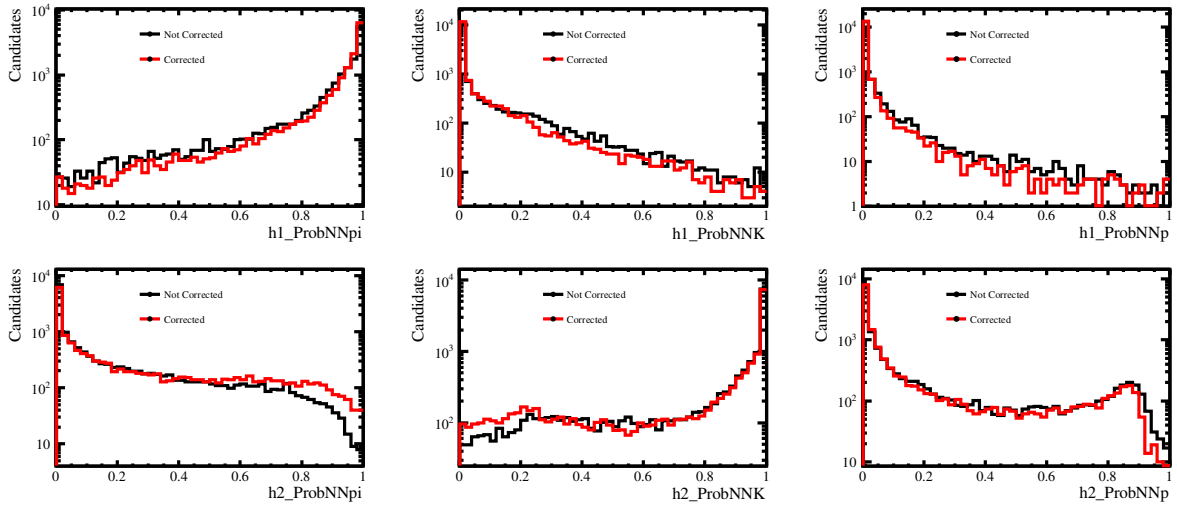

Figure A.62: Comparison between the Corrected (Red) and Non-corrected (Black) for $B^0 \to K^0_S \pi^+ K^-$ samples of 2015 *MagDown* for Long-LongK^0_S reconstructions. The Top (Bottom) row denote the distributions for h1 (h2) hadrons. The Plots are shown in logarithmic scale.

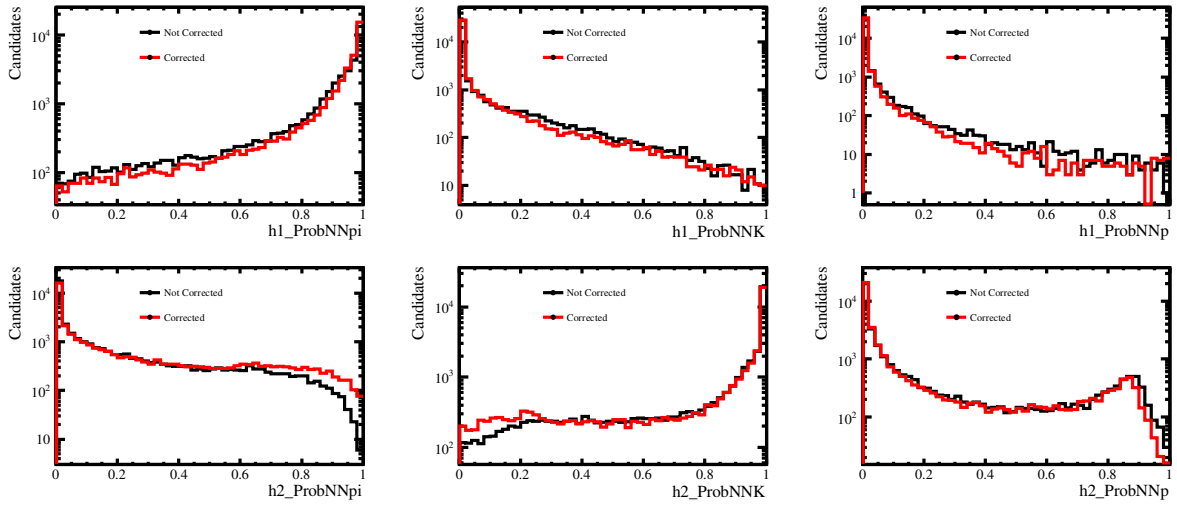

Figure A.63: Comparison between the Corrected (Red) and Non-corrected (Black) for $B_s \to K^0_S \pi^+ K^-$ samples of 2015 *MagDown* for Down-DownK^0_S reconstructions. The Top (Bottom) row denote the distributions for h1 (h2) hadrons. The Plots are shown in logarithmic scale.

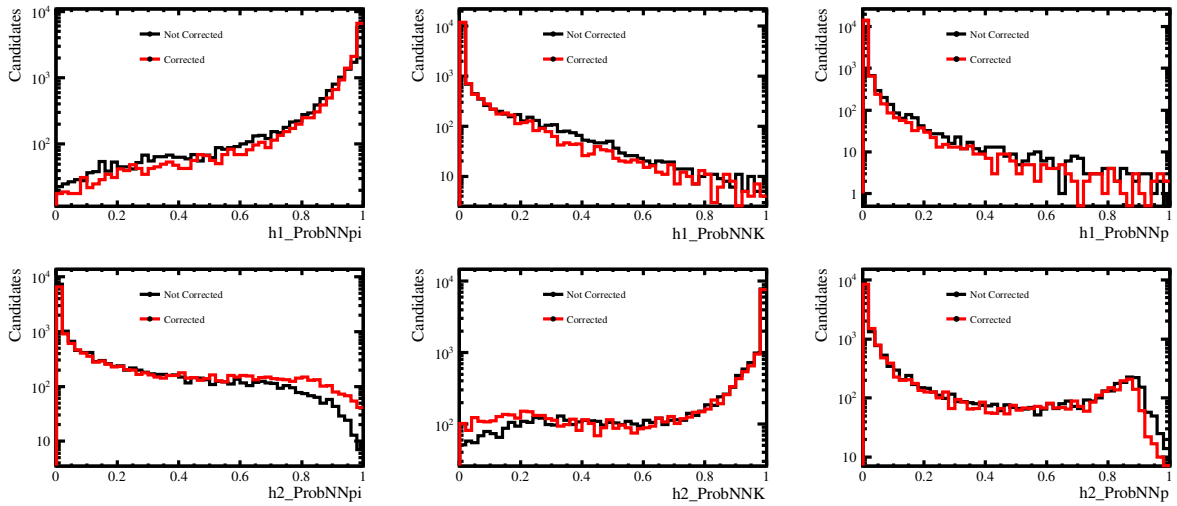

Figure A.64: Comparison between the Corrected (Red) and Non-corrected (Black) for $B_s \to K^0_S \pi^+ K^-$ samples of 2015 *MagDown* for Long-LongK^0_S reconstructions. The Top (Bottom) row denote the distributions for h1 (h2) hadrons. The Plots are shown in logarithmic scale.

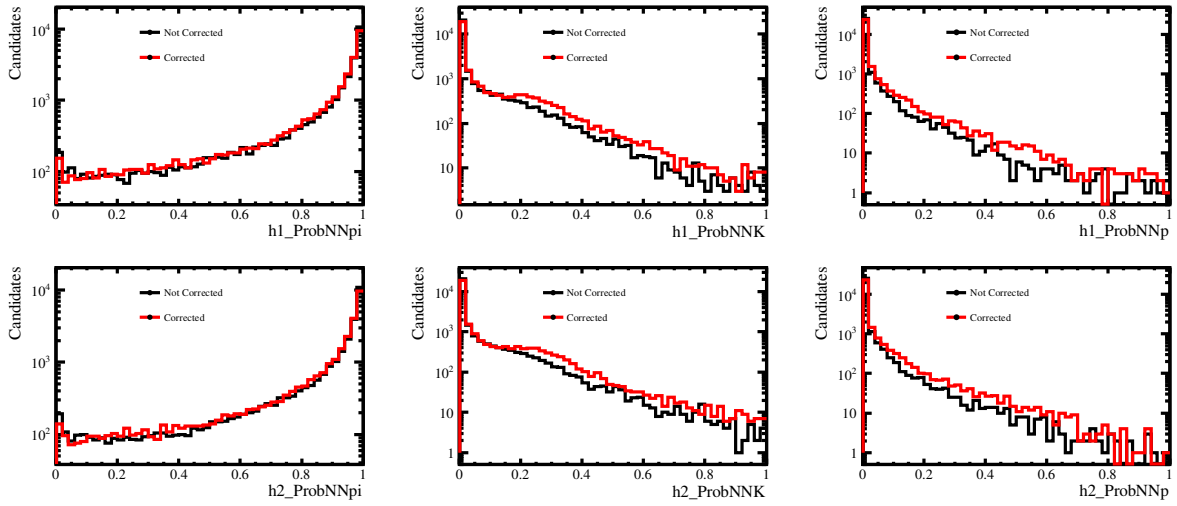

Figure A.65: Comparison between the Corrected (Red) and Non-corrected (Black) for $B^0 \to K^0_S \pi^+ \pi^-$ samples of 2012b *MagDown* for Long-LongK^0_S reconstructions. The Top (Bottom) row denote the distributions for h1 (h2) hadrons. The Plots are shown in logarithmic scale.

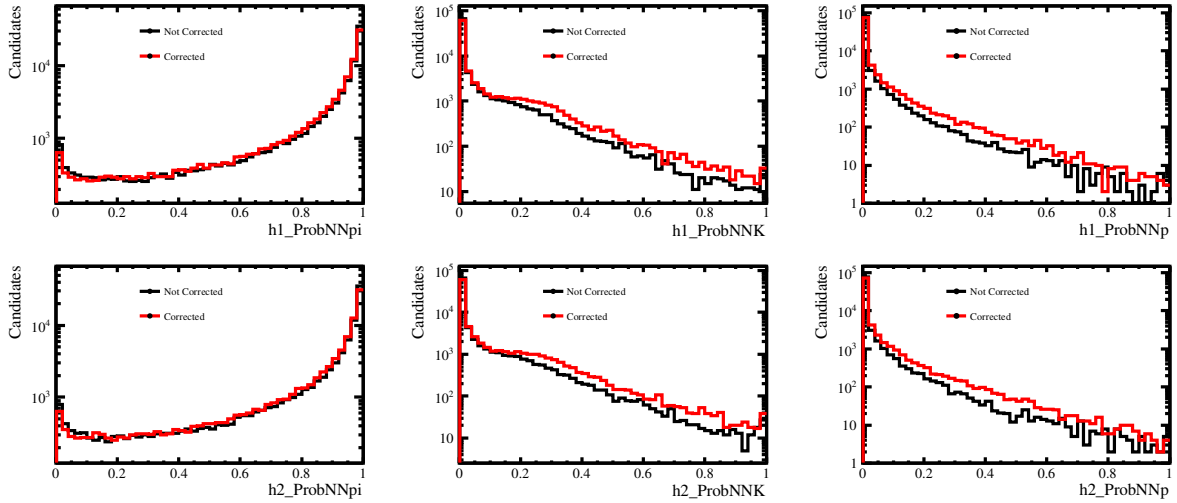

Figure A.66: Comparison between the Corrected (Red) and Non-corrected (Black) for $B_s \to K^0_S\pi^+\pi^-$ samples of 2012b *MagDown* for Down-DownK^0_S reconstructions. The Top (Bottom) row denote the distributions for h1 (h2) hadrons. The Plots are shown in logarithmic scale.

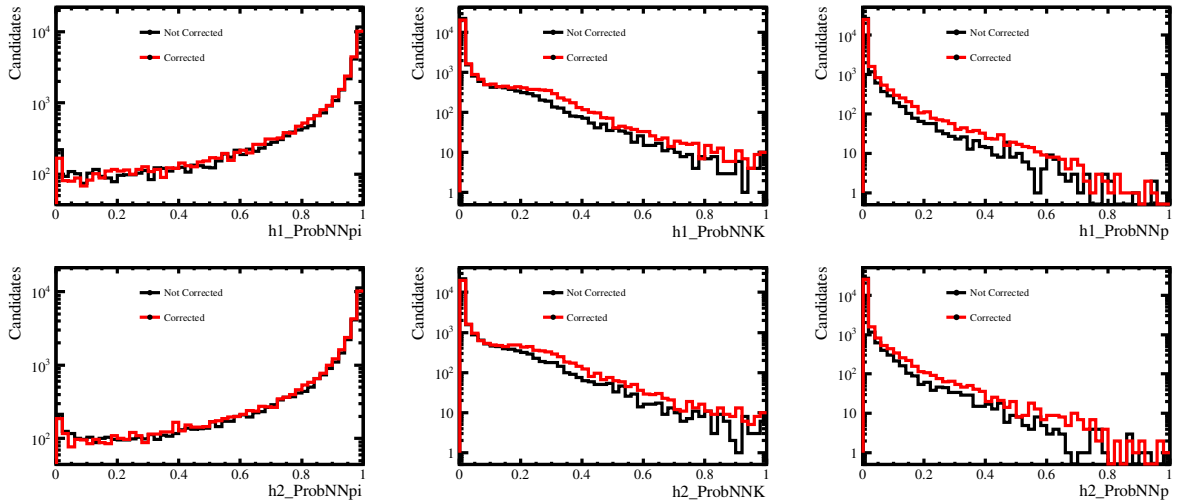

Figure A.67: Comparison between the Corrected (Red) and Non-corrected (Black) for $B_s \to K^0_S\pi^+\pi^-$ samples of 2012b *MagDown* for Long-LongK^0_S reconstructions. The Top (Bottom) row denote the distributions for h1 (h2) hadrons. The Plots are shown in logarithmic scale.

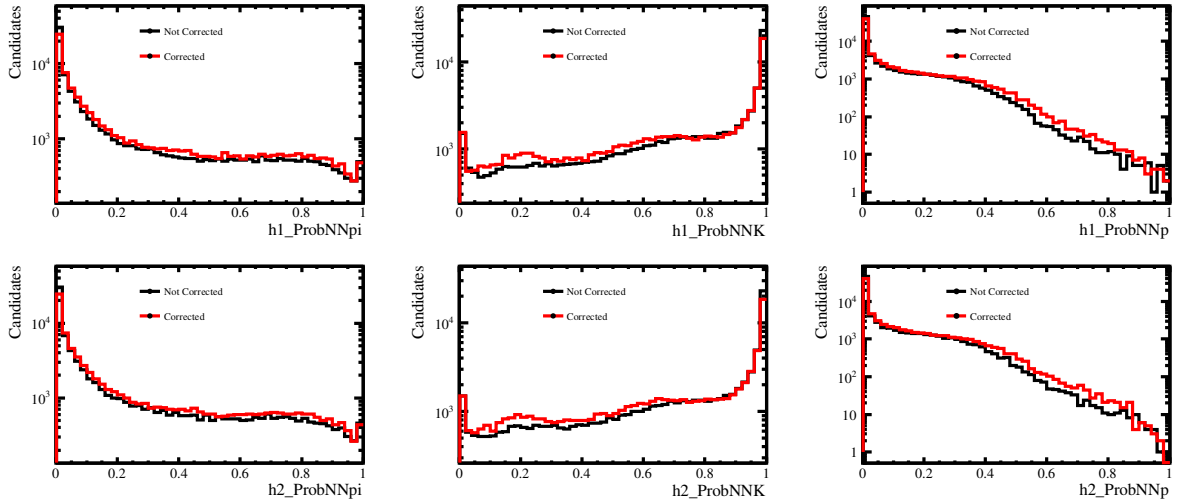

Figure A.68: Comparison between the Corrected (Red) and Non-corrected (Black) for $B^0 \to K^0_S K^+ K^-$ samples of 2012b *MagDown* for Down-DownK^0_S reconstructions. The Top (Bottom) row denote the distributions for h1 (h2) hadrons. The Plots are shown in logarithmic scale.

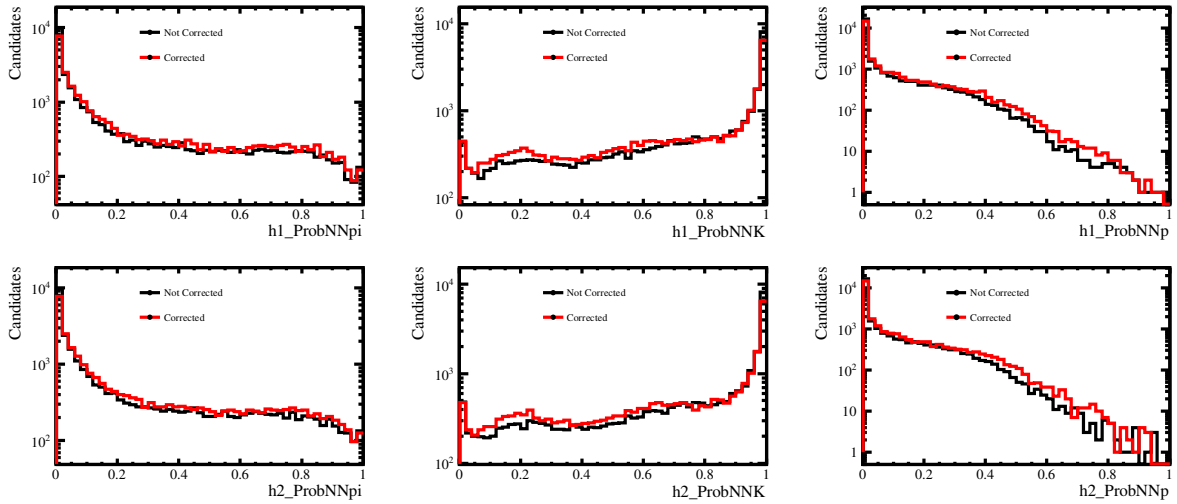

Figure A.69: Comparison between the Corrected (Red) and Non-corrected (Black) for $B^0 \to K^0_S K^+ K^-$ samples of 2012b *MagDown* for Long-LongK^0_S reconstructions. The Top (Bottom) row denote the distributions for h1 (h2) hadrons. The Plots are shown in logarithmic scale.

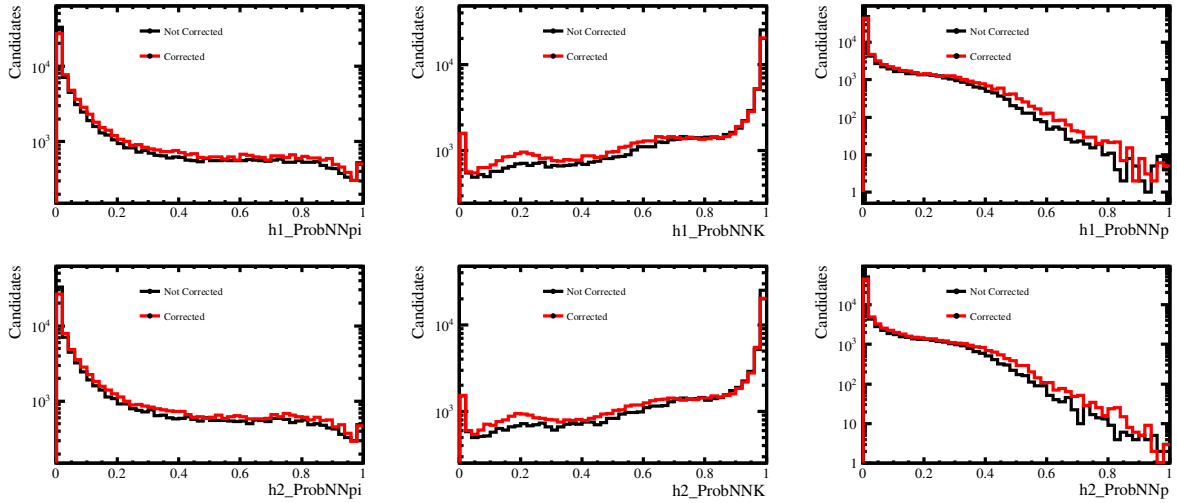

Figure A.70: Comparison between the Corrected (Red) and Non-corrected (Black) for $B_s \to K^0_S K^+ K^-$ samples of 2012b *MagDown* for Down-DownK^0_S reconstructions. The Top (Bottom) row denote the distributions for h1 (h2) hadrons. The Plots are shown in logarithmic scale.

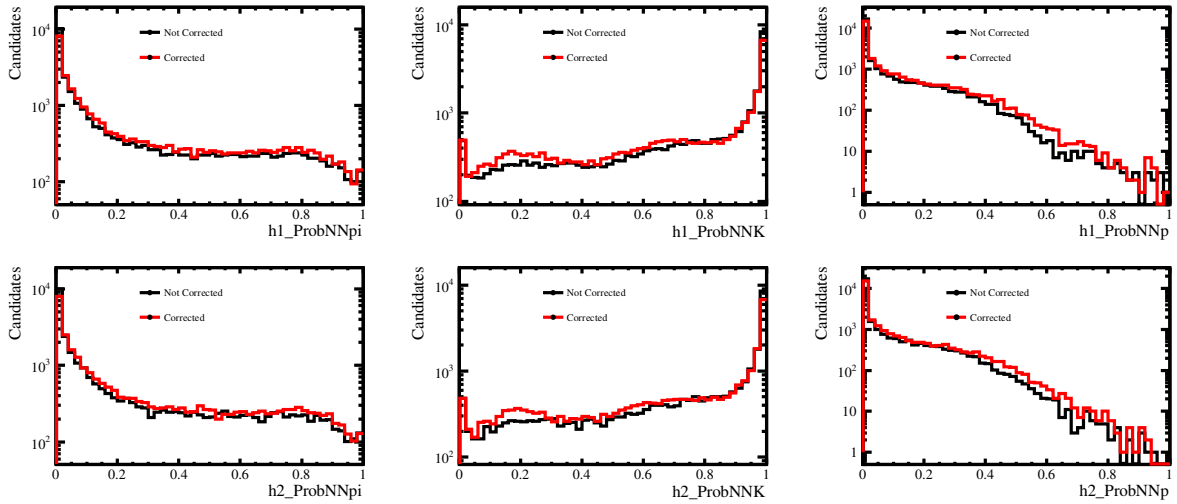

Figure A.71: Comparison between the Corrected (Red) and Non-corrected (Black) for $B_s \to K^0_S K^+ K^-$ samples of 2012b *MagDown* for Long-LongK^0_S reconstructions. The Top (Bottom) row denote the distributions for h1 (h2) hadrons. The Plots are shown in logarithmic scale.

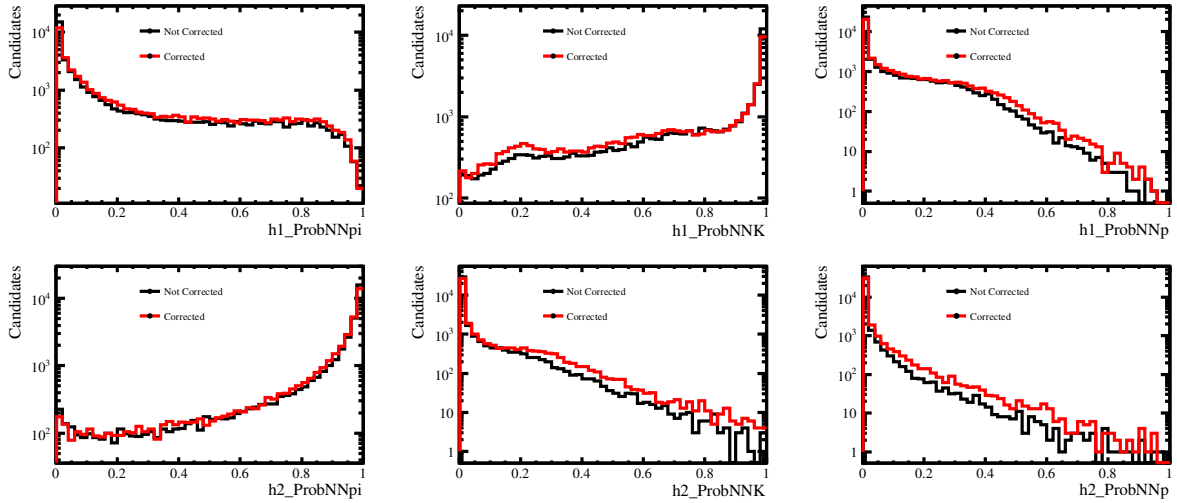

Figure A.72: Comparison between the Corrected (Red) and Non-corrected (Black) for $B^0 \to K^0_S K^+ \pi^-$ samples of 2012b *MagDown* for Down-DownK^0_S reconstructions. The Top (Bottom) row denote the distributions for h1 (h2) hadrons. The Plots are shown in logarithmic scale.

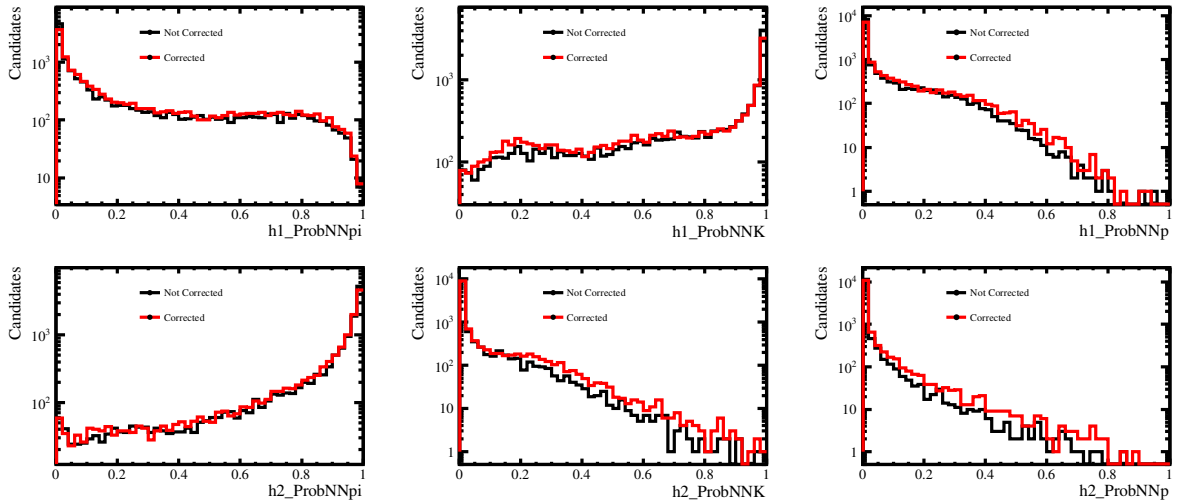

Figure A.73: Comparison between the Corrected (Red) and Non-corrected (Black) for $B^0 \to K^0_S K^+ \pi^-$ samples of 2012b *MagDown* for Long-LongK^0_S reconstructions. The Top (Bottom) row denote the distributions for h1 (h2) hadrons. The Plots are shown in logarithmic scale.

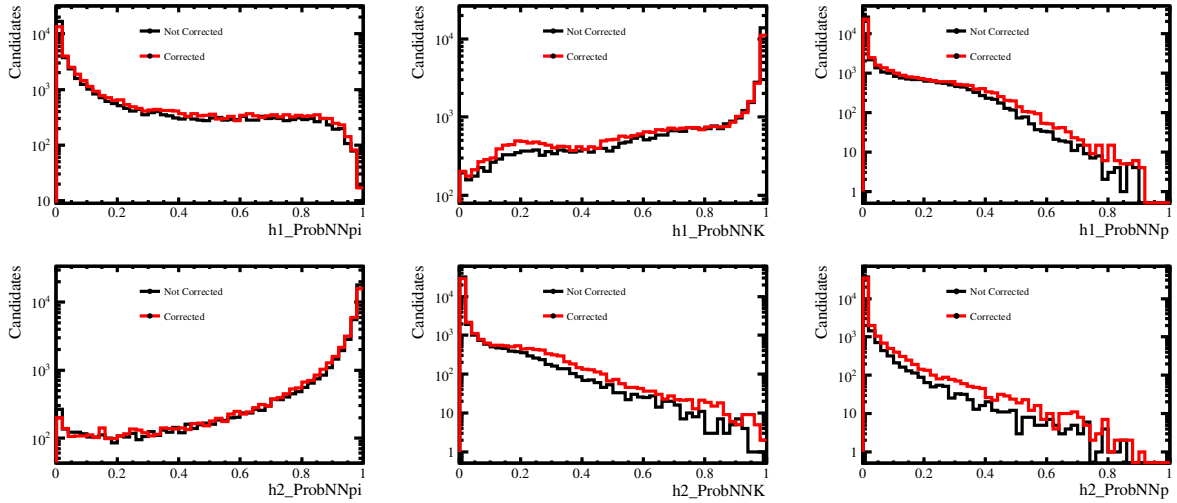

Figure A.74: Comparison between the Corrected (Red) and Non-corrected (Black) for $B_s \to K^0_S K^+ \pi^-$ samples of 2012b *MagDown* for Down-DownK^0_S reconstructions. The Top (Bottom) row denote the distributions for h1 (h2) hadrons. The Plots are shown in logarithmic scale.

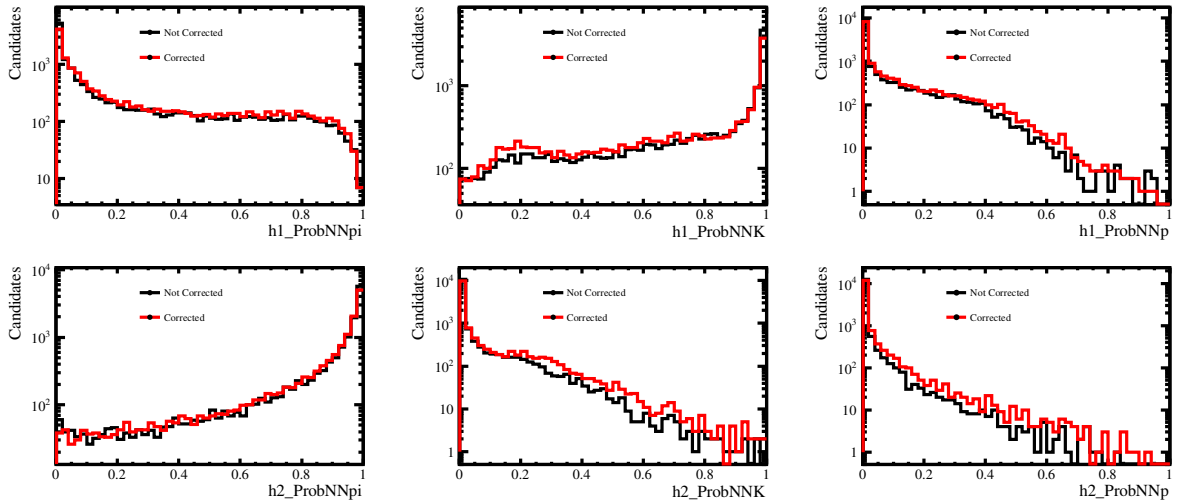

Figure A.75: Comparison between the Corrected (Red) and Non-corrected (Black) for $B_s \to K^0_S K^+ \pi^-$ samples of 2012b *MagDown* for Long-LongK^0_S reconstructions. The Top (Bottom) row denote the distributions for h1 (h2) hadrons. The Plots are shown in logarithmic scale.

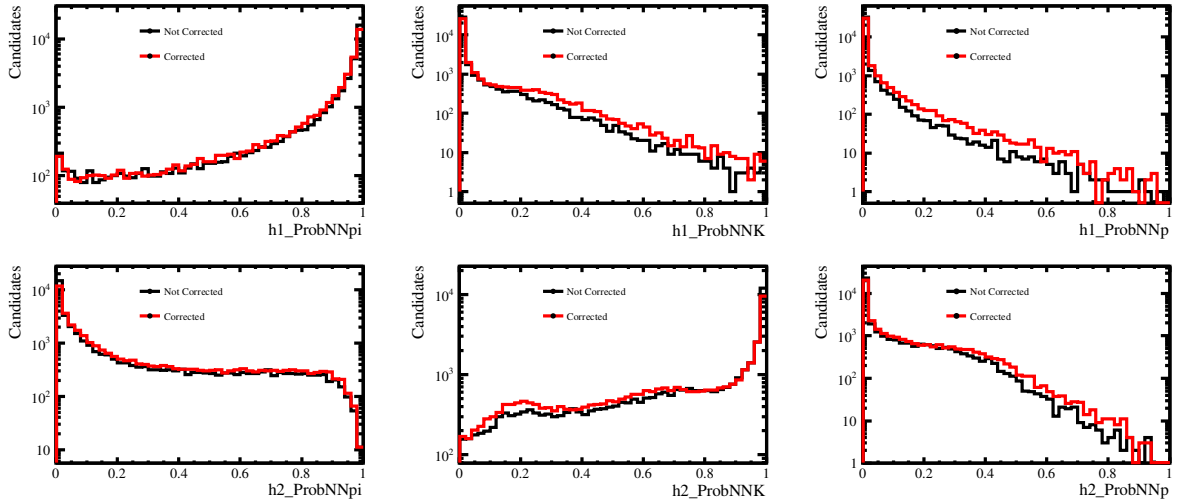

Figure A.76: Comparison between the Corrected (Red) and Non-corrected (Black) for $B^0 \to K^0_S \pi^+ K^-$ samples of 2012b *MagDown* for Down-DownK^0_S reconstructions. The Top (Bottom) row denote the distributions for h1 (h2) hadrons. The Plots are shown in logarithmic scale.

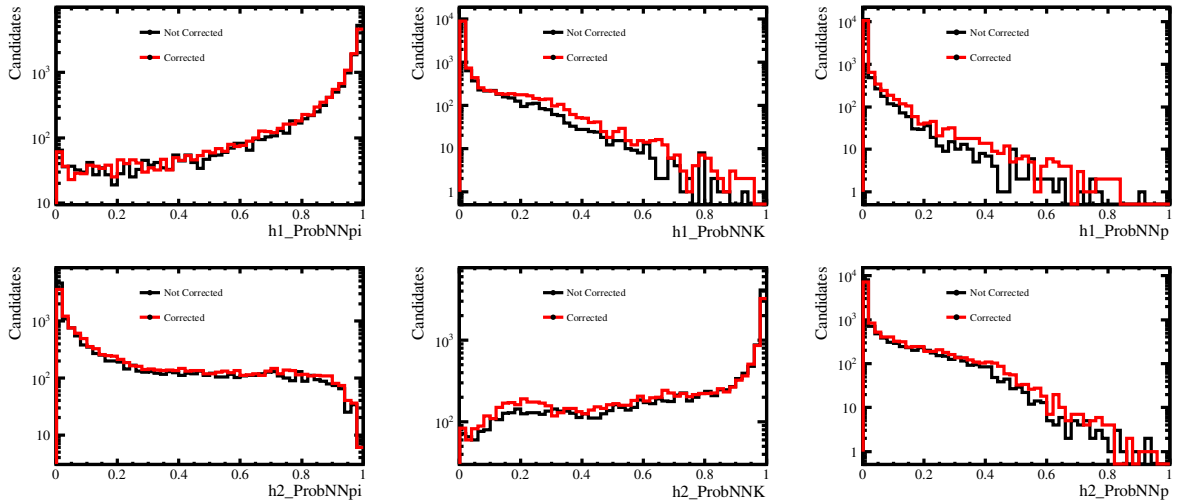

Figure A.77: Comparison between the Corrected (Red) and Non-corrected (Black) for $B^0 \to K^0_S \pi^+ K^-$ samples of 2012b *MagDown* for Long-LongK^0_S reconstructions. The Top (Bottom) row denote the distributions for h1 (h2) hadrons. The Plots are shown in logarithmic scale.

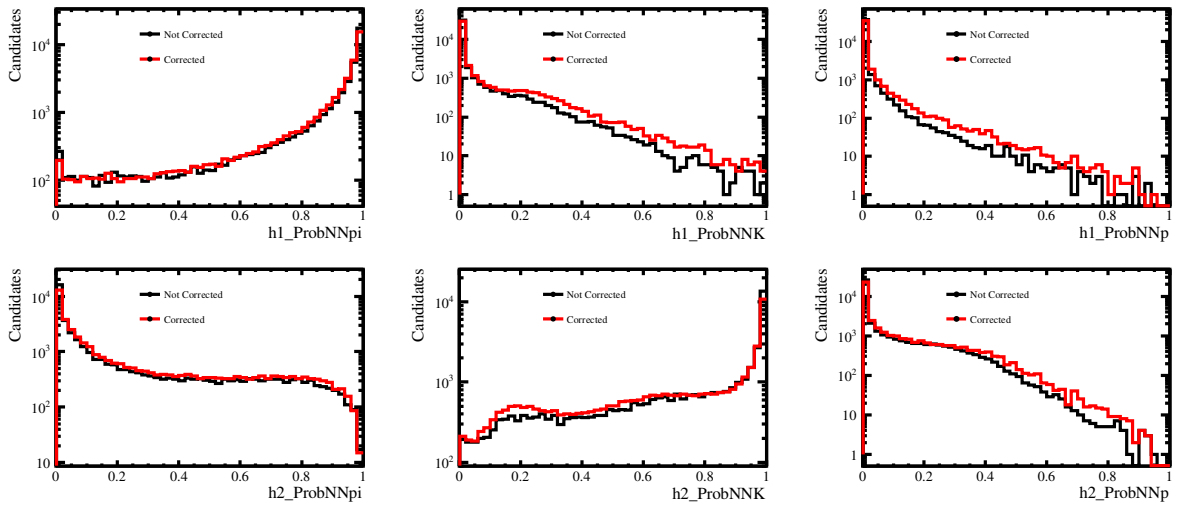

Figure A.78: Comparison between the Corrected (Red) and Non-corrected (Black) for $B_s \to K^0_S \pi^+ K^-$ samples of 2012b *MagDown* for Down-DownK^0_S reconstructions. The Top (Bottom) row denote the distributions for h1 (h2) hadrons. The Plots are shown in logarithmic scale.

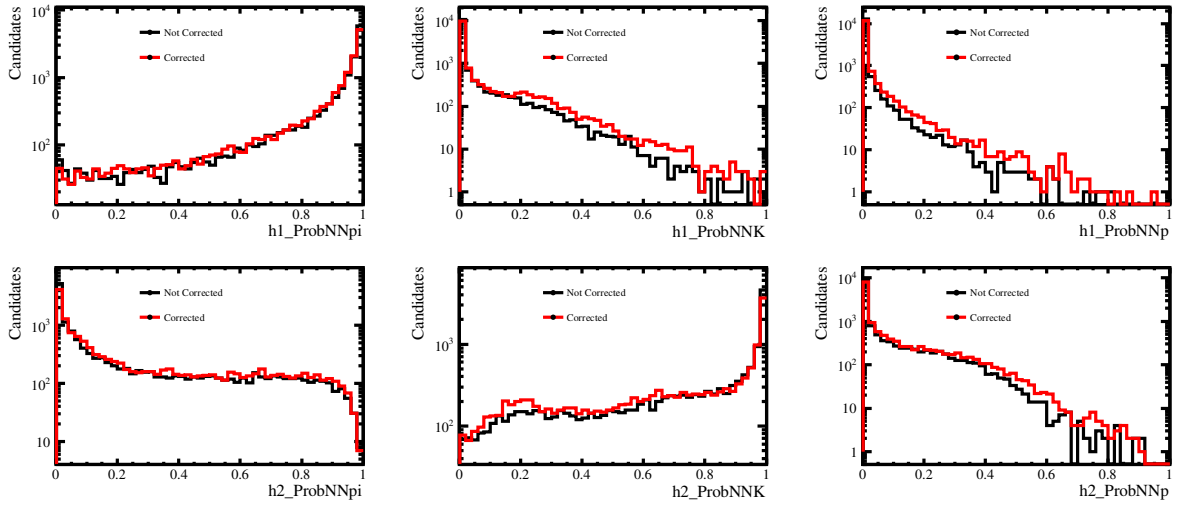

Figure A.79: Comparison between the Corrected (Red) and Non-corrected (Black) for $B_s \to K^0_S \pi^+ K^-$ samples of 2012b *MagDown* for Long-LongK^0_S reconstructions. The Top (Bottom) row denote the distributions for h1 (h2) hadrons. The Plots are shown in logarithmic scale.

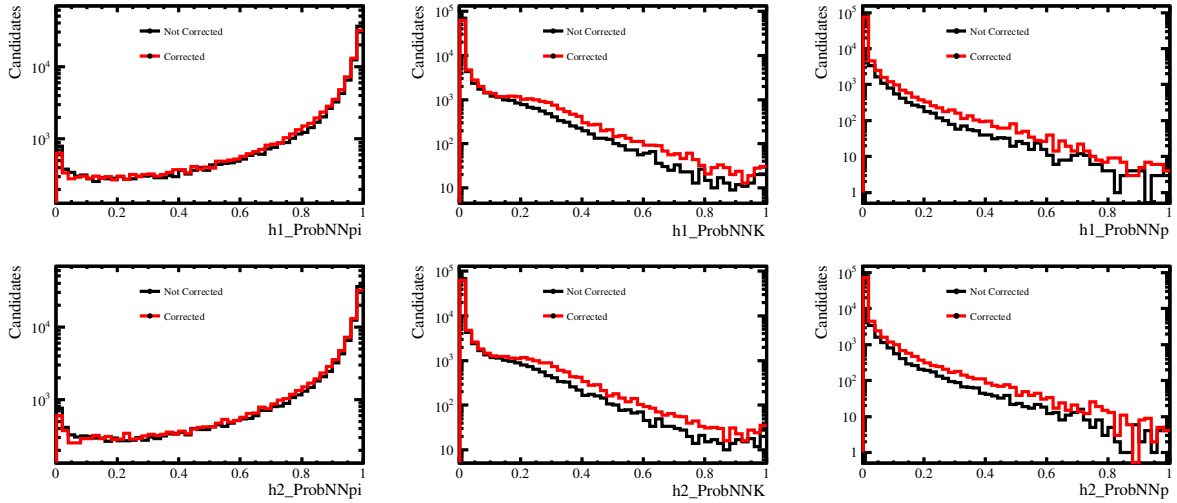

Figure A.80: Comparison between the Corrected (Red) and Non-corrected (Black) for $B^0 \to K^0_S \pi^+ \pi^-$ samples of 2012a *MagDown* for Down-DownK^0_S reconstructions. The Top (Bottom) row denote the distributions for h1 (h2) hadrons. The Plots are shown in logarithmic scale.

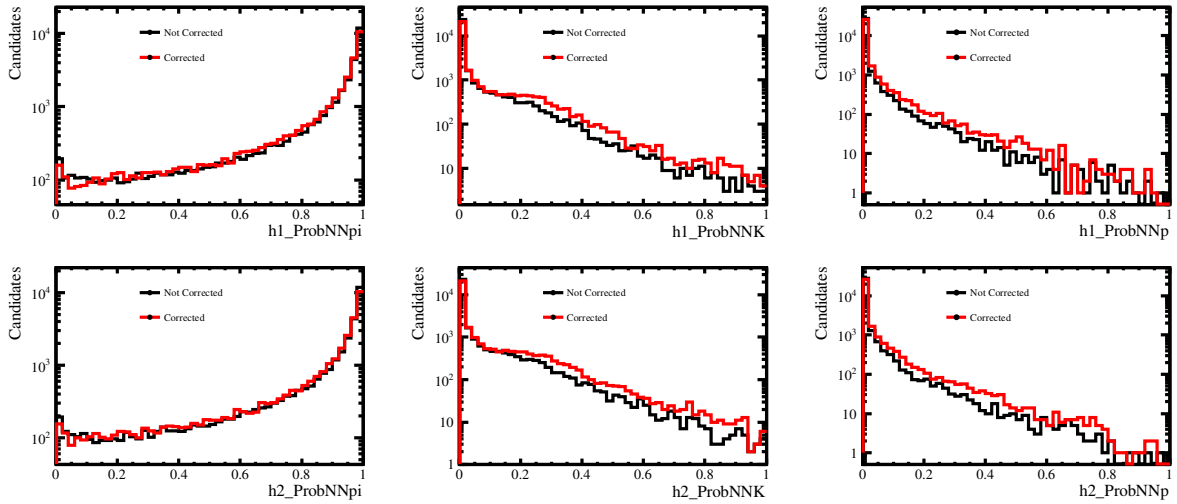

Figure A.81: Comparison between the Corrected (Red) and Non-corrected (Black) for $B^0 \to K^0_S \pi^+ \pi^-$ samples of 2012a *MagDown* for Long-LongK^0_S reconstructions. The Top (Bottom) row denote the distributions for h1 (h2) hadrons. The Plots are shown in logarithmic scale.

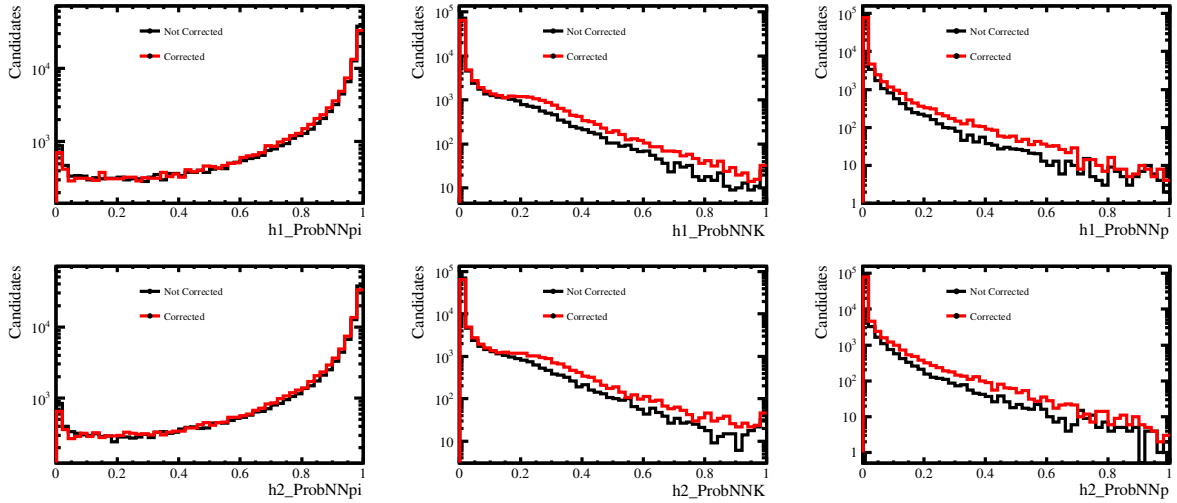

Figure A.82: Comparison between the Corrected (Red) and Non-corrected (Black) for $B_s \to K^0_S\pi^+\pi^-$ samples of 2012a *MagDown* for Down-DownK^0_S reconstructions. The Top (Bottom) row denote the distributions for h1 (h2) hadrons. The Plots are shown in logarithmic scale.

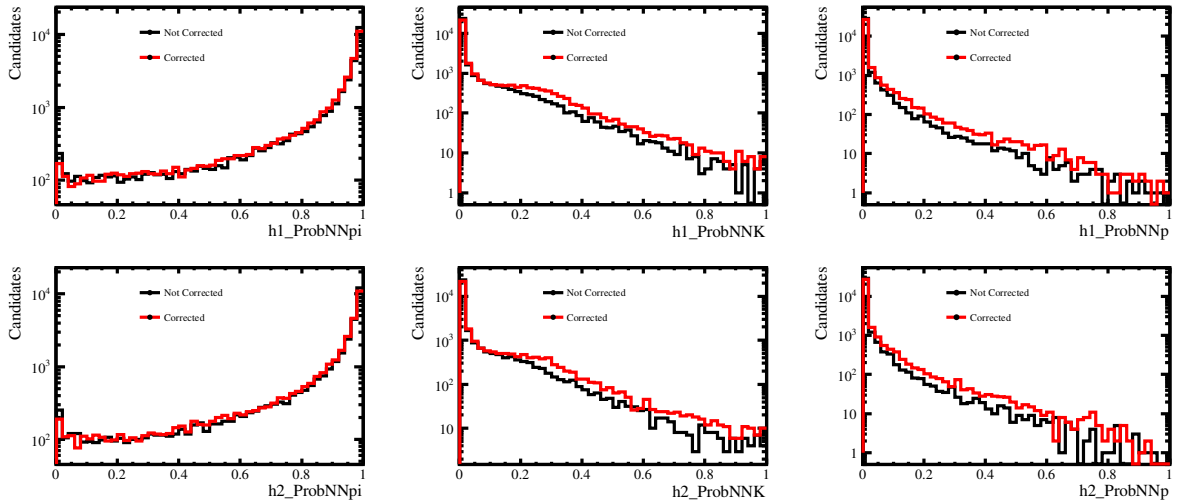

Figure A.83: Comparison between the Corrected (Red) and Non-corrected (Black) for $B_s \to K^0_S\pi^+\pi^-$ samples of 2012a *MagDown* for Long-LongK^0_S reconstructions. The Top (Bottom) row denote the distributions for h1 (h2) hadrons. The Plots are shown in logarithmic scale.

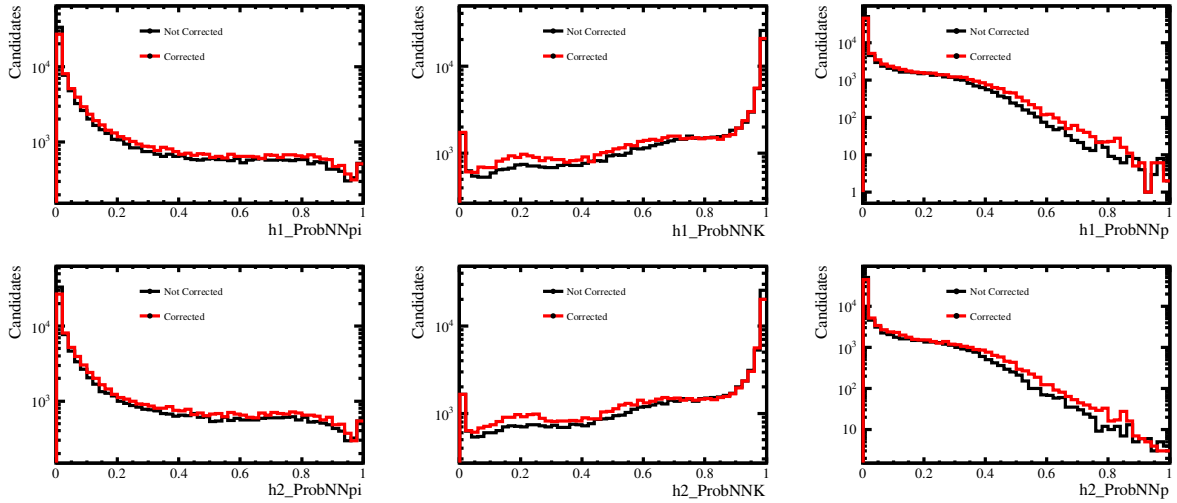

Figure A.84: Comparison between the Corrected (Red) and Non-corrected (Black) for $B^0 \to K^0_S K^+ K^-$ samples of 2012a *MagDown* for Down-DownK^0_S reconstructions. The Top (Bottom) row denote the distributions for h1 (h2) hadrons. The Plots are shown in logarithmic scale.

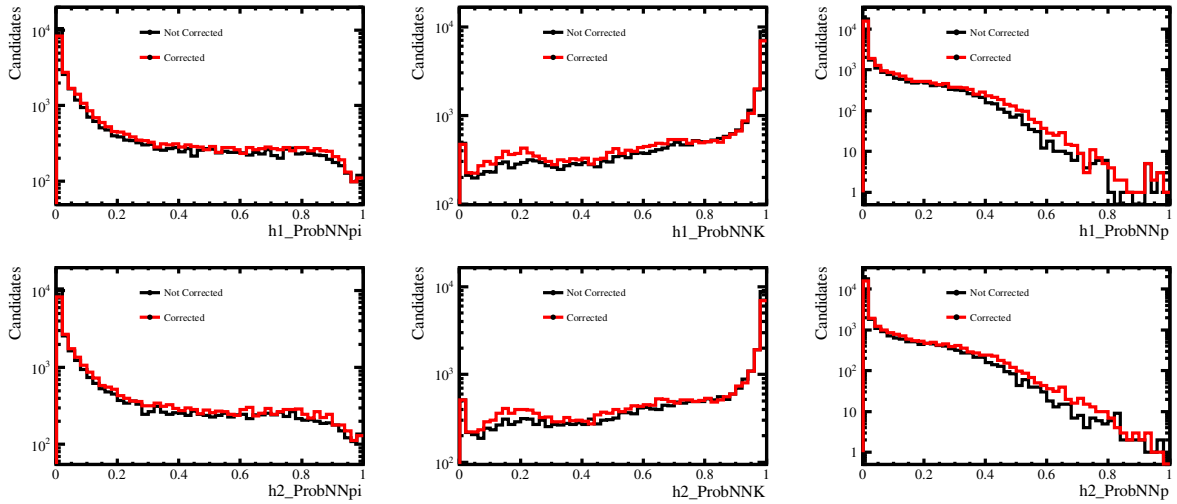

Figure A.85: Comparison between the Corrected (Red) and Non-corrected (Black) for $B^0 \to K^0_S K^+ K^-$ samples of 2012a *MagDown* for Long-LongK^0_S reconstructions. The Top (Bottom) row denote the distributions for h1 (h2) hadrons. The Plots are shown in logarithmic scale.

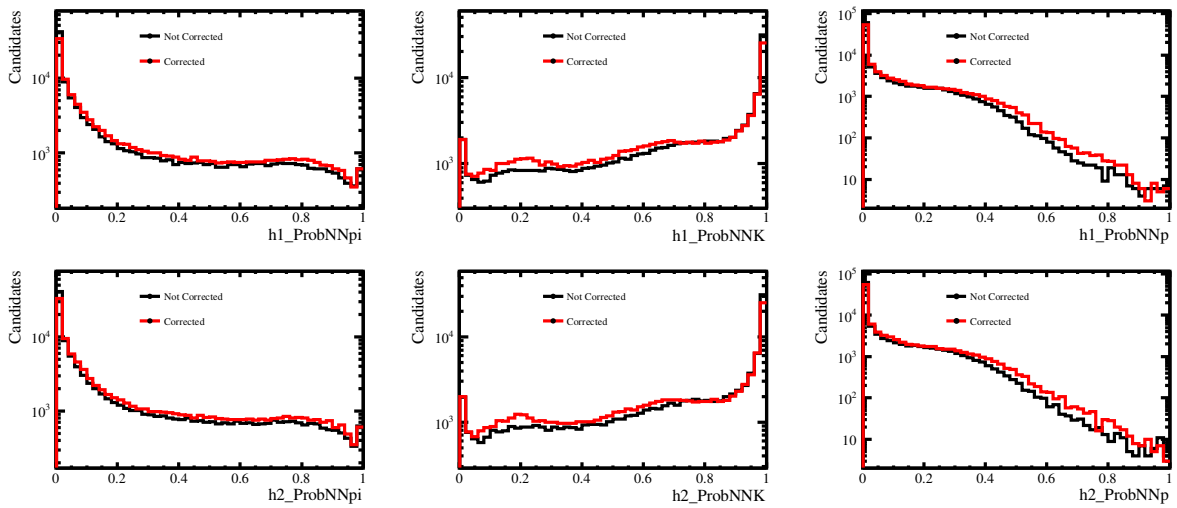

Figure A.86: Comparison between the Corrected (Red) and Non-corrected (Black) for $B_s \to K^0_S K^+ K^-$ samples of 2012a *MagDown* for Down-DownK^0_S reconstructions. The Top (Bottom) row denote the distributions for h1 (h2) hadrons. The Plots are shown in logarithmic scale.

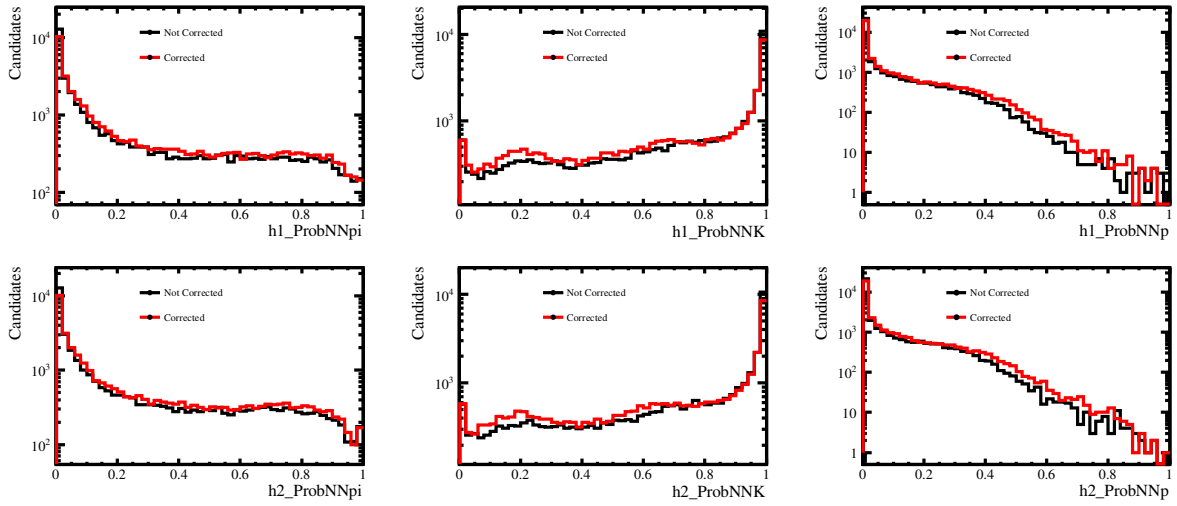

Figure A.87: Comparison between the Corrected (Red) and Non-corrected (Black) for $B_s \to K^0_S K^+ K^-$ samples of 2012a *MagDown* for Long-LongK^0_S reconstructions. The Top (Bottom) row denote the distributions for h1 (h2) hadrons. The Plots are shown in logarithmic scale.

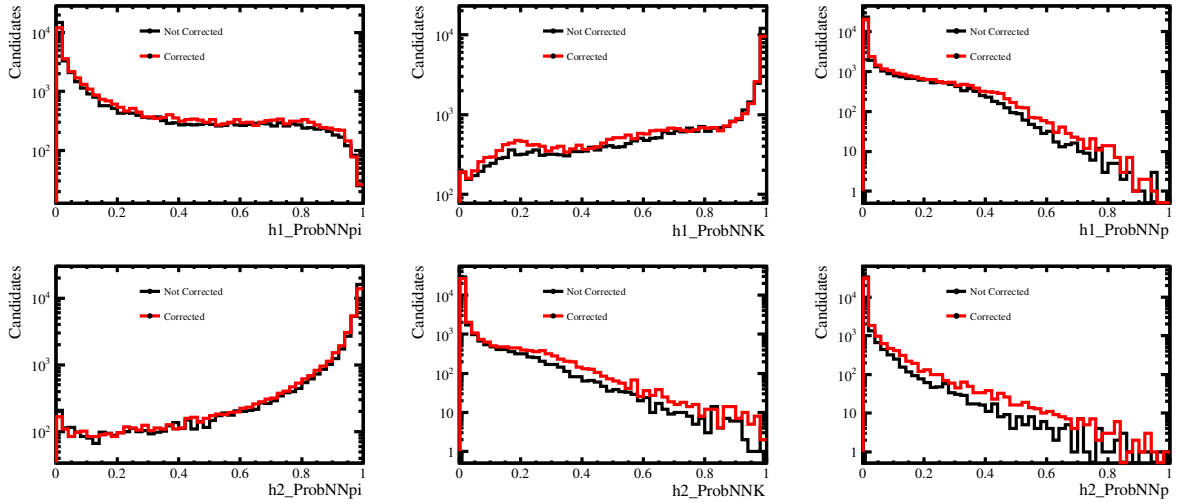

Figure A.88: Comparison between the Corrected (Red) and Non-corrected (Black) for $B^0 \to K^0_S K^+ \pi^-$ samples of 2012a *MagDown* for Down-DownK^0_S reconstructions. The Top (Bottom) row denote the distributions for h1 (h2) hadrons. The Plots are shown in logarithmic scale.

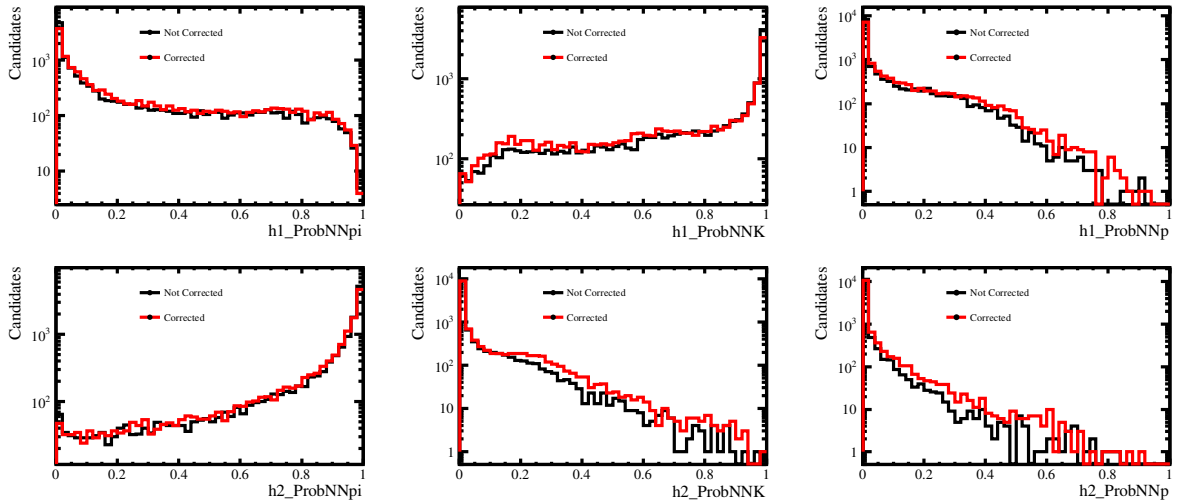

Figure A.89: Comparison between the Corrected (Red) and Non-corrected (Black) for $B^0 \to K^0_S K^+ \pi^-$ samples of 2012a *MagDown* for Long-LongK^0_S reconstructions. The Top (Bottom) row denote the distributions for h1 (h2) hadrons. The Plots are shown in logarithmic scale.

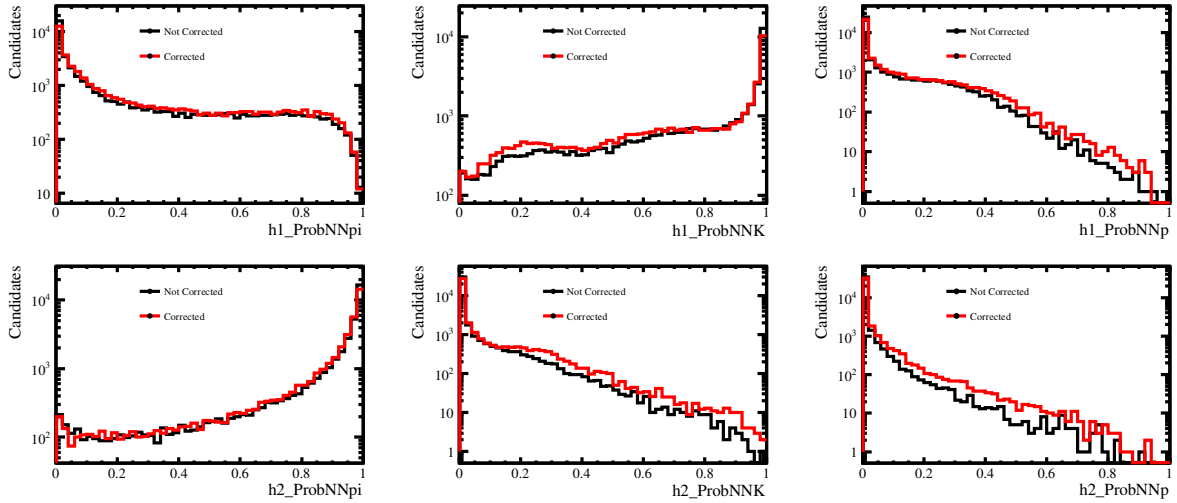

Figure A.90: Comparison between the Corrected (Red) and Non-corrected (Black) for $B_s \to K^0_S K^+ \pi^-$ samples of 2012a *MagDown* for Down-DownK^0_S reconstructions. The Top (Bottom) row denote the distributions for h1 (h2) hadrons. The Plots are shown in logarithmic scale.

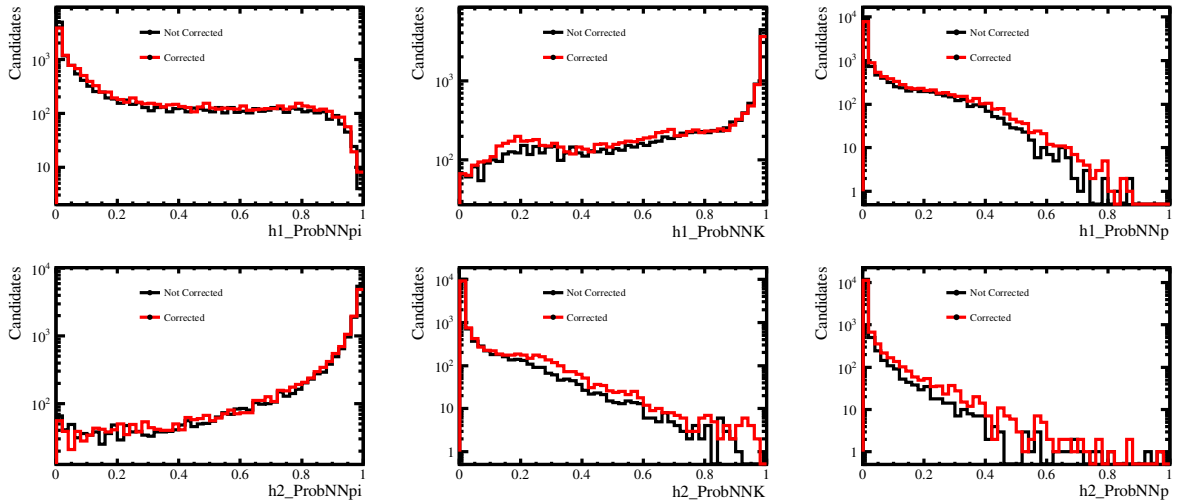

Figure A.91: Comparison between the Corrected (Red) and Non-corrected (Black) for $B_s \to K^0_S K^+ \pi^-$ samples of 2012a *MagDown* for Long-LongK^0_S reconstructions. The Top (Bottom) row denote the distributions for h1 (h2) hadrons. The Plots are shown in logarithmic scale.

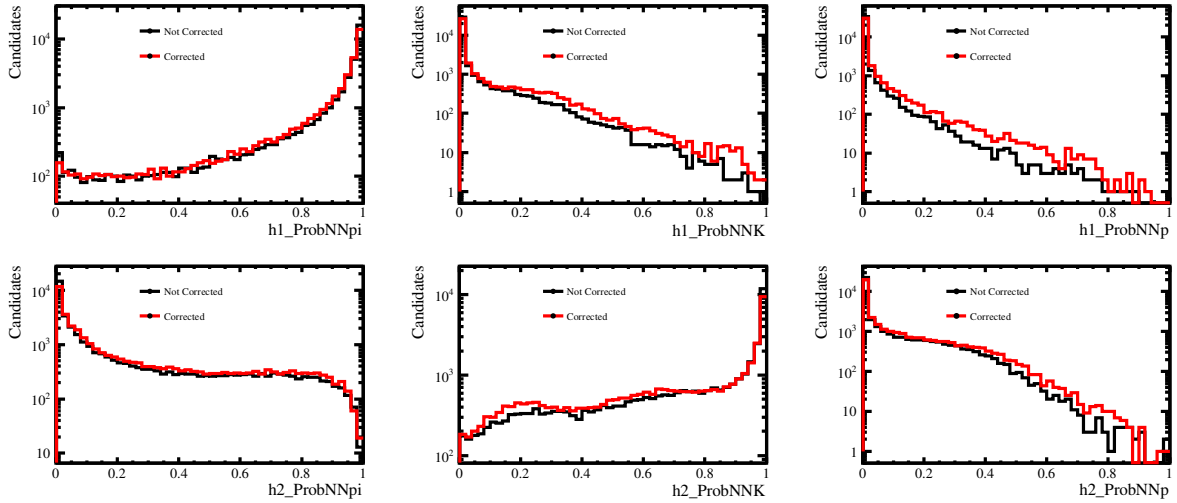

Figure A.92: Comparison between the Corrected (Red) and Non-corrected (Black) for $B^0 \to K^0_S \pi^+ K^-$ samples of 2012a *MagDown* for Down-DownK^0_S reconstructions. The Top (Bottom) row denote the distributions for h1 (h2) hadrons. The Plots are shown in logarithmic scale.

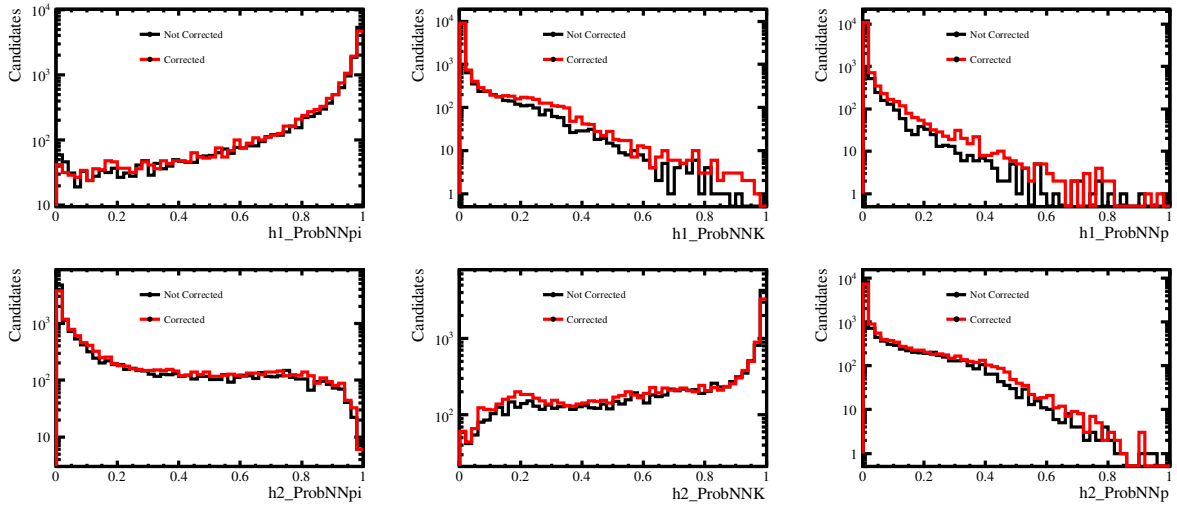

Figure A.93: Comparison between the Corrected (Red) and Non-corrected (Black) for $B^0 \to K^0_S \pi^+ K^-$ samples of 2012a *MagDown* for Long-LongK^0_S reconstructions. The Top (Bottom) row denote the distributions for h1 (h2) hadrons. The Plots are shown in logarithmic scale.

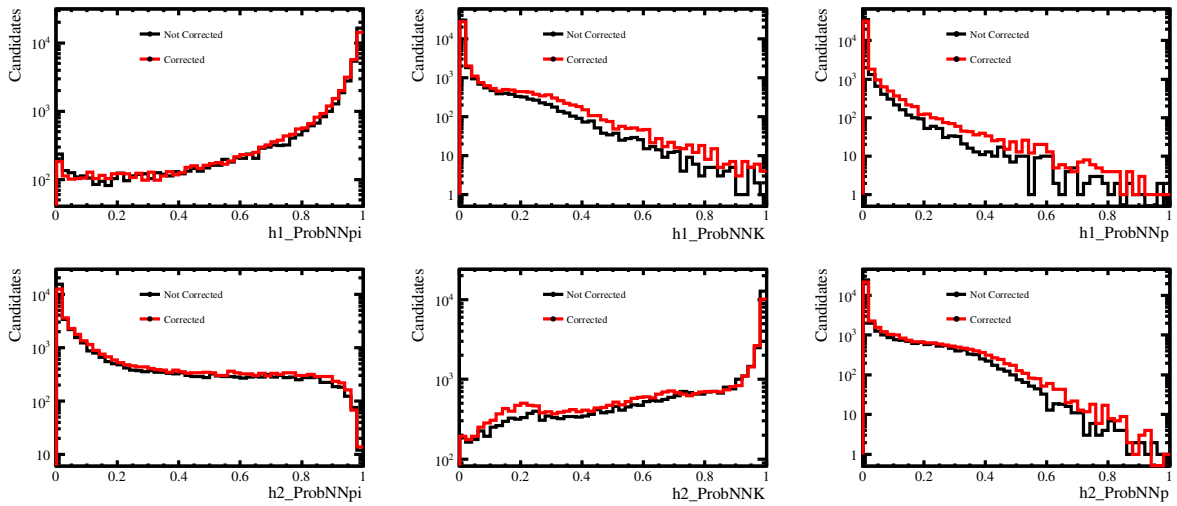

Figure A.94: Comparison between the Corrected (Red) and Non-corrected (Black) for $B_s \to K^0_S \pi^+ K^-$ samples of 2012a *MagDown* for Down-DownK^0_S reconstructions. The Top (Bottom) row denote the distributions for h1 (h2) hadrons. The Plots are shown in logarithmic scale.

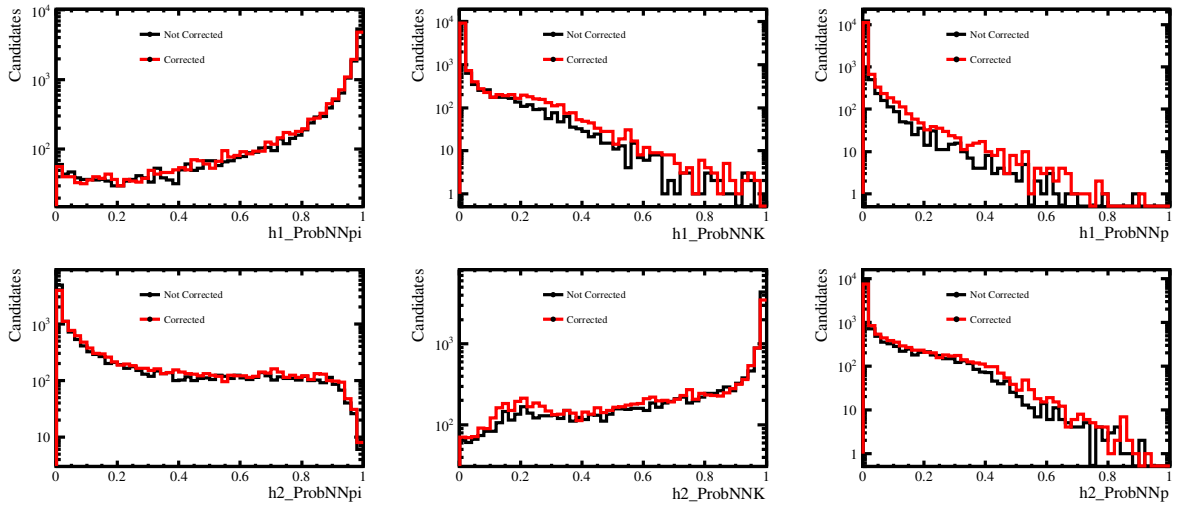

Figure A.95: Comparison between the Corrected (Red) and Non-corrected (Black) for $B_s \to K^0_S \pi^+ K^-$ samples of 2012a *MagDown* for Long-LongK^0_S reconstructions. The Top (Bottom) row denote the distributions for h1 (h2) hadrons. The Plots are shown in logarithmic scale.

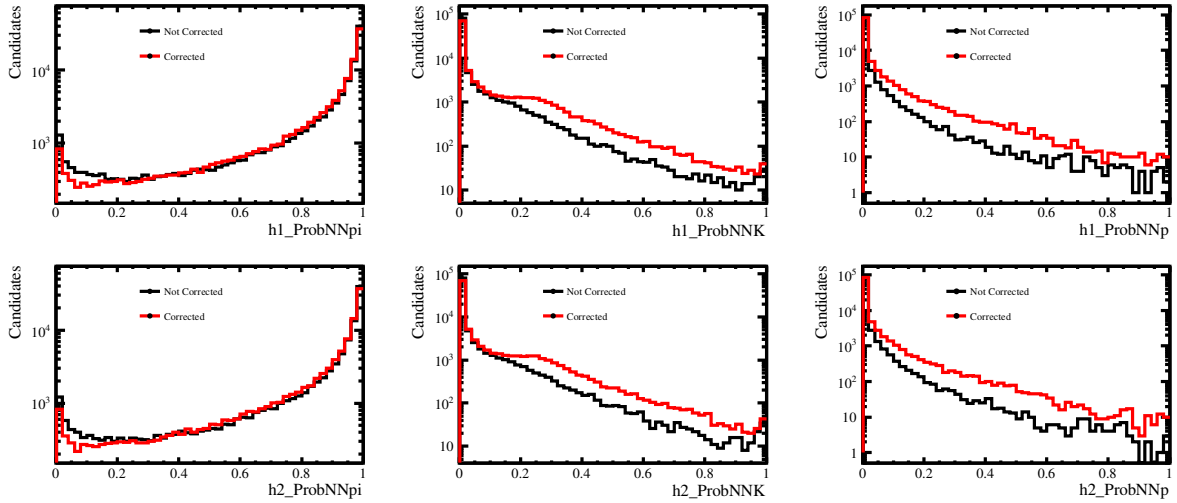

Figure A.96: Comparison between the Corrected (Red) and Non-corrected (Black) for $B^0 \to K^0_S \pi^+ \pi^-$ samples of 2011 *MagDown* for Down-DownK^0_S reconstructions. The Top (Bottom) row denote the distributions for h1 (h2) hadrons. The Plots are shown in logarithmic scale.

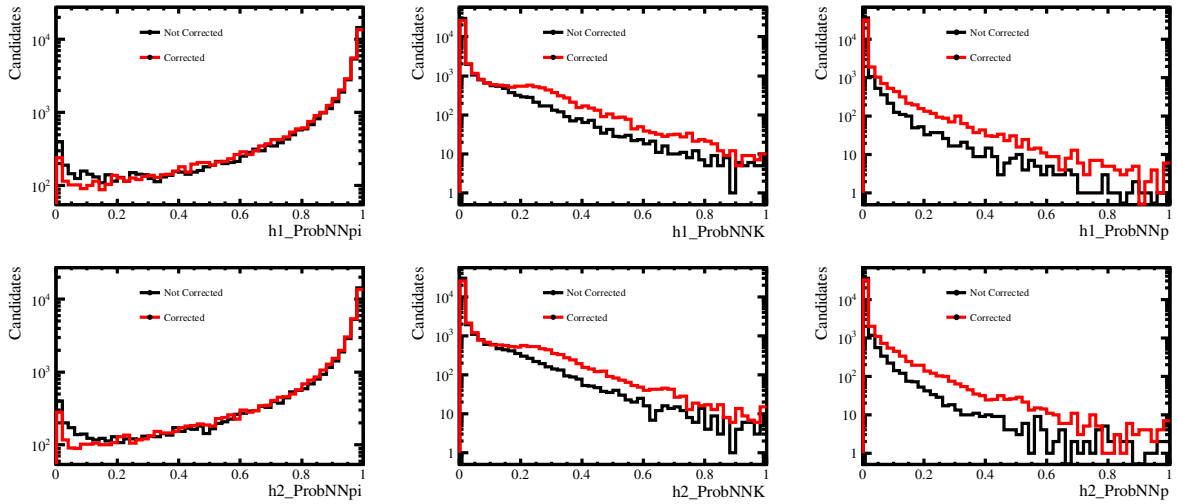

Figure A.97: Comparison between the Corrected (Red) and Non-corrected (Black) for $B^0 \to K^0_S \pi^+ \pi^-$ samples of 2011 *MagDown* for Long-LongK^0_S reconstructions. The Top (Bottom) row denote the distributions for h1 (h2) hadrons. The Plots are shown in logarithmic scale.

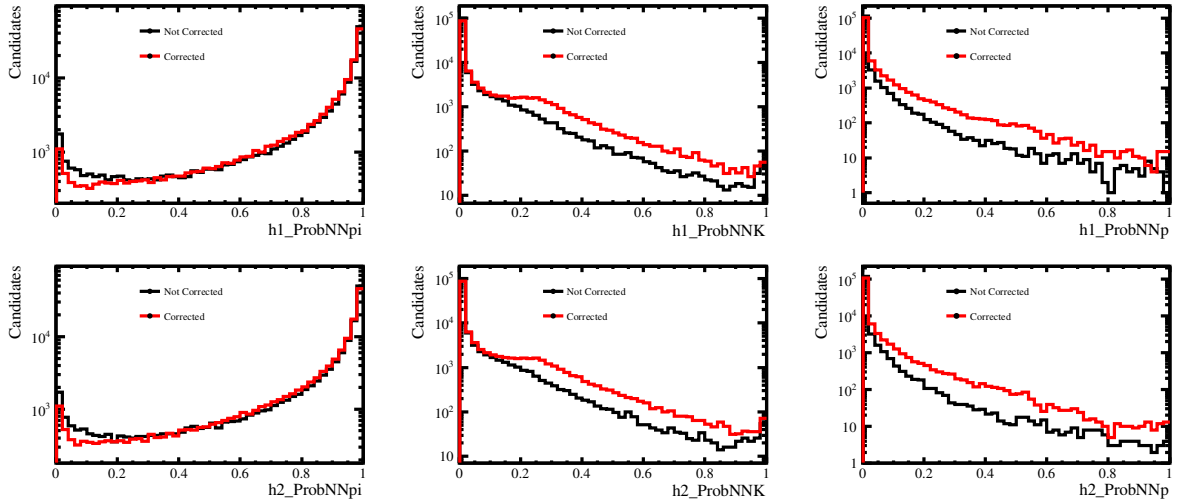

Figure A.98: Comparison between the Corrected (Red) and Non-corrected (Black) for $B_s \to K^0_S \pi^+ \pi^-$ samples of 2011 *MagDown* for Down-DownK^0_S reconstructions. The Top (Bottom) row denote the distributions for h1 (h2) hadrons. The Plots are shown in logarithmic scale.

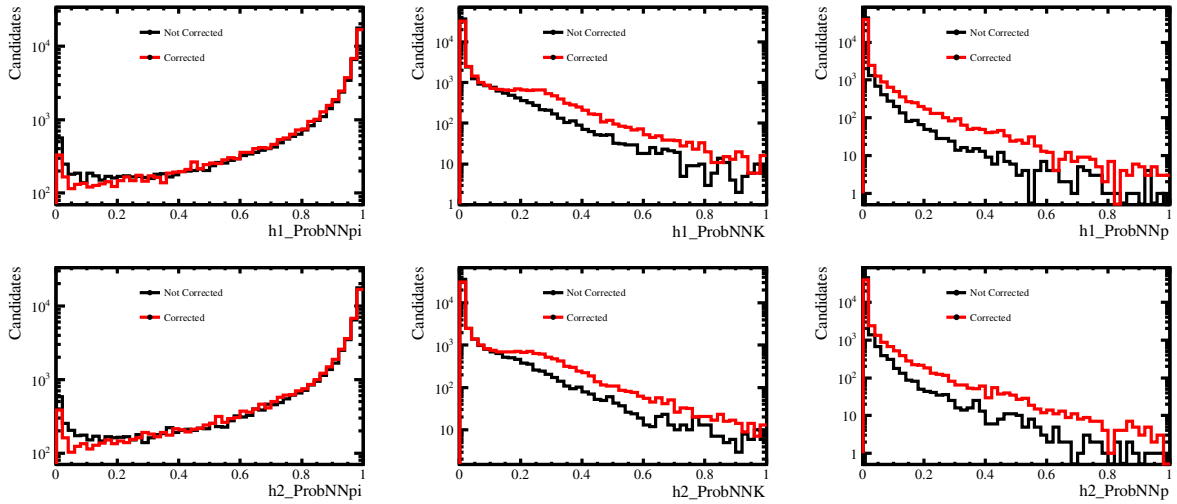

Figure A.99: Comparison between the Corrected (Red) and Non-corrected (Black) for $B_s \to K^0_S \pi^+ \pi^-$ samples of 2011 *MagDown* for Long-LongK^0_S reconstructions. The Top (Bottom) row denote the distributions for h1 (h2) hadrons. The Plots are shown in logarithmic scale.

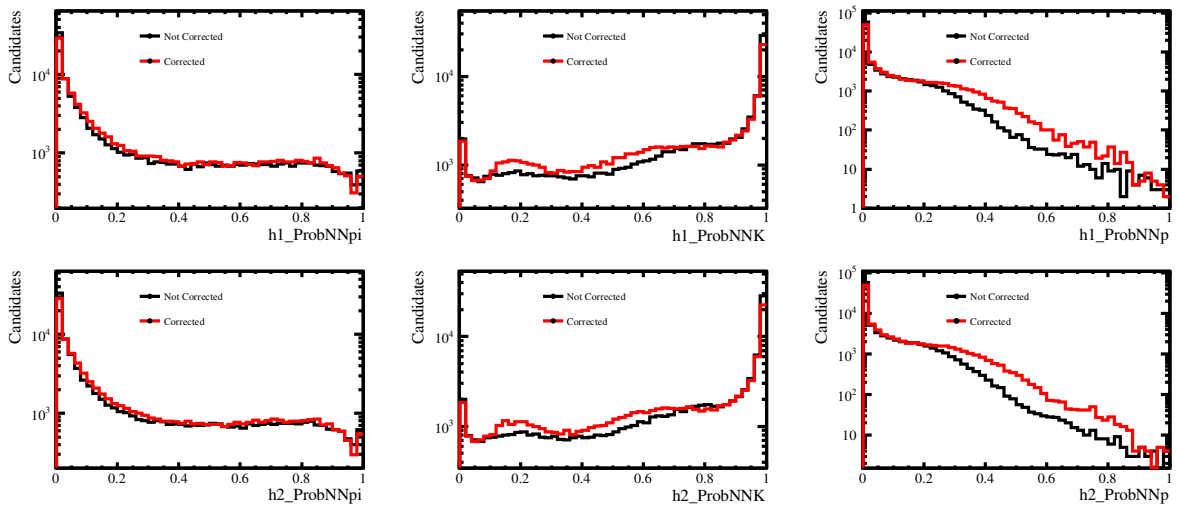

Figure A.100: Comparison between the Corrected (Red) and Non-corrected (Black) for $B^0 \to K^0_S K^+ K^-$ samples of 2011 *MagDown* for Down-DownK^0_S reconstructions. The Top (Bottom) row denote the distributions for h1 (h2) hadrons. The Plots are shown in logarithmic scale.

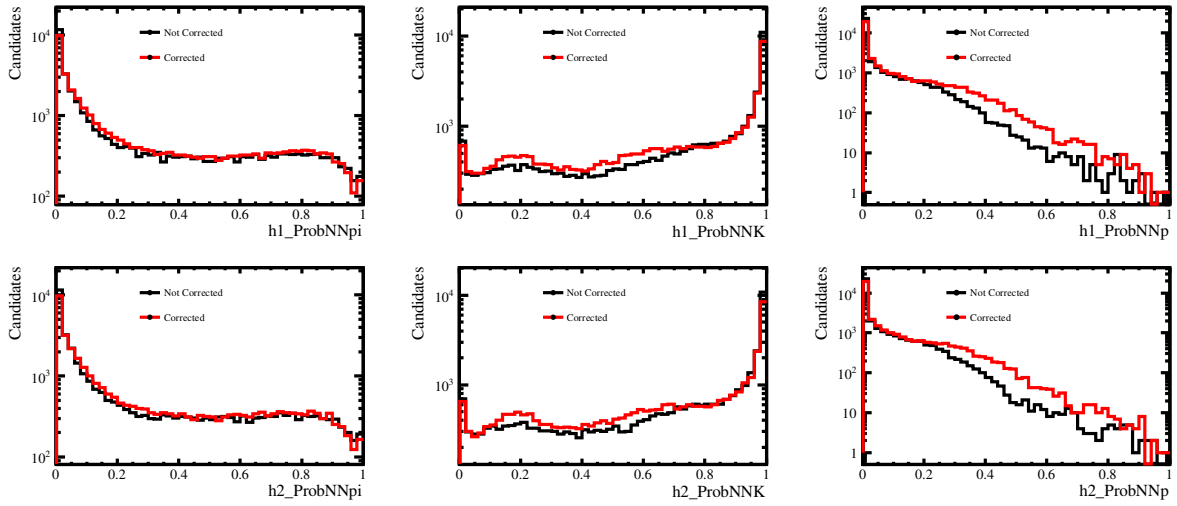

Figure A.101: Comparison between the Corrected (Red) and Non-corrected (Black) for $B^0 \to K^0_S K^+ K^-$ samples of 2011 *MagDown* for Long-LongK^0_S reconstructions. The Top (Bottom) row denote the distributions for h1 (h2) hadrons. The Plots are shown in logarithmic scale.

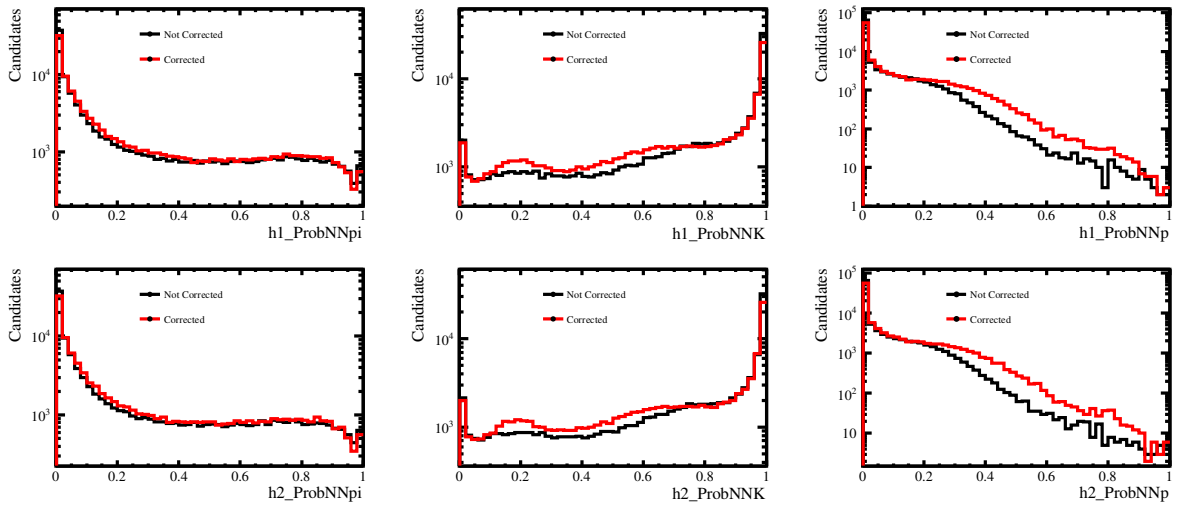

Figure A.102: Comparison between the Corrected (Red) and Non-corrected (Black) for $B_s \to K^0_S K^+ K^-$ samples of 2011 *MagDown* for Down-DownK^0_S reconstructions. The Top (Bottom) row denote the distributions for h1 (h2) hadrons. The Plots are shown in logarithmic scale.

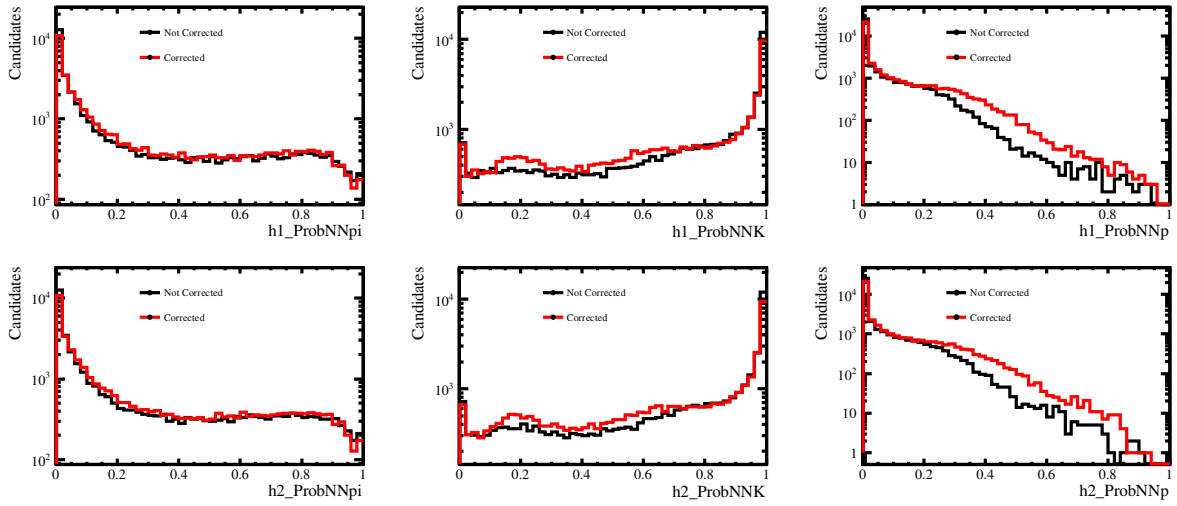

Figure A.103: Comparison between the Corrected (Red) and Non-corrected (Black) for $B_s \to K^0_S K^+ K^-$ samples of 2011 *MagDown* for Long-LongK^0_S reconstructions. The Top (Bottom) row denote the distributions for h1 (h2) hadrons. The Plots are shown in logarithmic scale.

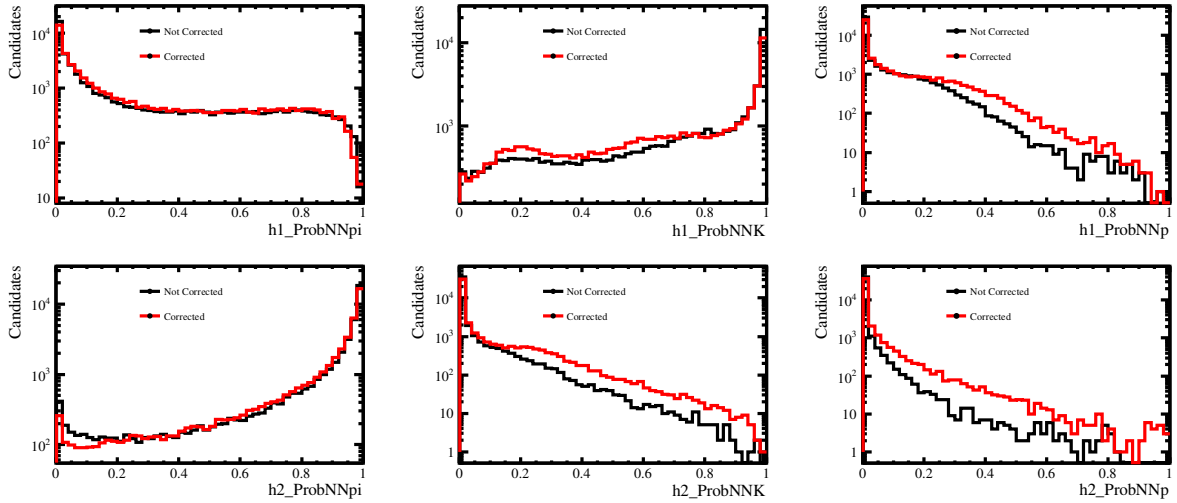

Figure A.104: Comparison between the Corrected (Red) and Non-corrected (Black) for $B^0 \to K^0_S K^+ \pi^-$ samples of 2011 *MagDown* for Down-DownK^0_S reconstructions. The Top (Bottom) row denote the distributions for h1 (h2) hadrons. The Plots are shown in logarithmic scale.

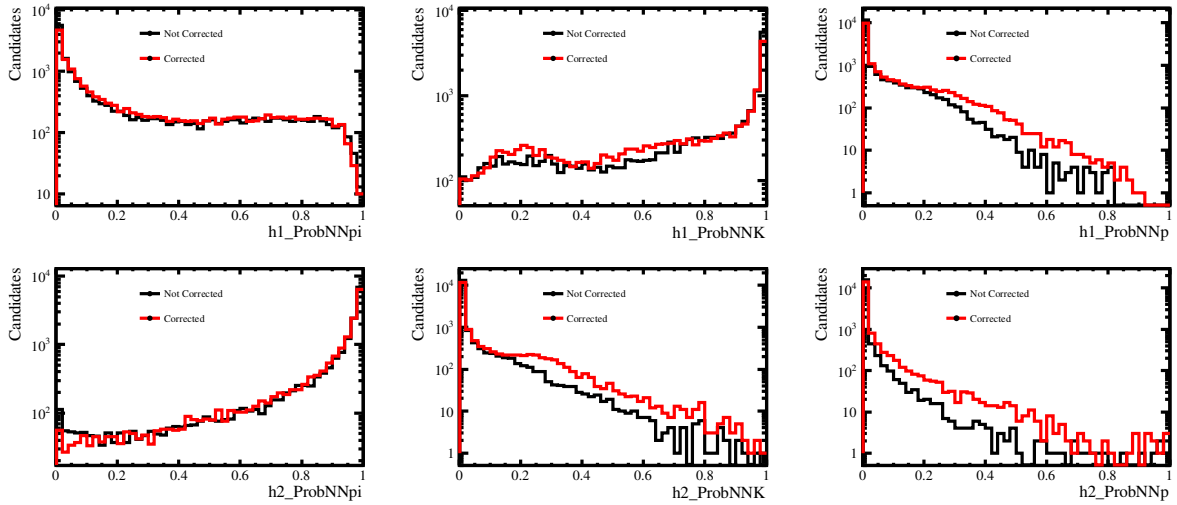

Figure A.105: Comparison between the Corrected (Red) and Non-corrected (Black) for $B^0 \to K^0_S K^+ \pi^-$ samples of 2011 *MagDown* for Long-LongK^0_S reconstructions. The Top (Bottom) row denote the distributions for h1 (h2) hadrons. The Plots are shown in logarithmic scale.

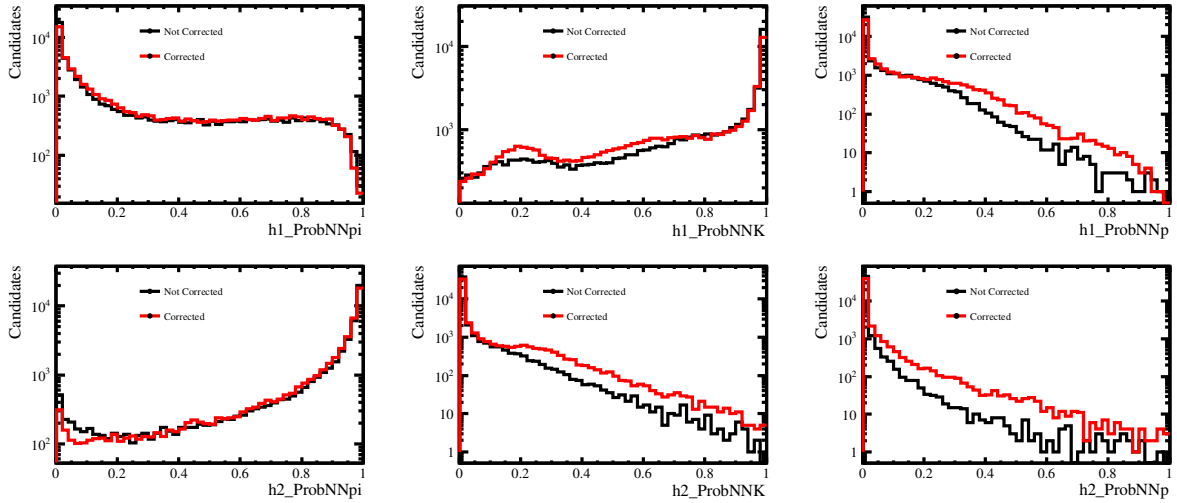

Figure A.106: Comparison between the Corrected (Red) and Non-corrected (Black) for $B_s \to K^0_S K^+ \pi^-$ samples of 2011 *MagDown* for Down-DownK^0_S reconstructions. The Top (Bottom) row denote the distributions for h1 (h2) hadrons. The Plots are shown in logarithmic scale.

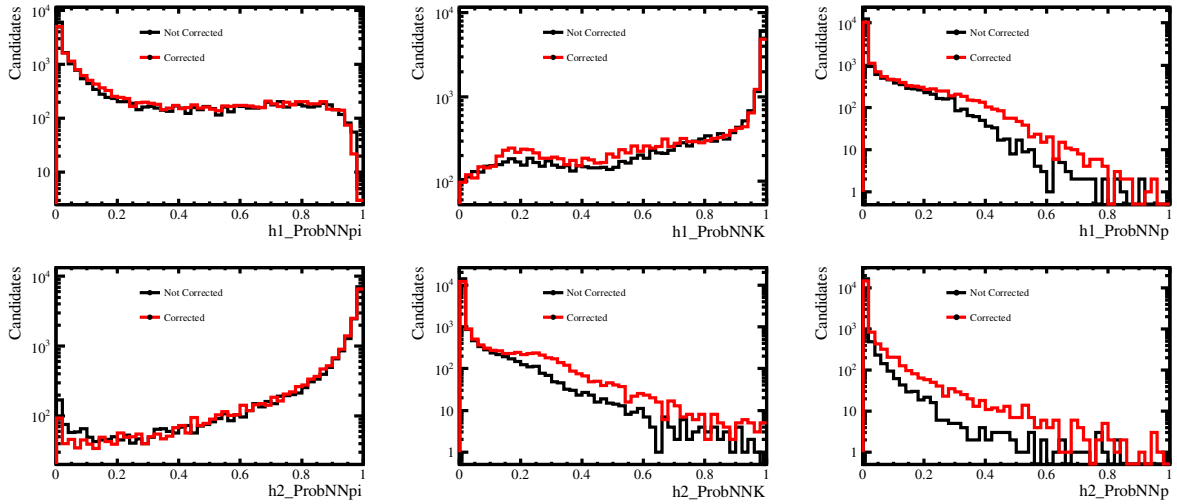

Figure A.107: Comparison between the Corrected (Red) and Non-corrected (Black) for $B_s \to K^0_S K^+ \pi^-$ samples of 2011 *MagDown* for Long-LongK^0_S reconstructions. The Top (Bottom) row denote the distributions for h1 (h2) hadrons. The Plots are shown in logarithmic scale.

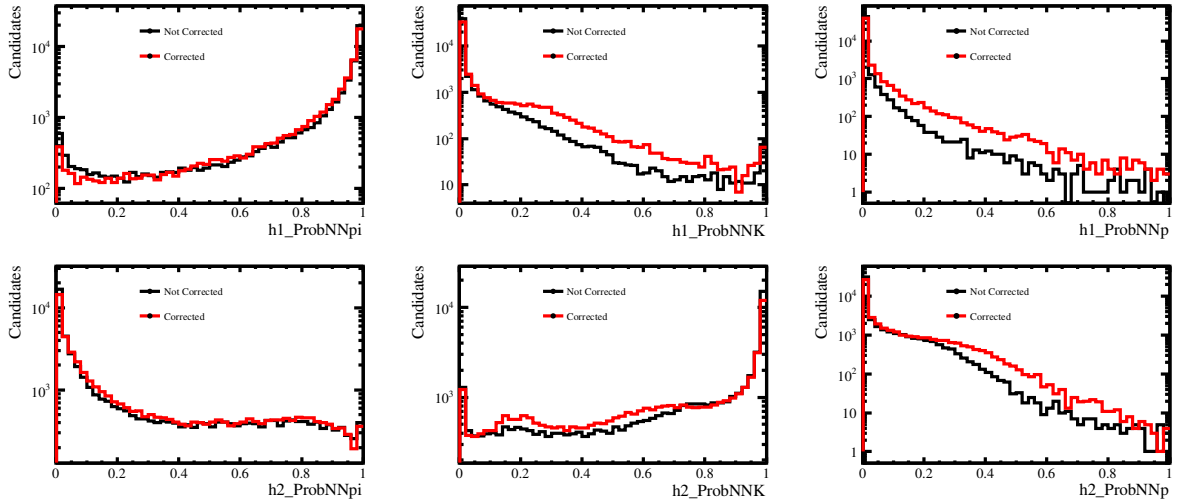

Figure A.108: Comparison between the Corrected (Red) and Non-corrected (Black) for $B^0 \to K^0_S \pi^+ K^-$ samples of 2011 *MagDown* for Down-DownK^0_S reconstructions. The Top (Bottom) row denote the distributions for h1 (h2) hadrons. The Plots are shown in logarithmic scale.

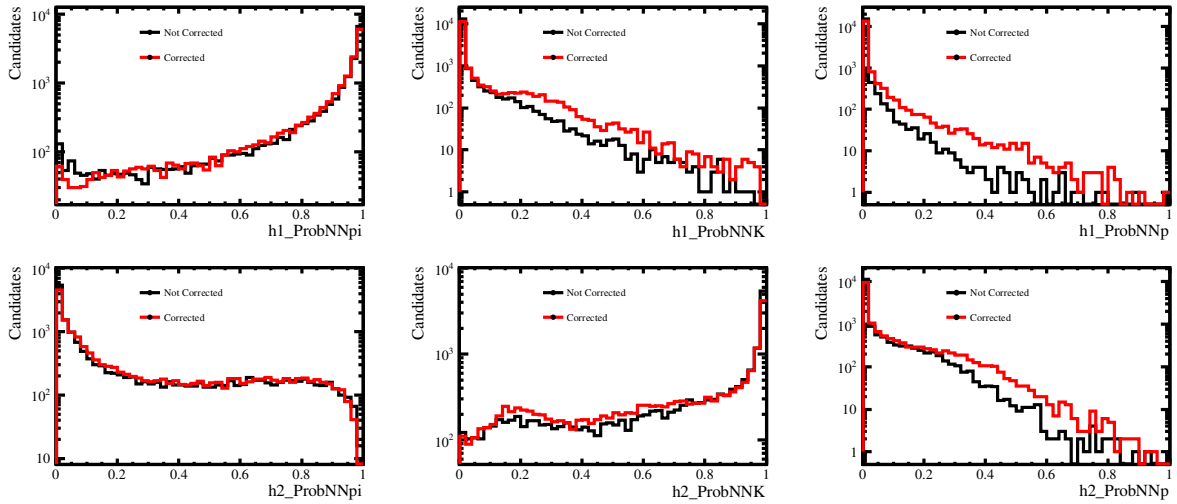

Figure A.109: Comparison between the Corrected (Red) and Non-corrected (Black) for $B^0 \to K^0_S \pi^+ K^-$ samples of 2011 *MagDown* for Long-LongK^0_S reconstructions. The Top (Bottom) row denote the distributions for h1 (h2) hadrons. The Plots are shown in logarithmic scale.

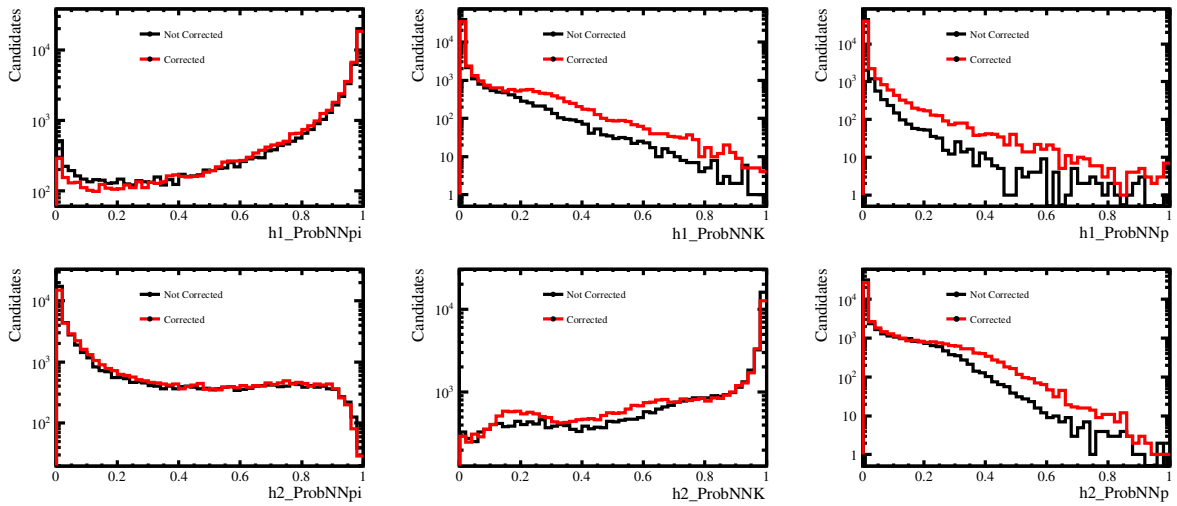

Figure A.110: Comparison between the Corrected (Red) and Non-corrected (Black) for $B_s \to K^0_S \pi^+ K^-$ samples of 2011 *MagDown* for Down-DownK^0_S reconstructions. The Top (Bottom) row denote the distributions for h1 (h2) hadrons. The Plots are shown in logarithmic scale.

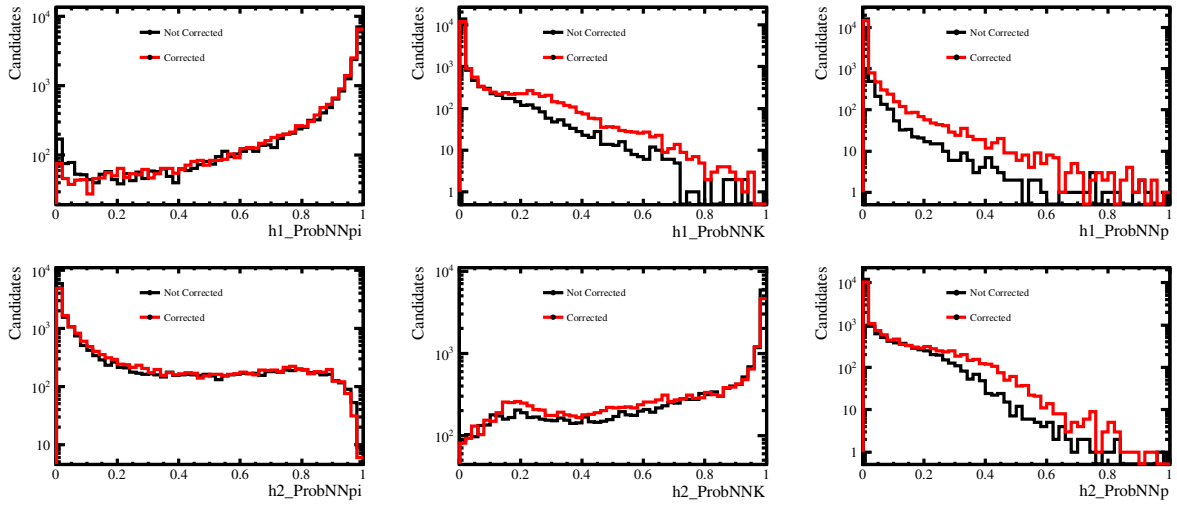

Figure A.111: Comparison between the Corrected (Red) and Non-corrected (Black) for $B_s \to K^0_S \pi^+ K^-$ samples of 2011 *MagDown* for Long-LongK^0_S reconstructions. The Top (Bottom) row denote the distributions for h1 (h2) hadrons. The Plots are shown in logarithmic scale.

Appendix B

2D Optimization

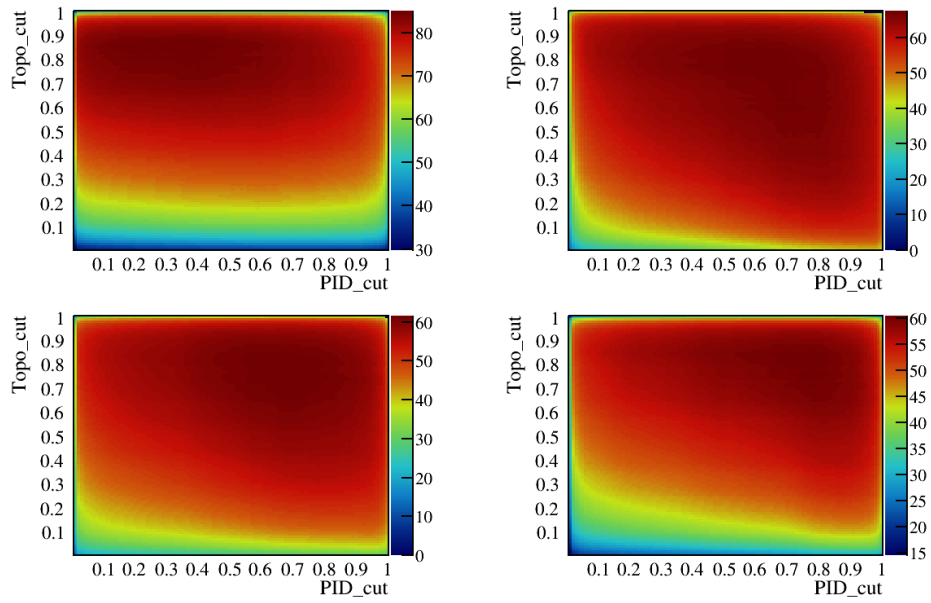

Figure B.1: The 2D Optimization of Cabbibo favored modes $B^0_{d,s} \to K^0_S h^+ h'^-$ decay for 2017 DD K^0_S reconstruction. Top: left (right) corresponds to the $B^0 \to K^0_S \pi^+ \pi^-$ ($B^0 \to K^0_S K^+ K^-$). Bottom: left(right) corresponds to $B_s \to K^0_S \pi^+ K^-$($B_s \to K^0_S K^+ \pi^-$)

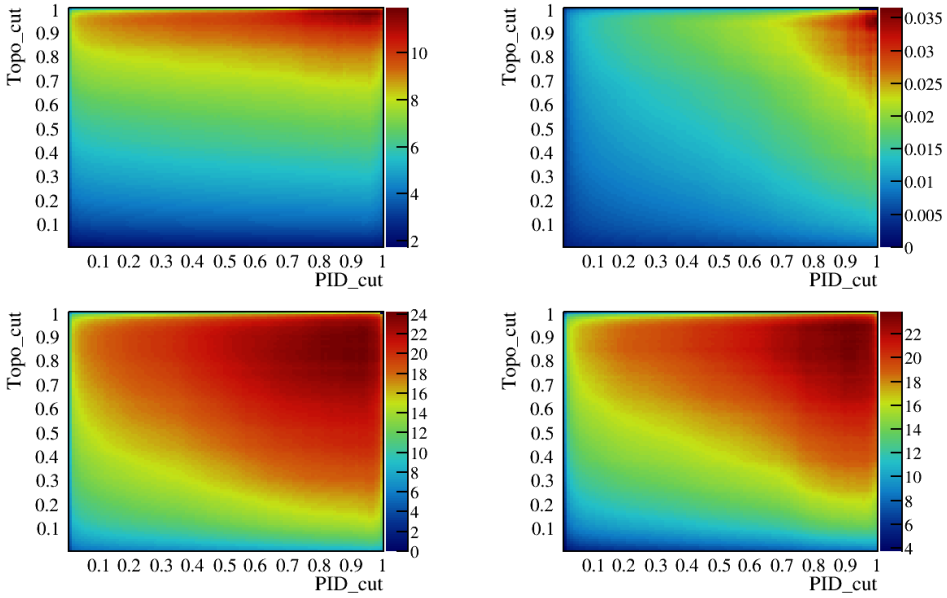

Figure B.2: The 2D Optimization of Cabbibo suppressed modes $B^0_{d,s} \to K^0_S h^+ h'^-$ decay for 2017 DD K^0_S reconstruction. Top: left (right) corresponds to the $B_s \to K^0_S \pi^+ \pi^-$ ($B_s \to K^0_S K^+ K^-$). Bottom: left(right) corresponds to $B^0 \to K^0_S \pi^+ K^-$($B^0 \to K^0_S K^+ \pi^-$)

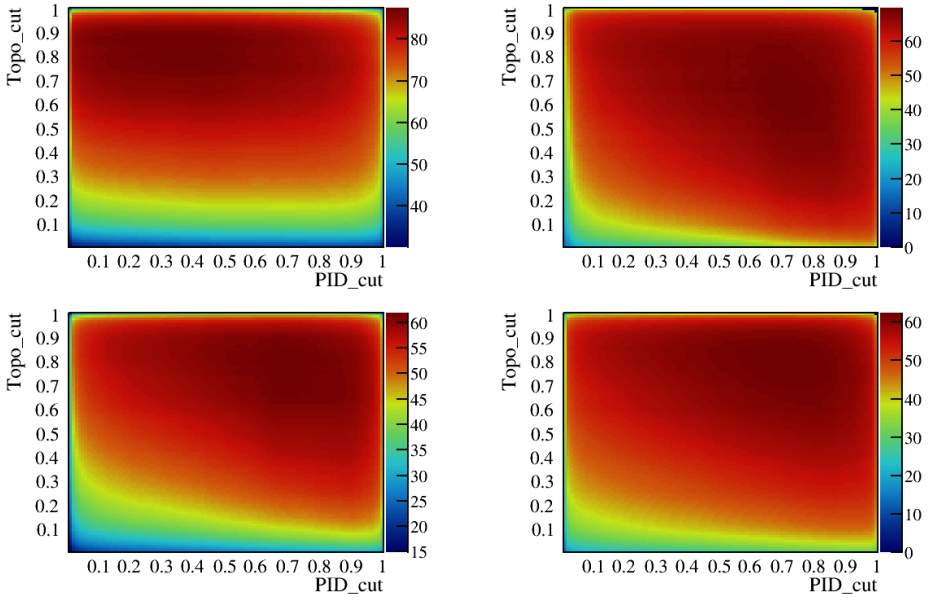

Figure B.3: The 2D Optimization of Cabbibo favored modes $B^0_{d,s} \to K^0_S h^+ h'^-$ decay for 2016 DD K^0_S reconstruction. Top: left(right) corresponds to the $B^0 \to K^0_S \pi^+ \pi^-$ ($B^0 \to K^0_S K^+ K^-$). Bottom: left(right) corresponds to $B_s \to K^0_S \pi^+ K^-$($B_s \to K^0_S K^+ \pi^-$)

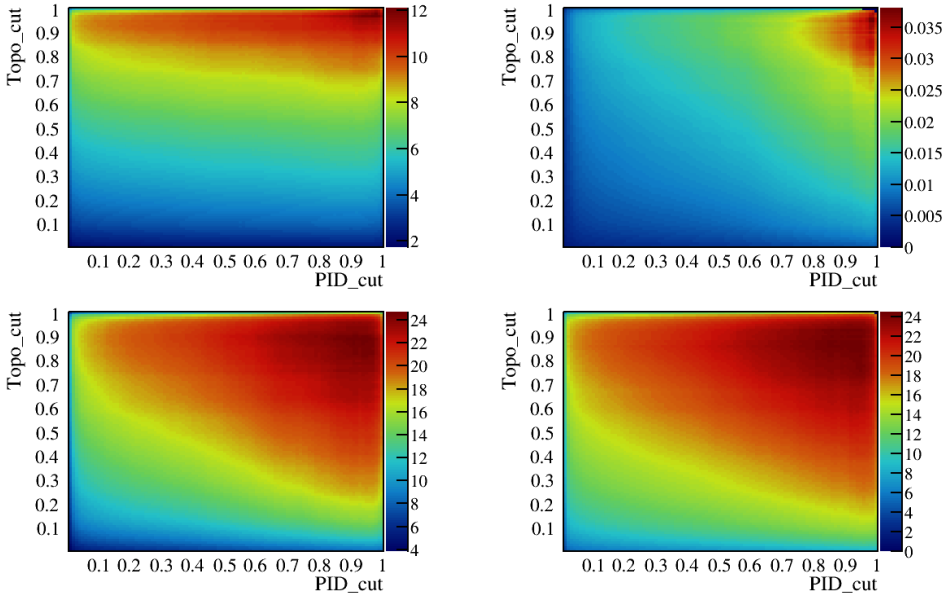

Figure B.4: The 2D Optimization of Cabbibo suppressed modes $B^0_{d,s} \to K^0_S h^+ h'^-$ decay for 2016 DD K^0_S reconstruction. Top: left(right) corresponds to the $B_s \to K^0_S \pi^+ \pi^-$ ($B_s \to K^0_S K^+ K^-$). Bottom: left(right) corresponds to $B^0 \to K^0_S \pi^+ K^-$($B^0 \to K^0_S K^+ \pi^-$)

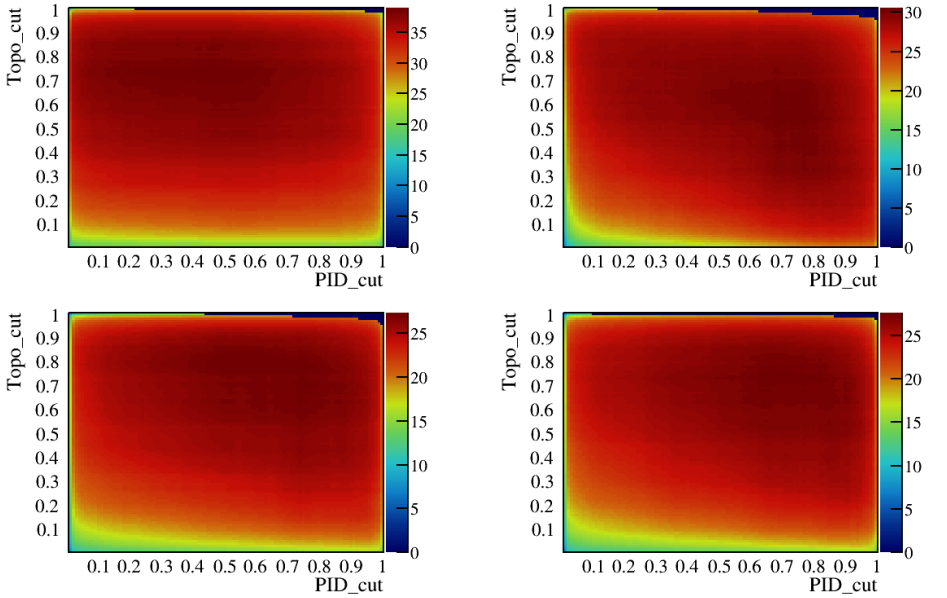

Figure B.5: The 2D Optimization of Cabbibo favored modes $B^0_{d,s} \to K^0_S h^+ h'^-$ decay for 2015 DD K^0_S reconstruction. Top: left (right) corresponds to the $B^0 \to K^0_S \pi^+ \pi^-$ ($B^0 \to K^0_S K^+ K^-$). Bottom: left (right) corresponds to $B_s \to K^0_S \pi^+ K^-$($B_s \to K^0_S K^+ \pi^-$)

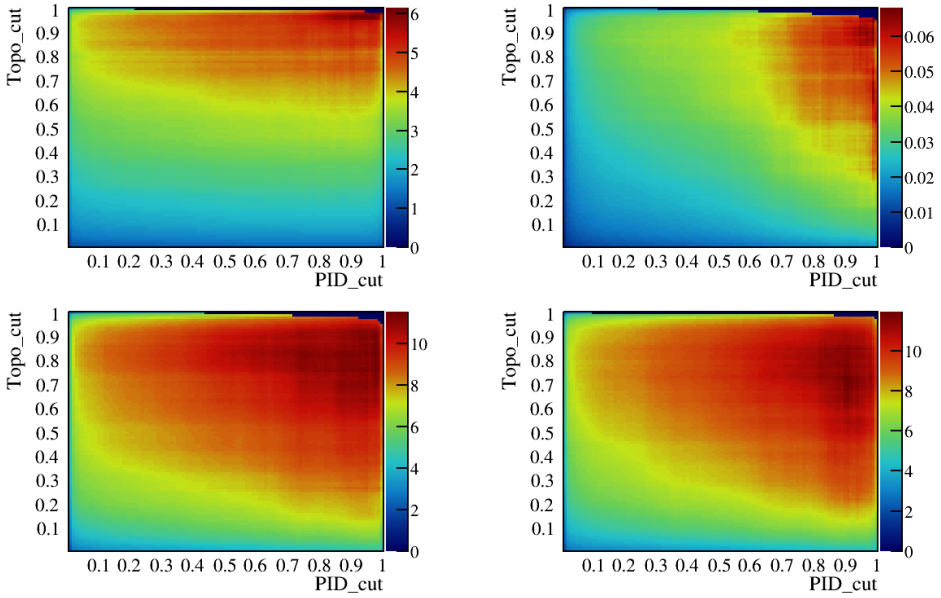

Figure B.6: The 2D Optimization of Cabbibo suppressed modes $B^0_{d,s} \to K^0_S h^+ h'^-$ decay for 2015 DD K^0_S reconstruction. Top: left(right) corresponds to the $B_s \to K^0_S \pi^+ \pi^-$ ($B_s \to K^0_S K^+ K^-$). Bottom: left(right) corresponds to $B^0 \to K^0_S \pi^+ K^-$($B^0 \to K^0_S K^+ \pi^-$)

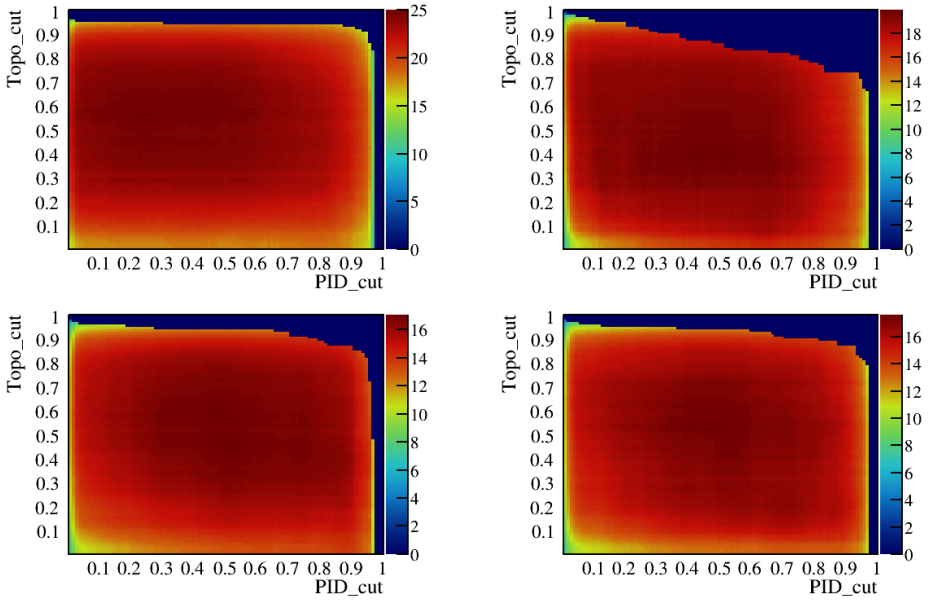

Figure B.7: The 2D Optimization of Cabbibo favored modes $B^0_{d,s} \to K^0_S h^+ h'^-$ decay for 2012a DD K^0_S reconstruction. Top: left(right) corresponds to the $B^0 \to K^0_S \pi^+ \pi^-$ ($B^0 \to K^0_S K^+ K^-$). Bottom: left(right) corresponds to $B_s \to K^0_S \pi^+ K^-$($B_s \to K^0_S K^+ \pi^-$)

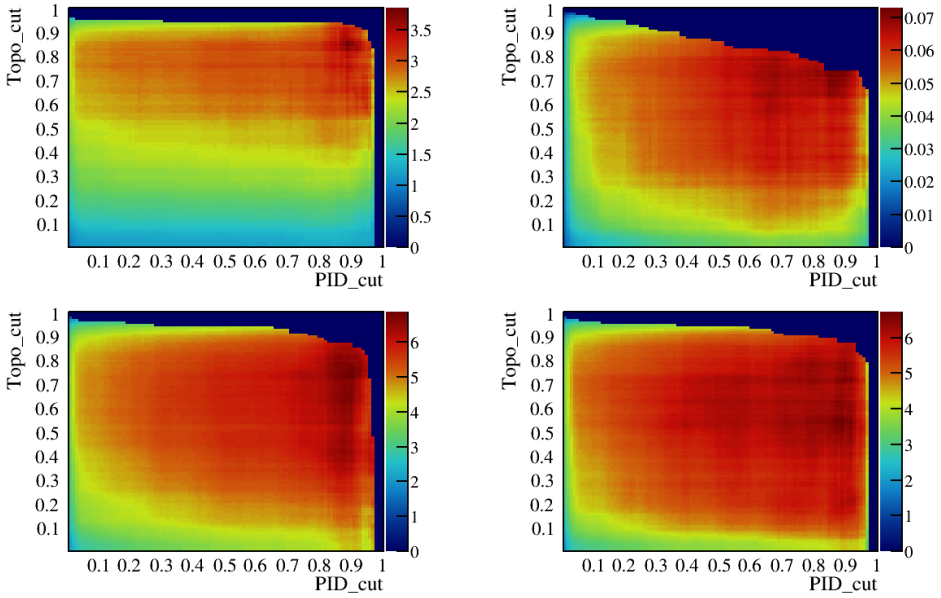

Figure B.8: The 2D Optimization of Cabbibo suppressed modes $B^0_{d,s} \to K^0_S h^+ h'^-$ decay for 2012a DD K^0_S reconstruction. Top: left (right) corresponds to the $B_s \to K^0_S \pi^+ \pi^-$ ($B_s \to K^0_S K^+ K^-$). Bottom: left (right) corresponds to $B^0 \to K^0_S \pi^+ K^-$($B^0 \to K^0_S K^+ \pi^-$)

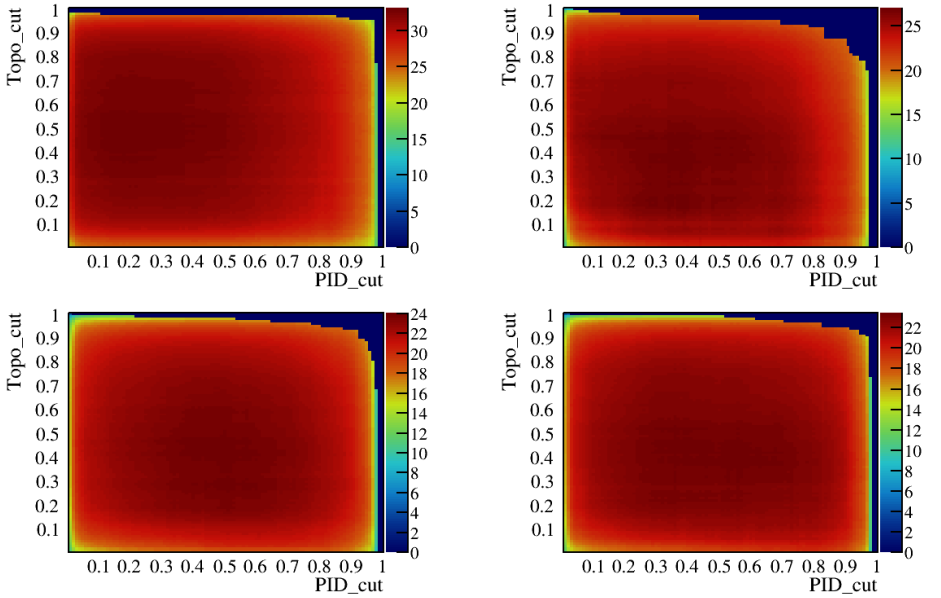

Figure B.9: The 2D Optimization of Cabbibo favored modes $B^0_{d,s} \to K^0_S h^+ h'^-$ decay for 2011 DD K^0_S reconstruction. Top: left (right) corresponds to the $B^0 \to K^0_S \pi^+ \pi^-$ ($B^0 \to K^0_S K^+ K^-$). Bottom: left (right) corresponds to $B_s \to K^0_S \pi^+ K^-$($B_s \to K^0_S K^+ \pi^-$)

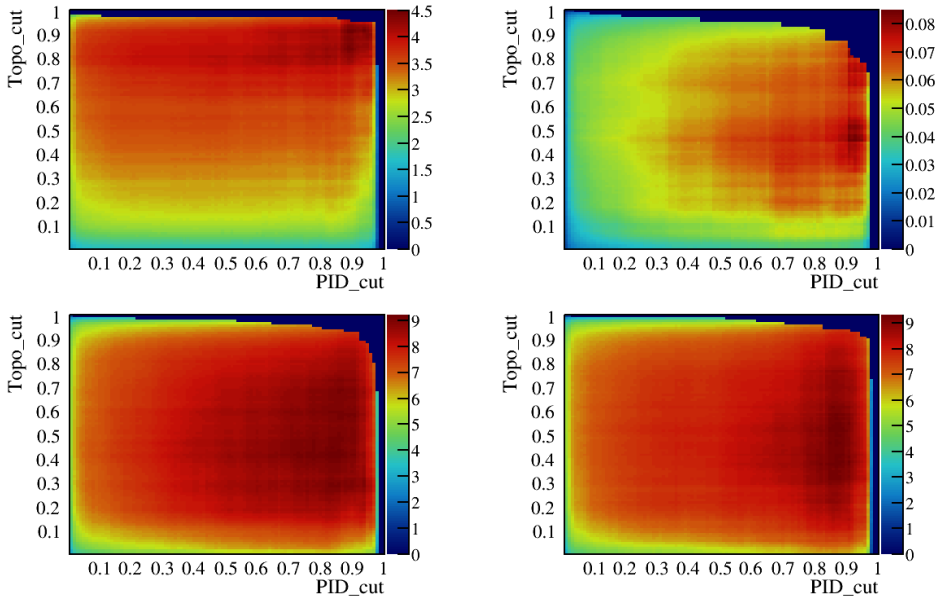

Figure B.10: The 2D Optimization of Cabbibo suppressed modes $B^0_{d,s} \to K^0_S h^+ h'^-$ decay for 2011 DD K^0_S reconstruction. Top: left(right) corresponds to the $B_s \to K^0_S \pi^+ \pi^-$ ($B_s \to K^0_S K^+ K^-$). Bottom: left(right) corresponds to $B^0 \to K^0_S \pi^+ K^-$($B^0 \to K^0_S K^+ \pi^-$)

Appendix C

Efficiency results of the Optimized Cut for $K^0_S K^{\pm}\pi^{\mp}$ decay modes

In this appendix the Efficiency results for the $K^0_S K^{\pm}\pi^{\mp}$ mode is presented. The reader must pay attention that the number 1 or 2 in the tables denote which hadron is misidentified and d or s denoted whether it results from the decay of B^0 or B_s. For example, for the Decay mode of `KpiKS`($K^0_S K^+\pi^-$) the `CrossFeed1_s` means that the π^+ in $B_s \to K^0_S\pi^+\pi^-$ is misidentified as K^+ and the `CrossFeed2_s` denoted the misidentified K^- as π^- for $B_s \to K^0_S K^+ K^-$.

Decay Mode	KS	Optimazation	Signal_s	Signal_d	CrossFeed1_s	CrossFeed2_s	CrossFeed1_d	CrossFeed2_d
KpiKS	DD	Loose	0.714(0.002)	0.698(0.002)	0.0392(0.0007)	0.0311(0.0006)	0.0388(0.0007)	0.0307(0.0007)
KpiKS	DD	Tight	0.561(0.002)	0.548(0.003)	0.0102(0.0004)	0.0082(0.0003)	0.0095(0.0004)	0.0074(0.0003)
KpiKS	LL	Loose	0.803(0.003)	0.796(0.003)	0.059(0.001)	0.051(0.001)	0.058(0.001)	0.049(0.001)
KpiKS	LL	Tight	0.615(0.004)	0.619(0.004)	0.0094(0.0006)	0.0094(0.0006)	0.0110(0.0006)	0.0088(0.0006)
piKKS	DD	Loose	0.688(0.002)	0.673(0.002)	0.0505(0.0008)	0.0402(0.0007)	0.0485(0.0008)	0.0383(0.0007)
piKKS	DD	Tight	0.514(0.002)	0.506(0.003)	0.0066(0.0003)	0.0049(0.0003)	0.0072(0.0003)	0.0050(0.0003)
piKKS	LL	Loose	0.791(0.003)	0.782(0.003)	0.048(0.001)	0.044(0.001)	0.050(0.001)	0.040(0.001)
piKKS	LL	Tight	0.622(0.004)	0.613(0.004)	0.0072(0.0005)	0.0072(0.0005)	0.0086(0.0006)	0.0067(0.0005)

Table C.1: Efficiency results based on the 2D optimized cuts for 2018 Monte Carlo samples. These MC samples consist of $B^0_{d,s} \to K^0_S K^{\pm}\pi^{\mp}$ signal and their corresponding cross-feed.

Decay Mode	KS	Optimazation	Signal_s	Signal_d	CrossFeed1_s	CrossFeed2_s	CrossFeed1_d	CrossFeed2_d
KpiKS	DD	Loose	0.725(0.002)	0.715(0.002)	0.0423(0.0007)	0.0336(0.0006)	0.0401(0.0007)	0.0318(0.0006)
KpiKS	DD	Tight	0.585(0.002)	0.577(0.002)	0.0076(0.0003)	0.0061(0.0003)	0.0068(0.0003)	0.0053(0.0003)
KpiKS	LL	Loose	0.799(0.003)	0.797(0.003)	0.046(0.001)	0.042(0.001)	0.049(0.001)	0.044(0.001)
KpiKS	LL	Tight	0.614(0.004)	0.605(0.004)	0.0073(0.0005)	0.0075(0.0005)	0.0075(0.0005)	0.0057(0.0004)
piKKS	DD	Loose	0.701(0.002)	0.688(0.002)	0.0363(0.0006)	0.0284(0.0006)	0.0361(0.0006)	0.0253(0.0006)
piKKS	DD	Tight	0.514(0.002)	0.502(0.002)	0.0072(0.0003)	0.0056(0.0003)	0.0078(0.0003)	0.0047(0.0002)
piKKS	LL	Loose	0.788(0.003)	0.791(0.003)	0.045(0.001)	0.043(0.001)	0.048(0.001)	0.041(0.001)
piKKS	LL	Tight	0.671(0.004)	0.681(0.004)	0.0145(0.0006)	0.0138(0.0007)	0.0162(0.0007)	0.0127(0.0006)

Table C.2: Efficiency results based on the 2D optimized cuts for 2017 Monte Carlo samples. These MC samples consist of $B^0_{d,s} \to K^0_S K^\pm \pi^\mp$ signal and their corresponding cross-feed.

Decay Mode	KS	Optimazation	Signal_s	Signal_d	CrossFeed1_s	CrossFeed2_s	CrossFeed1_d	CrossFeed2_d
KpiKS	DD	Loose	0.714(0.002)	0.709(0.002)	0.0383(0.0006)	0.0341(0.0006)	0.0395(0.0007)	0.0330(0.0006)
KpiKS	DD	Tight	0.559(0.002)	0.552(0.002)	0.0090(0.0003)	0.0062(0.0003)	0.0083(0.0003)	0.0065(0.0003)
KpiKS	LL	Loose	0.764(0.003)	0.764(0.003)	0.0306(0.0009)	0.0287(0.0009)	0.0335(0.0010)	0.0292(0.0009)
KpiKS	LL	Tight	0.590(0.004)	0.594(0.004)	0.0079(0.0005)	0.0061(0.0004)	0.0078(0.0005)	0.0067(0.0005)
piKKS	DD	Loose	0.723(0.002)	0.715(0.002)	0.0357(0.0006)	0.0263(0.0005)	0.0360(0.0006)	0.0262(0.0006)
piKKS	DD	Tight	0.521(0.002)	0.511(0.002)	0.0085(0.0003)	0.0057(0.0003)	0.0090(0.0003)	0.0054(0.0003)
piKKS	LL	Loose	0.774(0.003)	0.777(0.003)	0.044(0.001)	0.038(0.001)	0.044(0.001)	0.039(0.001)
piKKS	LL	Tight	0.639(0.004)	0.640(0.004)	0.0138(0.0006)	0.0101(0.0005)	0.0116(0.0006)	0.0109(0.0006)

Table C.3: Efficiency results based on the 2D optimized cuts for 2016 Monte Carlo samples. These MC samples consist of $B^0_{d,s} \to K^0_S K^\pm \pi^\mp$ signal and their corresponding cross-feed.

Decay Mode	KS	Optimazation	Signal_s	Signal_d	CrossFeed1_s	CrossFeed2_s	CrossFeed1_d	CrossFeed2_d
KpiKS	DD	Loose	0.735(0.002)	0.729(0.002)	0.0528(0.0008)	0.0442(0.0007)	0.0497(0.0008)	0.0433(0.0007)
KpiKS	DD	Tight	0.472(0.002)	0.478(0.002)	0.0018(0.0001)	0.0020(0.0002)	0.0025(0.0002)	0.0020(0.0002)
KpiKS	LL	Loose	0.790(0.003)	0.790(0.003)	0.055(0.001)	0.049(0.001)	0.054(0.001)	0.048(0.001)
KpiKS	LL	Tight	0.602(0.004)	0.607(0.004)	0.0031(0.0003)	0.0036(0.0003)	0.0025(0.0003)	0.0033(0.0003)
piKKS	DD	Loose	0.746(0.002)	0.737(0.002)	0.0439(0.0007)	0.0360(0.0006)	0.0440(0.0007)	0.0364(0.0007)
piKKS	DD	Tight	0.630(0.002)	0.624(0.002)	0.0090(0.0003)	0.0082(0.0003)	0.0103(0.0004)	0.0081(0.0003)
piKKS	LL	Loose	0.819(0.003)	0.823(0.003)	0.043(0.001)	0.042(0.001)	0.043(0.001)	0.042(0.001)
piKKS	LL	Tight	0.675(0.004)	0.671(0.004)	0.0179(0.0007)	0.0148(0.0007)	0.0139(0.0007)	0.0165(0.0008)

Table C.4: Efficiency results based on the 2D optimized cuts for 2015 Monte Carlo samples. These MC samples consist of $B^0_{d,s} \to K^0_S K^\pm \pi^\mp$ signal and their corresponding cross-feed.

Decay Mode	KS	Optimazation	Signal_s	Signal_d	CrossFeed1_s	CrossFeed2_s	CrossFeed1_d	CrossFeed2_d
KpiKS	DD	Loose	0.799(0.004)	0.790(0.004)	0.119(0.002)	0.116(0.002)	0.117(0.002)	0.119(0.002)
KpiKS	DD	Tight	0.552(0.005)	0.520(0.005)	0.0174(0.0009)	0.0119(0.0008)	0.0148(0.0009)	0.0093(0.0007)
KpiKS	LL	Loose	0.776(0.006)	0.769(0.006)	0.082(0.003)	0.069(0.003)	0.079(0.003)	0.067(0.003)
KpiKS	LL	Tight	0.632(0.007)	0.642(0.007)	0.032(0.002)	0.030(0.002)	0.033(0.002)	0.032(0.002)
piKKS	DD	Loose	0.842(0.003)	0.821(0.004)	0.160(0.003)	0.169(0.003)	0.152(0.003)	0.165(0.003)
piKKS	DD	Tight	0.583(0.005)	0.576(0.005)	0.0197(0.0010)	0.0098(0.0007)	0.020(0.001)	0.0097(0.0007)
piKKS	LL	Loose	0.826(0.005)	0.829(0.006)	0.086(0.003)	0.076(0.003)	0.079(0.003)	0.076(0.003)
piKKS	LL	Tight	0.530(0.007)	0.547(0.007)	0.013(0.001)	0.011(0.001)	0.014(0.001)	0.010(0.001)

Table C.5: Efficiency results based on the 2D optimized cuts for 2012b Monte Carlo samples. These MC samples consist of $B^0_{d,s} \to K^0_S K^{\pm}\pi^{\mp}$ signal and their corresponding cross-feed.

Decay Mode	KS	Optimazation	Signal_s	Signal_d	CrossFeed1_s	CrossFeed2_s	CrossFeed1_d	CrossFeed2_d
KpiKS	DD	Loose	0.819(0.003)	0.816(0.003)	0.123(0.002)	0.118(0.002)	0.114(0.002)	0.119(0.002)
KpiKS	DD	Tight	0.489(0.004)	0.478(0.004)	0.0161(0.0008)	0.0063(0.0005)	0.0109(0.0006)	0.0058(0.0005)
KpiKS	LL	Loose	0.841(0.006)	0.843(0.006)	0.832(0.004)	0.015(0.001)	0.128(0.004)	0.141(0.004)
KpiKS	LL	Tight	0.405(0.008)	0.443(0.008)	0.446(0.006)	0(0)	0.0035(0.0006)	0.0051(0.0009)
piKKS	DD	Loose	0.830(0.003)	0.814(0.003)	0.159(0.002)	0.141(0.002)	0.138(0.002)	0.146(0.002)
piKKS	DD	Tight	0.568(0.004)	0.566(0.004)	0.0204(0.0009)	0.0078(0.0005)	0.0140(0.0007)	0.0101(0.0007)
piKKS	LL	Loose	0.856(0.006)	0.853(0.006)	0.143(0.004)	0.138(0.004)	0.133(0.004)	0.131(0.004)
piKKS	LL	Tight	0.544(0.008)	0.537(0.008)	0.015(0.001)	0.009(0.001)	0.009(0.001)	0.008(0.001)

Table C.6: Efficiency results based on the 2D optimized cuts for 2012a Monte Carlo samples. These MC samples consist of $B^0_{d,s} \to K^0_S K^{\pm}\pi^{\mp}$ signal and their corresponding cross-feed.

Decay Mode	KS	Optimazation	Signal_s	Signal_d	CrossFeed1_s	CrossFeed2_s	CrossFeed1_d	CrossFeed2_d
KpiKS	DD	Loose	0.858(0.003)	0.850(0.003)	0.118(0.002)	0.122(0.002)	0.126(0.002)	0.114(0.002)
KpiKS	DD	Tight	0.643(0.004)	0.646(0.004)	0.0214(0.0009)	0.0179(0.0008)	0.029(0.001)	0.0151(0.0007)
KpiKS	LL	Loose	0.856(0.005)	0.846(0.005)	0.098(0.003)	0.088(0.003)	0.105(0.003)	0.088(0.003)
KpiKS	LL	Tight	0.708(0.006)	0.672(0.006)	0.036(0.002)	0.030(0.002)	0.035(0.002)	0.022(0.001)
piKKS	DD	Loose	0.843(0.003)	0.839(0.003)	0.108(0.002)	0.101(0.002)	0.115(0.002)	0.102(0.002)
piKKS	DD	Tight	0.610(0.004)	0.609(0.004)	0.0201(0.0008)	0.0132(0.0007)	0.024(0.001)	0.0112(0.0006)
piKKS	LL	Loose	0.828(0.005)	0.834(0.005)	0.084(0.003)	0.090(0.003)	0.099(0.003)	0.079(0.003)
piKKS	LL	Tight	0.646(0.006)	0.655(0.006)	0.014(0.001)	0.015(0.001)	0.020(0.001)	0.013(0.001)

Table C.7: Efficiency results based on the 2D optimized cuts for 2011 Monte Carlo samples. These MC samples consist of $B^0_{d,s} \to K^0_S K^{\pm}\pi^{\mp}$ signal and their corresponding cross-feed.

Bibliography

[1] M. Bauer, *Matter-antimatter asymmetry, cp violation and the time operator in relativistic quantum mechanics*, arXiv preprint arXiv:2208. 13864 (2022).

[2] L. Canetti, M. Drewes, and M. Shaposhnikov, *Matter and antimatter in the universe*, New Journal of Physics **14** (2012), no. 9 095012.

[3] P. Traczyk, *Largest matter-antimatter asymmetry observed*, `https://home.cern/news/news/physics/largest-matter-antimatter-asymmetry-observed`. Accessed: 2022-09-20.

[4] BABAR Collaboration, B. Aubert *et al.*, *Observation of CP violation in the b^0 meson system*, Phys. Rev. Lett. **87** (2001) 091801.

[5] Belle Collaboration, K. Abe *et al.*, *Observation of large CP violation in the neutral B meson system*, Phys. Rev. Lett. **87** (2001) 091802.

[6] J. H. Christenson, J. W. Cronin, V. L. Fitch, and R. Turlay, *Evidence for the 2π decay of the k_2^0 meson*, Phys. Rev. Lett. **13** (1964) 138.

[7] M. Beneke and M. Neubert, *QCD factorization for $B \to PP$ and $B \to PV$ decays*, Nuclear Physics B **675** (2003), no. 1 333.

[8] Heavy Flavor Averaging Group, Y. Amhis *et al.*, *Averages of b-hadron, c-hadron, and τ-lepton properties as of summer 2016*, Eur. Phys. J. **C77** (2017) 895, `arXiv:1612.07233`, updated results and plots available at `https://hflav.web.cern.ch`.

[9] Heavy Flavor Averaging Group, Y. Amhis *et al.*, *Averages of b-hadron, c-hadron, and τ-lepton properties as of summer 2018*, `arXiv:1909.12524`.

[10] S. Baek, C.-W. Chiang, and D. London, *The $B \to \pi K$ puzzle: 2009 update*, Physics Letters B **675** (2009), no. 1 59.

[11] H.-n. Li and S. Mishima, *Possible resolution of the $B \to \pi\pi$, πK puzzles*, Phys. Rev. D **83** (2011) 034023.

[12] S. Khalil, A. Masiero, and H. Murayama, *$B \to K\pi$ puzzle and new sources of CP violation in supersymmetry*, Physics Letters B **682** (2009), no. 1 74.

[13] LHCb collaboration, R. Aaij *et al.*, *Amplitude Analysis of the Decay $\bar{B}^0 \to K^0_S\pi^+\pi^-$ and First Observation of the CP Asymmetry in $\bar{B}^0 \to K^*(892)^-\pi^+$*, Phys. Rev. Lett. **120** (2018) 261801.

[14] M. Beneke, *Corrections to $sin(2\beta)$ from cp asymmetries in $b^0 \to (\pi^0, \rho^0, \eta, \eta, \omega, \phi)k^0_s$ decays*, Physics Letters B **620** (2005), no. 3 143.

[15] G. Buchalla, G. Hiller, Y. Nir, and G. Raz, *The pattern of CP asymmetries inib/i→is/itransitions*, Journal of High Energy Physics **2005** (2005) 074.

[16] D. Allor, T. D. Cohen, and D. A. McGady, *Schwinger mechanism and graphene*, Phys. Rev. D **78** (2008) 096009.

[17] Y. Grossman and M. P. Worah, *Cp asymmetries in b decays with new physics in decay amplitudes*, Physics Letters B **395** (1997), no. 3 241.

[18] W. Satuła *et al.*, *On the origin of the wigner energy*, Physics Letters B **407** (1997), no. 2 103.

[19] M. Ciuchini *et al.*, *Cp violating b decays in the standard model and supersymmetry*, Phys. Rev. Lett. **79** (1997) 978.

[20] and R. Aaij *et al.*, *Updated branching fraction measurements of $B^0_{(s)} \to K^0_S h^+ h'^-$ decays*, Journal of High Energy Physics **2017** (2017) .

[21] Belle Collaboration, J. Dalseno *et al.*, *Time-dependent dalitz plot measurement of cp parameters in $B^0 \to K^0_S\pi^+\pi^-$ decays*, Phys. Rev. D **79** (2009) 072004.

[22] BABAR Collaboration, B. Aubert *et al.*, *Time-dependent amplitude analysis of $B^0 \to K^0_S\pi^+\pi^-$*, Phys. Rev. D **80** (2009) 112001.

[23] The Belle Collaboration, Y. Nakahama *et al.*, *Measurement of cp violating asymmetries in $B^0 \to K^+K^-K^0_S$ decays with a time-dependent dalitz approach*, Phys. Rev. D **82** (2010) 073011.

[24] BABAR Collaboration, J. P. Lees *et al.*, *Study of cp violation in dalitz-plot analyses of $B^0 \to K^+K^-K^0_S$, $B^+ \to K^+K^-K^+$, and $B^+ \to K^0_S K^0_S K^+$*, Phys. Rev. D **85** (2012) 112010.

[25] H.-Y. Cheng and C.-K. Chua, *Branching fractions and direct cp violation in charmless three-body decays of b mesons*, Phys. Rev. D **88** (2013) 114014.

[26] D. Bisello *et al.*, *Observation of an isoscalar vector meson at approximately = 1650MeV/c^2 in the $e^+e^- \to K\bar{K}\pi$ reaction*, Z. Phys. **C52** (1991) 227.

[27] H.-Y. Cheng and C.-K. Chua, *Charmless three-body decays of B_s mesons*, Phys. Rev. D **89** (2014) 074025.

[28] Y. Li, *Branching fractions and direct cp asymmetries of* $\bar{B}_s^0 \to k^0 h^+ h'^-(h^{(\prime)} = k, \pi)$ *decays*, Science China Physics, Mechanics & Astronomy **58** (2015), no. 3 1.

[29] Y. Li, *Comprehensive study of* $\overline{b}^0 \to K^0(\overline{k}^0)K^{\mp}\pi^{\pm}$ *decays in the factorization approach*, Phys. Rev. D **89** (2014) 094007.

[30] W.-F. Wang and H. nan Li, *Quasi-two-body decays* $b \to k\rho \to k\pi\pi$ *in perturbative qcd approach*, Physics Letters B **763** (2016) 29.

[31] Y. Li, A.-J. Ma, W.-F. Wang, and Z.-J. Xiao, *Quasi-two-body decays* $b_{(s)} \to p\rho'(1450), p\rho''(1700) \to p\pi\pi$ *in the perturbative qcd approach*, Phys. Rev. D **96** (2017) 036014.

[32] X.-G. He, G.-N. Li, and D. Xu, $su(3)$ *and isospin breaking effects on* $b \to ppp$ *amplitudes*, Phys. Rev. D **91** (2015) 014029.

[33] A. Brancacci and P.-M. Morel, *Democritus: Science, The Arts, and the Care of the Soul: Proceedings of the International Colloquium on Democritus (Paris, 20-22 September 2003)*, Brill, 2006.

[34] E. Gregersen *et al.*, *The Britannica guide to the atom*, Britannica Educational Publishing, 2010.

[35] F. Greenaway, *John Dalton and the atom*, Ithaca, N.Y., Cornell University Press, 1966.

[36] E. A. Davis and I. Falconer, *JJ Thompson and the Discovery of the Electron*, CRC Press, 2002.

[37] A. Di Giacomo, *Confinement of color: A review*, arXiv preprint hep-lat/0310023 (2003).

[38] *Table of standard model of particle physics*, `https://texample.net/tikz/examples/model-physics/`. Accessed: 2021-10-30.

[39] T. D. Lee and C. N. Yang, *Question of parity conservation in weak interactions*, Phys. Rev. **104** (1956) 254.

[40] C. S. Wu *et al.*, *Experimental test of parity conservation in beta decay*, Phys. Rev. **105** (1957) 1413.

[41] R. L. Garwin, L. M. Lederman, and M. Weinrich, *Observations of the failure of conservation of parity and charge conjugation in meson decays: the magnetic moment of the free muon*, Phys. Rev. **105** (1957) 1415.

[42] J. I. Friedman and V. L. Telegdi, *Nuclear emulsion evidence for parity nonconservation in the decay chain* $\pi^+ \to \mu^+ \to e^+$, Phys. Rev. **106** (1957) 1290.

[43] S. Weinberg, *Charge symmetry of weak interactions*, Physical Review **112** (1958), no. 4 1375.

[44] C. A. Eleftheriadis, *Time reversal, CP and CPT violation studies in the CPLEAR experiment at CERN*, PoS **corfu98** (1998) 043.

[45] The BABAR Collaboration, J. P. Lees *et al.*, *Observation of time-reversal violation in the B^0 meson system*, Phys. Rev. Lett. **109** (2012) 211801.

[46] L. Landau, *On the conservation laws for weak interactions*, Nuclear Physics **3** (1957), no. 1 127.

[47] Y. Nir, *CP violation in meson decays*, in *High-energy physics. Proceedings, 3rd Latin American CERN-CLAF School, Malargue, Argentina, February 27-March 12, 2005*, pp. 79–145, 2006. arXiv:hep-ph/0510413.

[48] S. L. Glashow, *Partial-symmetries of weak interactions*, Nuclear Physics **22** (1961), no. 4 579.

[49] S. Weinberg, *A model of leptons*, Phys. Rev. Lett. **19** (1967) 1264.

[50] A. Salam and J. C. Ward, *Weak and electromagnetic interactions*, Il Nuovo Cimento **11** (1959) .

[51] F. Englert and R. Brout, *Broken symmetry and the mass of gauge vector mesons*, Phys. Rev. Lett. **13** (1964) 321.

[52] P. W. Higgs, *Broken symmetries and the masses of gauge bosons*, Phys. Rev. Lett. **13** (1964) 508.

[53] ATLAS, G. Aad *et al.*, *Observation of a new particle in the search for the Standard Model Higgs boson with the ATLAS detector at the LHC*, Phys. Lett. **B716** (2012) 1, arXiv:1207.7214.

[54] N. Cabibbo, *Unitary symmetry and leptonic decays*, Phys. Rev. Lett. **10** (1963) 531.

[55] M. Kobayashi and T. Maskawa, *CP-Violation in the Renormalizable Theory of Weak Interaction*, Progress of Theoretical Physics **49** (1973) 652, arXiv:https://academic.oup.com/ptp/article-pdf/49/2/652/5257692/49-2-652.pdf.

[56] L.-L. Chau and W.-Y. Keung, *Comments on the parametrization of the kobayashi-maskawa matrix*, Phys. Rev. Lett. **53** (1984) 1802.

[57] L. Wolfenstein, *Parametrization of the kobayashi-maskawa matrix*, Phys. Rev. Lett. **51** (1983) 1945.

[58] The CKMfitter Group, http://ckmfitter.in2p3.fr.

[59] A. Höcker and Z. Ligeti, *Cp violation and the ckm matrix*, Annual Review of Nuclear and Particle Science **56** (2006) 501–567.

[60] G. R. Farrar and M. E. Shaposhnikov, *Baryon asymmetry of the universe in the standard model*, Physical Review D **50** (1994) 774–818.

[61] J. H. Christenson, J. W. Cronin, V. L. Fitch, and R. Turlay, *Evidence for the* 2π *Decay of the* K_2^0 *Meson*, Phys. Rev. Lett. **13** (1964) 138.

[62] BABAR Collaboration, B. e. a. Aubert, *Evidence for* $D^0-\overline{D}^0$ *Mixing*, Phys. Rev. Lett. **98** (2007) 211802.

[63] Belle Collaboration, M. and G. et al., *Evidence for* $D^0-\overline{D}^0$ *Mixing*, Phys. Rev. Lett. **98** (2007) 211803.

[64] Y. Amhis *et al.*, *Averages of b-hadron, c-hadron, and* τ*-lepton properties as of 2018*, The European Physical Journal C **81** (2021) .

[65] B. Aubert *et al.*, *Time-dependent amplitude analysis of* $B^0 \to K^0_S\pi^+\pi^-$, Physical Review D **80** (2009), no. 11 112001.

[66] J. Lees *et al.*, *Study of* $\mathcal{CP}$ *violation in Dalitz-plot analyses of* $B^0 \to K^0_{\rm S}K^+K^-$, $B^+ \to K^+K^-K^+$, *and* $B^+ \to K^0_{\rm S}K^0_{\rm S}K^+$, Physical Review D **85** (2012), no. 11 112010.

[67] A. Garmash *et al.*, *Study of B meson decays to three-body charmless hadronic final states*, Physical Review D **69** (2004).

[68] A. Garmash *et al.*, *Dalitz analysis of three-body charmless* $B^0 \to K^0\pi^+\pi^-$ *decay*, Physical Review D **75** (2007), no. 1 012006.

[69] P. del Amo Sanchez *et al.*, *Observation of the rare decay* $B_0 \to K^0_S K^\pm\pi^\mp$, Physical Review D **82** (2010), no. 3 031101.

[70] L. Collaboration *et al.*, *Study of* $B^0_{(s)} \to K^0_S h^+h'^-$ *decays with first observation of* $B^{0s} \to K^0_S K \pm \pi^\mp$*and* $B^0_s \to K^0_S\pi^+\ \pi^-$, Journal of High Energy Physics **2013** (2013), no. 10 143.

[71] M. Baalouch, *Dalitz analysis of the three-body charmless decay* $B^0 \to K^0_S\pi^+\pi^-$ *with the LHCb spectrometer*, 2015. presented 14 Dec 2015.

[72] B. Aubert *et al.*, *Amplitude analysis of the decay* $B^\pm \to \pi^\pm\pi^\pm\pi^\mp$, Physical Review D **72** (2005) .

[73] L. Evans and P. Bryant, *LHC Machine*, vol. 3, 2008. doi: 10.1088/1748-0221/3/08/S08001.

[74] E. Mobs, *The CERN accelerator complex - August 2018. Complexe des accélérateurs du CERN - Août 2018*, , General Photo.

[75] LHCb collaboration, R. Aaij *et al.*, *Study of the kinematic dependences of Λ_b^0 production in pp collisions and a measurement of the $\Lambda_b^0 \to \Lambda_c^+\pi^-$ branching fraction*, JHEP **08** (2014) 143, arXiv:1405.6842.

[76] R. Aaij *et al.*, *Measurement of b-hadron fractions in 13 tev pp collisions*, Physical Review D **100** (2019) .

[77] LHCb Collaboration, R. Aaij *et al.*, *Measurement of the b-quark production cross section in 7 and 13 tev pp collisions*, Phys. Rev. Lett. **118** (2017) 052002.

[78] LHCb, R. Aaij *et al.*, *Measurement of the inelastic pp cross-section at a centre-of-mass energy of $\sqrt{s} = 7$ TeV*, JHEP **02** (2015) 129, arXiv:1412.2500.

[79] R. Aaij *et al.*, *Measurement of the inelastic pp cross-section at a centre-of-mass energy of 13 tev*, Journal of High Energy Physics **2018** (2018) .

[80] LHCb, A. A. Alves, Jr. *et al.*, *The LHCb Detector at the LHC*, JINST **3** (2008) S08005.

[81] LHCb Collaboration, R. Antunes-Nobrega *et al.*, *LHCb reoptimized detector design and performance: Technical Design Report*, Technical design report. LHCb, CERN, Geneva, 2003.

[82] LHCb, R. Aaij *et al.*, *LHCb Detector Performance*, Int. J. Mod. Phys. A **30** (2015), no. 07 1530022, arXiv:1412.6352.

[83] LHCb, *LHCb magnet: Technical design report*, CERN-LHCC-2000-007, 2000.

[84] LHCb collaboration, C. Elsässer, *$\bar{b}b$ production angle plots*, https://texample.net/tikz/examples/model-physics/. Accessed: 2021-11-20.

[85] LHCb, R. Aaij *et al.*, *LHCb Detector Performance*, Int. J. Mod. Phys. **A30** (2015), no. 07 1530022, arXiv:1412.6352.

[86] LHCbcollaboration, R. Aaij *et al.*, *LHCb Detector Performance*, Int. J. Mod. Phys. A **30** (2015) 1530022, arXiv:1412.6352.

[87] LHCb Collaboration, *LHCb VELO (VErtex LOcator): Technical Design Report*, CERN-LHCC-2001-011, CERN, Geneva, 2001.

[88] LHCb, R. Aaij *et al.*, *Precision measurement of the B_s^0-$\bar{B}_s^0$ oscillation frequency with the decay $B_s^0 \to D_s^-\pi^+$*, New J. Phys. **15** (2013) 053021, arXiv:1304.4741.

[89] LHCb collaboration, *Approved velo conference plots*, ,https://lbtwiki.cern.ch/bin/view/VELO/VELOConferencePlots.

[90] R. Aaij *et al.*, *Performance of the LHCb Vertex Locator*, JINST **9** (2014) 09007, arXiv:1405.7808.

[91] LHCb, *LHCb technical design report: Reoptimized detector design and performance*, CERN-LHCC-2003-030, 2003.

[92] LHCb Collaboration, R. Aaij *et al.*, *Design and performance of the LHCb trigger and full real-time reconstruction in Run 2 of the LHC. Performance of the LHCb trigger and full real-time reconstruction in Run 2 of the LHC*, JINST **14** (2018) P04013. 43 p.

[93] LHCb, *LHCb: Inner tracker technical design report*, CERN-LHCC-2002-029, 2002.

[94] G. Knoll, *Radiation Detection and Measurement*, Wiley, 2000.

[95] LHCb Outer Tracker Group, R. Arink *et al.*, *Performance of the LHCb Outer Tracker*, JINST **9** (2014), no. 01 P01002, arXiv:1311.3893.

[96] J. J. van Hunen, *The lhcb tracking system*, Nuclear Instruments and Methods in Physics Research Section A: Accelerators, Spectrometers, Detectors and Associated Equipment **572** (2007), no. 1 149, Frontier Detectors for Frontier Physics.

[97] LHCb RICH Group, M. Adinolfi *et al.*, *Performance of the LHCb RICH detector at the LHC*, Eur. Phys. J. **C73** (2013) 2431, arXiv:1211.6759.

[98] LHCb, *LHCb calorimeters: Technical design report*, CERN-LHCC-2000-036, 2000.

[99] William R. Leo, *Techniques for Nuclear and Particle Physics Experiments - 2nd Revised Edition*, Springer (1994).

[100] LHCb, P. Perret, *First Years of Running for the LHCb Calorimeter System*, PoS **TIPP2014** (2014) 030, arXiv:1407.4289.

[101] LHCb, R. Aaij *et al.*, *Angular analysis of the $B^0 \to K^{*0}\mu^+\mu^-$ decay using 3 fb^{-1} of integrated luminosity*, JHEP **02** (2016) 104, arXiv:1512.04442.

[102] LHCb, R. Aaij *et al.*, *Measurement of the CP-violating phase ϕ_s in the decay $B_s^0 \to J/\psi\phi$*, Phys. Rev. Lett. **108** (2012) 101803, arXiv:1112.3183.

[103] LHCb, R. Aaij *et al.*, *First Evidence for the Decay $B_s^0 \to \mu^+\mu^-$*, Phys. Rev. Lett. **110** (2013), no. 2 021801, arXiv:1211.2674.

[104] LHCb, R. Aaij *et al.*, *Measurement of the $B_s^0 \to \mu^+\mu^-$ branching fraction and search for $B^0 \to \mu^+\mu^-$ decays at the LHCb experiment*, Phys. Rev. Lett. **111** (2013) 101805, arXiv:1307.5024.

[105] LHCb, *LHCb: Addendum to the muon system technical design report*, CERN-LHCC-2003-002, 2003.

[106] J. J. Hopfield, *Neural networks and physical systems with emergent collective computational abilities*, Proceedings of the National Academy of Sciences **79** (1982), no. 8 2554, arXiv:https://www.pnas.org/content/79/8/2554.full.pdf.

[107] B. J. Quintana, *Search for radiative B decays to orbitally excited mesons at LHCb*, Feb, 2020. Presented 25 Nov 2019.

[108] A. Dziurda, *The lhcb trigger and its upgrade*, Nuclear Instruments and Methods in Physics Research Section A: Accelerators, Spectrometers, Detectors and Associated Equipment **824** (2016) 277, Frontier Detectors for Frontier Physics: Proceedings of the 13th Pisa Meeting on Advanced Detectors.

[109] R. Aaij *et al.*, *The LHCb trigger and its performance in 2011*, JINST **8** (2013) P04022, arXiv:1211.3055.

[110] G. Barrand *et al.*, *Gaudi — a software architecture and framework for building hep data processing applications*, Computer Physics Communications **140** (2001), no. 1 45, CHEP2000.

[111] I. Bird *et al.*, *Update of the Computing Models of the WLCG and the LHC Experiments*, tech. rep., Apr, 2014.

[112] R. Brun and F. Rademakers, *Root — an object oriented data analysis framework*, Nuclear Instruments and Methods in Physics Research Section A: Accelerators, Spectrometers, Detectors and Associated Equipment **389** (1997), no. 1 81, New Computing Techniques in Physics Research V.

[113] T. Sjöstrand, S. Mrenna, and P. Skands, *A brief introduction to pythia 8.1*, Computer Physics Communications **178** (2008), no. 11 852.

[114] I. Beiyaev *et al.*, *Handling of the generation of primary events in gauss, the lhcb simulation framework*, in *IEEE Nuclear Science Symposuim Medical Imaging Conference*, pp. 1155–1161, 2010. doi: 10.1109/NSSMIC.2010.5873949.

[115] D. J. Lange, *The evtgen particle decay simulation package*, Nuclear Instruments and Methods in Physics Research Section A: Accelerators, Spectrometers, Detectors and Associated Equipment **462** (2001), no. 1 152, BEAUTY2000, Proceedings of the 7th Int. Conf. on B-Physics at Hadron Machines.

[116] P. Golonka and Z. Was, *PHOTOS Monte Carlo: A precision tool for QED corrections in Z and W decays*, Eur. Phys. J. **C45** (2006) 97, arXiv:hep-ph/0506026.

[117] M. Clemencic *et al.*, *The LHCb simulation application, Gauss: Design, evolution and experience*, J. Phys. Conf. Ser. **331** (2011) 032023.

[118] Geant4 collaboration, S. Agostinelli *et al.*, *Geant4: A simulation toolkit*, Nucl. Instrum. Meth. **A506** (2003) 250.

[119] L. Anderlini *et al.*, *The PIDCalib package*, tech. rep., CERN, Geneva, Jul, 2016.

[120] R. Aaij *et al.*, *Selection and processing of calibration samples to measure the particle identification performance of the LHCb experiment in run 2*, EPJ Techniques and Instrumentation **6** (2019) .

[121] O. Lupton, L. Anderlini, B. Sciascia, and V. Gligorov, *Calibration samples for particle identification at LHCb in Run 2*, tech. rep., CERN, Geneva, Mar, 2016.

[122] M. Pivk and F. L. Diberder, *: A statistical tool to unfold data distributions*, Nuclear Instruments and Methods in Physics Research Section A: Accelerators, Spectrometers, Detectors and Associated Equipment **555** (2005) 356.

[123] A. Poluektov, *Kernel density estimation of a multidimensional efficiency profile*, Journal of Instrumentation **10** (2015) P02011.

[124] A. Poluektov, *Correction of simulated particle identification response in lhcb using kernel density estimation*, Tech. Rep. LHCb-INT-2017-007, University of Warwick, May, 2017.

[125] M. Rosenblatt, *Remarks on some nonparametric estimates of a density function*, The annals of mathematical statistics (1956) 832.

[126] E. Parzen, *On estimation of a probability density function and mode*, The annals of mathematical statistics **33** (1962), no. 3 1065.

[127] V. A. Epanechnikov, *Non-parametric estimation of a multivariate probability density*, Theory of Probability & Its Applications **14** (1969), no. 1 153.

[128] J. L. Hodges Jr and E. L. Lehmann, *The efficiency of some nonparametric competitors of the t-test*, The Annals of Mathematical Statistics (1956) 324.

[129] F. Pedregosa *et al.*, *Scikit-learn: Machine learning in Python*, J. Machine Learning Res. **12** (2011) 2825, `arXiv:1201.0490`, and online at `http://scikit-learn.org/stable/`.

[130] T. Chen and C. Guestrin, *XGBoost: A scalable tree boosting system*, in *Proceedings of the 22nd ACM SIGKDD International Conference on Knowledge Discovery and Data Mining*, KDD '16, (New York, NY, USA), pp. 785–794, ACM, 2016. doi: 10.1145/2939672.2939785.

[131] P. D. Group *et al.*, *Review of Particle Physics*, Progress of Theoretical and Experimental Physics **2020** (2020) , `arXiv:https://academic.oup.com/ptep/article-pdf/2020/8/083C01/34673722/ptaa104` 083C01.

[132] M. Baalouch , E. Ben-Haim , T. Gershon , M. Grabalosa , C. Hadjivasiliou , L. Henry ,T. Latham , J.M. Maratas , J. McCarthy , D. Milanes , S. Monteil , R. Silva Coutinho , N. Watson., *Search for the decay $B_s \to K^0_S K^+ K^-$ and updated measurements of the relative branching fractions of $B^0_{d,s} \to K^0_S h^+ h^-$ decay with 3 fb^{-1}*, , LHCb-ANA-2014-043.

[133] V. V. Gligorov and M. Williams, *Efficient, reliable and fast high-level triggering using a bonsai boosted decision tree*, JINST **8** (2013) P02013, arXiv:1210.6861.

[134] M. Baalouch , E. Ben-Haim, E. Cogneras, T. Gershon, M. Grabalosa, L. Henry, T. Latham, J.M. Maratas, J. McCarthy, D. Milanes, S. Monteil, R. Silva Coutinho,N. Watson, *Dalitz plot analysis of the decay $B^0 \to K^0_S \pi^+ \pi^-$*, , LHCb-ANA-2014-044.

[135] W. D. Hulsbergen, *Decay chain fitting with a Kalman filter*, Nucl. Instrum. Meth. **A552** (2005) 566, arXiv:physics/0503191.

[136] G. Punzi, *Sensitivity of searches for new signals and its optimization*, eConf **C030908** (2003) MODT002, arXiv:physics/0308063.

[137] LHCb Collaboration, *Branching fraction measurements of $B^0_{d,s}$ decays to $K^0_S h^\pm h'^\mp$ final states, including first observation of $B^0_s \to K^0_S K^\pm \pi^\mp$*, , Link to LHCb-ANA-2012-026.

[138] J. Back *et al.*, *Laura ++: A dalitz plot fitter*, Computer Physics Communications **231** (2018) 198.

[139] M. De Cian *et al.*, *Measurement of the track finding efficiency*, tech. rep., CERN, Geneva, Apr, 2012.

[140] A. Martin Sanchez, P. Robbe, and M.-H. Schune, *Performances of the LHCb L0 Calorimeter Trigger*, tech. rep., CERN, Geneva, Jun, 2012.

[141] V. Lisovskyi, *The calorimeter objects tools group : Documentation page*, 2021.

[142] M. De Cian, *Track Reconstruction Efficiency and Analysis of $B^0 \to K^{*0}\mu^+\mu^-$ at the LHCb Experiment*, Sep, 2013. Presented 14 Mar 2013.

[143] R. W. Johnson, *An introduction to the bootstrap*, Teaching statistics **23** (2001), no. 2 49.

[144] T. Grammatico, *Measurement of the branching fractions of $B^0_{d,s} \to K^0_S h^+ h^-$ decays in LHCb, insights on the CKM angle gamma and monitoring of the Scintillating Fibre Tracker for the LHCb upgrade*, 2022. Presented 27 Jan 2022.

[145] L. Henry, *Charmless hadronic three-body decays of neutral B mesons with a K^0_s in the final state in the LHCb experiment: branching fractions and an amplitude analysis: Désintégrations hadroniques à trois corps sans charme de mésons B avec un K^0_s*

dans l'état final dans l'expérience LHCb : mesure de rapports d'embranchement et une analyse en amplitude, PhD thesis, Sep, 2016, Presented 30 Sep 2016.

[146] G. G. Lorentz, *Bernstein polynomials*, American Mathematical Soc., 2013.

[147] T. Skwarnicki, *A study of the radiative cascade transitions between the Upsilon-prime and Upsilon resonances*, PhD thesis, Institute of Nuclear Physics, Krakow, 1986, DESY-F31-86-02.

[148] R. Aaij *et al.*, *Precise measurement of the f_s/f_d ratio of fragmentation fractions and of B^0_s decay branching fractions*, Physical Review D **104** (2021), no. 3 032005.

[149] B. K. Sinha, J. Hartung, and G. Knapp, *Statistical meta-analysis with applications*, John Wiley & Sons, 2011.